Audrey COTTET

Quantronics group

Implementation of a quantum bit in a superconducting circuit

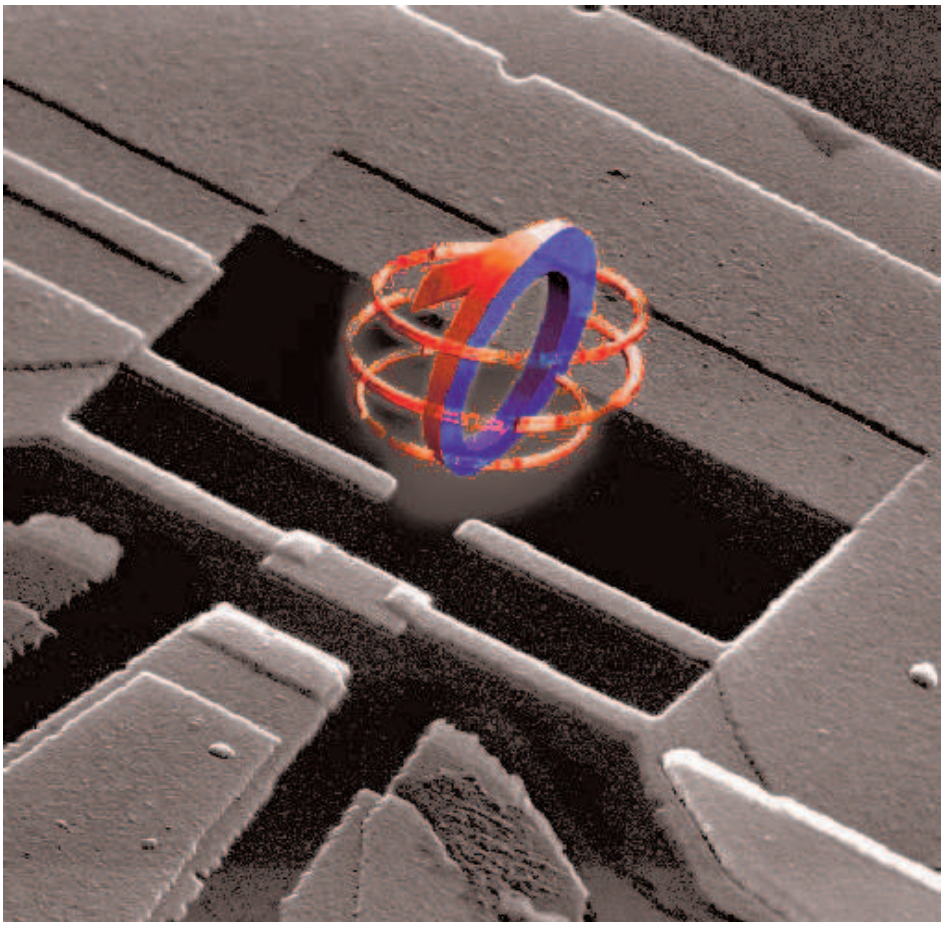

This thesis is also available as a pdf file
on the Quantronics group website:
http://www-drecam.cea.fr/drecam/spec/Pres/Quantro

THESE DE DOCTORAT DE L'UNIVERSITE PARIS VI
spécialité:
Physique des Solides

présentée par:

Audrey COTTET

pour obtenir le grade de DOCTEUR de l'UNIVERSITE PARIS VI

Sujet de la thèse:
IMPLEMENTATION D'UN BIT QUANTIQUE DANS UN CIRCUIT SUPRACONDUCTEUR

Soutenue le 30 Septembre 2002
Devant le jury composé de MM.

Isaac Chuang,
Roland Combescot
Daniel Estève
Frank Hekking,
John Martinis
Hans Mooij

A mes parents,
Françoise Durand et André Cottet

A ma moitié,
Takis Kontos

Remerciements

Le fait que j'aie vivement été attirée par ce sujet de thèse n'est pas étranger à la frustration que je ressentis lorsque, étudiante, on me présenta le principe de la mesure quantique "à l'ancienne mode", c'est à dire comme quelque chose de tout à fait arbitraire. Je voulais comprendre comment fonctionne une mesure quantique, et c'est pourquoi l'annonce passée par le groupe quantronique du Service de Physique de l'Etat Condensé du CEA retint mon attention. Réaliser un appareil de mesure pour un bit quantique m'offrait l'opportunité de voir enfin "de près" comment fonctionne une mesure quantique. J'eus la chance d'être admise dans ce groupe durant l'hiver 1999.

Mon travail de thèse est venu se poser comme une suite logique à des années de recherches effectuées dans le groupe quantronique à propos des circuits supraconducteurs à base de jonctions Josephson. Les expériences dans ce domaine ne sont pas à proprement parler des expériences "coin de table". Elles nécessitent l'apprentissage de nombreuses techniques: nanolithographie électronique poussée à ses limites, cryogénie avec l'utilisation d'un réfrigérateur à dilution, techniques de mesures à bas bruit, utilisation d'hyperfréquences. Autre difficulté, le développement des bits quantiques est soumis à une rude concurrence internationale. Pour augmenter mes chances de succès, il fut convenu que je participerais à un travail d'équipe. Ceci fut extrêmement enrichissant pour moi car je pus aborder bien plus de domaines que je n'aurais pu le faire seule. L'expérience 1, soit la mesure de la caractéristique I-V d'une jonction Josephson à l'aide d'un réseau de SQUIDs, a été principalement réalisée par Andy Steinbach lors de mon stage de DEA. Je l'ai suivi durant quelques jours pour m'initier aux techniques expérimentales utilisées dans le groupe. J'ai ensuite eu beaucoup plus de responsabilités techniques dans la réalisation des deux expériences d'électrométrie (expériences 2 et 3), de la fabrication des échantillons à l'interprétation des données, en passant par la prise de mesures. Après ces expériences, nous avons fait des calculs de temps de décohérence qui m'ont particulièrement tenu à cœur. Ces calculs nous ont permis de comprendre que la voie dans laquelle nous nous étions engagés était trop difficile à suivre et qu'il fallait changer de stratégie pour atteindre l'objectif fixé. Je trouve très émouvant que le dispositif "quantronium" sur lequel nous ayons finalement abouti soit une combinaison d'une grosse jonction Josephson hystérétique, le premier dispositif étudié par le trio fondateur du groupe quantronique, Michel Devoret, Daniel Estève et Christian Urbina, et de la boîte à paires de Cooper développée dans le groupe lors de la thèse de Vincent Bouch-

iat. J'ai été très impliquée dans la définition de cette nouvelle stratégie et dans la réalisation matérielle de l'expérience de faisabilité associée (expérience 4). Lors de l'expérience finale (expérience 5), je me suis plus particulièrement consacrée à interpréter les données et à parfaire ma compréhension des phénomènes de décohérence.

Je tiens à remercier les différentes personnes que j'ai côtoyées durant cette thèse. Merci tout d'abord à Michel Devoret, qui m'a accueillie au SPEC lors de mon stage de DEA et dont j'ai apprécié les qualités de pédagogue. Merci à Andy Steinbach avec qui j'ai interagi au tout début de ma thèse. Pendant ces trois années, j'ai eu la chance d'être encadrée par Daniel Estève, dont l'inspiration et la hauteur de vue forcent l'admiration, et dont j'ai pu également apprécier la disponibilité et la gentillesse. J'ai également eu la chance d'interagir avec Denis Vion, expérimentateur hors pair dont la ténacité et la virtuosité technique ne sont plus à démontrer. Un grand merci également à Abdel Aassime pour s'être beaucoup investi dans la partie expérimentale lorsque j'ai été irrépressiblement attirée par les calculs. Je remercie Philippe Joyez, Hugues Pothier, et Cristian Urbina pour leur esprit critique. Merci à P.F. Orfila, sans les compétences techniques duquel la vie quotidienne au laboratoire serait impossible, et dont j'ai pu également apprécier les compétences en matière de mécanique automobile. Merci aussi à Frédéric Pierre, Ronald Cron, et Anne Anthore dont j'ai apprécié la bonne humeur. Merci à toutes les personnes que j'ai pu rencontrer au SPEC et qui ont contribué à rendre ce séjour agréable. Merci F.I.B Williams, qui, un an avant le début de cette thèse, m'a accueillie pour un stage d'été dans son groupe, et qui m'a ainsi permis de découvrir le monde de la physique. Thanks very much to the members of my thesis committee: Isaac Chuang, Roland Combescot, Frank Hekking, John Martinis and Hans Mooij. Thanks very much to Christoph Bruder and Wolfgang Belzig who have nicely let me finish the writing of this thesis after the beginning of my theoretical post doc at Basel university. Merci à ma chère Capucine, qui a passé tant d'heures à étudier avec moi. Merci enfin à mes parents, André et Françoise Cottet, pour leur amour et leur soutien inconditionnels. Je leur dédie cette thèse, ainsi qu'à Takis Kontos, avec qui l'interaction est toujours très fructueuse, que ce soit en physique ou dans d'autres domaines...

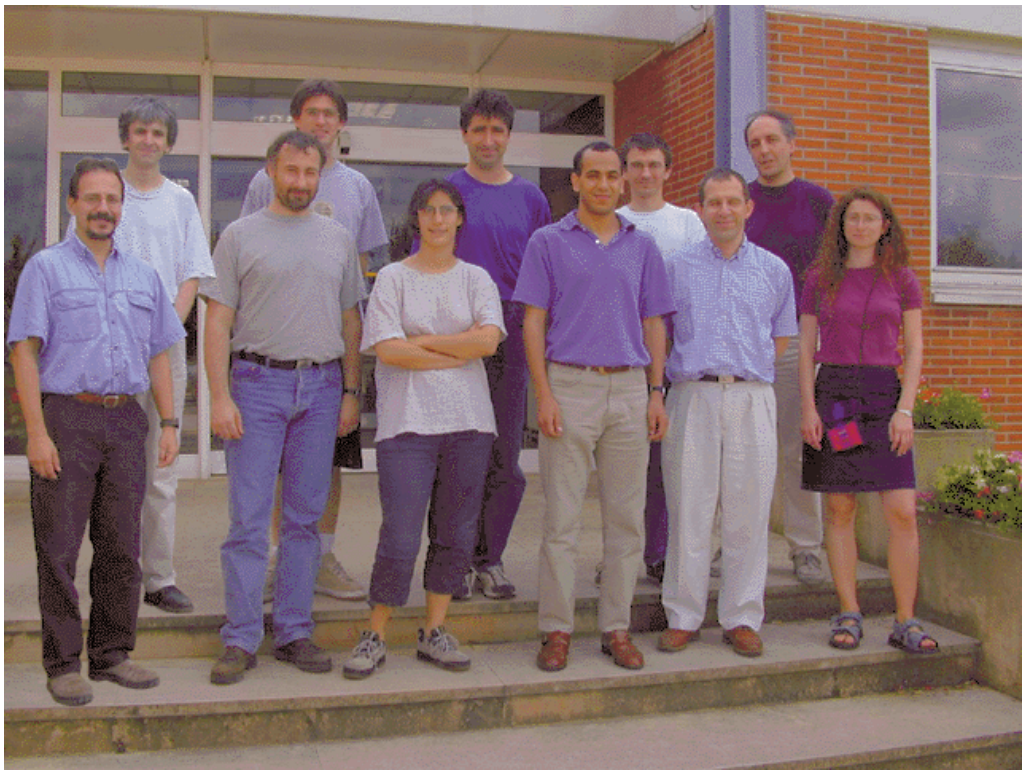

The Quantronics group in August 2001. From left to right and top to bottom: Hugues Pothier, Ronald Cron, "Pief" Orfila, Philippe Joyez, Daniel Estève, Cristian Urbina, Denis Vion, Anne Anthore, Abdel Aassime, Michel Devoret and Audrey Cottet

Contents

Introduction

A. Quantum electrical circuits

A.1 Decoherence of macroscopic systems

Although quantum mechanics was developed to explain the properties of microscopic systems like electrons in atoms, its formalism treats all degrees of freedom, microscopic or macroscopic, on the same footing. Hence, the pioneers of quantum mechanics were puzzled by the non observation of quantum phenomena at the macroscopic level. Why macroscopic objects, made of atoms that behave quantum mechanically, never display quantum effects themselves? Answering this question requires to establish the connection between the quantum and the classical descriptions. The Copenhagen interpretation of quantum mechanics actually circumvents this problem since it treats quantum and classical systems differently. The projection postulate states that when a quantum system interacts with a classical measurement apparatus, the quantum system is projected onto a subspace determined by the result of the measurement. Despite internal consistency and agreement with the experimental facts, this formalism is a black box which explains neither the mechanisms involved in a measurement process, nor the apparent irrelevancy of quantum mechanics at the macroscopic level. This slackness is best captured by the famous Schrödinger's cat paradox [1]. This thought experiment focuses on a macroscopic system, namely a cat, with two types of states: "dead states" and "alive states". The cat's state gets entangled with that of a radioactive atom, so that after some time it becomes a superposition of both the dead and the alive states. Why such strange states never show up was fully justified only in the late seventies, when the theory of decoherence explained within the framework of quantum mechanics that the cat is only in a statistical sense in a superposition of the dead and the alive states [2]. Within very general hypotheses, this theory proves that the reduced density matrix of a quantum system in interaction with the numerous degrees of freedom of a measurement apparatus becomes diagonal after a usually very short time. This coherence time is furthermore incredibly short for a quantum system with many degrees of freedom itself, which explains why macroscopic objects behave classically.

A.2 Macroscopic quantum electrical circuits

However, nothing forbids for a macroscopic system to behave quantum mechanically when its numerous microscopic degrees of freedom are tied together to form a few collective ones. This point was made particularly clear by A. J. Leggett who suggested at the beginning of the eighties that macroscopic electrical circuits could behave quantum mechanically provided they are sufficiently decoupled from the outside world. Together with O. Caldeira, they proved that a quantum property like tunneling should be observable for a collective electrical variable of a micron-sized junction between two superconductors [3]. Moreover, they predicted that the tunneling rate would be affected only moderately by the other degrees of freedom of the circuit. These predictions were found in excellent agreement with the tunneling rate measurements conducted at Berkeley and at Saclay on current-biased Josephson junctions [4]. The direct spectroscopy of quantum levels in various junction circuits further proved beyond any doubt that electrical circuits can indeed behave quantum mechanically [4, 5].

A.3 The art of quantum computing

The general interest in quantum electrical circuits strongly increased in the nineties, when the power of quantum mechanics for computing purposes was discovered. At first glance, using quantum mechanics for processing information appears paradoxical because the underlying uncertainty in quantum mechanics seems incompatible with exactness. However, Deutsch and Joza exhibited a quantum algorithm solving a simple discrimination problem more efficiently than any classical one [6]. This pioneering work demonstrated that quantum computers could perform better than classical ones for some specific tasks. Shor's discovery in 1994 of a quantum algorithm able to factorize large numbers in polynomial time with the number size [7] came as breaking news. It indeed proved that quantum computers could perform strategic tasks beyond reach of usual computers whatever their speed gains in the future.

Quantum computing is based on the linearity of quantum mechanics combined with a clever evolution of the quantum state of the machine [8, 9]. First, linearity ensures that any unitary quantum processor treating a superposition of input states produces the corresponding superposition of output states. However, this massive built-in parallelism is not directly useful : its benefit is in general lost when the output state is measured since only one particular outcome state is obtained. Quantum algorithms combine evolution and measurement steps in such a way that the answer to the problem is necessarily the outcome of the final projective measurement. Up to now only a handful of quantum algorithms have been discovered.

The issue of the robustness of quantum computers with respect to computational errors was the next problem in line after the algorithms. Quantum error correcting codes based on redundancy were invented in 1996 [10, 11]. They prove that a quantum processor does not need to be perfect and can endure a small amount of decoherence[1]. As a rule of thumb, these

[1]It is worth noticing that a significant fraction of the ressources of a conventional processor is dedicated to

codes can be used in a quantum processor provided it is able to perform in average 10^4 logic operations without error [12].

A.4 Physical implementations of quantum computers

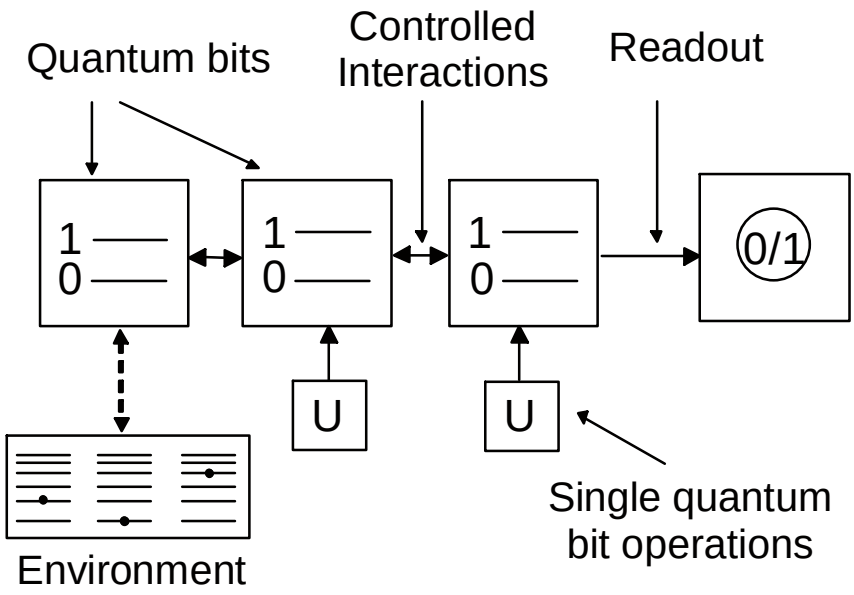

Figure 1: *A quantum processor consists of a collection of interacting quantum bits which can be independently manipulated and measured. The coupling with the environment should be kept low enough to maintain quantum coherence.*

This series of theoretical breakthroughs triggered an intense search for physical systems in which quantum algorithms could be implemented. An ideal quantum processor would consist of a collection of two level systems called quantum bits, or qubits (Figure 1). These qubits must be quantum coherent, independently addressable, measurable when necessary, and their interactions must be controllable. These requirements are extremely difficult to conciliate, and only a few systems, fulfilling at most some of these criteria, have been proposed.

The first ones were microscopic systems like atoms and ions because they are naturally quantum coherent. Quantum gates have already been demonstrated using an assembly of a few trapped ions [13]. However, addressing the optical levels and performing the readout for each ion in larger systems remains a tremendous challenge. Presently, the most advanced system consists of the nuclear spins of well-chosen organic molecules, manipulated and measured using NMR techniques. Recently, Shor's factorization algorithm has been implemented for the integer 15 using 7 spin-1/2 nuclei of a molecule [14]. However, this technique which makes use of a large number of ancillas does not allow to address and measure the qubits independently. Due to the

error correction.

randomness in the initial thermal population of the Zeeman states, the NMR signal arising from multi qubit entanglement decreases exponentially with the number of qubits involved, which sets an upper limit to the size of a processor.

At the opposite of microscopic systems, electronic circuits are not naturally quantum coherent, but they are more easily scalable because they are fabricated using lithography techniques [15]. They are furthermore simple to drive and to readout since they only require electrical signals propagating on wires. At the time of this writing, about ten electronic qubit projects are being developed [16], and many other ones have been proposed. This thesis describes some strategies to implement a quantum bit in a particular type of superconducting circuit, the so-called "Cooper-pair box".

B. Previous experiments on the Cooper pair box

The "Cooper pair box", a circuit based on the competition between the Josephson and single Cooper pair charging effects, was first investigated at the beginning of the nineties [17]. Soon after, it was shown to be a good candidate to implement a quantum bit [18, 19].

B.1 Energy levels

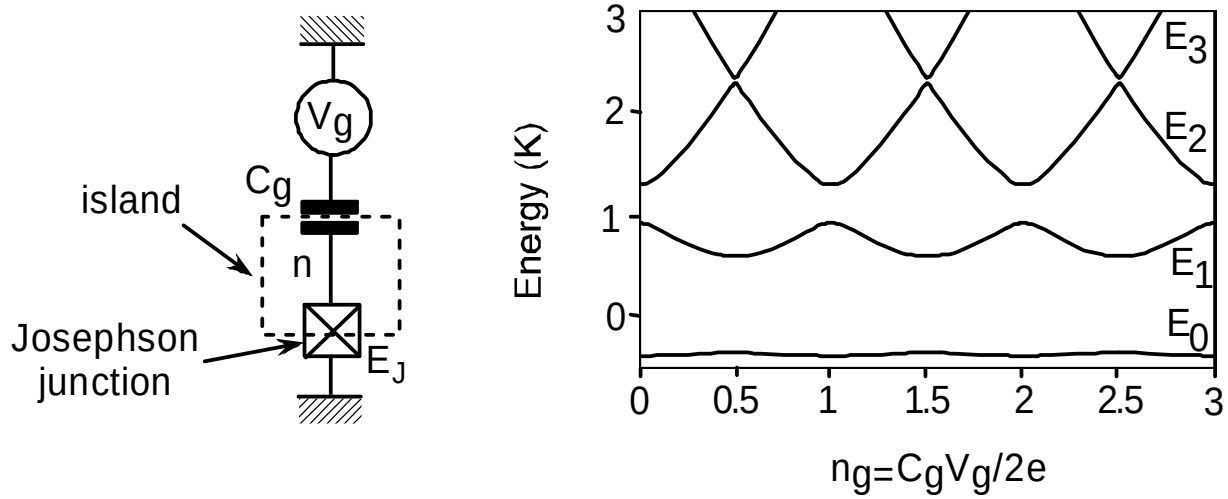

Figure 2: *The Cooper pair box. Left panel: Electrical scheme showing the Josephson junction, the superconducting island, the gate, and the gate source of the box. Right panel: Low energy region of the energy spectrum calculated for* $E_J = E_C = 1$ $\mathrm{k}_b\mathrm{K}$ *and plotted as a function of the gate voltage expressed in reduced units. The spectrum is* $2e$*-periodic with the gate charge.*

The basic Cooper pair box consists of a low capacitance superconducting electrode, the island, connected to a superconducting reservoir by a Josephson junction with capacitance C_J and

Josephson energy E_J, and biased by a voltage source V_g in series with a gate capacitance C_g (Figure 2). In addition to E_J, the box has a second energy scale, the Cooper pair Coulomb energy $E_C = (2e)^2/(2(C_J + C_g))$, where e is the charge of one electron. The electrostatic Hamiltonian is diagonal in the charge state basis $|\mathbf{n}\rangle$, where $\mathbf{n}$ is the number of extra Cooper pairs in the island, whereas the Josephson Hamiltonian couples state $|\mathbf{n}\rangle$ to states $|\mathbf{n} \pm \mathbf{1}\rangle$. As a result of this competition, the eigenstates of the box are superpositions of several charge states. The energy spectrum is anharmonic, and varies periodically with the reduced gate charge $n_g = C_g V_g/2e$. For a wide range of parameters, the ground and first excited states $|0\rangle$ and $|1\rangle$ form an effective two level system which can be used as a qubit. The manipulation of this qubit can be achieved by applying resonant microwave pulses on the gate. The qubit state determination can be done through a measurement of the island charge, which depends on the state of the box.

B.2 Determination of the energy of state $|0\rangle$

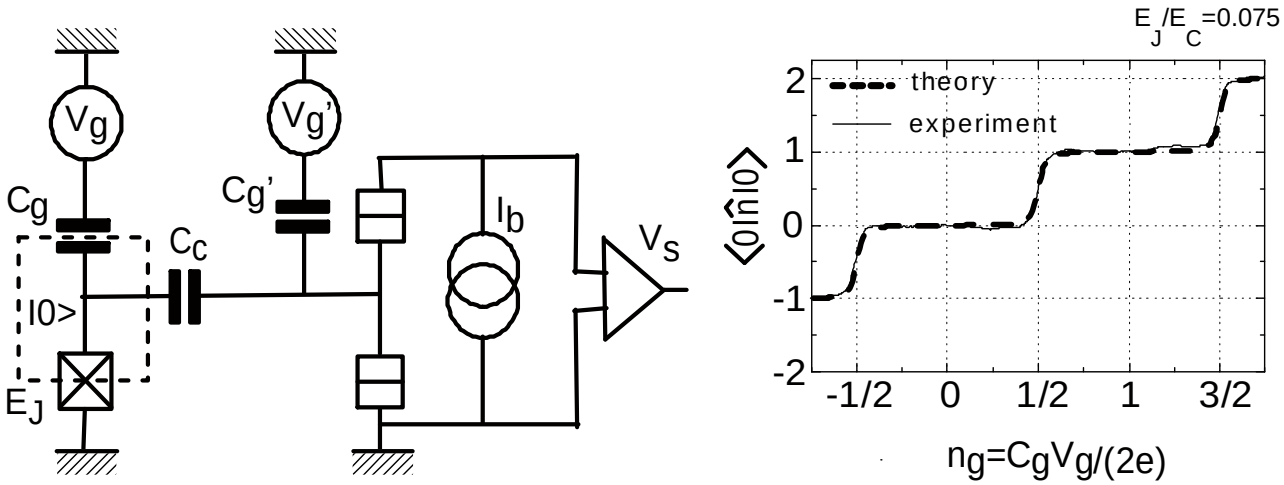

Figure 3: *Left panel: Electrical scheme of the experiment of V. Bouchiat et al* [17]. *The average charge of the Cooper pair box island is measured with a single electron transistor based electrometer, coupled capacitively to the island box. Right panel: Measured mean charge* $\langle 0|\,\widehat{\mathbf{n}}\,|0\rangle$ *of the box in its ground state* $|0\rangle$ *as a function of the reduced gate charge, for* $E_J/E_C = 0.075$. *Due to this small ratio, the ground state* $|0\rangle$ *is almost an eigenstate of the charge operator, except in the neighborhood of half integer values of* n_g, *where it is a superposition of two charge states differing by one Cooper pair.*

V. Bouchiat *et al.* [17, 18] first determined the dependence of the ground state energy on the gate voltage. In this experiment (Figure 3), the Cooper-pair box island is weakly coupled through a small capacitor to a single electron transistor which measures the mean island voltage V, and thus the mean average number of extra Cooper-pairs in the island, $\langle 0|\,\widehat{\mathbf{n}}\,|0\rangle = eV/E_c + n_g$. This

measurement is equivalent to the determination of the ground state energy since $\partial E_0/\partial n_g = 2eV$. When the gate charge is varied, the island charge displays a Coulomb staircase pattern in good agreement with the predictions.

B.3 Preparation of coherent superpositions of states $|0\rangle$ and $|1\rangle$

The next step was performed by Nakamura *et al.*, from NEC, who succeeded in performing the spectroscopy of a Cooper pair box and preparing coherent superpositions of the states $|0\rangle$ and $|1\rangle$ [19]. In this experiment, the population of state $|1\rangle$ was inferred from the current I_d through an auxiliary ultrasmall Josephson junction connected to the island, and permanently biased above the gap voltage by a constant voltage source V_d (Figure 4). The spectroscopy was carried out by applying a continuous microwave voltage to the gate, and by sweeping the DC gate voltage (Figure 5). Resonant population of state $|1\rangle$ is revealed by a peak in the measured current I_d when the energy splitting matches the microwave frequency ν_{RF}, i.e. when $h\nu_{RF} = h\nu_{01} = (E_1 - E_0)$.

The manipulation of the quantum state was performed through non adiabatic perturbation of the Hamiltonian by applying to the gate square pulses with a very short rise time. The average current I_d, measured while repeating the gate pulses, oscillates with the pulse duration τ, revealing coherent Rabi oscillations between states $|0\rangle$ and $|1\rangle$. However, the coherence time of this superposition never exceeded a few nanoseconds because of the decoherence induced by the invasive readout device and/or by the charge noise generated by microscopic charges randomly moving in the vicinity of the island and possibly in the junction oxide itself [20]. This charge noise exists in all charging devices, and has a $1/f$ power spectrum with a typical amplitude $10^{-7}\ e^2$ for metallic devices (probed up to $f = 10$ MHz).

B.4 Can the Cooper-pair box be used as a qubit?

Although this last experiment proved that the Cooper pair box is an appealing candidate for implementing a qubit, its readout strategy, based on a permanent measurement of the quantum state, does not allow to perform single measurements and to achieve long coherence times. An ideal readout system should be switchable in order to allow for time-resolved single measurements, induce negligible decoherence when it is off, and provide high-fidelity measurements when it is on. In order to perform single measurements, we have investigated two types of readout strategies, respectively based on charge and current measurements. These readout strategies should also be designed so that the Cooper-pair box is as immune as possible to the charge noise which has possibly limited the coherence time in the experiments we have described.

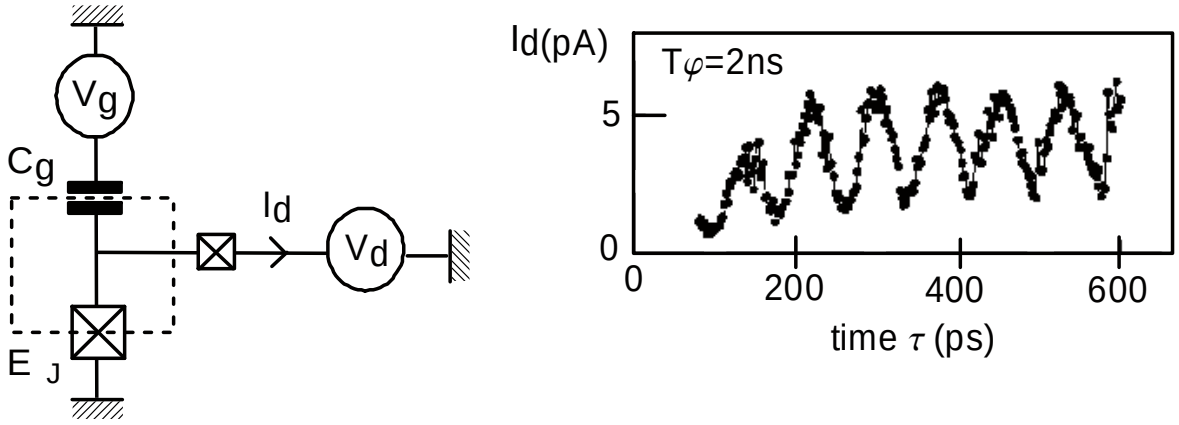

Figure 4: *Coherent manipulation of the quantum state of a Cooper pair box, in the experiment of Y. Nakamura et al.* [19]. *Left panel: Simplified electrical scheme of the experiment. A fast voltage pulse is applied to the gate to bring the system at the charge degeneracy point* $n_g = 1/2$. *The sudden change of the hamiltonian induces Rabi oscillations between the* $|0\rangle$ *and* $|1\rangle$ *states during the pulse duration* τ. *Right panel: Oscillations of the occupation probability of state* $|1\rangle$ *are revealed by oscillations of the current probe* I_d *with* τ.

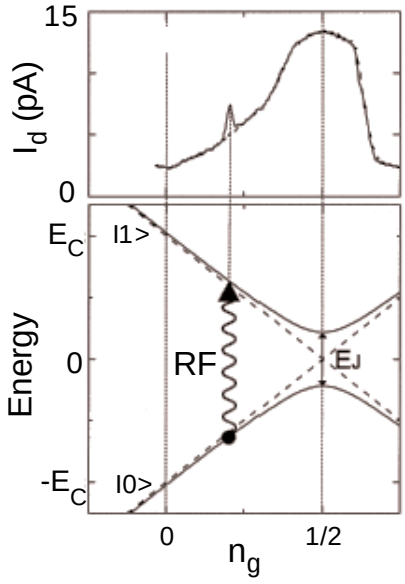

Figure 5: *Spectroscopy of the Cooper pair box. The energy difference between states* $|0\rangle$ *and* $|1\rangle$ *is measured by applying to the gate continuous radiofrequency signals at different frequencies and by sweeping the gate charge* n_g. *Top panel: A resonant increase of the current* I_d *through the probe junction (see text) is observed when* n_g *is such that the energy difference matches the applied frequency. Bottom panel: Energy diagram illustrating the excitation of the box by radiofrequency irradiation. Solid lines represent eigenenergies of the box whereas dashed lines show the electrostatic energy of charge states.*

C. Charge measurement of the Cooper pair box

We have developed new types of electrometers in order to discriminate qubit states from the difference of their average island charges. The usual single electron transistor set-up is indeed far too slow for time-resolved measurements because of the high impedance of the transistor. The group at Chalmers University has developed a radiofrequency impedance measurement technique which allows submicrosecond measurements [21]. However, the RF-SET induces unwanted relaxation from state $|1\rangle$ to state $|0\rangle$. Our motivation for developing new electrometers was thus to achieve time-resolved charge measurements while inducing as little relaxation as possible. These new electrometers are based on the single Cooper pair transistor, which behaves as a charge-controlled Josephson junction.

C.1 The single Cooper pair transistor

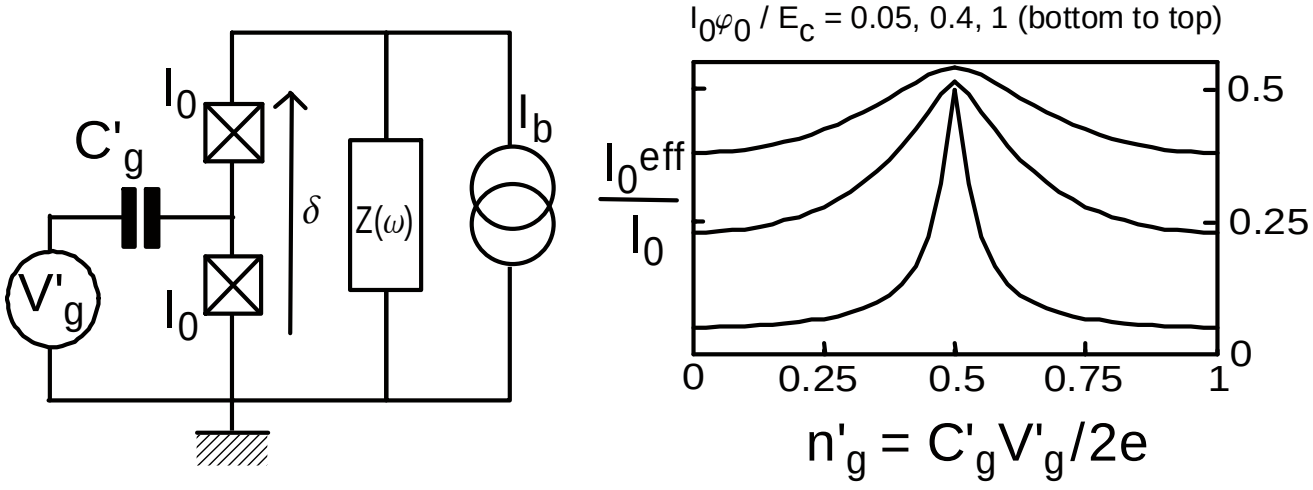

Figure 6: *The Cooper pair transistor or Bloch transistor. Left panel: Electrical scheme. Two Josephson junctions (with critical current I_0) and a gate capacitor delimit the transistor island. The gate voltage V_g' determines the effective critical current of the transistor, which is biased by a current source with impedance $Z(\omega)$. Right panel: Predicted modulation of the critical current I_0^{eff} of the transistor with the reduced gate charge $n_g^{'}$.*

The Cooper pair transistor [22] consists of a Cooper pair box with its Josephson junction split into two junctions connected to a biasing circuit (Figure 6). When maintained in its ground state $|0\rangle$, the Cooper pair transistor behaves as a tunable Josephson junction with a critical current $I_0^{eff}(n_g')$ varying periodically with the gate charge n_g'. This superconducting device can thus be used as a sub-electron electrometer, that is an electrometer able to detect a charge smaller than $2e$. Contrarily to the single electron transistor, in which the electrons entering and

exiting the transistor island produce a back-action on the measured system with a shot noise spectrum, the supercurrent through the single Cooper pair transistor produces a back-action which follows the fluctuations of the phase across it, and thus has no shot-noise. The dynamics of this phase is controlled by the embedding circuit, and the noise arises from the thermal fluctuations in the dissipative elements. The mechanisms responsible for decoherence during the measurements are thus very different from those acting in the single electron transistor, which is a further reason for investigating this type of electrometer. Depending on the impedance seen by the transistor, two types of measurement are possible, as discussed below.

C.2 Continuous charge measurement with a DC-shunted Cooper pair transistor

We have measured the $I-V$ characteristic of a DC shunted transistor using a SQUID series array developed at NIST [23]. We have first tested this SQUID-based technique by measuring the $I-V$ of a single small Josephson junction (experiment 1, reference [24]). Then, we have fabricated the circuit described in Figure 7, in which a fraction of the current flowing through the shunt resistor of the transistor is diverted in the input coil of the SQUID array amplifier (experiment 2, reference [25]). We have measured the response of this electrometer to a gate charge step $\Delta n_g'$. The achieved sensitivity is $3.10^{-4}\ e/\sqrt{\mathrm{Hz}}$ within a 1 MHz bandwidth, limited by the SQUID array noise and cut-off frequency. Although the bandwidth compares to that of the RF-SET, the sensitivity is worse by about two orders of magnitude, which could however be greatly improved by optimizing the array characteristics for this specific application. We have also found that heavy filtering was required in order to protect the circuit under measurement from the noise produced by the Josephson oscillations in the array. Our conclusion is that this electrometer is not presently suitable for the readout of the Cooper-pair box.

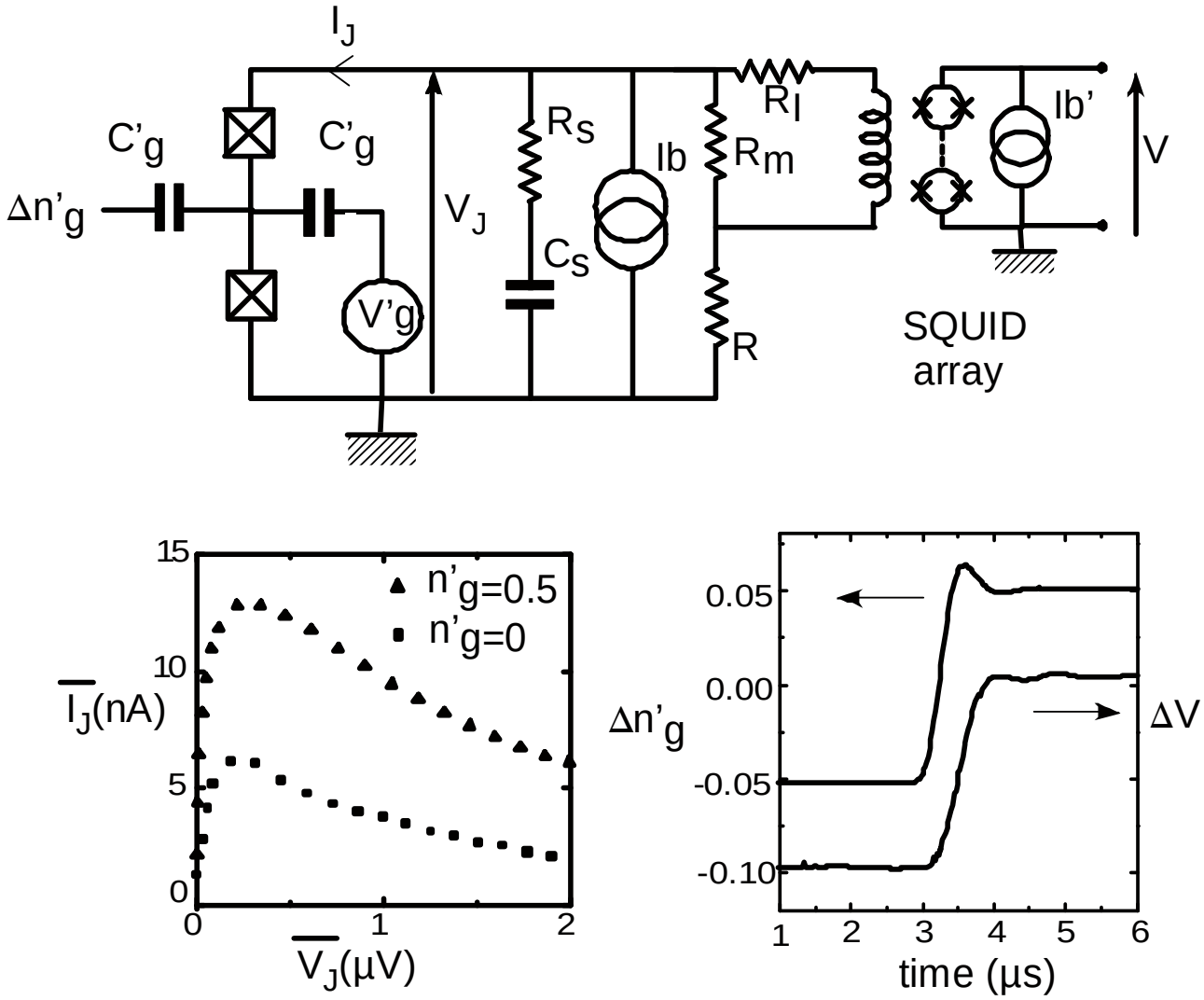

Figure 7: *Electrometer based on a DC shunted single Cooper pair transistor. Top panel: Electrical scheme. Bottom left panel: Measured current voltage characteristic of the transistor for* $n_g' = 0$ *and* $n_g' = 0.5$. *(*$\overline{I_J}$ *and* $\overline{V_J}$ *correspond to* I_J *and* V_J *averaged over the phase dynamics of the transistor). Bottom right panel: Detection of a charge step of the input charge (*1 MHz *bandwidth, averaged over* 4000 *traces).*

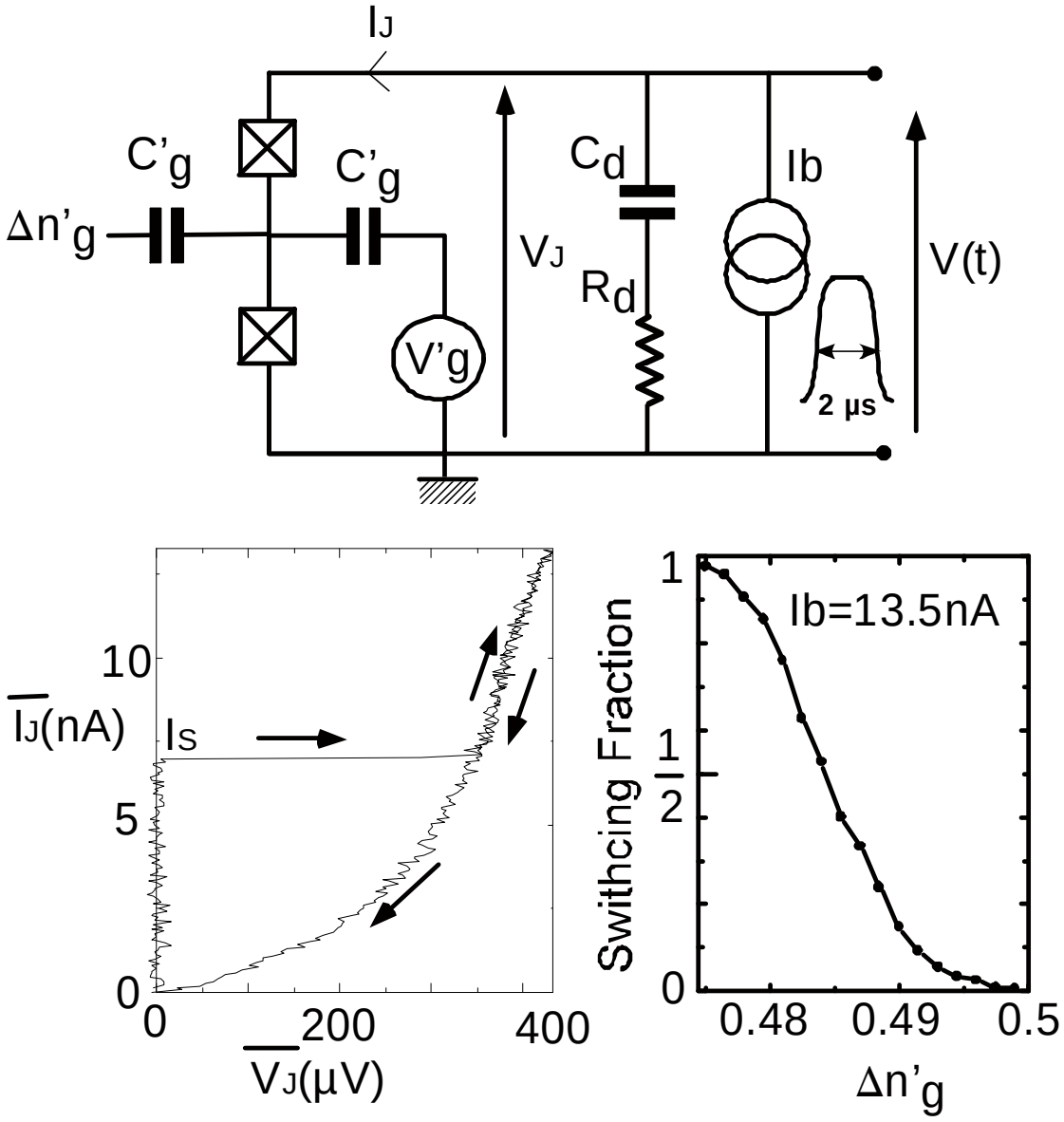

Figure 8: *Superconducting electrometer based on an overdamped DC unshunted single Cooper pair transistor. Top panel: Electrical scheme showing the RC shunt in parallel with the current source and the transistor. Bottom left panel: Single shot current voltage characteristic of the transistor for a bias current ramping speed of* 690 nA/s. *The transistor jumps to a non-zero voltage state at a value I_s of the bias current, called the switching current. When a square bias current pulse is applied, the transistor switches with a probability that depends on the height of the pulse and on the gate charge. Bottom right panel: Experimental switching probability of a transistor as a function of the gate charge for* 2 μs *long current pulses with amplitude* 13.5 nA.

C.3 Pulsed charge measurement with a DC-unshunted Cooper pair transistor

The second strategy to measure the critical current of the Cooper pair transistor is to keep it unshunted at DC (Figure 8), so that it switches to the voltage-state when the bias current I_b approaches the critical current [26]. The voltage which develops after this stochastic switching can then be detected using a room temperature amplifier. We have measured the probability of switching as a function of n'_g, for square bias current pulses with duration τ (experiment 3, reference [27] and Figure 8). We have found that such an electrometer allows to detect a gate charge variation $\Delta n'_g$ as small as 2% of a Cooper pair in a measuring time $\tau = 2$ μs with a confidence level of 97%. This corresponds to an equivalent sensitivity of 2 10^{-5} e/$\sqrt{\text{Hz}}$ within a 1 MHz bandwidth. Again, this sensitivity is not as good as that of the best RF-SET, but this design allows better control of the back-action on the Cooper pair box. We have calculated in detail this back-action, and found in particular that the decoherence due to the transistor can be made negligible when the readout current is zero, and that the induced relaxation from state $|1\rangle$ to state $|0\rangle$ can be made low enough during the measurement itself. We note however that the superconducting electrometer does not reach the quantum limit in the sense that it would induce full decoherence of the Cooper pair box before it has completed the measurement.

It is important to point out that the above mentioned sensitivity was obtained only over short periods of time during which the gate charge was by-chance sufficiently stable. Indeed, low frequency charge fluctuators with amplitudes larger than the 0.01 e accuracy required in the gate tuning were often observed, thus preventing the proper operation of the device.

C.4 The drawback of charge measurements

Whatever the electrometer, the charge measurement strategy suffers from a severe drawback: measuring the charge of the Cooper-pair box island indeed requires biasing the Cooper-pair box at values of n_g where both states $|0\rangle$ and $|1\rangle$ have different island charges, i.e. when $\partial\nu_{01}/\partial n_g \neq 0$. But it is clearly more favorable to manipulate the quantum state at a value of n_g where $\partial\nu_{01}/\partial n_g = 0$, since there charge fluctuations have no effect on the transition frequency at first order. The charge readout of the Cooper-pair box thus requires to vary n_g just before measuring the qubit state. Furthermore, better immunity to charge noise is achieved when $\partial\nu_{01}^2/\partial n_g^2$ is small, which requires large ratios E_J/E_C, i.e. a small difference between the island charges in states $|0\rangle$ and $|1\rangle$. All this makes difficult to conciliate charge noise immunity and high resolution charge measurements in the Cooper pair box.

D. The quantronium: a quantum bit prototype

In view of the weaknesses plaguing the charge readout strategy of the Cooper-pair box, we have considered an alternative strategy based on the measurement of a current in a modified Cooper pair box circuit.D.1 The split Cooper pair box

D.1 The split Cooper pair box

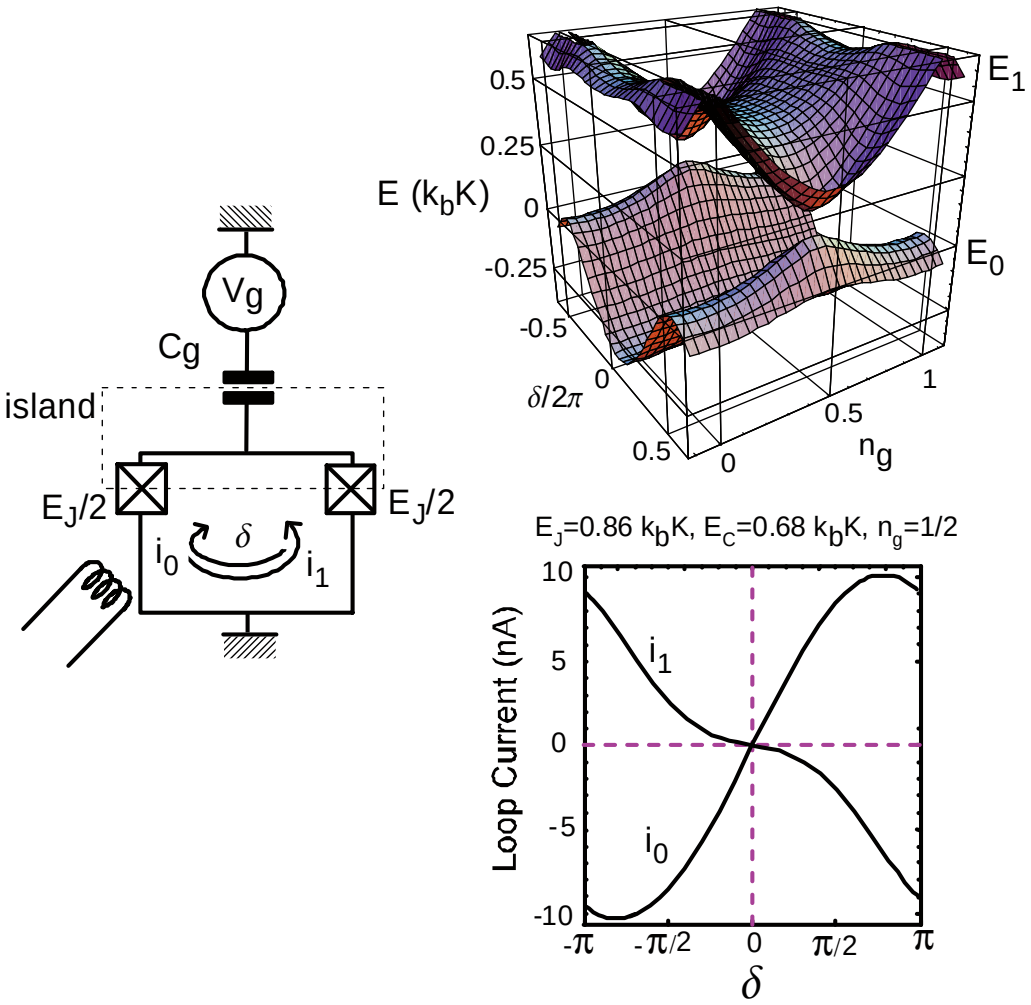

Figure 9: *The split Cooper pair box. Left panel: Electrical scheme. The Josephson junction of a Cooper pair box is split in two nominally identical junctions in order to form a superconducting loop, which can sustain state-dependent persistent currents. The superconducting phase difference δ across the series combination of the two junctions can be controlled by the magnetic flux through the loop. Top right panel: Energy of states $|0\rangle$ and $|1\rangle$ as a function of the gate charge n_g and of the phase difference δ. Bottom right panel: Loop currents i_0 and i_1 of $|0\rangle$ and $|1\rangle$, as a function of δ for $n_g = 1/2$.*

In this circuit [28], shown in Figure 9, the junction is split into two junctions with energy $E_J/2$ forming a superconducting loop. The superconducting phase difference δ across the series combination of the two junctions, proportional to the flux through the loop, is a new external parameter that controls the energy spectrum. Persistent mean loop currents $i_0 = \frac{2e}{\hbar}\frac{\partial E_0}{\partial \delta}$ and $i_1 = \frac{2e}{\hbar}\frac{\partial E_1}{\partial \delta}$ are present in the states $|0\rangle$ and $|1\rangle$ and provide a new readout port different from the charge port used for state manipulation: instead of measuring a charge, the states can be discriminated through the loop currents. A Cooper pair box with a larger E_J/E_C ratio can thus be used, leading to a reduced sensitivity to charge noise. As explained below, protection from charge and phase noise during state manipulation is achieved by biasing the circuit at the working point ($n_g = 1/2,\ \delta = 0$) where the transition frequency ν_{01} is stationary with respect to both external parameters.

D.2 State readout

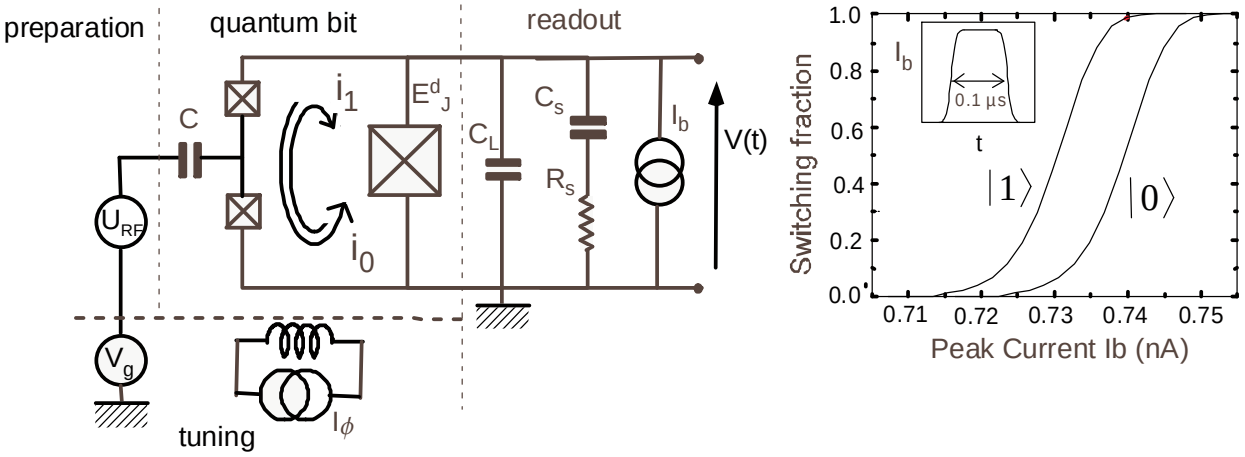

Figure 10: *The quantronium. Left panel: Electrical scheme showing the different functional blocks. The readout block biases and measures an additional Josephson junction used as a current threshold detector. This junction switches to the non-zero voltage state when a readout current pulse is applied with different probabilities for the two states* $|0\rangle$ *and* $|1\rangle$*. Right panel: Switching probabilities of the readout junction for state* $|0\rangle$ *(measured) and for state* $|1\rangle$ *(calculated) for a* 100 ns *long readout pulse with variable height.*

In order to measure the loop currents, we have inserted in the loop of the split box a third, large Josephson junction with an energy $E_J^d \gg E_J$ (Figure 10). The resulting circuit has been nicknamed "quantronium". When a bias current pulse with a suitable amplitude I_b is applied to the parallel combination of the large junction and of the two small junctions, the phase δ deviates from 0 and the loop current which develops adds to I_b in the large junction. The large junction can then be made to switch with a large probability for state $|1\rangle$ and a small one for

state $|0\rangle$, so that the outcome of each single measurement is switching (no switching) with a probability equal to the weight of state $|1\rangle$ ($|0\rangle$) in the measured quantum state. The circuit remains at the optimal working point during quantum state manipulation and the measurement process can be triggered at will. In a preliminary experiment, we have characterized the isolated detection junction, by measuring its switching probability as a function of the height of bias current pulses (experiment 4, reference [28]). This experiment has shown that pulsed measurements of the switching current of the junction are possible without degrading the current resolution, despite the large bandwidth of the biasing circuit. We have then implemented a complete device (experiment 5, reference [29, 30, 31, 32, 33]).

D.3 Spectroscopy of the quantronium

We have performed the spectroscopy of a quantronium sample as a function of δ at $n_g = 1/2$, and as a function of n_g at $\delta = 0$, by detecting the resonant increase of the switching probability when a microwave voltage with a small amplitude is applied at the qubit transition frequency before readout (Figure 12). As predicted, the linewidth gets sharper when the bias point gets closer to the optimal point ($n_g = 0.5,\ \delta = 0$) where the transition frequency is stationary with respect to both control parameters. The best quality factor, obtained at this point, is 2×10^4 (Figure 12, inset), which is sufficient to perform coherent manipulations of the quantum state.

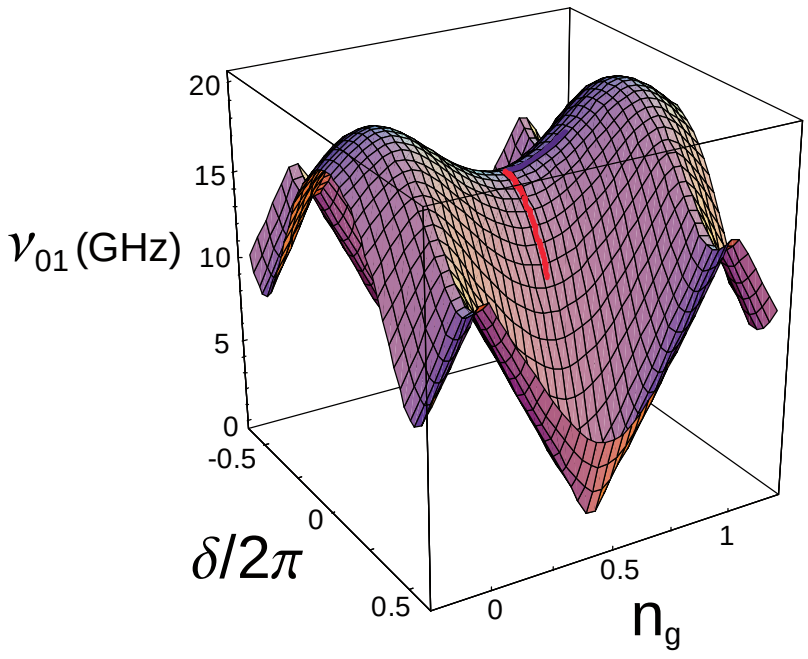

Figure 11: *Calculated transition frequency* ν_{01} *as a function of* n_g *and* δ *for* $E_J = 0.86$ k_bK *and* $E_C = 0.68$ k_bK.

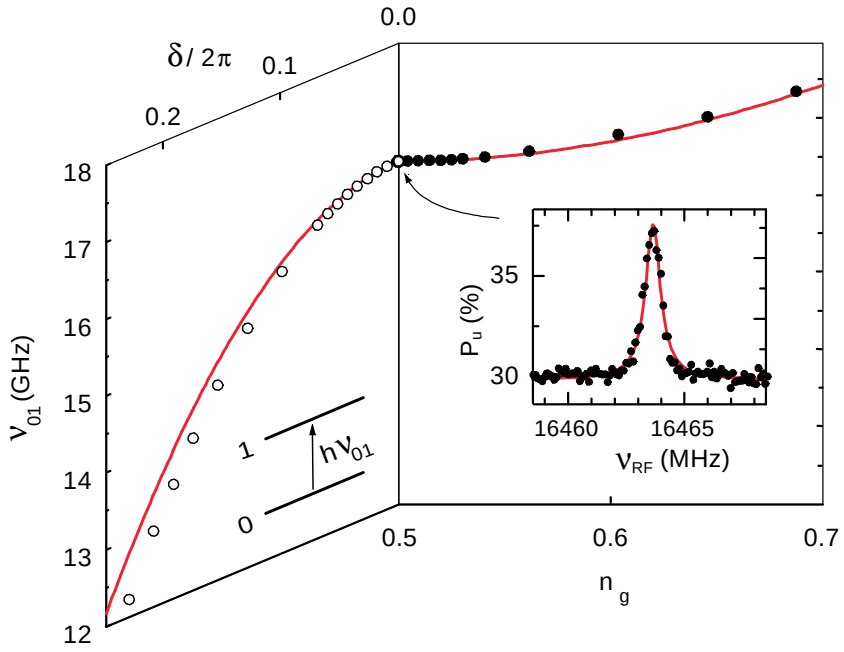

Figure 12: *Measured* ν_{01} *at* 15 mK *for* $n_g = 0.5$ *(open symbols), and for* $\delta = 0$ *(full symbols). Solid lines have been calculated with* $E_J = 0.86$ k_bK *and* $E_C = 0.68$ k_bK. *Inset: resonance lineshape at the optimal working point* $n_g = 1/2$ *and* $\delta = 0$. *The corresponding quality factor is* 2.10^4.

D.4 Coherent manipulation of the quantronium

The manipulation of the quantum state has been performed by applying microwave pulses to the gate electrode, at frequencies ν_{RF} close to the transition frequency ν_{01}. Starting from state $|0\rangle$, such a pulse builds a superposition $\cos(\theta_u/2)\,|0\rangle + \sin(\theta_u/2)\,|1\rangle$ of the eigenstates, where the rotation angle θ_u is proportional to the pulse amplitude U_{RF} and to its duration τ. After the pulse, the quantum state evolves ideally as $\cos(\theta_u/2)\,|0\rangle + \sin(\theta_u/2)\,e^{i\varphi_u(t)}\,|1\rangle$, with $\varphi_u(t) = 2\pi\nu_{01}t$. Any arbitrary quantum state can thus be prepared by combining a microwave pulse and a free evolution.

Observation of Rabi oscillations

The evolution of the quantum state over multiple turn rotations, *i.e.* Rabi oscillations [34], was observed by measuring the switching probability as a function of the pulse duration τ (Figure 13). The frequency of these oscillations varies linearly with the amplitude U_{RF} of the radiofrequency signal, as expected. That many turns can be piled up without significant decay of the amplitude further demonstrates that the qubit state is manipulated without inducing much decoherence. Note that Rabi oscillations have also been recently observed in other Josephson qubit circuits [35, 36, 37].

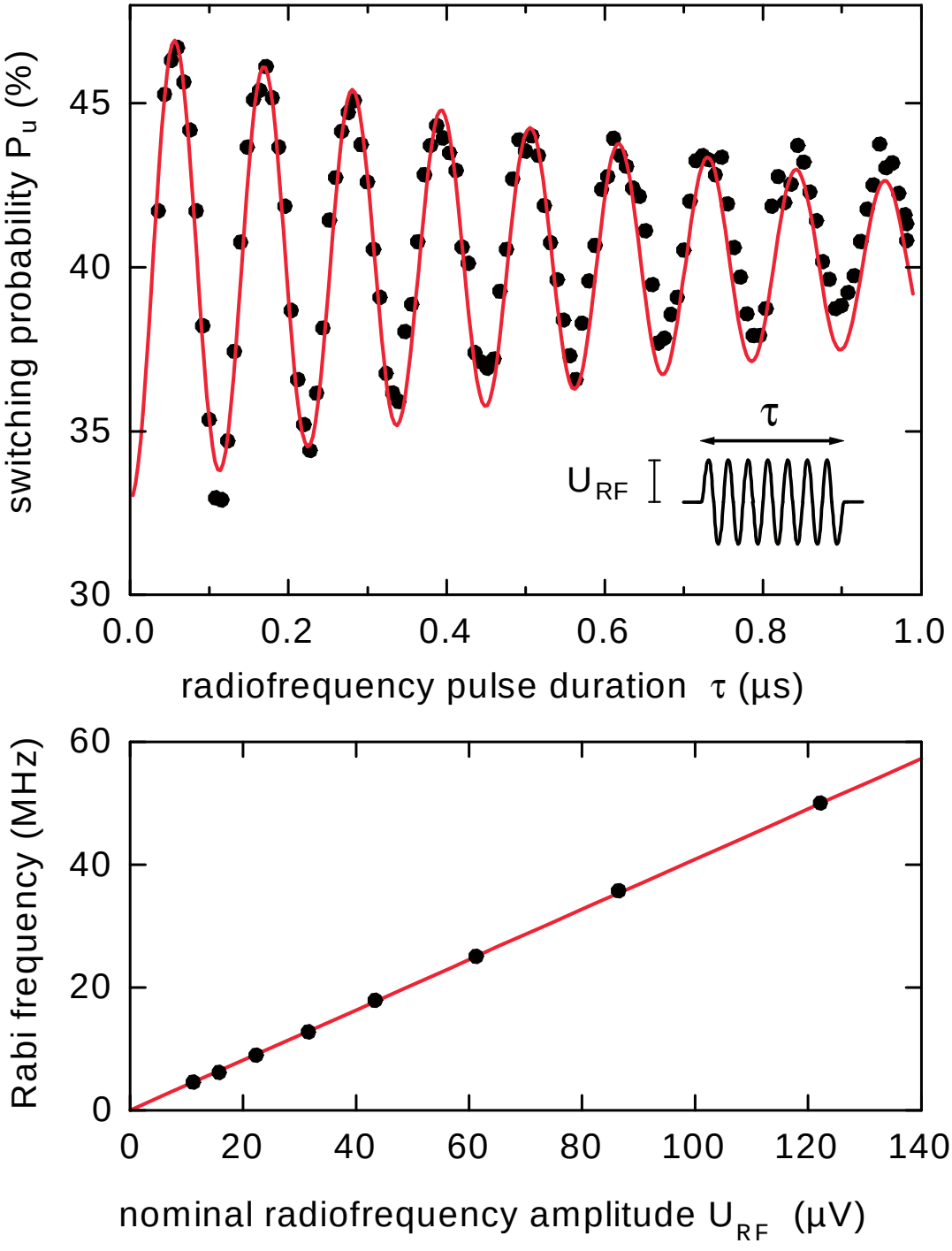

Figure 13: *Observation of microwave driven Rabi oscillations between the* $|0\rangle$ *and* $|1\rangle$ *states of the quantronium. Top panel: Experimental switching probability (dots) of the readout junction, immediately after a resonant microwave pulse with duration* τ*. The line is a fit by an exponentially damped sinusoid giving the Rabi frequency. Bottom panel: Measured Rabi frequency (dots) as a function of the amplitude of the radiofrequency pulse. The observed linear dependence is in agreement with theory.*

Probing decoherence during free evolution

In order to determine the coherence time of the quantronium during its free evolution, the system was first driven from state $|0\rangle$ to the superposed state $(|0\rangle + |1\rangle)/\sqrt{2}$ by a first microwave pulse. Then, it was left to evolve freely during a time Δt, during which uncontrolled degrees of freedom of the whole circuit induce decoherence. A second pulse finally drives the quantronium to a state having probability amplitudes on $|0\rangle$ and $|1\rangle$ that depend on the phase $\varphi_u(\Delta t)$. The resulting Ramsey-like oscillations of the switching probability [38] occur at the stroboscopic frequency $\nu_{RF} - \nu_{01}$, and decoherence is revealed by the decay of the amplitude of the oscillations with Δt. The longest coherence time obtained is $T_2 = 0.5$ μs, which corresponds to a quality factor $Q = \pi \nu_{01} T_2 \approx 2.5 \times 10^4$.

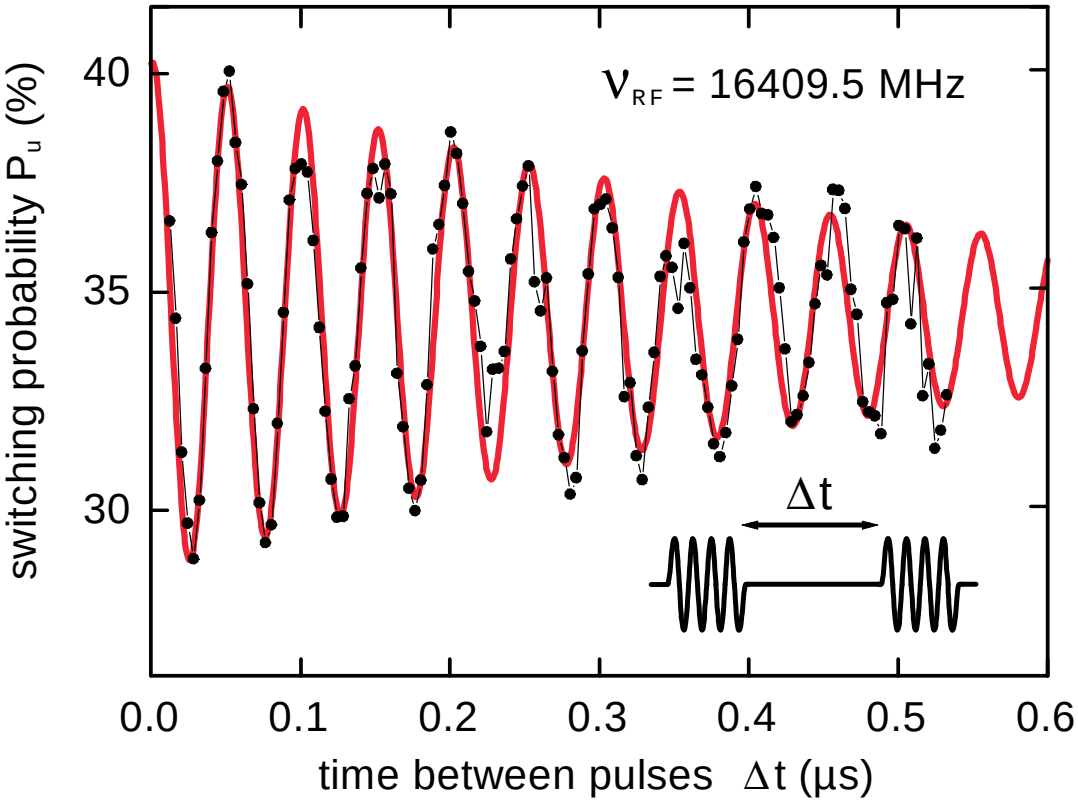

Figure 14: *Determination of the coherence time T_2 during the free evolution of the quantronium. A sequence of two phase-coherent microwave pulses separated by time Δt is applied to the gate. This sequence prepares at time 0 a coherent superposition of states $(|0\rangle + |1\rangle)/\sqrt{2}$ and analyses it at time Δt. The amplitude of the observed Ramsey oscillations decays with the characteristic time T_2. Dots: Measured switching probability of the readout junction after the pulse sequence. Continuous line: Fit of the oscillatory pattern by an exponentially damped sinusoid with time constant $T_2 = 0.5$ μs.*

E. Conclusion

Electrical circuits are in general so strongly coupled to their environment that they do not behave quantum mechanically. Nevertheless, we have shown in this thesis work that, by an appropriate design of a superconducting circuit, it is possible to reduce the coupling to a sufficient extent so that the quantum state of the circuit can be manipulated over the coherence time scale. Even if the goal of a high fidelity readout of the state was not reached, the measurement scheme we have developed has the great advantage of being switchable, so that its effect during manipulation of the state is weak. In these respects, the quantronium can be considered as a qubit. The next step towards a quantum processor is to demonstrate quantum logic gate operations with coupled quantronium circuits, which seems feasible given the level of quantum coherence already achieved.

The Josephson junction

A Josephson junction consists of two superconducting electrodes separated by a thin insulating layer [39, 40]. It can be modeled by a capacitance C_J in parallel with a pure Josephson element with Josephson energy E_J. The Josephson element allows for the tunnelling of Cooper pairs. Its hamiltonian $\widehat{H}_J$ can be written on the basis of charge eigenstates $\{|\mathbf{n}\rangle, \mathbf{n} \in \mathbb{Z}\}$ associated to the number $\widehat{\mathbf{n}}$ of Cooper pairs having crossed the junction:

$$\widehat{H}_J = -\tfrac{E_J}{2} \sum_{n\in\mathbb{Z}} \left(|\mathbf{n}\rangle \langle \mathbf{n}+\mathbf{1}| + |\mathbf{n}+\mathbf{1}\rangle \langle \mathbf{n}|\right) |\mathbf{n}\rangle \ , \tag{1.1}$$

with $$\widehat{\mathbf{n}}\,|\mathbf{n}\rangle = \mathbf{n}\,|\mathbf{n}\rangle.$$

The usual expression for $\widehat{H}_J$ is recovered using the fact that $\widehat{\mathbf{n}}$ and the superconducting phase difference $\widehat{\delta}$ across the junction are conjugated variables (see Appendix 1-A):

$$\widehat{H}_J = -E_J \cos(\widehat{\delta}). \tag{1.2}$$

The actual hamiltonian of the junction must also include the electrostatic hamiltonian associated to its capacitance C_J.

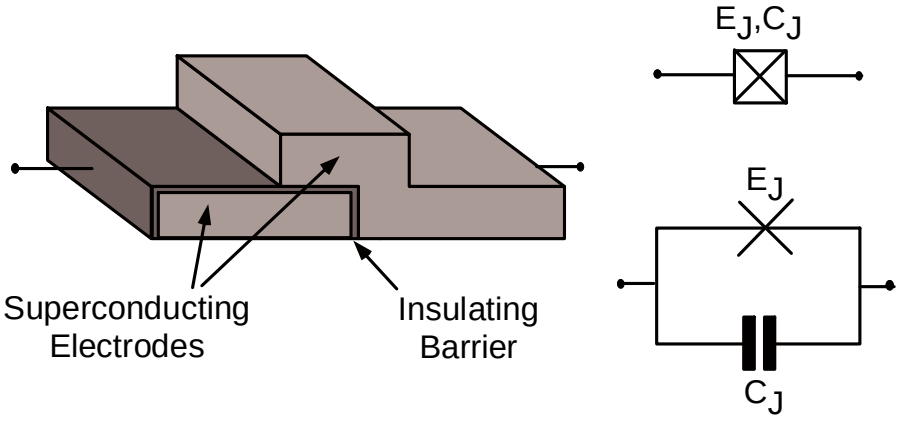

Left: Sketch of a Josephson junction. Top Right: Electrical symbol. Bottom Right: Decomposition into a capacitor and a pure Josephson element.

Chapter 1

Cooper pair boxes and transistors

In this chapter, we describe the Cooper pair box [17, 41]*, which is the simplest single Cooper pair device, and two split-junction versions, namely the split Cooper pair box and the single Cooper pair transistor* [22, 42].

1.1 The basic Cooper pair box

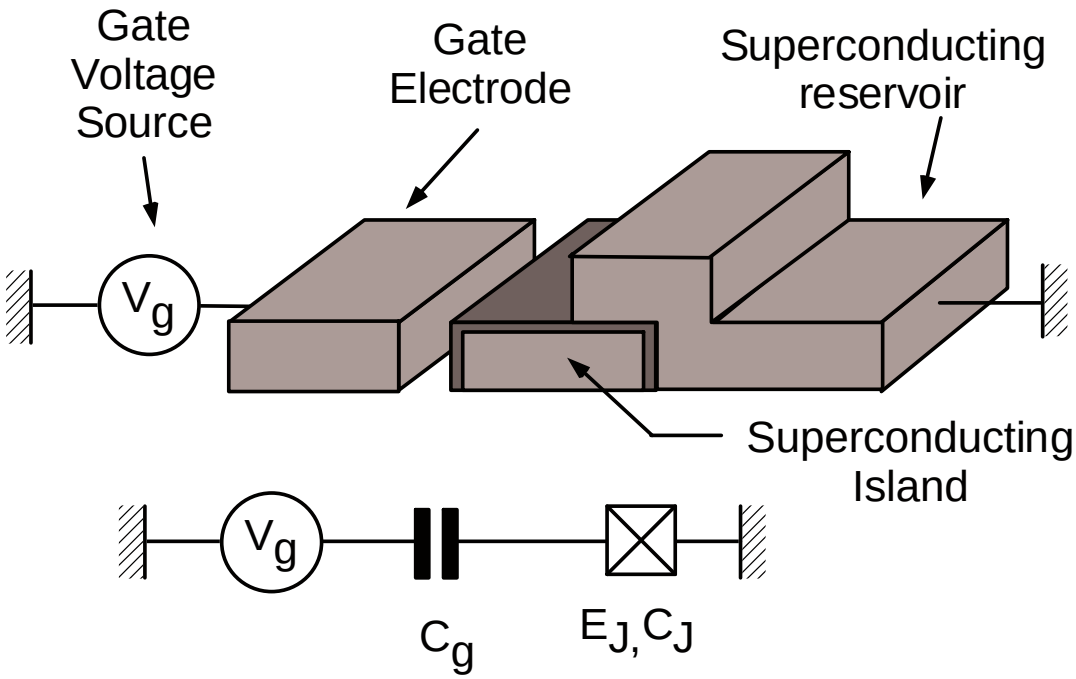

Figure 1.1: *The Cooper pair box. Top: Schematic representation of the Cooper pair box and of its biasing circuit, showing the Josephson junction with energy E_J and capacitance C_J, the superconducting island, the gate, and the gate voltage source V_g. Bottom: Corresponding electrical scheme.*

1.1.1 The Cooper pair box circuit

The basic Cooper pair box [17, 41] consists of a low capacitance superconducting electrode, called the island, connected to a superconducting reservoir by a Josephson junction with capacitance C_J and Josephson energy E_J, and biased by a voltage source V_g in series with a gate capacitance C_g (Figure 1.1). In addition to E_J, the box has a second energy scale, the Cooper Pair Coulomb energy:

$$E_C = \frac{(2e)^2}{2C_\Sigma} \ , \tag{1.3}$$

where

$$C_\Sigma = C_g + C_J \tag{1.4}$$

is the total capacitance of the island[1].

1.1.2 Charge representation

Let $\widehat{\mathbf{n}}$ be the operator associated to the number of Cooper pairs in excess from neutrality in the metallic island (more commonly called "the number of excess Cooper pairs"). The eigenstates $|\mathbf{n}\rangle$ of $\widehat{\mathbf{n}}$ verify[2]:

$$\widehat{\mathbf{n}}\,|\mathbf{n}\rangle = \mathbf{n}\,|\mathbf{n}\rangle \ , \ \mathbf{n} \in \mathbb{Z} \ .$$

At energies lower than the BCS gap, i.e. when no quasiparticles are present in the island, the set $\{|\mathbf{n}\rangle \, , \mathbf{n} \in \mathbb{Z}\}$ forms a complete basis for the states of the box. The total hamiltonian of the box includes two different terms. First, the electrostatic hamiltonian of the circuit writes [43]:

$$\widehat{H}_{el} = E_C(\widehat{\mathbf{n}} - n_g)^2 \ , \tag{1.5}$$

where

$$n_g = \frac{C_g V_g}{2e} \tag{1.6}$$

is the reduced gate charge. The hamiltonian of the box also includes the Josephson hamiltonian which accounts for the tunneling of the Cooper pairs through the Josephson junction. Since $\widehat{\mathbf{n}}$ identifies with the number of Cooper pairs having passed through the junction, the Josephson term writes [see (1.1) p.35]:

[1] We have typically fabricated islands with an area of 1 μm×100 nm and aluminum Josephson junctions with an area of 100 nm×100 nm. This results in C_g of the order of 10 aF, C_J of the order of 1 fF, and $E_C \simeq (2e)^2/(2C_J)$ of the order of 4 k_bK. E_J is controlled independently with the oxydation of the junctions and falls in the same range for the experiments we have performed.

[2] The index $\mathbf{n} \in \mathbb{Z}$ used in the charge state $|\mathbf{n}\rangle$ is written in bold type in order to distinguish $|\mathbf{n}\rangle$ from the total energy eigenstates $|k\rangle$, $k \in \mathbb{N}$ of the Cooper pair box, which are defined in next page. For instance, $|\mathbf{0}\rangle$ is the charge state with no extra Cooper pairs in the island whereas $|0\rangle$ is the ground state of the Cooper pair box.

$$\widehat{H}_J = -\frac{E_J}{2}(\sum_{\mathbf{n}\in\mathbb{Z}} |\mathbf{n}\rangle \langle \mathbf{n+1}| + |\mathbf{n+1}\rangle \langle \mathbf{n}|) \ . \tag{1.7}$$

This term couples consecutive charge states. In summary, the total hamiltonian of the box writes in the charge representation:

$$\boxed{\widehat{H}(n_g) = \sum_{\mathbf{n}\in\mathbb{Z}} \left[E_C(\mathbf{n}-n_g)^2 |\mathbf{n}\rangle \langle \mathbf{n}| - \tfrac{E_J}{2}(|\mathbf{n}\rangle \langle \mathbf{n+1}| - |\mathbf{n+1}\rangle \langle \mathbf{n}|)\right] \ .} \tag{1.8}$$

The spectrum associated to this hamiltonian is discrete and 1-periodic on n_g . Let us call $|k\rangle$ the energy eigenstates and E_k their associated energies:

$$\widehat{H}(n_g)\,|k\rangle = E_k\,|k\rangle \ , \tag{1.9}$$

with $k \in \mathbb{N}$. The convention used in this thesis is to label the levels such that E_k increases with k, starting from $k = 0$ for the ground state. In order to determine the states $|k\rangle$ and the energies E_k, one can diagonalize numerically the restriction of $\widehat{H}(n_g)$ to a subspace of a few charge states. An example of energy spectrum obtained with this method is given in Figure 1.2. Note that the Josephson coupling lifts the electrostatic energy degeneracies present at $n_g = 1/2$ [mod 1] .

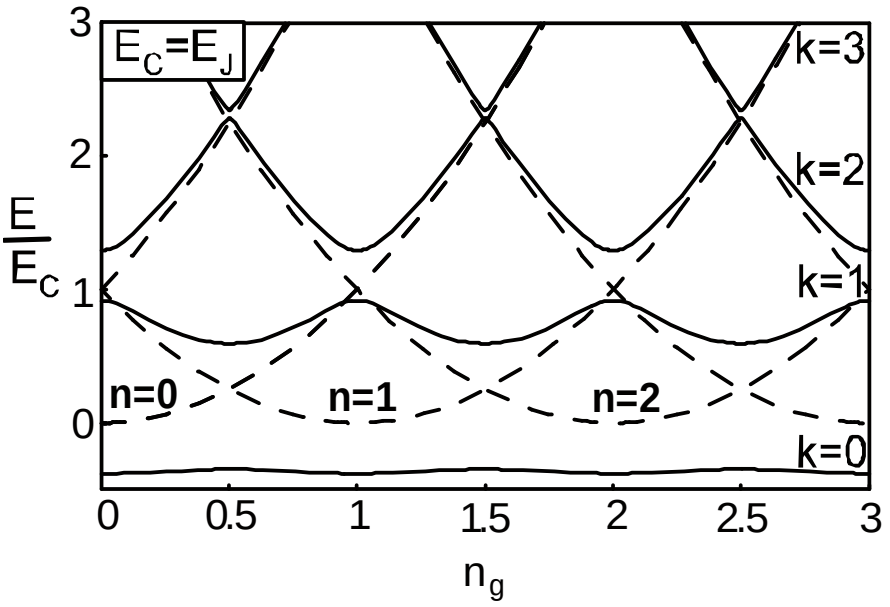

Figure 1.2: *Full lines: Eigenenergies of a Cooper pair box with $E_C = E_J$, calculated by diagonalizing the hamiltonian $\widehat{H}$ in the charge representation, in a subspace of 10 charge states. Dotted lines: Electrostatic energies of the charge states. Note that the degeneracies between the energies of neighbouring charge states occurring at $n_g = \frac{1}{2}$ [mod 1] are lifted by the Josephson coupling.*

1.1.3 Phase representation

Hamiltonian in the phase representation

The operator conjugated to $\widehat{\mathbf{n}}$ is the superconducting phase $\widehat{\theta}$ of the island (Appendix 1-A), with eigenstates $|\theta\rangle$ such that:

$$\widehat{\theta}\,|\theta\rangle = \theta\,|\theta\rangle \ . \tag{1.10}$$

The phase space associated to $\widehat{\theta}$ has a circular topology:

$$|\theta\rangle \equiv |\theta + 2\pi\rangle \ . \tag{1.11}$$

The set $\{|\theta\rangle\ ,\ \theta \in [0, 2\pi[\}$ forms a complete basis of the box states. In the phase representation, the operator $\widehat{\mathbf{n}}$ writes [Appendix 1-A formula (1.77)]:

$$\widehat{\mathbf{n}} = \frac{1}{\mathbf{i}}\frac{\partial}{\partial\theta}\ , \tag{1.12}$$

with $\mathbf{i} = \sqrt{-1}$ the unitary imaginary number. The effect of the operators $\exp(\mathbf{i}\widehat{\theta})$ and $\exp(-\mathbf{i}\widehat{\theta})$ on the charge states is [Appendix 1-A formula (1.75)]:

$$\exp(\pm\mathbf{i}\widehat{\theta})\,|\mathbf{n}\rangle = |\mathbf{n} \pm 1\rangle \ . \tag{1.13}$$

Therefore, in the phase representation, the total hamiltonian $\widehat{H}$ of the box is:

$$\boxed{\widehat{H}(n_g) = E_C(\tfrac{1}{\mathbf{i}}\tfrac{\partial}{\partial\theta} - n_g)^2 - E_J\cos(\widehat{\theta})\ .} \tag{1.14}$$

Analytical expressions of the eigenstates $|k\rangle$ and of their energies E_k can be obtained by solving the Schrödinger equation associated to this hamiltonian.

Schrödinger equation in the phase representation

From (1.14), the wavefunction $\Psi_k(\theta) = \langle\theta\,|k\rangle$ and its associated energy E_k satisfy the Schrödinger equation:

$$E_C(\frac{1}{\mathbf{i}}\frac{\partial}{\partial\theta} - n_g)^2\Psi_k(\theta) - E_J\cos(\theta)\Psi_k(\theta) = E_k\Psi_k(\theta)\ . \tag{1.15}$$

Boundary condition

Since the phase space associated to θ is circular, $\Psi_k(\theta)$ must satisfy the periodic boundary condition:

$$\Psi_k(\theta) = \Psi_k(\theta + 2\pi)\ . \tag{1.16}$$

Solutions of the Schrödinger equation in terms of Mathieu functions

Since (see Appendix 1-A, formula 1.75):

$$\exp(-\mathbf{i}n_g\widehat{\theta})\widehat{H}(n_g)\exp(\mathbf{i}n_g\widehat{\theta}) = \widehat{H}(n'_g = 0) \ , \tag{1.17}$$

the function

$$\varphi_k(\theta) = \exp(-\mathbf{i}n_g\theta)\Psi_k(\theta)$$

is a solution of the equation:

$$-E_C\frac{\partial^2}{\partial\theta^2}\varphi_k(\theta) - E_J\cos(\theta)\varphi_k(\theta) = E_k\varphi_k(\theta) \ . \tag{1.18}$$

The equation (1.18) takes the form of a Mathieu equation:

$$\frac{\partial^2 y(z)}{\partial z^2} - 2q\cos(2z)y(z) = -ay(z) \ , \ z \in \ ]-\infty, +\infty[\ , \tag{1.19}$$

with

$$\theta = 2z, \ y(z) = \varphi_k(2z), \ q = -2E_J/E_C, \ a = 4E_k/E_C \ . \tag{1.20}$$

The solutions of this equation are analytically known [44]. The Mathieu functions[3] $\mathcal{M}_C(a,q,z)$ and $\mathcal{M}_S(a,q,z)$, are the textbook solutions of (1.19) respectively even and odd in z . Note that when $q = 0$, these Mathieu functions are simply:

$$\begin{aligned} \mathcal{M}_C(a,0,z) &= \cos(\sqrt{a}z) \\ \mathcal{M}_S(a,0,z) &= \sin(\sqrt{a}z) \ . \end{aligned} \tag{1.21}$$

According to Floquet's theorem, the Mathieu functions can be recast in the form:

$$\begin{aligned} \mathcal{M}_C(a,q,z) &= \exp(\mathbf{i}rz) * mc(z) \\ \mathcal{M}_S(a,q,z) &= \exp(\mathbf{i}rz) * ms(z) \ , \end{aligned} \tag{1.22}$$

with $r(a,q)$ a real parameter and $mc(z)$ and $ms(z)$ π-periodic on z . The Mathieu functions $\mathcal{M}_C(a,q,z)$ and $\mathcal{M}_S(a,q,z)$ are periodic only if r is integer or rational. The eigenvalue a associated to a given Mathieu function can be expressed as a function of the parameters r and q . For instance, the eigenvalues a associated respectively to $\mathcal{M}_C(a,q,z)$ and $\mathcal{M}_S(a,q,z)$ are the textbook functions $a = \mathcal{M}_A(r,q)$ and $a = \mathcal{M}_B(r,q)$. If r is not an integer, $\mathcal{M}_A(r,q) = \mathcal{M}_B(r,q)$. Therefore, for $n_g \in \ ]0, 1/2[$, the functions Ψ_k can be written using the Mathieu functions:

$$\Psi_k(r,q,\theta) = \mathcal{C}_1\exp(\mathbf{i}n_g\theta)\mathcal{M}_C(\frac{4E_k}{E_C}, -\frac{2E_J}{E_C}, \frac{\theta}{2}) + \mathcal{C}_2\exp(\mathbf{i}n_g\theta)\mathcal{M}_S(\frac{4E_k}{E_C}, -\frac{2E_J}{E_C}, \frac{\theta}{2}) \ . \tag{1.23}$$

[3] The Mathieu functions are implemented in the software Mathematica 4 as:
$\mathcal{M}_A(a,q,z) = MathieuCharacteristicA[a,q,z]$
$\mathcal{M}_C(a,q,z) = MathieuC[a,q,z]$
$\mathcal{M}_S(a,q,z) = MathieuS[a,q,z]$

with

$$E_k = \frac{E_C}{4}\mathcal{M}_A(r, -\frac{2E_J}{E_C}) \ .$$

One then just has to find the values r, $\mathcal{C}_1$ and $\mathcal{C}_2$ associated to Ψ_k . The periodic boundary condition (1.16) together with (1.20), (1.22) and (1.23) implies $n_g + \frac{r}{2} \in \mathbb{Z}$. Therefore, for each value of n_g, only a discrete set of values of r, called r_k, with $k \in \mathbb{N}$, are possible. Each value r_k can be associated to an eigenfunction Ψ_k . The convention used in this thesis is to order the values of r_k such that E_k increases with k . This leads to:

$$r_k = k + 1 - (k+1)[\text{mod } 2] + 2n_g(-1)^k \ . \tag{1.24}$$

Note that k even corresponds to $n_g + \frac{r_k}{2} \geq 0$ and k odd to $n_g + \frac{r_k}{2} < 0$. These equations also allow to find the coefficients $\mathcal{C}_1$ and $\mathcal{C}_2$ associated to each Ψ_k . For $n_g \in]0, 1/2[$:

$$\boxed{\begin{cases} E_k = E_C\mathcal{M}_A(k+1-(k+1)[\text{mod } 2] + 2n_g(-1)^k, -\frac{2E_J}{E_C}) \\ \langle\theta\,|k\rangle = \Psi_k(\theta) = \frac{\exp(\mathbf{i}n_g\theta)}{\sqrt{2\pi}}[\mathcal{M}_C(\frac{4E_k}{E_C}, -\frac{2E_J}{E_C}, \frac{\theta}{2}) + \mathbf{i}(-1)^{k+1}\mathcal{M}_S(\frac{4E_k}{E_C}, -\frac{2E_J}{E_C}, \frac{\theta}{2})] \ . \end{cases}} \tag{1.25}$$

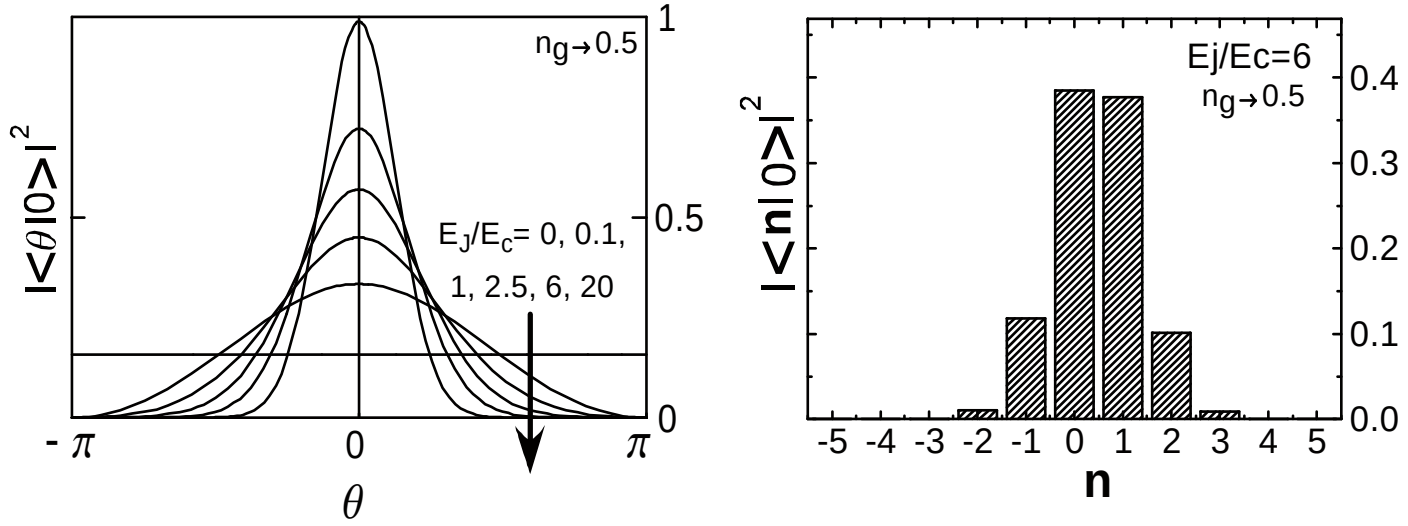

Figure 1.3: *Left panel: Probability amplitude* $|\Psi_0(\theta)|^2$ *in the ground state* $|0\rangle$*, for* $n_g \to 0.5$ *and* $E_J/E_C = 0,\ 0.1\ ,2.5\ ,6\ ,20$*. Right panel: Charge decomposition of* $|0\rangle$ *for* $E_J/E_C = 6$ *and* $n_g \to 0.5^-$*.*

These results can be used to plot the probability amplitude $|\Psi_0(\theta)|^2$ of θ in the ground state $|0\rangle$ (Figure 1.3, left panel). When $E_J/E_C = 0$, the eigenstate $|0\rangle$ is just the charge state $|\mathbf{0}\rangle$. Hence, in agreement with the Heisenberg uncertainty principle, the phase θ is completely undetermined and $|\Psi_0(\theta)|^2$ is constant. When E_J/E_C increases, the phase θ becomes more localized, because the number of charge states $|\mathbf{n}\rangle$ contributing to $|k\rangle$ increases (Figure 1.3, right panel).

We have checked that the diagonalisations of the hamiltonian in the charge and the phase representations lead to identical results. The resolution in phase space is more convenient when one needs to calculate the derivatives of the eigenenergies with respect to n_g and δ .

1.1.4 Island potential

The potential of a superconducting electrode is related to its superconducting phase $\widehat{\theta}$ by the generalized Josephson equation [39] {see Appendix 1-A, Formulas (1.70) and (1.85)}:

$$\widehat{V} = \varphi_0 \frac{d\widehat{\theta}}{dt} \ . \tag{1.26}$$

where

$$\varphi_0 = \frac{\hbar}{2e}$$

is the reduced flux quantum. Since $\widehat{\theta}$ and $\widehat{\mathbf{n}}$ are conjugated variables, Equation (1.26) can be recast as [Appendix 1-A Formulas (1.79) and (1.81)]:

$$\widehat{V} = \frac{\mathbf{i}}{2e}\left[\widehat{\theta}, \widehat{H}\right] = -\frac{1}{2e}\widehat{\left(\frac{\partial H}{\partial \mathbf{n}}\right)} \ . \tag{1.27}$$

Since $\widehat{H}$ is a function of only $(n_g - \widehat{\mathbf{n}})$, this relation transforms into:

$$\widehat{V} = \frac{1}{2e}\frac{\partial \widehat{H}}{\partial n_g} \ . \tag{1.28}$$

By inserting the expression (1.5) of $\widehat{H}$ in this formula, one recovers the textbook result:

$$\widehat{V} = \frac{(2e)(n_g - \widehat{\mathbf{n}})}{C_\Sigma} \ . \tag{1.29}$$

This expression implies that a measurement of the instantaneous potential of the island projects the box on the charge states $|\mathbf{n}\rangle$. An electrometer weakly coupled the box rather projects the box on one of the states $|k\rangle$ (see chapter 3) and measures the average potential $\left\langle k \left| \widehat{V} \right| k \right\rangle$ associated to it, which is, from (1.28),

$$\left\langle k \left| \widehat{V} \right| k \right\rangle (n_g) = \frac{1}{2e}\frac{\partial E_k(n_g)}{\partial n_g} \ . \tag{1.30}$$

1.2 The split Cooper pair box

1.2.1 Physical structure

The split Cooper pair box is a Cooper pair box with a Josephson junction split into two junctions with respective Josephson energies $E_J(1+d)/2$ and $E_J(1-d)/2$, where $d \in [0,1]$ is an asymmetry coefficient (Figure 1.4). These two junctions form a superconducting loop which can be biased by a magnetic flux $\Phi = \varphi_0\delta$ in order to impose a superconducting phase difference δ across the two junctions in series. The loop is designed such that its inductance is negligible compared to the junction inductance φ_0^2/E_J .

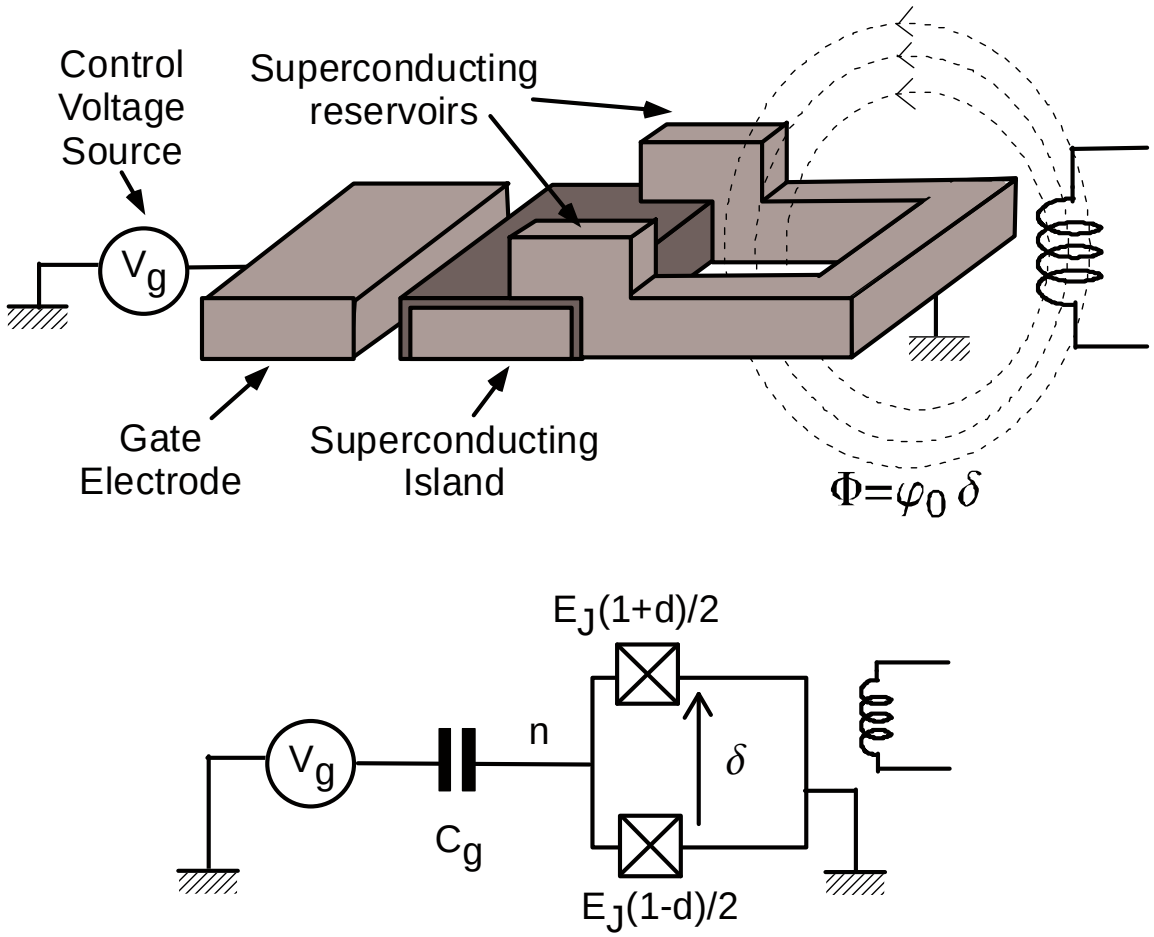

Figure 1.4: *The split Cooper pair box. Top: Schematic representation. The box is voltage biased through its gate by a generator supplying the voltage V_g, and flux biased through its loop to impose the phase difference δ across the series combination of the two Josephson junctions. Bottom: Corresponding electrical scheme.*

1.2.2 Charge representation

The electrostatic hamiltonian of the split box is that of a basic box [see (1.5)] with total capacitance $C_\Sigma = C_g + C_{J1} + C_{J2}$, where C_{J1} and C_{J2} are the capacitances of the two junctions. The Josephson hamiltonian of the split box is the sum of the Josephson terms of the two junctions:

$$\widehat{H}_J = -E_J \frac{1+d}{2} \cos(\widehat{\delta}_1) - E_J \frac{1-d}{2} \cos(\widehat{\delta}_2) \ , \tag{1.31}$$

with $\widehat{\delta_1}$ and $\widehat{\delta_2}$ the phases across each junction, conjugated to the respective number $\widehat{N_1}$ and $\widehat{N_2}$ of Cooper pairs transferred through them. Trigonometric transformations lead to:

$$\widehat{H}_j = -E_J \cos(\frac{\widehat{\delta}}{2}) \cos(\widehat{\theta}) + dE_J \sin(\frac{\widehat{\delta}}{2}) \sin(\widehat{\theta}) \ , \tag{1.32}$$

where:

$$\widehat{\theta} = \frac{\widehat{\delta_1} - \widehat{\delta_2}}{2}$$

is the operator associated to the superconducting phase of the island and:

$$\widehat{\delta} = \widehat{\delta_1} + \widehat{\delta_2}$$

is the operator associated to the phase difference δ . In the following, the impedance across the junctions is always lower than the resistance quantum $R_k = \mathtt{h}/e^2$. The phase $\widehat{\delta}$ can thus be considered as a classical parameter δ (see chapter 2). Since $\widehat{\theta}$ is conjugated to $\widehat{\mathbf{n}}$, the charge shift operators $\exp(\pm i\widehat{\theta})$ translate the charge $\widehat{\mathbf{n}}$ by ± 1 [Appendix 1-A formula (1.75)]. In the basis of charge states $\{|\mathbf{n}\rangle \, , \mathbf{n} \in \mathbb{Z}\}$, the split box hamiltonian thus writes:

$$\boxed{\begin{aligned} \widehat{H}(n_g,\delta) = & \sum_{n\in\mathbb{Z}} [E_C(\mathbf{n}-n_g)^2 \, |\mathbf{n}\rangle \langle \mathbf{n}| \\ & - \left(\tfrac{E_J}{2}\cos(\tfrac{\delta}{2}) - \mathbf{i}d\tfrac{E_J}{2}\sin(\tfrac{\delta}{2})\right) |\mathbf{n}\rangle \langle \mathbf{n}+\mathbf{1}| \\ & - \left(\tfrac{E_J}{2}\cos(\tfrac{\delta}{2}) + \mathbf{i}d\tfrac{E_J}{2}\sin(\tfrac{\delta}{2})\right) |\mathbf{n}+\mathbf{1}\rangle \langle \mathbf{n}|] \ . \end{aligned}} \tag{1.33}$$

For $d = 0$, the split Cooper pair box has the same energy spectrum as a basic box with effective Josephson energy:

$$E_J^* = E_J \cos(\frac{\delta}{2}) \ . \tag{1.34}$$

A symmetric split box can thus be used as a basic Cooper pair box with a tunable Josephson energy [17]. In the general case $d \neq 0$, the relation (1.34) is not valid, but in practice, it is easy to reduce the asymmetry down to $d < 0.1$. The effect of such an asymmetry is important only at the points $(n_g = 1/2 \ [\text{mod } 1] \, , \delta = \pi \ [\text{mod } 2\pi])$, where it lifts the energy degeneracies existing for $d = 0$ (Figure 1.5).

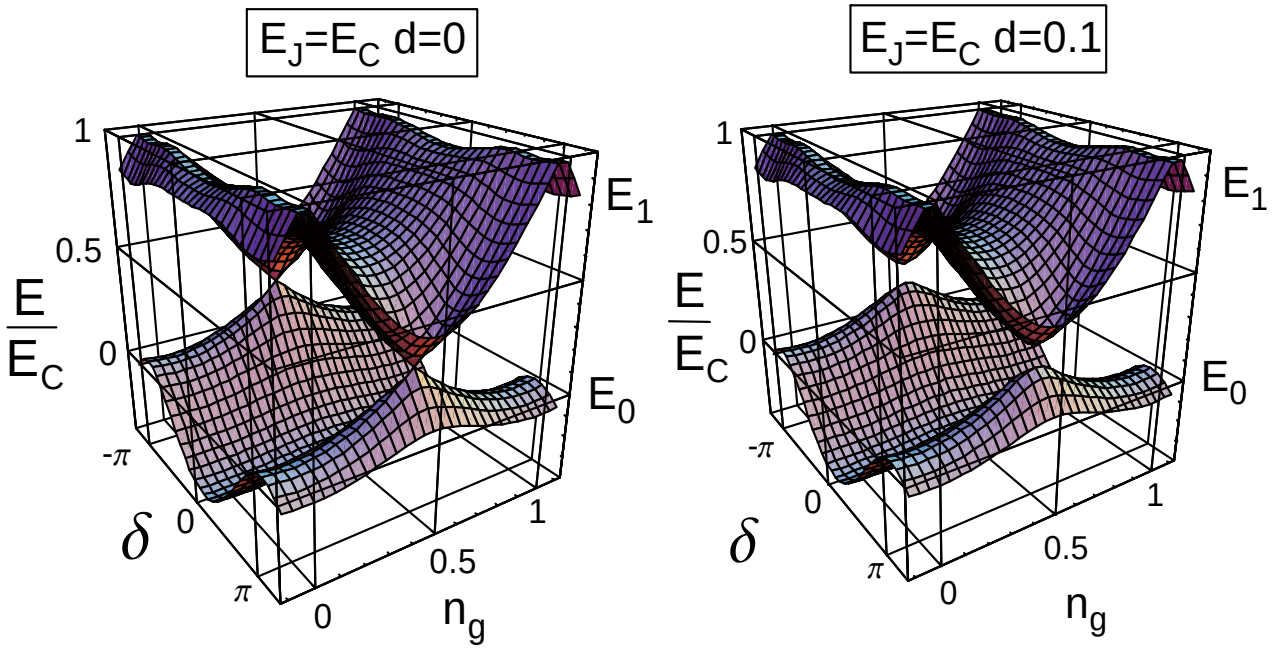

Figure 1.5: *The two lowest energy levels of the split Cooper pair box for* $E_J = E_C$, $d = 0$ *(left), and* $d = 0.1$ *(right). When* $d \neq 0$, *the energy degeneracies present at* $n_g = \frac{1}{2}$ [mod 1] *and* $\delta = \pi$ [mod 2π] *are lifted.*

1.2.3 Phase representation

The phase description of the Cooper pair box can be generalised to the split box. Using (1.12) and trigonometric transformations, the hamiltonian (1.33) of the split box can be recast in the form [45]:

$$\widehat{H}(n_g, \delta) = E_C(\frac{1}{\mathbf{i}}\frac{\partial}{\partial\widehat{\theta}} - n_g)^2 - E_J^*(d, \delta)\cos[\widehat{\theta} + \Upsilon(\delta)] \ , \tag{1.35}$$

where:

$$\boxed{\begin{array}{l} E_J^*(d, \delta) = E_J\sqrt{\frac{1+d^2+(1-d^2)\cos(\delta)}{2}} \\ \tan\Upsilon(d, \delta) = -d\tan(\frac{\delta}{2}) \ . \end{array}} \tag{1.36}$$

Consequently, the expressions (1.25) of the eigenenergies and of the eigenstates of the box are still valid provided we substitute E_J and θ according to:

$$\begin{cases} E_J \rightarrow E_J^*(d, \delta) \\ \theta \rightarrow \theta + \Upsilon(d, \delta) \ . \end{cases}$$

1.2.4 Loop current

The operator associated to the current circulating around the loop of the split Cooper pair box is:

$$\widehat{I}(n_g,\delta) = -2e\frac{d\widehat{K}}{dt} ,$$

where $\widehat{K} = \left(\widehat{N_1} + \widehat{N_2}\right)/2$ is the number of Cooper pairs having passed through the junctions. Since $\widehat{\delta}$ and $\widehat{K}$ are conjugated variables, this leads to [Appendix 1-A, (1.79) and (1.80)]:

$$\widehat{I}(n_g,\delta) = -\frac{1}{\mathbf{i}\varphi_0}\left[\widehat{K},\widehat{H}\right] = \frac{1}{\varphi_0}\frac{\partial\widehat{H}}{\partial\delta} . \tag{1.37}$$

Note that this relation between $\widehat{I}$ and δ is analogous to the relation (1.27) between $\widehat{V}$ and $\widehat{\mathbf{n}}$. From (1.37), the average loop current i_k in the state $|k\rangle$ follows the generalised Josephson relation [39]:

$$i_k(n_g,\delta) = \left\langle k\left|\widehat{I}\right|k\right\rangle = \frac{1}{\varphi_0}\frac{\partial E_k(n_g,\delta)}{\partial\delta} . \tag{1.38}$$

The current i_k is 2π-periodic on δ and 1-periodic on n_g . Examples of the average loop currents i_0 and i_1 in the states $|0\rangle$ and $|1\rangle$ are given in Figure 1.6. Note that for n_g close to 1/2 and $E_J < 3E_c$, these currents have opposite signs.

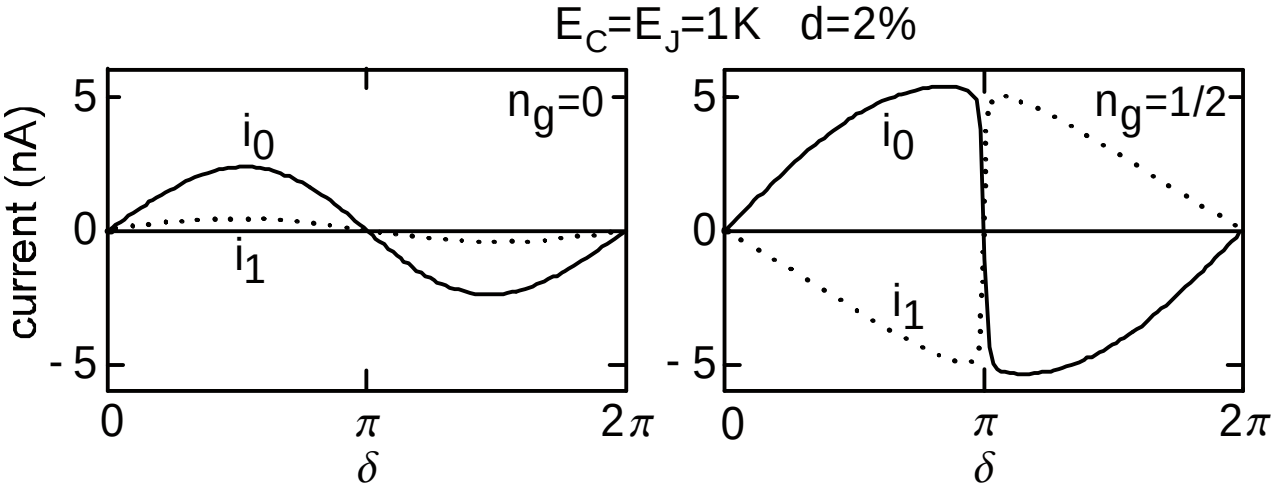

Figure 1.6: *Mean loop currents i_0 in the ground state (solid line), and i_1 in the first excited state (dotted line), calculated for $E_C = E_J = 1$ k_bK, $d = 2\%$, $n_g = 0$ (left panel) and $n_g = 1/2$ (right panel).*

1.3 The Cooper pair box as a quantum bit

When the energy spectrum of a Cooper pair box is sufficiently anharmonic, its two lowest energy eigenstates form an effective two level system. Within this subspace, the quantum state of the box can be manipulated at will by applying suitable radiofrequency signals to the gate, at a frequency close to the $|0\rangle \leftrightarrow |1\rangle$ transition frequency ν_{01} . This two level system can be used as a quantum bit when it is supplemented with an appropriate readout.

1.3.1 Bloch sphere description of the box

The description of a two level system by a fictitious spin 1/2, namely the Bloch sphere representation, is useful to visualize the preparation and measurement of the state of a Cooper pair box [46].

Restriction of the box hamiltonian to the two lowest energy states

The components of a spin 1/2 in an orthonormal basis $\mathcal{R} = (\overrightarrow{x}, \overrightarrow{y}, \overrightarrow{z})$ are described by the Pauli operators:

$$\widehat{\sigma}_x = \begin{bmatrix} 0 & 1 \\ 1 & 0 \end{bmatrix}, \widehat{\sigma}_y = \begin{bmatrix} 0 & -\mathbf{i} \\ \mathbf{i} & 0 \end{bmatrix}, \widehat{\sigma}_z = \begin{bmatrix} 1 & 0 \\ 0 & -1 \end{bmatrix} . \tag{1.39}$$

Together with the identity matrix

$$\widehat{\mathbb{I}} = \begin{bmatrix} 1 & 0 \\ 0 & 1 \end{bmatrix} ,$$

these operators form a complete basis for the space of the operators acting on a two dimensional Hilbert space. Within the subspace $\{|0\rangle, |1\rangle\}$, the hamiltonian $\widehat{H}$ can thus be written as that of a fictitious spin 1/2 in a magnetic field $\mathtt{h}\nu_{01}\overrightarrow{z}$:

$$\widehat{H} = -\frac{\mathtt{h}\nu_{01}}{2}\widehat{\sigma}_z + Tr(\widehat{H})\widehat{\mathbb{I}} , \tag{1.40}$$

where

$$\nu_{01} = \frac{E_1 - E_0}{\mathtt{h}} = \frac{\Omega_{01}}{2\pi} \tag{1.41}$$

is the transition frequency of the box and $\mathtt{h}$ is the Planck constant. The state $|0\rangle$ corresponds to the spin state pointing along $\overrightarrow{z}$ (i.e. $\widehat{\sigma}_z |0\rangle = |0\rangle$) and the state $|1\rangle$ to the spin state pointing along $-\overrightarrow{z}$ (i.e. $\widehat{\sigma}_z |1\rangle = -|1\rangle$). The unit sphere on which this fictitious spin moves while the system evolves is called the "Bloch sphere". Beware that in the general case, this representation is correct only for δ and n_g constant because the subspace $\{|0\rangle, |1\rangle\}$ varies with δ and n_g .

Representation of the quantum states

Up to a phase factor, any normalized coherent superposition $|u\rangle$ of $|0\rangle$ and $|1\rangle$ can be written as:

$$|u\rangle = \cos(\theta_u/2)\exp(-\mathbf{i}\varphi_u/2)\,|0\rangle + \sin(\theta_u/2)\exp(\mathbf{i}\varphi_u/2)\,|1\rangle \ , \tag{1.42}$$

where the angles θ_u and φ_u can be interpreted as the polar coordinates of the representative vector $\overrightarrow{u}$ of $|u\rangle$ (Figure 1.7):

$$\overrightarrow{u} = \overrightarrow{x}\sin\theta_u\cos\varphi_u + \overrightarrow{y}\sin\theta_u\sin\varphi_u + \overrightarrow{z}\cos\theta_u \ . \tag{1.43}$$

The state $|u\rangle$ corresponds to the spin state pointing along $\overrightarrow{u}$, that is:

$$\widehat{\sigma}_u\,|u\rangle = |u\rangle$$

where

$$\widehat{\sigma}_u = \overrightarrow{u}\cdot\overrightarrow{\sigma} = u_x\widehat{\sigma}_x + u_y\widehat{\sigma}_y + u_z\widehat{\sigma}_z \ , \tag{1.44}$$

is the operator associated to the $\overrightarrow{u}$ component of the fictitious spin.

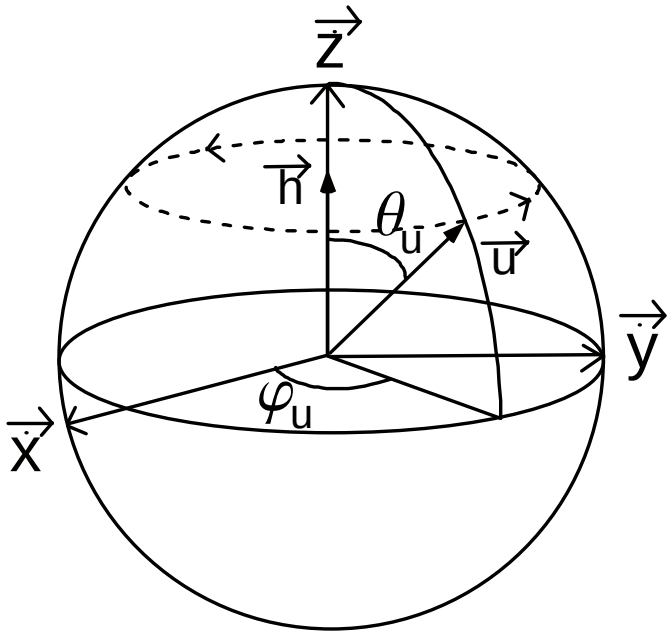

Figure 1.7: *Bloch sphere representation of the Cooper pair box.*

Representation of an operator

Any operator $\widehat{A}$ can be written as:

$$\widehat{A} = -\frac{1}{2}\overrightarrow{a}\cdot\overrightarrow{\sigma} + Tr(\widehat{A})\widehat{\mathbb{I}} \ ,$$

where:

$$\overrightarrow{a} \cdot \overrightarrow{\sigma} = a_x \widehat{\sigma}_x + a_y \widehat{\sigma}_y + a_z \widehat{\sigma}_z$$

is a symbolic notation. The vector $\overrightarrow{a}$, which is unique, is called the representative vector of $\widehat{A}$. As an example, the representative vector of the hamiltonian $\widehat{H}$ of the box is:

$$\overrightarrow{h} = \hbar \Omega_{01} \overrightarrow{z} \ . \tag{1.45}$$

Note that in the general case, the representative vector of the derivative of an operator respectively to n_g or δ is not the derivative of the representative vector of this operator since the subspace $\{|0\rangle, |1\rangle\}$ varies with δ and n_g . In this thesis, the vectors $\overrightarrow{D}_\delta$ and $\overrightarrow{D}_{n_g}$ will be the representative vectors of respectively the restrictions of $\frac{\partial \widehat{H}}{\partial \delta}$ and $\frac{\partial \widehat{H}}{\partial n_g}$ to the subspace $\{|0\rangle, |1\rangle\}$:

$$\frac{\partial \widehat{H}}{\partial \delta} = -\frac{1}{2} \overrightarrow{D}_\delta \cdot \overrightarrow{\sigma} \tag{1.46}$$

$$\frac{\partial \widehat{H}}{\partial n_g} = -\frac{1}{2} \overrightarrow{D}_{n_g} \cdot \overrightarrow{\sigma} \ . \tag{1.47}$$

Using the Bloch sphere representation

The Bloch sphere representation can be used to express any information concerning a two level system. For instance, the Schrödinger equation describing the hamiltonian evolution of the two level system can be replaced with the equation describing the precession of the spin $\overrightarrow{u}$ at the frequency ν_{01} around the magnetic field $\overrightarrow{h}$:

$$\frac{d\overrightarrow{u}}{dt} = \frac{1}{\hbar} \overrightarrow{h} \wedge \overrightarrow{u} \ . \tag{1.48}$$

The average value of the operator $\widehat{A}$ in the state $|u\rangle$ is:

$$\langle u | \widehat{A} | u \rangle = -\frac{1}{2} \overrightarrow{a} \cdot \overrightarrow{u} + Tr(\widehat{A}) \ . \tag{1.49}$$

Let $|B_0\rangle$ and $|B_1\rangle$ be the eigenstates of a second operator $\widehat{B}$ with representative vector $\overrightarrow{b}$. The matrix element $\left| \left\langle B_1 \left| \widehat{A} \right| B_0 \right\rangle \right|$ verifies:

$$\left| \left\langle B_1 \left| \widehat{A} \right| B_0 \right\rangle \right| = \frac{\left| \overrightarrow{a} \wedge \overrightarrow{b} \right|}{2 \left| \overrightarrow{b} \right|} \ . \tag{1.50}$$

For two states $|u_1\rangle$ and $|u_2\rangle$ with respective representative vectors $\overrightarrow{u_1}$ and $\overrightarrow{u_2}$, it can be verified that:

$$|\langle u_1 | u_2 \rangle|^2 = \frac{1}{2}(1 + \overrightarrow{u_1} \cdot \overrightarrow{u_2}) \ . \tag{1.51}$$

Two charge states restriction

A further simplification occurs when $E_J \ll E_C$ and n_g is close to $1/2$. In that case, the two lowest energy eigenstates of the box belong to the subspace spanned by the subset $\{|0\rangle, |1\rangle\}$ of charge states. Let $\mathcal{R}' = (\overrightarrow{x'}, \overrightarrow{y'}, \overrightarrow{z'})$ be an orthonormal basis with $\overrightarrow{z'}$ the charge axis, i.e.:

$$\widehat{n} = -\frac{1}{2}\widehat{\sigma'}_z + \frac{1}{2} ,$$

where:

$$\widehat{\sigma'}_x = \begin{bmatrix} 0 & 1 \\ 1 & 0 \end{bmatrix} , \ \widehat{\sigma'}_y = \begin{bmatrix} 0 & -\mathbf{i} \\ \mathbf{i} & 0 \end{bmatrix} , \ \widehat{\sigma'}_z = \begin{bmatrix} 1 & 0 \\ 0 & -1 \end{bmatrix} , \tag{1.52}$$

and with $\overrightarrow{x'}$ parallel to the Josephson term for $d = 0$. From (1.33), the hamiltonian of the box is:

$$\widehat{H} = -\frac{1}{2}\overrightarrow{\sigma'} \cdot \overrightarrow{h} + Tr(\widehat{H})\widehat{\mathbb{I}} , \tag{1.53}$$

with (Figure 1.8):

$$\boxed{\overrightarrow{h}(n_g,\delta) = E_J \cos(\tfrac{\delta}{2})\overrightarrow{x'} + dE_J \sin(\tfrac{\delta}{2})\overrightarrow{y'} + E_C(1-2n_g)\overrightarrow{z'} ,} \tag{1.54}$$

and

$$Tr(\widehat{H}) = E_C(\frac{1}{2} + n_g + \frac{n_g^2}{2}) .$$

On the opposite of the general case, it is here possible to use the Bloch sphere scheme when n_g and δ vary because the subspace $\{|0\rangle, |1\rangle\}$ do not depend on n_g and δ . Therefore, the representative vector of the loop current of a split box can be calculated using:

$$\overrightarrow{i}(n_g, \delta) = \frac{1}{\varphi_0}\frac{\partial \overrightarrow{h}}{\partial \delta} ,$$

which leads to:

$$\overrightarrow{i}(n_g, \delta) = \frac{E_J}{2\varphi_0}\sin(\frac{\delta}{2})\overrightarrow{x'} + \frac{dE_J}{2\varphi_0}\cos(\frac{\delta}{2})\overrightarrow{y'} . \tag{1.55}$$

The basis $\mathcal{R} = (\overrightarrow{x}, \overrightarrow{y}, \overrightarrow{z})$ previously defined can be related to $\mathcal{R}' = (\overrightarrow{x'}, \overrightarrow{y'}, \overrightarrow{z'})$ using (1.45) and (1.54). The angle $\theta = \left(\widehat{\overrightarrow{z}, \overrightarrow{z'}}\right)$ between $\overrightarrow{z}$ and $\overrightarrow{z'}$ simply varies with n_g and δ:

$$\tan(\theta) = \frac{E_C(1-2n_g)}{E_J\sqrt{\cos^2(\frac{\delta}{2}) + d^2\sin^2(\frac{\delta}{2})}} .$$

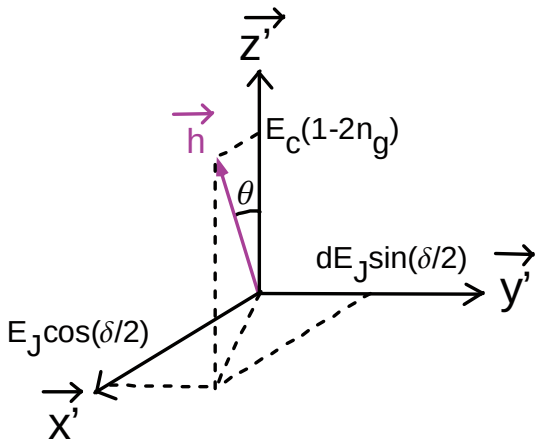

Figure 1.8: *Representative vector* $\overrightarrow{h}$ *of the box hamiltonian in the two charge states restriction.*

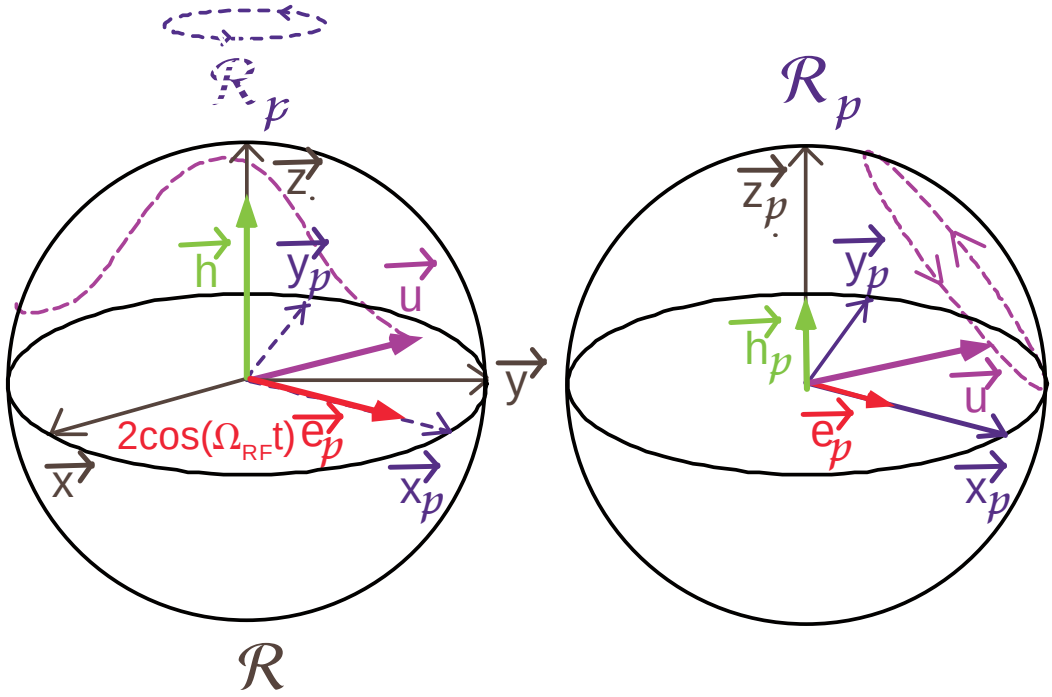

Figure 1.9: *Bloch representation of the radiofrequency excitation of a two level system. Left: Representation in the static frame* $\mathcal{R} = (\overrightarrow{x}, \overrightarrow{y}, \overrightarrow{z})$*. The motion of the fictitious spin* $\overrightarrow{u}$ *representing the state of the two level system is determined by the constant field* $\overrightarrow{h}$ *representing the free hamiltonian of the box and the oscillating field* $2\cos(\omega t)\overrightarrow{e}_p$ *representing the radiofrequency excitation. The frame* $\mathcal{R}_p = (\overrightarrow{x_p}, \overrightarrow{y_p}, \overrightarrow{z_p})$ *rotating at the frequency* ν_{RF} *around* $\overrightarrow{z}$ *is represented in dashed lines. Right: Representation of the same process in this rotating frame. Using the rotating frame approximation,* $2\cos(\omega t)\overrightarrow{e}_p$ *is represented in* $\mathcal{R}_p$ *by a constant field* $\overrightarrow{e}_p$*. The vector* $\overrightarrow{h}$ *is represented by the constant field* $\overrightarrow{h}_p$*. The spin* $\overrightarrow{u}$ *thus precesses around* $\overrightarrow{e}_p + \overrightarrow{h}_p$*.*

1.3.2 Quantum bit manipulation

We suppose that the state of the box initially belongs to the subspace[4] spanned by the subset $\{|0\rangle, |1\rangle\}$. The state of the box can be manipulated within this subspace using a technique inspired from Nuclear Magnetic Resonance [48]. A radiofrequency voltage signal with amplitude U_{RF} and with frequency ν_{RF} is applied to the gate. The voltage amplitude U_{RF} corresponds to a reduced gate voltage amplitude Δn_g . The hamiltonian (1.5) has thus a time dependent term:

$$\widehat{H}_{RF} = -2E_C \Delta n_g \cos(2\pi\nu_{RF}t)\widehat{n} \ . \tag{1.56}$$

The notations n_g and δ will now refer to the DC values of the gate charge and superconducting flux imposed to the box. The hamiltonian $\widehat{H}$ of the box in the absence of radiofrequency excitation will be called the free hamiltonian of the box. Supposing the amplitude Δn_g of the radiofrequency signal used is small, one can use the Bloch sphere representation associated to n_g and δ for describing the evolution of the box under the effect of the radiofrequency excitation. In the referential $\mathcal{R} = (\overrightarrow{x}, \overrightarrow{y}, \overrightarrow{z})$ of the Bloch sphere defined in the previous section, following (1.49), the restriction of $\widehat{H}_{RF}$ to $\{|0\rangle,|1\rangle\}$ writes:

$$\widehat{H}_{RF} = -\frac{1}{2}\overrightarrow{\sigma} \cdot \overrightarrow{e} \ .$$

In $\mathcal{R}$, the representative vector $\overrightarrow{u}$ of the box state is submitted to the field $\overrightarrow{h}$ representing the free hamiltonian $\widehat{H}$ and to the field $\overrightarrow{e}$ representing $\widehat{H}_{RF}$ (Figure 1.9, left). The transverse part $\overrightarrow{e}_{\perp}$ of $\overrightarrow{e}$ is:

$$\overrightarrow{e}_{\perp} = 2\cos(2\pi\nu_{RF}t)\overrightarrow{e}_p$$

with $\overrightarrow{e}_p$ a vector perpendicular to $\overrightarrow{z}$ with modulus:

$$e_p = 2E_C \Delta n_g \left|\langle 1|\,\widehat{n}\,|0\rangle\right| \ .$$

When ν_{RF} is close to ν_{01}, the effect of the longitudinal part $\overrightarrow{e} - \overrightarrow{e}_{\perp}$ of $\overrightarrow{e}$ on the motion of $\overrightarrow{u}$ can be neglected. The states $|0\rangle$ and $|1\rangle$ are simply coupled by the transverse field $\overrightarrow{e}_{\perp}$. In order to evaluate quantitatively the effect of $\overrightarrow{e}_{\perp}$, it is interesting to work in the rotating frame $\mathcal{R}_p = (\overrightarrow{x}_p, \overrightarrow{y}_p, \overrightarrow{z}_p)$ precessing at the frequency $+\nu_{RF}$ around $\overrightarrow{z}_p = \overrightarrow{z}$ (Figure 1.9, right), with

$$\overrightarrow{x}_p = \frac{\overrightarrow{e}_p}{e_p} \ .$$

Within the rotating wave approximation [48], the field $\overrightarrow{e}_{\perp}$ corresponds in $\mathcal{R}_p$ to the constant field $\overrightarrow{e}_p$, and the representative vector $\overrightarrow{h}$ of the box free hamiltonian $\widehat{H}$ corresponds to:

$$\overrightarrow{h_p} = \mathtt{h}\left(\nu_{01} - \nu_{RF}\right)\overrightarrow{z}_p \ . \tag{1.57}$$

[4] In the experiments described in this thesis, E_C and E_J are typically of the order of 1 K. Hence, at temperatures of a few tens of mK, when the box is at rest, it relaxes to its ground state $|0\rangle$ by dissipating its excitation energy in the electrical lines (see chapter 4). The condition of initially being in the subspace $\{|0\rangle, |1\rangle\}$ is thus easily satisfied.

In the frame $\mathcal{R}_p$, $\overrightarrow{u}$ precesses around $\overrightarrow{e}_p + \overrightarrow{h}_p$ at the frequency:

$$\nu_p = \sqrt{\left(\frac{e_p}{\mathtt{h}}\right)^2 + (\nu_{01} - \nu_{RF})^2} \ .$$

When ν_{01} is very close to ν_{RF}, $\overrightarrow{e_p}$ dominates $\overrightarrow{h_p}$ and the motion of $\overrightarrow{u}$ in $\mathcal{R}_p$ is a precession around $\overrightarrow{x}_p$ at the Rabi frequency [34]:

$$\nu_{Rabi} = \frac{e_p}{\mathtt{h}} = \frac{2E_C \Delta n_g \left|\langle 1| \widehat{n} |0\rangle\right|}{\mathtt{h}} \ . \tag{1.58}$$

On the contrary, when the box evolves freely, $\overrightarrow{u}$ precesses around $\overrightarrow{z}_p = \overrightarrow{z}$ at the Ramsey frequency [38]:

$$\nu_{Ramsey} = \nu_{01} - \nu_{RF} \ . \tag{1.59}$$

As a consequence, by combining a radiofrequency excitation with a free evolution stage, both of adapted durations, $\overrightarrow{u}$ can be brought to any point of the Bloch sphere.

Although the box state manipulation is possible for all the values of n_g and δ at which the energy spectrum is anharmonic, the particular point ($n_g = 1/2,\ \delta = 0$) plays a special role. At this point, the transition frequency is stationary with respect to small variations of n_g and δ, which suppresses at first order the decoherence induced by the noise in these control parameters (see chapter 3). In the following, the energy spectrum, anharmonicity, resonance frequency ν_{01} and Rabi frequency ν_{Rabi} of the box are plotted[5] at this optimal point ($n_g = 1/2,\ \delta = 0$) . These plots can be used as abacus for optimizing the fabrication parameters E_J and E_C of the box. In each plot, points corresponding to the experiments described in chapter 2 and 4 are indicated.

Resonance frequency

The resonance frequency at the optimal point is plotted in Figure 1.10. Note that it is equal to $E_J/\mathtt{h}$ at low E_J/E_C and to $\sqrt{2E_JE_C}/\mathtt{h}$ at large E_J/E_C . In order to avoid the relaxation of the state $|1\rangle$, the resonance frequency of the box must be different from the resonance frequencies of all the other elements included in the circuit, like, for example, the Cooper pair transistor used in the case of a charge readout (see chapter 2) or the auxiliary Josephson junction used in the case of a current readout (see chapter 4).

Rabi frequency

The Rabi frequency ν_{Rabi} (Formula 1.58, Figure 1.11) is proportional to the amplitude Δn_g of the radiofrequency signal used. The rotation angle of $\overrightarrow{u}$ around $\overrightarrow{x}_p$ due to a radiofrequency pulse with duration τ is $\Delta\theta_u = \tau\nu_{Rabi}$. Note that at the optimal point ($n_g = 1/2,\ \delta = 0$), the Rabi frequency is equal to $\Delta n_g E_C/(2\mathtt{h}) = \Delta n_g \nu_{01}/2/(E_J/E_C)$ at low E_J/E_C and to $\Delta n_g \sqrt{2E_J/E_C} E_C/\mathtt{h} = \Delta n_g \nu_{01}$ at large E_J/E_C .

[5] These plots are made for the most general case of the split Cooper pair box. The irrelevant informations for the unsplit box can be eliminated by setting $\delta = 0$ and $d = 0$.

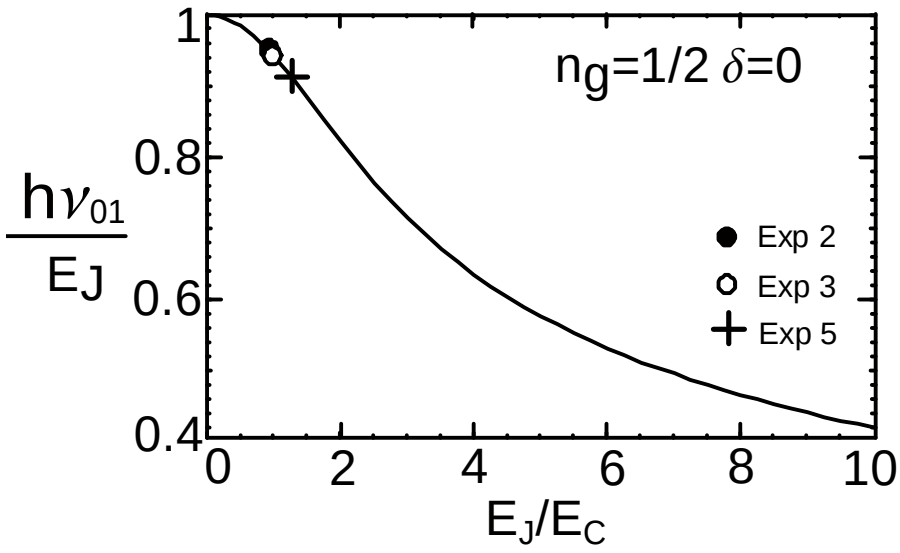

Figure 1.10: *Reduced resonance frequency of the box for $n_g = 1/2$, $\delta = 0$ and $d = 0$. The cross corresponds to the split box of experiment 5 (see chapter 4). Note that this graph can also be used as an abacus to evaluate the transition frequency of a Cooper pair transistor (see section 1.4), which exhibits the same gate and phase dependencies as that of a split box. The circles correspond to the transistors of experiments 2 and 3 (see chapter 2).*

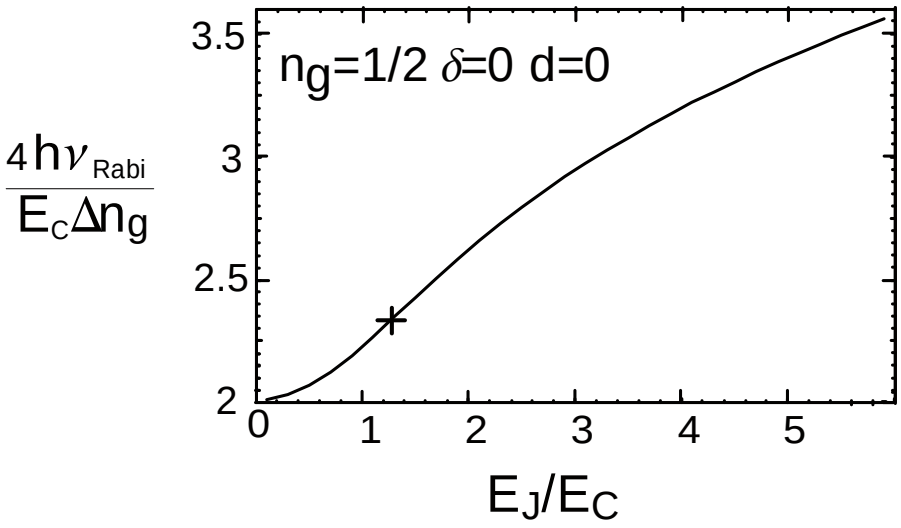

Figure 1.11: *Rabi frequency of the Cooper pair box for $n_g = 1/2$, $\delta = 0$ and $d = 0$. The cross corresponds to experiment 5.*

Anharmonicity

The intrinsic anharmonicity factor of the box can be defined as (Figure 1.12):

$$\mathcal{A}(n_g, \delta) = 2\frac{\nu_{12} - \nu_{01}}{\nu_{12} + \nu_{01}} ,$$

where $\nu_{12} = (E_2 - E_1)/\mathtt{h}$ is the transition frequency between the states $|1\rangle$ and $|2\rangle$. When $\mathcal{A}(n_g,\delta)$ is close to 0, the transition frequency ν_{01} is not well separated from ν_{12} .

Inducing selective transitions between the ground and first excited states of the box

The box can be used as an effective two level system if the $|0\rangle \leftrightarrow |1\rangle$ transition can be excited selectively. This depends on the anharmonicity of the box but also on the characteristics of the radiofrequency signal used. From the definition (3.94) of the power spectrum, a square radiofrequency pulse with duration τ, with amplitude Δn_g and with frequency ν_{RF} close to ν_{01} has a spectral density which can be approximated with [46]:

$$S_{n_g}(\omega) = \frac{\Delta n_g^2}{4}\left(\tau^2 \mathrm{sinc}^2((\omega + 2\pi\nu_{RF})\frac{\tau}{2}) + \tau^2 \mathrm{sinc}^2(\omega - 2\pi\nu_{RF})\frac{\tau}{2})\right) \qquad (1.60)$$

if

$$||\omega/2\pi| - \nu_{RF}| \ll \nu_{RF} .$$

This spectral density presents two peaks with height $\Delta n_g^2\tau^2/4$ and width $\Delta\omega = 4\pi/\tau$, centered at $\omega = \pm 2\pi\nu_{RF}$ (Figure 1.13). These primary peaks are surrounded by secondary peaks with height $\Delta n_g^2\tau^2/72\pi^3$, that is $\simeq 4.5\%$ of the primary peaks. Thus, in a rough approximation, the spectral density can be considered as negligible outside the primary peaks.

Such a radiofrequency pulse applied on the gate of the box will induce transitions between the states $|p\rangle$ and $|m\rangle$ if the transition frequency:

$$\nu_{pm} = \frac{E_p - E_m}{\mathtt{h}}$$

falls inside the radiofrequency spectrum primary peak. In order to induce a precession of $\overrightarrow{u}$ by an angle $\Delta\theta_u = \tau\nu_{Rabi}$ around $\overrightarrow{x}_p$ without exciting the level $|2\rangle$, one must have:

$$\nu_{RF} \simeq \nu_{01}$$

and

$$|\nu_{12} - \nu_{01}| \gg \frac{\Delta\omega}{2} .$$

This second condition can be recast in the form of a condition on the separation factor (Figure 1.14):

$$\mathcal{B}(n_g, \delta) = \frac{\nu_{12} - \nu_{01}}{\nu_{Rabi}}$$

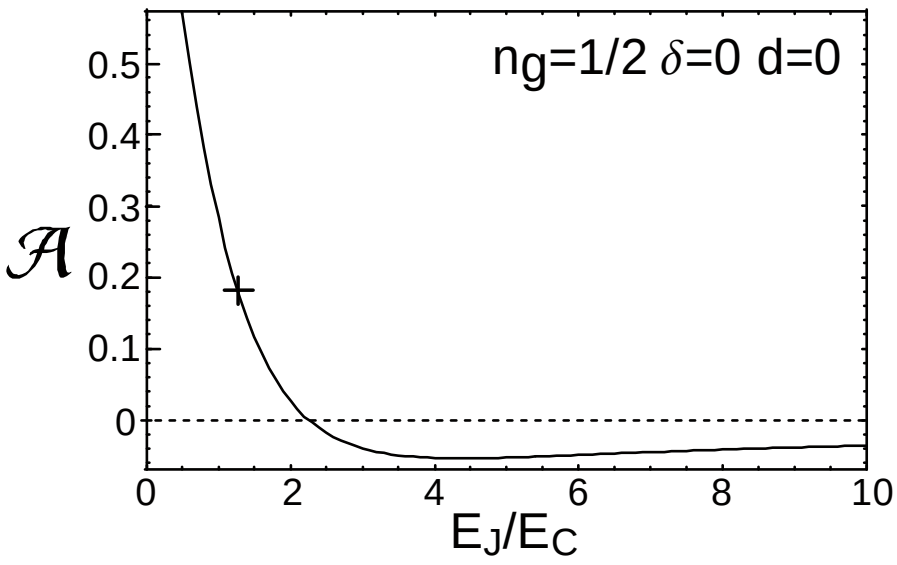

Figure 1.12: *Anharmonicity factor for $n_g = 1/2$, $\delta = 0$ and $d = 0$. The cross corresponds to experiment 5.*

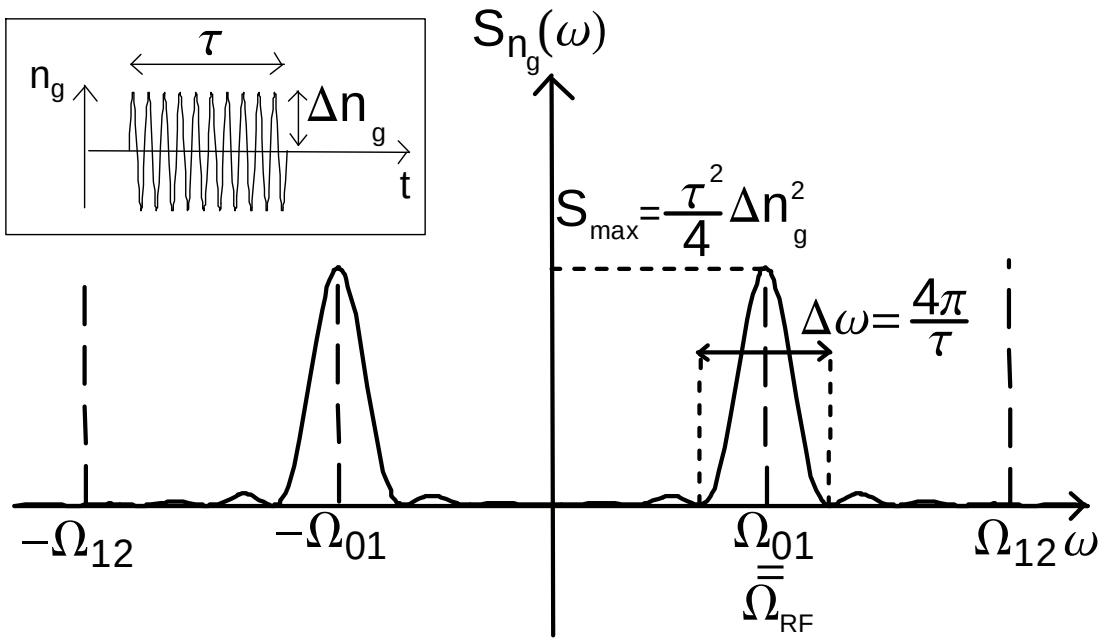

Figure 1.13: *The spectral density of a radiofrequency square pulse with frequency $\nu_{RF} = \Omega_{01}/2\pi$, with amplitude Δn_g, and with duration τ presents two strong peaks with height $\tau^2 \Delta n_g^2/4$ and with width $4\pi/\tau$ at the pulsations $\pm\,\Omega_{01}$. The secondary peaks are negligible. Such a radiofrequency pulse applied on the gate of a box can excite selectively the transition between $|0\rangle$ and $|1\rangle$ if the width $4\pi/\tau$ is smaller then the separation $\Omega_{12} - \Omega_{01}$.*

which must be such that:

$$|\mathcal{B}(n_g, \delta)| \gg \frac{2\pi}{\Delta\theta_u} \ . \tag{1.61}$$

In the experiment 5 performed on a split box (with $E_J = 0.86$ k$_b$K and $E_C = 0.68$ k$_b$K), the radiofrequency pulses used have a maximum amplitude of $U_{RF} = 100$ μV, which corresponds to $\Delta n_g = 5.10^{-4}$ and to a Rabi frequency $\nu_{Rabi} \simeq 50$ MHz . At this frequency, the criterion to avoid the excitation of $|2\rangle$ while performing a $\Delta\theta_u = \pi/10$ pulse at the optimal point is easily satisfied: $\mathcal{B}(n_g,\delta)\Delta n_g = 0.9 > 2\pi\Delta n_g/\Delta\theta_u = 0.01$.

Having $E_J/E_C > 2$ is interesting in order to increase the immunity to charge noise. In the domain $E_J/E_C \in [3, 8]$, the Rabi frequency can reach 1% of the transition frequency, for a population of level $|2\rangle$ at the % level after a pulse with $\Delta\theta_u = \pi$.

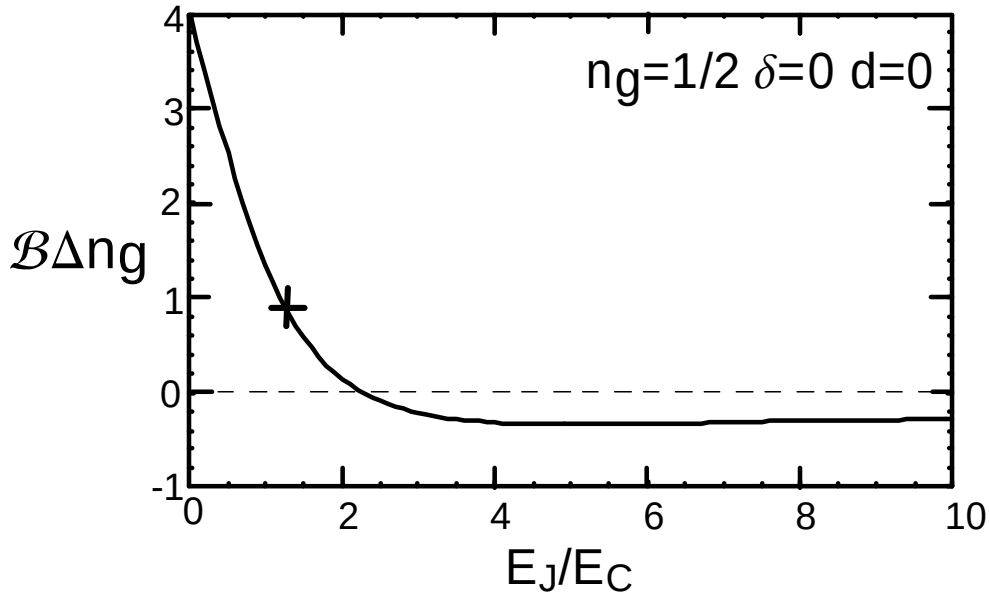

Figure 1.14: *Separation factor $\mathcal{B}$ of the box times Δn_g for $n_g = 1/2$, $\delta = 0$ and $d = 0$. The cross corresponds to experiment 5.*

1.3.3 Measurement of the box state

During this thesis work, two different measurement strategies have been explored for measuring the state of a Cooper pair box. The first one consists in measuring the charge of the island of a basic Cooper pair box. The second one consists in measuring the loop current of a split box. The readout device used must be weakly coupled to the box in order to limit the back-action. It is shown in chapter 3 that, due to the weakness of this coupling, during the measurement, the readout devices we have implemented project the box on its energy eigenstates rather than on its current or charge eigenstates. Hence, the value indicated by the readout device will be the mean island charge (1.30) or the mean loop current (1.38) of the states $|0\rangle$ or $|1\rangle$. At the

optimal point, these quantities are zero and thus no measurement can be performed. Before a mean charge measurement, n_g must be taken away from 1/2, and similarly, before a mean current measurement, δ must be taken away from 0 . The charge and current output signals are given in the following as a function of E_J/E_C, n_g and/or δ .

Charge Output signal

When an electrometer is weakly coupled to a box, the signal measured by the electrometer is proportional to:

$$\Delta n_{01}(n_g) = \langle 1 \left| \widehat{n} \right| 1 \rangle - \langle 0 \left| \widehat{n} \right| 0 \rangle \big|_{n_g, \delta=0, d=0} \quad . \tag{1.62}$$

From (1.29), (1.30) and (1.41), Δn_{01} can be recast as:

$$\Delta n_{01}(n_g) = -\frac{\hbar}{2E_C} \frac{\partial \Omega_{10}}{\partial n_g} \bigg|_{n_g, \delta=0} \quad .$$

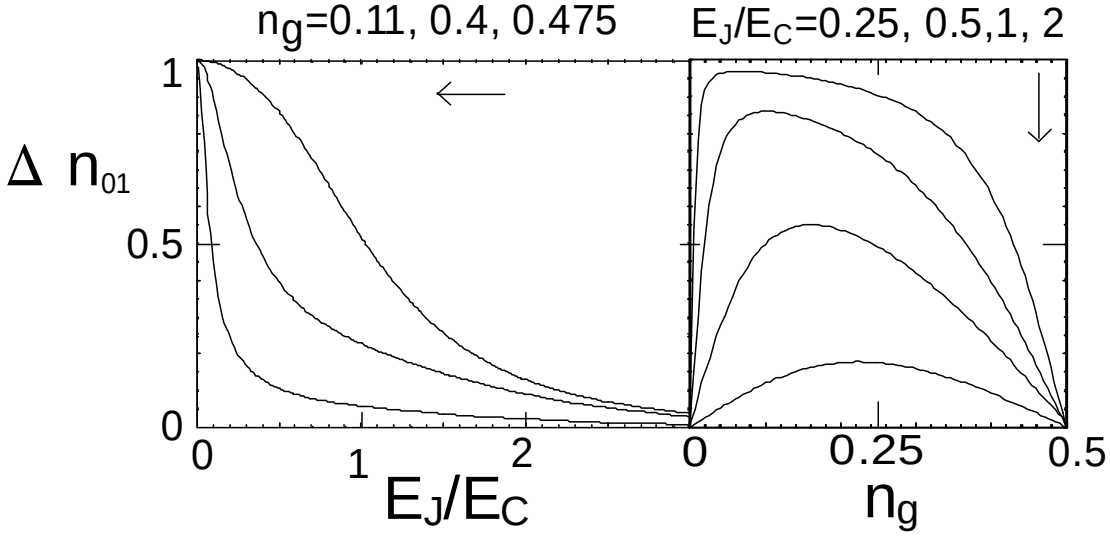

Figure 1.15: *Left panel: Variations of the charge output signal Δn_{01} of a basic Cooper pair box with E_J/E_C for different values of n_g. Right panel: Variation of Δn_{01} with n_g for different values of E_J/E_C.*

For symmetry reasons, $\Delta n_{01}(0) = \Delta n_{01}(0.5) = 0$. The signal Δn_{01} presents a maximum at an intermediate value of n_g which depends on E_J/E_C (Figure 1.15, right panel). Note that Δn_{01} decreases with E_J/E_C (Figure 1.15, left panel). The ratio E_J/E_C must be taken lower than 1 in order to have a charge signal stronger than 0.5 .

Current output signal

When a current meter is weakly coupled to a split box, the signal measured is proportional to the difference:

$$\Delta i_{01}(n_g, \delta) = i_1 - i_0|_{n_g,\delta}$$

between the average currents in the states $|0\rangle$ and $|1\rangle$. Using (1.38) and (1.41), Δi_{01} can be recast in the form:

$$\Delta i_{01}(n_g, \delta) = 2e \frac{\partial \Omega_{10}}{\partial \delta}\bigg|_{n_g,\delta} .$$

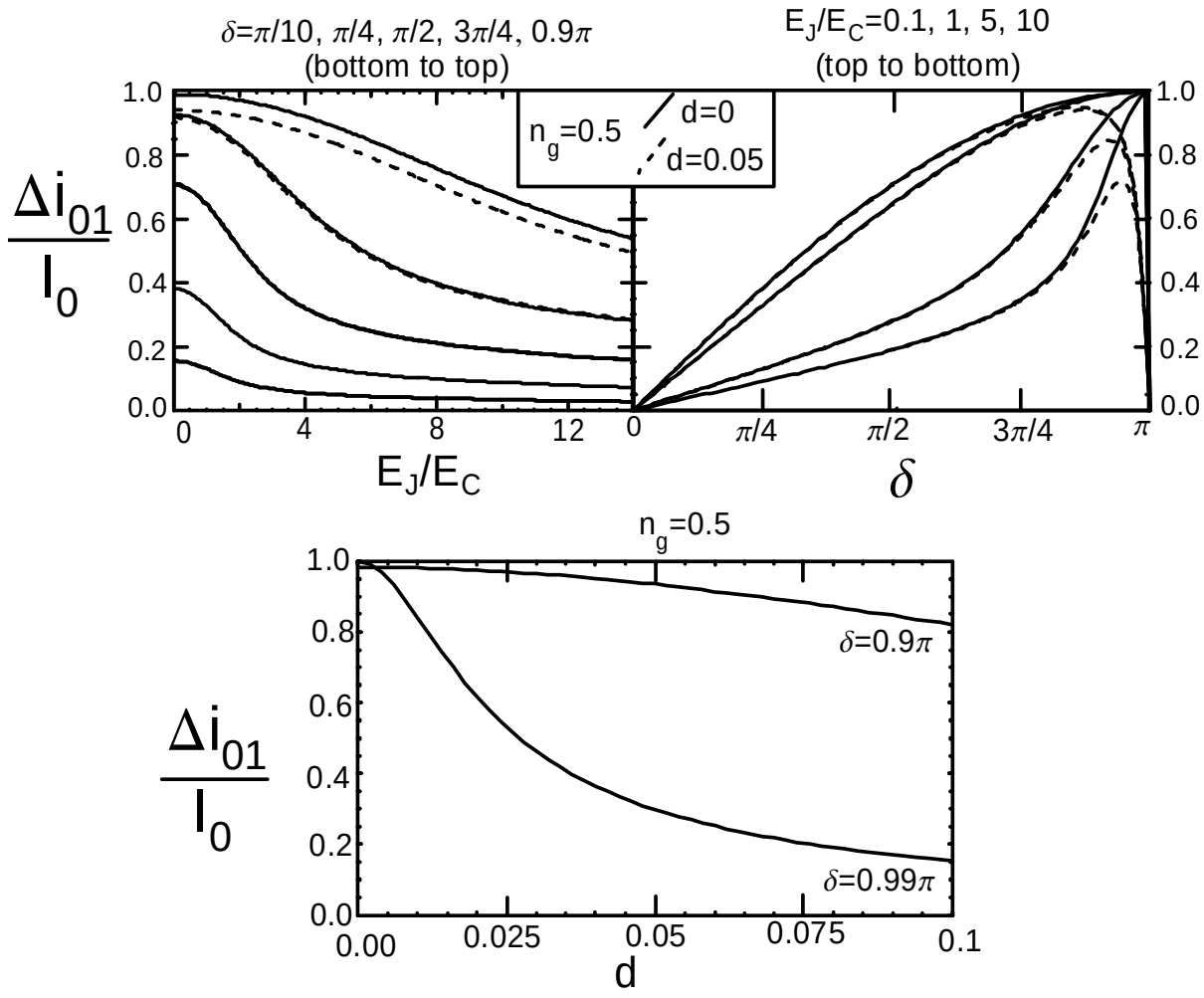

Figure 1.16: *Difference Δi_{01} between the loop currents i_0 and i_1 of a split Cooper pair box tuned at $n_g = 1/2$, normalized to the average critical current I_0 of a single junction [see (1.63)]. Top left panel: Variations of $\Delta i_{01}/I_0$* with *E_J/E_C in the perfectly symmetric case $d = 0$ (solid line) and the asymmetric case $d = 0.05$ (dotted line), for different values of δ. Top right: Variations of $\Delta i_{01}/I_0$ with δ, in the case $d = 0$ (full line) and the case $d = 0.05$ (dotted line), for different values of E_J/E_C. Bottom: Variations of $\Delta i_{01}/I_0$ with d for $E_J/E_C = 1$ and different values of δ. The influence of d shows up at $\delta \sim \pi$.*

In order to maximize the signal $\Delta i_{01}(n_g = 1/2,\delta)$, one should take a large E_J (Figure 1.16, top left panel). If $d = 0$ and $\delta = \pi$, the bands E_0 and E_1 form joining cusps and Δi_{01} reaches its maximum, which is, with a great accuracy (1% for $E_J/E_C < 20$) (Figure 1.16, right top panel):

$$\Delta i_{01}(n_g = \frac{1}{2}, \delta = \pi, d = 0) \simeq I_0 \ ,$$

where

$$I_0 = \frac{E_J}{2\varphi_0} \ . \tag{1.63}$$

is the average critical current of one Josephson junction. When the asymmetry factor d is non zero, $\Delta i_{01}(n_g = \frac{1}{2}, \delta = \pi, d = 0)$ is drastically reduced (Figure 1.16, bottom panel), so that the maximum of Δi_{01} is located at $\delta < \pi$. This maximum remains close to I_0 for $d < 0.05$.

1.3.4 The optimal Cooper pair box

A trade-off must be found between the different parameters entering in the manipulation and the measurement steps. The optimal fabrication parameters E_J and E_C to choose for the implementation of a quantum bit depend on the measurement strategy adopted.

- In the case of a charge readout, the value of E_J/E_C adopted must be smaller than 1 in order to have a large readout signal. This is compatible with the requirements on the separation factor, but it is antagonist with having a good immunity to charge noise, which requires a high ratio E_J/E_C (see chapter 3). We advise to make the trade-off:

$$\boxed{\text{for a charge readout: } E_J/E_C \simeq 1/2} \ .$$

- In the case of a current readout, E_J must be large in order to have a large signal. However, the value of E_J/E_C adopted must correspond to a sufficient separation factor. In our first operation of a split box (experiment 5), we had $E_J/E_C \simeq 1.3$, which ensures a strong separation factor, but is not optimal for decoherence and the signal amplitude. We made this choice in order to keep a strong gate oscillation signal measurable directly with the current, without resorting to spectroscopic techniques. For further experiments, we rather advise to take

$$\boxed{\text{for a current readout: } 3 \leq E_J/E_C \leq 8 \text{ and } E_J \text{ as strong as possible}} \ ,$$

  which will increase the immunity to charge noise. Note that in this case, the Rabi frequency can reach $\nu_{01}/30$ without any risk of exciting the level $|2\rangle$. Beware that in practice, the condition $E_C < \sqrt{2C_\Sigma \mathbf{\Delta}}$, with $\mathbf{\Delta}$ the BCS gap, must nevertheless be respected to ensure the $2e$-periodicity of the box.

1.4 The Cooper pair transistor

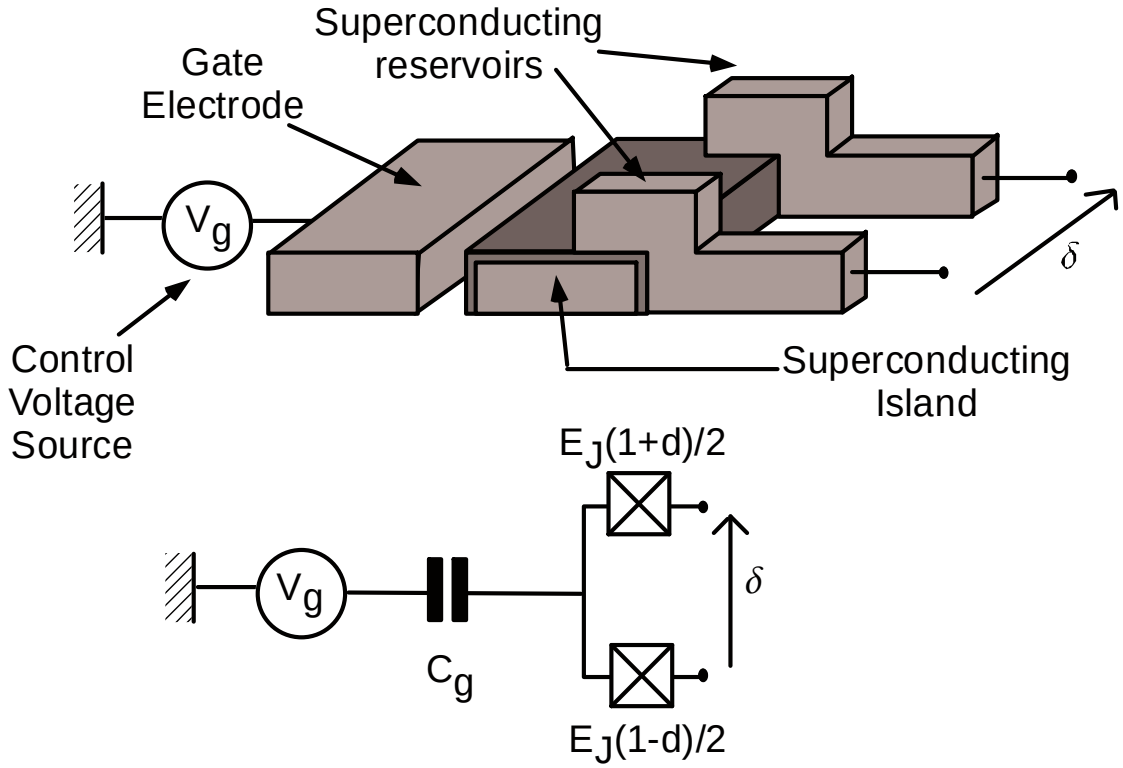

Figure 1.17: *The Cooper pair transistor. Top panel: Schematic representation. Bottom panel: Corresponding electrical scheme.*

The Cooper pair transistor [22, 42] can be seen as a split Cooper pair box whose Josephson junctions do not form a superconducting loop but are rather connected to an outside circuit (Figure 1.17). Therefore, in this thesis, the transistor is described with the same conventions and notations as the split box. Instead of representing a mean loop current, $i_k(n_g,\delta)$ simply represents the average current through the series of the two junctions for a box in the state $|k\rangle$. The specificity of the transistor is that the dynamics of δ is imposed by the outside circuit.

Critical current of the transistor

In the ground state, the current $i_0(n_g,\delta)$ passing through the transistor is 2π-periodic on δ . The transistor behaves as a tunable Josephson junction with a critical current:

$$I_0^{eff}(n_g) = \max_{\delta}[i_0(n_g,\delta)] \ . \tag{1.64}$$

This current is 1-periodic on the gate charge n_g, with maxima at half integer values of n_g (Figure 1.18, left panel). Hence, the transistor is a charge-current transducer. An electrometer is obtained when this transducer is embedded in a current measuring circuit.

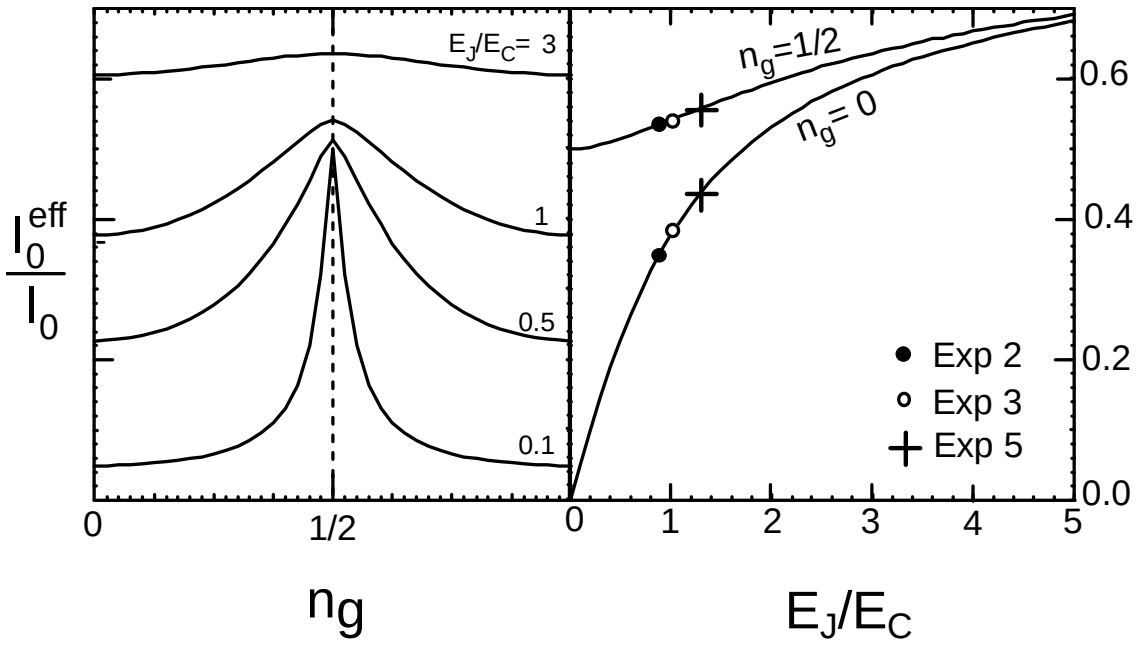

Figure 1.18: *Left panel: Gate charge modulation of the reduced critical current I_0^{eff}/I_0 of the transistor [see (1.63)], for different values of E_J/E_C. Right panel: Variations of I_0^{eff}/I_0 with E_J/E_C for $n_g = 1/2$ (top curve) and $n_g = 0$ (bottom curve). The circles correspond to the current through the transistors of the experiments 2 and 3. Note that this graph can also be used as an abacus to evaluate the effective current $I_0^{eff}(n_g, \delta)$ of a split box in state $|0\rangle$. The cross corresponds to the split box of experiment 5.*

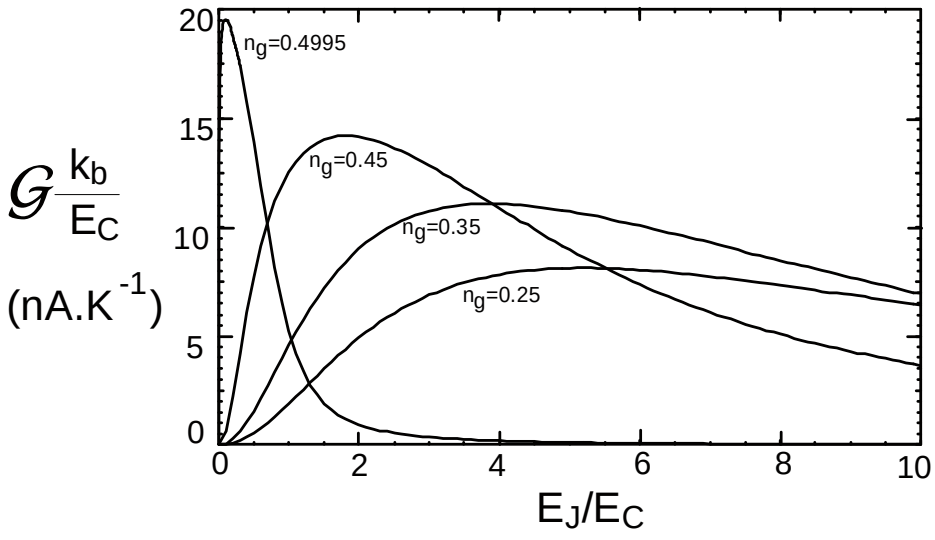

Figure 1.19: *Variations of the transduction coefficient $\mathcal{G}$ of the Cooper pair transistor with E_J/E_C for different values of n_g.*

Charge-current transduction coefficient

The transduction coefficient from the gate charge to the current of the transistor,

$$\mathcal{G}(n_g) = \frac{\partial I_0^{eff}(n_g)}{\partial n_g} \ , \tag{1.65}$$

is plotted in Figure 1.19 for different values of n_g . For $E_J/E_C \ll 1$, the maximum value of $\mathcal{G}$ is located near $n_g = \frac{1}{2}$. When E_J/E_C is increased, this maximum softens and shifts towards $n_g = 1/4$. Although the largest transduction coefficient is obtained at low E_J/E_C, the associated sharp gate charge dependence of $\mathcal{G}$ is inconvenient. In order to measure charges with a Cooper pair transistor, we suggest to take a value $E_J = E_C$ as high as possible.

Sinusoidal approximation

The energy $E_0(n_g,\delta)$ of the ground state $|0\rangle$ of the Cooper pair transistor can be decomposed into a Fourier series:

$$E_0(n_g, \delta) = \sum_{p \in \mathbb{N}} c_p(n_g) \cos(p\delta) \ .$$

When the anharmonicity coefficient:

$$\mathcal{F}(n_g) = 1 - \frac{c_1^2}{\sum\limits_{p \geq 1} c_p^2}$$

of the ground state is lower than 1% (Figure 1.20), we consider that the sinusoidal approximation:

$$E_0(n_g, \delta) = -E_0^{eff}(n_g) \cos(\delta) \tag{1.66}$$

is valid. In this case, the supercurrent passing through the transistor is:

$$i_0(n_g, \delta) = I_0^{eff}(n_g) \sin(\delta) \ ,$$

with:

$$I_0^{eff}(n_g) = \frac{E_0^{eff}(n_g)}{\varphi_0} \ . \tag{1.67}$$

The results valid for a single Josephson junction can thus be used to predict quantitatively the behaviour of the Cooper pair transistor, provided one replaces the Josephson energy E_J and the critical current I_0 of the junction by $E_0^{eff}(n_g)$ and $I_0^{eff}(n_g)$.

The optimal Cooper pair transistor for a quantum bit experiment

The sensitivity of the electrometer formed by a Cooper pair transistor embedded in a measuring circuit depends on the transistor charge-current transduction coefficient and on the sensitivity of the measuring circuit. This sensitivity is not the only important parameter when the electrometer is used to measure a quantum system. It is also fundamental that the back-action of the transistor on the quantum system be appropriate. The fulfillment of this last requirement will be studied in chapter 3.

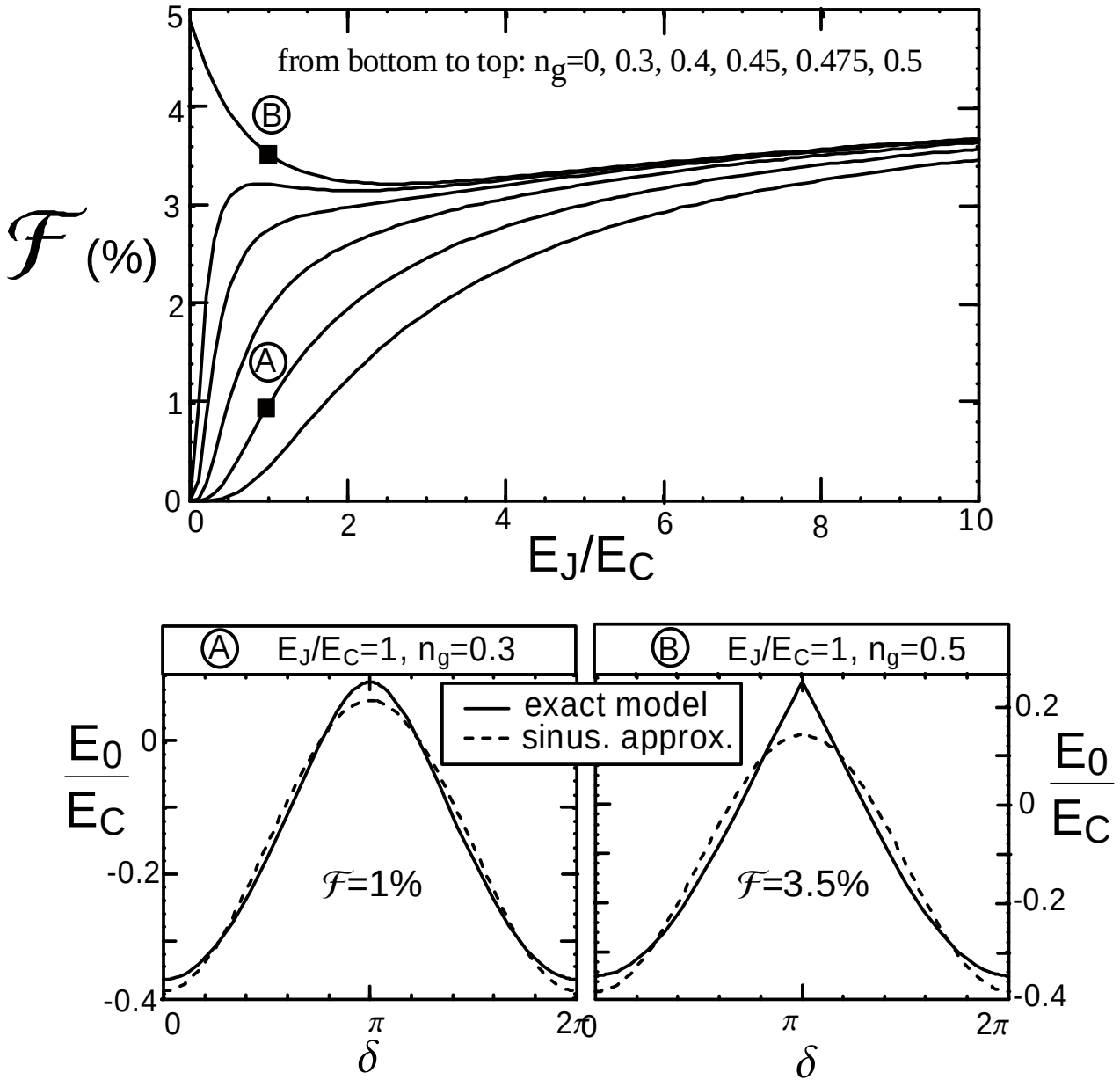

Figure 1.20: *When the ground state of a transistor has an anharmonicity coefficient $\mathcal{F}$ (top panel) lower than 1% , its energy varies almost sinusoidally with the phase δ (case A in the bottom left panel). For the value $n_g = 0.5$ corresponding to the maximum sensitivity of the transistor, this approximation is incorrect (case B in the bottom right panel).*

Appendix 1-A: Quantum description of superconducting circuits

A superconducting circuit composed of capacitors, inductors and Josephson junctions can be described with an hamiltonian formalism. The form of the hamiltonian depends on the choice of the independent variables used to describe the circuit [49].

1-A-1 Case of continuous charge transport

We first consider a circuit which only includes capacitors and inductors. This circuit can be decomposed into two terminal devices called branches, connected at points called "nodes". Two different types of variables are available, one related to the nodes of the circuits and one to the branches.

Classical node variables

In order to define node variables, one has to set arbitrarily a reference potential, by choosing a ground node where the voltage potential is zero. The classical description of a node at time t is based on the potential $V_{node}(t)$ of the node, and on the sum $I_{node}(t)$ of the currents arriving on it from the different branches connected to it. If the circuit was at rest at $t = -\infty$ with no voltages and currents, the charge Q_{node} and the flux Φ_{node} of the node at time t can be defined as:

$$Q_{node}(t) = \int_{-\infty}^{t} I_{node}(\tau) d\tau \ ,$$

and

$$\Phi_{node}(t) = \int_{-\infty}^{t} V_{node}(\tau) d\tau \ .$$

In classical electrodynamics, Φ_{node} and Q_{node} are conjugated variables as shown by the Poisson bracket [50]:

$$\{\Phi_{node}, Q_{node}\} = 1 \ . \tag{1.68}$$

Classical branch variables

The classical description of a branch at time t is based on the current $I_{branch}(t)$ through the branch and the voltage $V_{branch}(t)$ across it. If the circuit was at rest at $t = -\infty$ with no voltages and currents, the charge Q_{branch} and flux Φ_{branch} of the branch can be defined as:

$$Q_{branch} = \int_{-\infty}^{t} I_{branch}(\tau) d\tau \ , \tag{1.69}$$

and

$$\Phi_{branch} = \int_{-\infty}^{t} V_{branch}(\tau) d\tau \ . \tag{1.70}$$

Similarly to the node representation, Φ_{branch} and Q_{branch} are conjugated variables as shown by the Poisson bracket[49, 50]:

$$\{\Phi_{branch}, Q_{branch}\} = 1 \ . \tag{1.71}$$

Quantum description

In the general case, we will note conjugate flux and charge variables Φ and Q, disregarding their node or branch nature. The quantum description of Φ and Q can be made by associating to them a couple of conjugate operators $\left(\widehat{\Phi}, \widehat{Q}\right)$. Following the correspondence principle, the Poisson Brackets (1.68) and (1.71) become:

$$\left[\widehat{\Phi}, \widehat{Q}\right] = \mathbf{i}\hbar \ .$$

This conjugation relation causes that $\widehat{\Phi}$ and $\widehat{Q}$ follow the same textbook relations as the position and impulsion of a particle. In particular,

$$|Q\rangle = \frac{1}{\sqrt{2\pi\hbar}} \int_{-\infty}^{+\infty} d\Phi \exp(\frac{\mathbf{i}}{\hbar} Q\Phi) \, |\Phi\rangle \Leftrightarrow |\Phi\rangle = \frac{1}{\sqrt{2\pi\hbar}} \int_{-\infty}^{+\infty} dQ \exp(-\frac{\mathbf{i}}{\hbar} Q\Phi) \, |Q\rangle \ . \tag{1.72}$$

1-A-2 Case of quantized charge transport

There are cases where the charge $\widehat{Q}$ of a branch or a node is quantized in packets of $2e$. It is the case, for instance, for the charge through a Josephson junction. It is also the case for the charge of the nodes which are connected exclusively to Josephson junctions and capacitors, called in this manuscript "metallic islands". In these cases, the convention used in this thesis is to work with the quantized number of Cooper pairs:

$$\widehat{n} = \widehat{Q}/2e \ . \tag{1.73}$$

associated to $\widehat{Q}$.

Conjugate of a 2e-quantized charge

According to the BCS theory, the conjugate of the number $\widehat{N}$ of Cooper pairs in an electrode is the superconducting phase $\widehat{\theta}$ of the electrode. The conjugate of the number $\widehat{N}$ of Cooper pairs having passed through a Josephson junction, is the superconducting phase difference $\widehat{\theta}$ through the junction. Let us note $|\theta\rangle$ the eigenstates of $\widehat{\theta}$:

$$\widehat{\theta}\,|\theta\rangle = \theta\,|\theta\rangle \ ,$$

with $\theta \in \mathbb{R}$. In the BCS theory, the discreteness of $\widehat{N}$ causes that $|\theta\rangle$ and $|\theta + 2\pi\rangle$ have the same physical meaning. As a consequence, in order to describe the states of the node or branch, it is enough to work on the basis $\{|\theta\rangle\,, \theta \in [0, 2\pi[\}$.

Properties of conjugate variables

Because of the circular topology of the phase space associated to $\widehat{\theta}$, physical expressions can only contain $\widehat{\theta}$ through trigonometric expressions. The analog of formulas (1.72) are the Fourier transforms between the eigenstates $\{|\mathbf{n}\rangle\,, \mathbf{n} \in \mathbb{Z}\}$ of $\widehat{\mathbf{n}}$ and the eigenstates $\{|\theta\rangle\,, \theta \in [0, 2\pi[\}$ of $\widehat{\theta}$ [51]:

$$|\theta\rangle = \frac{1}{\sqrt{2\pi}} \sum_{\mathbf{n}\in\mathbb{Z}} \exp(\mathbf{i}\widehat{\mathbf{n}}\theta)\,|\mathbf{n}\rangle \Leftrightarrow |\mathbf{n}\rangle = \frac{1}{\sqrt{2\pi}} \int_0^{2\pi} d\theta \exp(-\mathbf{i}\widehat{\mathbf{n}}\theta)\,|\theta\rangle \ . \tag{1.74}$$

This relation ensures the validity of some fundamental properties likes the translational relations:

$$\exp(\mathbf{i}p\widehat{\theta})\,|\mathbf{n}\rangle = |\mathbf{n}+p\rangle \tag{1.75}$$

and

$$\exp(-\mathbf{i}\theta_0\widehat{\mathbf{n}})\,|\theta\rangle = |\theta - \theta_0\rangle \ , \tag{1.76}$$

with $\mathbf{p} \in \mathbb{N}$ and $\theta_0 \in \mathbb{R}$. It also infers that $\widehat{\mathbf{n}}$ can be expressed in the phase space as:

$$\widehat{\mathbf{n}} = \frac{1}{\mathbf{i}} \frac{\partial}{\partial\theta} \ , \tag{1.77}$$

and that $\widehat{\theta}$ can be expressed in the charge space as:

$$\widehat{\theta} = \mathbf{i} \frac{\partial}{\partial\mathbf{n}} \ . \tag{1.78}$$

Eventually, for any observable $\widehat{A}$,

$$\left[\widehat{A}, \widehat{H}\right] = \mathbf{i}\hbar \frac{\partial\widehat{A}}{\partial t} \ , \tag{1.79}$$

$$\left[\widehat{A}, \widehat{\mathbf{n}}\right] = \mathbf{i} \frac{\partial\widehat{A}}{\partial\widehat{\theta}} \ , \tag{1.80}$$

and:

$$\left[\widehat{A}, \widehat{\theta}\right] = -\mathbf{i} \frac{\partial\widehat{A}}{\partial\widehat{\mathbf{n}}} \ . \tag{1.81}$$

1-A-3 Eliminating variables

The different branch and node variables which can be defined for a given circuit are not independent. There exists a certain number of topological relations between them.

Continuous charge case

The branch and node variables are linked by the quantum version of the Kirchhoff's laws. At a node n,

$$\widehat{Q}_{node} = \sum_{\substack{branch \\ \text{connected to the } node}} \widehat{Q}_{\ branch} \ , \tag{1.82}$$

and around a loop crossed by a magnetic flux Φ_m,

$$\Phi_m = \sum_{\substack{branch \text{ included} \\ \text{in the } loop}} \widehat{\Phi}_{branch} \ . \tag{1.83}$$

There is also a topological relation between the flux of a branch b and the flux of the two nodes *node* 1 and *node* 2 delimitating this branch:

$$\Phi_{branch} = \pm \left(\Phi_{node\ 1} - \Phi_{node\ 2}\right) \ . \tag{1.84}$$

The arbitrary sign in this last relation determines the orientation of the branch.

Quantized charge case

In the case of a quantized number of charge $\widehat{\mathbf{n}}$, the relations (1.82) must include the charge $\widehat{Q} = 2e\widehat{\mathbf{n}}$. The relationship between the superconducting phase $\widehat{\theta}$ conjugated to $\widehat{\mathbf{n}}$ and the flux $\widehat{\Phi}$ included in the Equations (1.83) and (1.84) is:

$$\widehat{\theta} = \widehat{\Phi}/\varphi_0 \ [\text{mod } 2\pi] \ . \tag{1.85}$$

Choice of the description

In order to describe a quantum circuit, one must eliminate the redundant variables. This procedure is not unique. The most convenient set of parameters will depend on what one wants to calculate.

Chapter 2

The single Cooper pair transistor as an electrometer

The gate charge modulation of the current $i_0(n_g,\delta)$ passing through a Cooper pair transistor in its ground state provides a charge-current transduction mechanism. This mechanism can be used for electrometry by embedding the transistor in a suitable measuring circuit. We describe in this chapter the two types of electrometers based on the single Cooper pair transistor that we have developed for the purpose of measuring the island voltage of a Cooper pair box.

Since a single Cooper pair transistor in its ground state almost behaves as a tunable Josephson junction with an effective critical current $I_0^{eff}(n_g)$, all the techniques for measuring Josephson junctions with a similar critical current can be used to develop electrometers. For optimized electrometers, this critical current range is solely determined by the junction technology. Indeed, the Josephson energy of the transistor junctions should be as large as possible in order to achieve at first place a large critical current, while remaining smaller than or comparable to the charging energy E_C of the transistor in order to have a sharp modulation pattern. In this regime, the transduction coefficient $\mathcal{G}(n_g) = \partial I_0^{eff}(n_g)/\partial n_g$ is maximum slightly below and above $n_g = 1/2$ (see chapter 1). In order to avoid the entry of quasiparticles in the transistor island, which would suppress the modulation peak of $I_0^{eff}(n_g)$ at $n_g = 1/2$, the charging energy is constrained by the condition $E_C \leq 4\Delta$, where Δ is the gap energy in the island [51, 52]. For aluminum, these conditions impose a maximum critical current I_0 in the 100 nA range.

2.1 Measuring small critical current Josephson junctions

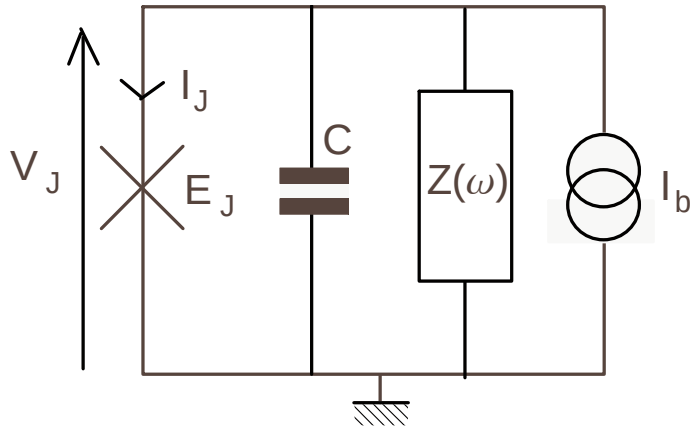

Figure 2.1: *Electrical scheme of a Josephson junction shunted by an impedance $Z(\omega)$ and biased by a current source I_b. The capacitive part $1/\mathbf{i}\omega C_{env}$ of $Z(\omega)$ has been incorporated in the total capacitance seen by the junction $C = C_J + C_{env}$.*

Although the Josephson effect has been extensively investigated over the years, the observation of a supercurrent approaching the critical current was achieved only recently in the case of Josephson junctions with a critical current smaller than 100 nA . Having a supercurrent close to the critical current indeed requires to have a stable state $\bar{\delta} \approx \pi/2$ for the superconducting phase difference δ across the junction. For that purpose, the dynamics of δ must be strongly damped by the embedding circuit [26, 53], so that δ does not present strong fluctuations. In this so-called overdamped regime, the phase across the junction is a classical variable which obeys a first order Langevin equation.

2.1.1 The classical regime for the phase

The validity of the classical description can be estimated from the phase fluctuations. Let us consider the general case of a current-biased Josephson junction with Josephson energy $E_J = \varphi_0 I_0$ and with capacitance C_J , shunted by an impedance $Z(\omega)$ (Figure 2.1). We consider that the capacitive part $1/\mathbf{i}\omega C_{env}$ of $Z(\omega)$ is included in the total capacitance seen by the junction:

$$C = C_J + C_{env} \ . \tag{2.1}$$

Assuming that phase fluctuations are indeed small, the quadratic average $\left\langle \delta^2 \right\rangle$ can be calculated at zero bias current by treating the junction as an effective inductor $L = \varphi_0 / I_0$. One finds [49]:

$$\left\langle \left(\frac{\delta}{2\pi} \right)^2 \right\rangle = \int_0^\infty \frac{\mathrm{Re}\, Z_{eff}(\omega)}{R_K} \coth \frac{\hbar\omega}{2k_B T} \, \frac{d\omega}{\omega} \ , \tag{2.2}$$

where:

$$Z_{eff}(\omega) = (1/\mathbf{i}\omega L + \mathbf{i}\omega C + Z^{-1}(\omega))^{-1} \tag{2.3}$$

is the impedance of the effective RLC circuit.

2.1.2 The Resistively Shunted Junction model (RSJ model)

In the case when the impedance $Z(\omega)$ is a pure resistor $Z(\omega) = R$, the average fluctuations $\langle\delta^2\rangle$ can be analytically calculated [49]. They are plotted in Figure 2.2 as a function of the reduced temperature $k_BT/\hbar\omega_0$, where:

$$\omega_0 = \frac{1}{\sqrt{LC_J}} \tag{2.4}$$

is the plasma frequency, and for different values of the quality factor $Q = R\sqrt{C/L}$.

When the thermal fluctuations dominate the quantum ones, it is valid to treat the phase as a classical variable, as justified by the full calculation of H. Grabert and G.L. Ingold [54]. The evolution equation for the phase is then obtained by inserting in the classical Kirchhoff's laws of the circuit the Josephson relations [40, 55]:

$$V_J = \varphi_0 \frac{d\delta}{dt} \ , \tag{2.5}$$

and

$$I_J = I_0 \sin\delta(t) \ , \tag{2.6}$$

where V_J and I_J are the instantaneous voltage and currents across the junction. One then obtains the following Langevin equation[1] [56]:

$$\frac{1}{R}\varphi_0^2\frac{d\delta}{dt} = -C\varphi_0^2\frac{d^2\delta}{dt^2} + \varphi_0\left[I_b - I_0\sin(\delta) + i_R(t)\right] \tag{2.7}$$

where $i_R(t)$ is the current noise produced by the thermal fluctuations in the resistor (Appendix 3-B), characterised by:

$$\langle i_R(t)i_R(0)\rangle = \frac{2k_bT}{R}\delta_D(t) \ , \tag{2.8}$$

with $\delta_D(t)$ the Dirac function. The evolution of δ is analogous to that of a fictitious particle with position δ and mass $C\varphi_0^2$, placed in the tilted washboard potential $\mathcal{U}(\delta) = -E_J\cos(\delta) - I_b\varphi_0\delta$, submitted to a random force -$i_R(t)\varphi_0$ and to an instantaneous frictional force $-(\varphi_0^2/R)\,d\delta/dt$. When the particle escapes out of a well under the effect of thermal fluctuations, two types of dynamics can occur. Either the friction is small and the particle accelerates continuously, either the friction is so large that the particle is retrapped in another well. This large friction regime, for which the mass can be neglected, is characterised by $Q \ll 1$ and is called the overdamped regime. We now discuss the circuits which allow to implement this overdamped regime.

[1] This equation is valid provided $e\overline{V_J} < 2\Delta$ and $k_bT \ll 2\Delta$.

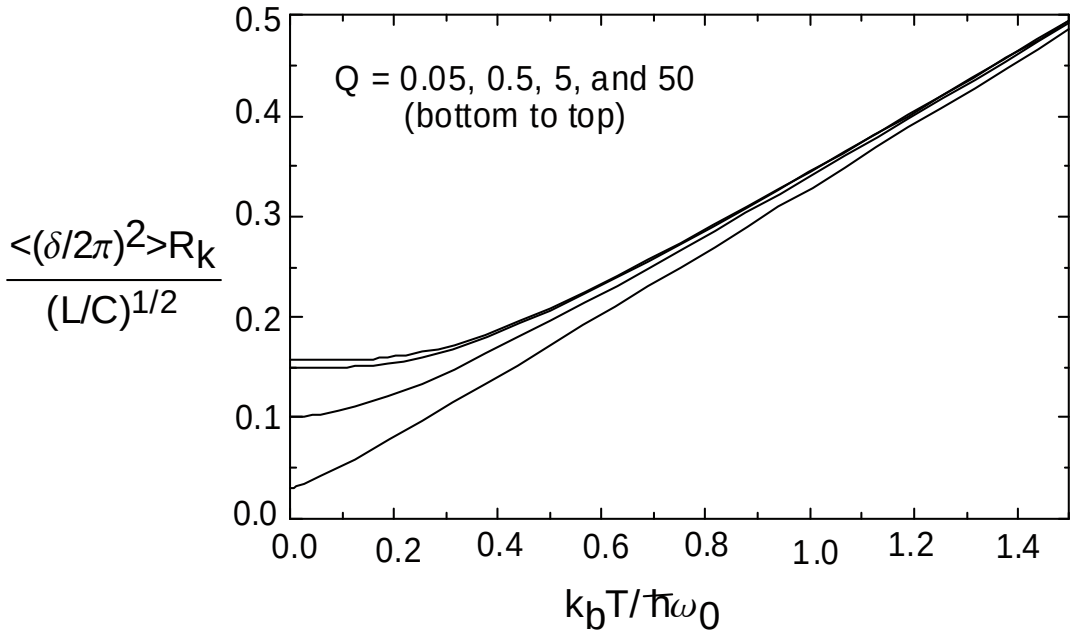

Figure 2.2: *Reduced phase fluctuations* $\langle \delta^2 \rangle$ *as a function of the reduced temperature* $k_B T/\hbar\omega_0$ *for different values of the quality factor* Q.

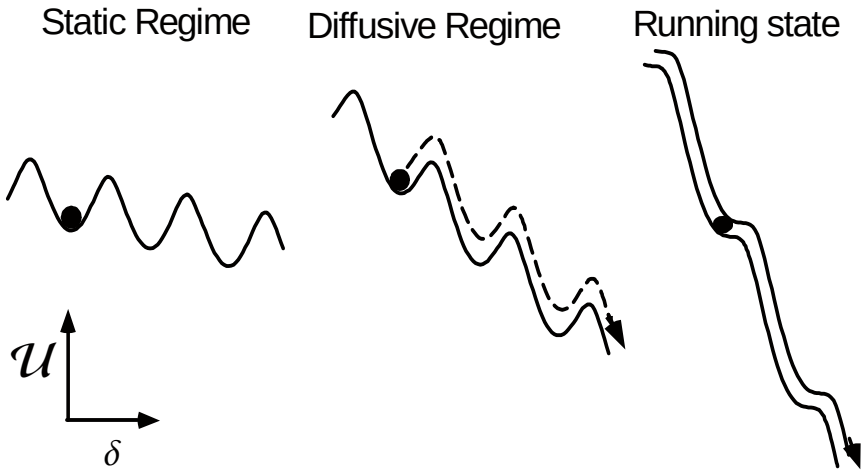

Figure 2.3: *The phase of a current biased Josephson junction has the same dynamics as that of a particle in a tilted potential whose average slope is controlled by the bias current. Different dynamical states can exist, depending on mass, damping, and temperature. At low temperature, the particle is trapped in one of the potential wells when the bias current is smaller than the critical current. At finite temperature, the particle can either undergo a diffusive motion from well to well when the damping is strong and the mass small enough, or a continuous motion without being retrapped in a well when the potential energy gain is large enough to overcome frictional losses.*

2.1.3 The overdamped RSJ model

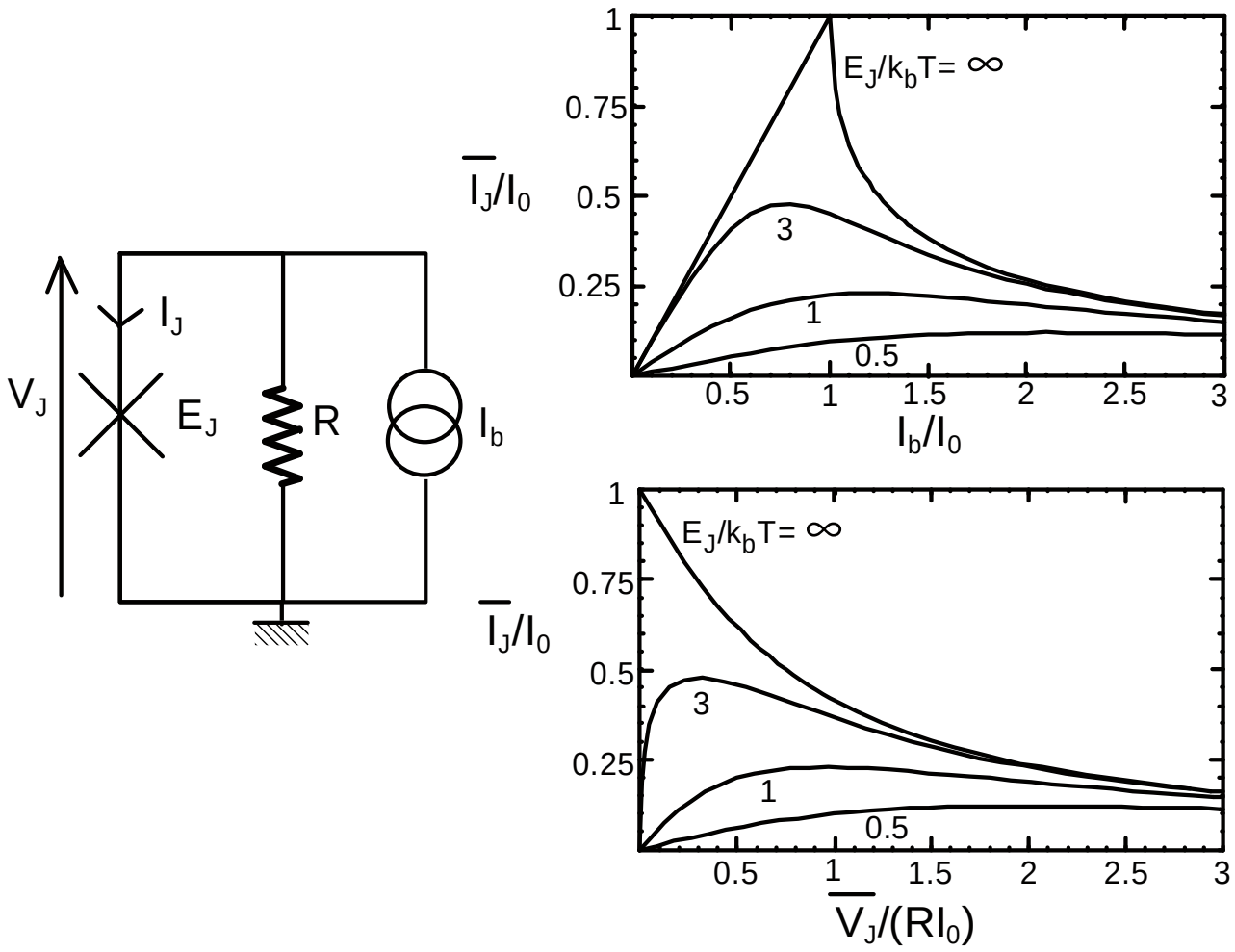

Figure 2.4: *Left panel: Electrical scheme of a Josephson junction shunted by a resistor R and biased with a current source I_b. The notations I_J and V_J refer to the instantaneous values of respectively the current through the junction and the voltage across it. Right panel: Predicted $\overline{I_J} - I_b$ and $\overline{I_J} - \overline{V_J}$ characteristics of the circuit for different reduced temperatures ($\overline{I_J}$ and $\overline{V_J}$ correspond to the values of I_J and V_J averaged over the phase dynamics).*

The overdamped RSJ model [40] corresponds to the circuit of Figure 2.4. The Langevin equation obeyed by $\delta(t)$ reduces to:

$$\frac{\varphi_0^2}{R}\frac{d\delta}{dt} = \varphi_0 \left[I_b - I_0 \sin(\delta) + i_R(t) \right] \ . \tag{2.9}$$

Yu. M. Ivanchenko and L.A. Zil'berman have solved the stationary Fokker-Planck equation associated to this equation [57].

Ivanchenko-Zil'berman solution

Let $\overline{V_J}$ and $\overline{I_J}$ be the values of the voltage V_J across the junction and of the current I_J passing through it, averaged over the phase dynamics[2] being made over the so called "Josephson period" of the oscillations of the phase δ in the potential $\mathcal{U}$. The Ivanchenko-Zil'berman equation give $\overline{V_J}$ and $\overline{I_J}$ [40, 57, 58] as a function of I_b:

$$\begin{cases} \overline{I_J}(I_0, I_b, T) = I_0 \, \mathrm{Im}[\frac{B_{1-i\eta}(\varepsilon)}{B_{-i\eta}(\varepsilon)}] \\ \overline{V_J}(I_0, I_b, T) = RI_b - R\overline{I_J} \ , \end{cases} \tag{2.10}$$

with

$$\varepsilon = \frac{I_0 \varphi_0}{k_b T} \ ,$$
$$\eta = \frac{I_b \varphi_0}{k_b T} \ ,$$

and with $B_a(b)$ the modified Bessel function with complex order a . The maximum predicted supercurrent is close to I_0 for $\eta \gg 1$.

Phase dynamics

The $\overline{I_J} - I_b$ and $\overline{V_J} - \overline{I_J}$ characteristics resulting from the Ivanchenko-Zil'berman relations (Figure 2.4, right panel) can be explained qualitatively using the picture of the fictitious particle (Figure 2.3) in the potential $\mathcal{U}$. If $I_b < I_0$ and $T = 0$, the particle, slowed down by the friction, stops at a local minimum δ_0 of the potential, so that $I_j = I_0 \sin(\delta_0)$ and $V_J = 0$. The particle can be activated out of this metastable position under the influence of thermal fluctuations. If $I_b < I_0$ and $T \neq 0$, the particle diffuses from well to well, which explains the apparition of a finite voltage across the junction. For $I_b > I_0$, the potential has no local minimum and the particle goes down the potential whatever the temperature is. However, the friction provided by the resistor prevents the fictitious particle from accelerating indefinitely: it reaches a stationary regime when the energy lost by friction is balanced by the potential energy gain. In this regime, $d\delta/dt$ is periodic, with a Josephson frequency:

$$\Omega_J = \frac{2\pi}{T_J} = \frac{\overline{V_J}}{\varphi_0} \ . \tag{2.11}$$

The noise spectrum of V_J present peaks at harmonics of Ω_J [55, 56].

[2] More precisely, $\overline{V_J}$ and $\overline{I_J}$ correspond to V_J and I_J averaged over the correlation time of the phase δ, which depends on I_b. Performing such an average is relevant because the Josephson oscillations have a too high frequency to be observable experimentally in standard current and voltage measurements. (see (2.11)). The quantities $\overline{V_J}$ and $\overline{I_J}$ thus correspond to the signals measured in practice. Since this average is performed on a short timescale, $\overline{V_J}$ and $\overline{I_J}$ are time dependent signals. Time variations of $\overline{V_J}$ and $\overline{I_J}$, due to sudden switching to a voltage state (see 2.2.2 and 2.3.2) or to fast variations of an external parameter can be observed within the bandwidth of the measuring system, which is larger than 1 MHz in our setup.(Figure 2.10 of section 2.3.1).

2.1.4 The (R+C)SJ model

The classical (R+C)SJ model corresponds to a Josephson junction shunted by an impedance (Figure 2.5):

$$Z(\omega) = \left(\mathbf{i}\omega C + \frac{1}{1/R_s + \mathbf{i}\omega C_s} \right)^{-1} .$$

The main difference with the RSJ model is the absence of damping at zero frequency: one says that the junction is AC shunted, instead of being DC shunted. This model is important because it corresponds to the usual set-up for measuring the current-voltage characteristic of Josephson junctions. When the condition $R_s C_s \omega_0 \gg 1$ is fulfilled, the classicality conditions for the phase are not changed [26]. In this regime, the phase δ and the voltage V_s across the capacitor C_s obey the set of Langevin equations:

$$\frac{1}{R_s}\varphi_0^2 \frac{d\delta}{dt} = -C\varphi_0^2 \frac{d^2\delta}{dt^2} + \varphi_0 \left[I_b - I_0 \sin(\delta) + \frac{V_s}{R_s} + i_R(t) \right] \tag{2.12}$$

$$C_s \frac{dV_s}{dt} = I_b - I_0 \sin(\delta) - C\varphi_0^2 \frac{d^2\delta}{dt^2} , \tag{2.13}$$

where $i_R(t)$ is the thermal current noise due to the resistor (Appendix 3-B), with:

$$\langle i_R(t) i_R(0) \rangle = \frac{2k_b T}{R_s} \delta_D(t) .$$

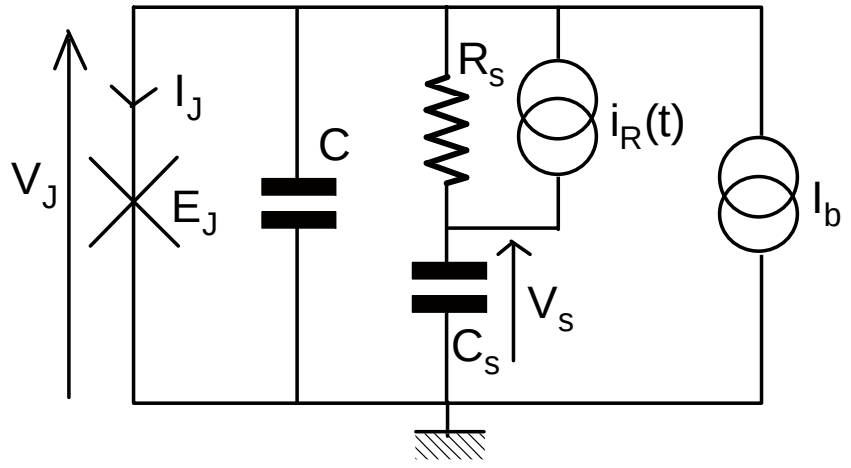

Figure 2.5: *Electrical scheme of the $(R+C)SJ$ model.*

Phase dynamics

The behaviour of the junction can again be explained qualitatively with the picture of the fictitious particle. The particle with mass $C\varphi_0^2$, placed in the potential $\mathcal{U}$, is now submitted to a random force $i_R(t)\varphi_0$, a friction force $-(\varphi_0^2/R_s)(d\delta/dt)$ and an accelerating force $\varphi_0 V_s/R_s$. For $I_b < I_0$, as long as V_s is negligible, the phase slowly diffuses in the tilted potential like in

the DC case. However, there is a finite probability that a thermal fluctuation, stronger than the others, makes the particle accelerate significantly. From that moment, the acceleration force $\varphi_0 V_s/R_s$ increases inexorably and is bound to beat the friction forces. Consequently, the junction develops a high voltage and jumps to the quasiparticle branch. This event, called "switching", occurs at a rate $\Gamma_s(I_b)$ which depends on the bias current I_b . This is precisely this effect which prevents to observe supercurrents close to the critical current for most AC shunted set-ups [59].

2.1.5 The overdamped (R+C)SJ model

When the junction capacitance C can be neglected, the characteristic evolution times for δ and for V_s predicted by Equations (2.12) and (2.13) are $T_\delta = \frac{\varphi_0}{R_s I_0}$ and $T_s = R_s C_s$. When the condition :

$$C_s \gg \frac{\varphi_0}{I_0} R_s^2 \tag{2.14}$$

is satisfied, one has $T_s \gg T_\delta$. The dynamics of V_s is then much slower than that of δ, and one can use an adiabatic approximation for V_s in order to solve the equations (2.12) and (2.13) [26]. In the infinite C_s limit, this theory predicts that the supercurrent branch of the current-voltage characteristic is exactly the same as for the RSJ model till the maximum value is reached, at which switching to the voltage-state occurs. A large supercurrent can thus be observed at low temperature in this regime. When C_s is finite, this theory allows to calculate the switching rate from the phase diffusion state to the voltage state. The switching process corresponds to the activation above an effective dynamical barrier, whose height increases with damping. The conclusion of this analysis is that a well developed supercurrent branch can be observed in the overdamped regime, even when the escape probability out of a well is large on the time-scale of the experiment, because retrapping in the neighboring wells prevents the particle to run-away. Numerical simulations show that a large supercurrent can be observed even when the junction capacitance C cannot be fully neglected.

2.2 Implementation of the overdamped RSJ and (R+C)SJ models

2.2.1 Case of the overdamped RSJ model (Experiment 1)

In practice, it is difficult to have a circuit implementing exactly the classical RSJ model with a value of R constant at all frequencies. Let us first suppose that the junction is only connected to an off-chip resistor R . The connections between the junction and R have an inductance L of typically 1 nH.mm^{-1} . At high frequencies, this inductance dominates the impedance seen by the junction. One could imagine to avoid this effect by placing the resistor R on-chip, very close to the junction. However, this is not possible because the dissipation would heat R .

We have adopted a mixed strategy where the DC part of the impedance is off-chip and the AC part on-chip (Figure 2.6). The behaviour of the circuit is probed with a SQUID array amplifier [23, 60] developed by the NIST (Appendix 2-B-2). The interest of that amplifier, apart from its large bandwidth, is its low input impedance, which makes possible the implementation of the overdamped case.

At low frequencies, the effective impedance R seen by the Josephson junction is the sum:

$$R = R_b + R_m + R_c \simeq 24\ \Omega\ ,$$

where $R_c = 12.1\ \Omega$ is the total resistance of the contacts between the electrical lines and the sample and where R_b and R_m are discrete electronic components implemented off-chip. The high frequency impedance of the junction is controlled by the $(R_s + C_s)$ series circuit fabricated on-chip very close to the junction. The resistor $R_s = 11.8\ \Omega$ has been chosen so that the impedance seen by the junction above 10 GHz still equals:

$$R_s + R_c \simeq 24\ \Omega = R\ .$$

We have calculated the expected $\overline{V_J} - \overline{I_J}$ characteristic using numerical simulations of the phase dynamics for the exact circuit. This characteristic is very close to the one predicted by the equation (2.9) with $R = 24\ \Omega$. This environment thus closely implements the RSJ model.

The experimental $\overline{I_J} - \overline{V_J}$ curves are presented in Figure (2.6). We have fitted them using the equations (2.10), and the values $I_0 = 44.9$ nA, and $R = 24\ \Omega$.

Further details about this experiment can be found in Appendix 2.B.4 *and in the article* [24] *which is reproduced at the end of this chapter.*

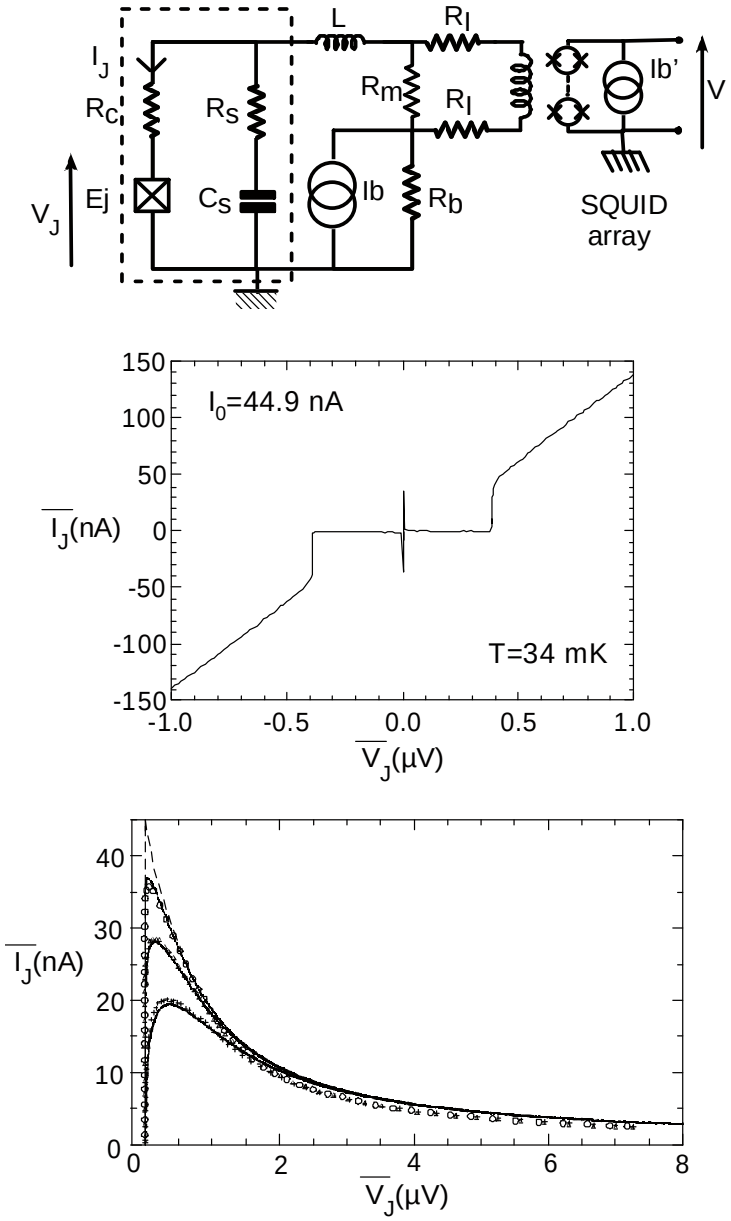

Figure 2.6: *Top panel: Circuit used for the measurement of the DC shunted junction. The chip is indicated by the dotted box. The components* $R_s = 11.8\ \Omega$ *and* $C_s = 100$ pF *are implemented on-chip. The elements* $R_b = 10.1\ \Omega$, $R_m = 1.6\ \Omega$ *and* $R_I = 10\ \Omega$ *are Surface Mounted Components (SMC). The stray inductance of the connection between the on-chip and the off-chip circuitry is* $L \simeq 4$ nH. *The contact resistance* $R_c = 12.1\ \Omega$ *results from the junction fabrication process. A 7.5 % fraction of the current passing through the junction is derived in the input coil of a SQUID array. Middle panel: Large scale* $\overline{I_J} - \overline{V_J}$ *characteristic measured at* $T = 34$ mK. *Bottom panel: The low scale* $\overline{I_J} - \overline{V_J}$ *characteristics measured for different temperatures (symbols) can be fit using equations* (2.10), *with* $I_0 = 44.9$ nA, *and an effective bias resistance* $R = 24\ \Omega$. *From top to bottom,* $T = 34$, 157 *and* 440 mK *respectively. The dashed line represents the characteristic predicted for* $T = 0$.

2.2.2 Case of the overdamped (R+C)SJ model

The circuit of Figure 2.5 has been implemented by P. Joyez et al. [26] for $R = 70\ \Omega$ and $C = 150$ pF . An $\overline{I_J} - \overline{V_J}$ is shown in Figure 2.7. The junction switches to the voltage-state when the bias current I_b reaches the switching current I_s . The values of I_s are distributed with an histogram whose shape is determined by the switching rate $\Gamma_s(I_b)$ and by the ramping speed v_I used to measure the $\overline{I_J} - \overline{V_J}$ characteristic [61]. This histogram is in good agreement with theory.

We now report the experimental implementations of the overdamped RSJ and (R+C)SJ models for measuring single Cooper pair transistors.

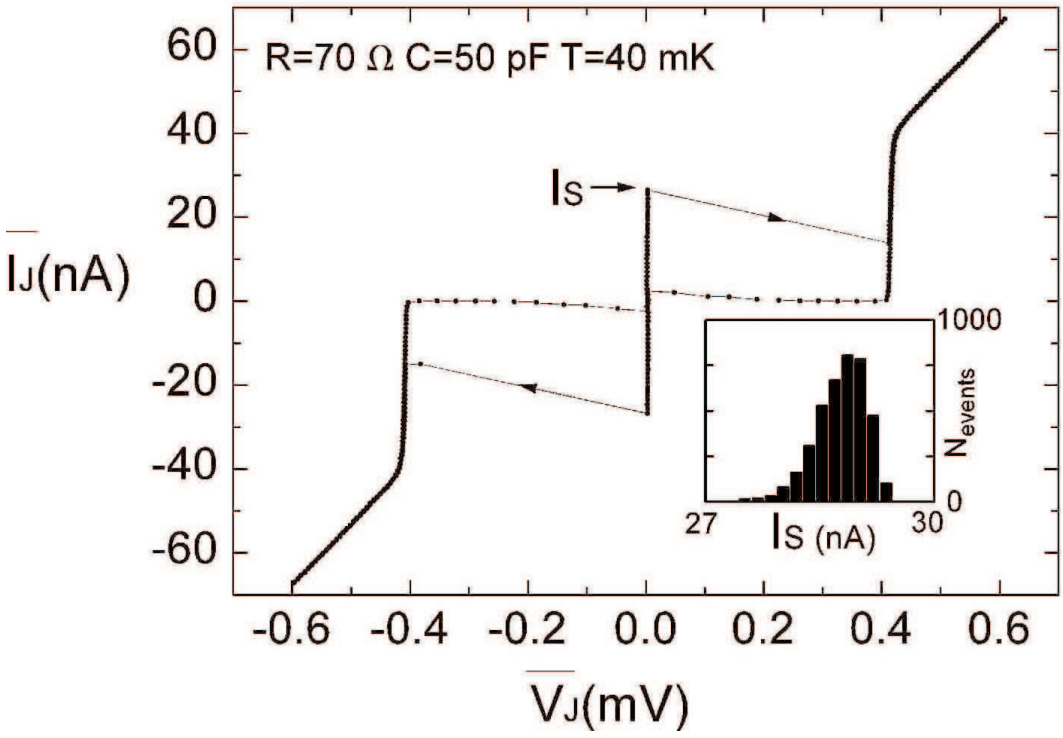

Figure 2.7: *Large scale $\overline{I_J}-\overline{V_J}$ characteristic of a (R+C) shunted junction, taken at $T = 40$ mK for $R = 70\ \Omega$ and $C_r = 150$ pF and a reduced bias current ramping speed $v_I^r = d(I_b/I_0)/dt = 8.5$ s^{-1} (from reference [26]). The switching current I_s is probabilistic and its values are distributed on a histogram (inset).*

2.3 Electrometers based on the Cooper pair transistor

Qualitatively, a Cooper pair transistor embedded in the two preceding circuits behaves as an effective Josephson junction with an effective critical current $I_0^{eff}(n_g)$. We discuss here the sensitivity of the electrometers obtained with both methods.

2.3.1 Resistively shunted Cooper Pair transistor (Experiment 2)

Principle and design of the experiment

The first electrometer circuit we have operated is represented in Figure 2.9. The main difference with the circuit of experiment 1 is that we have placed the SQUID array in the resistor branch and not in series with the transistor, hoping that it would lower the effect of the Josephson oscillations of the SQUIDs on the transistor. We thought it would allow us to reduce the filtering of the input line of the SQUID in order to have an electrometer with a larger bandwidth.

Experimental current-voltage characteristic and gate modulation curves

The $\overline{I_J} - \overline{V_J}$ and $n_g - \overline{I_J}$ curves measured at $T = 40$ mK are shown in Figure (2.9). We have fitted them using equations (2.10), with $I_0 = I_0^{eff}(n_g)$, $E_C = 2.8$ k$_b$K, $E_J = 2.2$ k$_b$K, $d = 0$, an effective impedance $R = 38\ \Omega$ seen by the transistor instead of the expected value $R = 24\ \Omega$, and $T = 200$ mK. The input line of the SQUID array being been less filtered than in experiment 1, this excess temperature can probably be attributed to SQUID array noise

Charge-current transduction coefficient

In the circuit of Figure (2.9), a variation Δn_g of the gate charge n_g placed on the transistor causes a variation $\Delta\overline{I_J}$ of current $\overline{I_J}$. The transduction coefficient:

$$\beta = \frac{\partial \overline{I_J}}{\partial n_g} \ ,$$

which depends on I_b, can be calculated as:

$$\beta = \mathcal{G}(n_g)\frac{\partial \overline{I_J}}{\partial I_0} \ ,$$

where $\overline{I_J}(I_b,T)$ is given by the Ivanchenko-Zil'berman relation (2.10), and where $\mathcal{G}(n_g) = \partial I_0^{eff}(n_g)/\partial n_g$ has already been calculated in section 1.4. The transistor must be operated at $I_b \simeq I_0^{eff}$ in order to have the maximum value of β (Figure 2.8)

Electrometry performances

A Cooper pair transistor used as a charge-current transducer has a large intrinsic bandwidth. Indeed, we have simulated numerically the response of the phase to a change Δn_g of the gate charge n_g and found that the new permanent regime is reached in a time comparable to the Josephson period $T_J = \frac{1}{\Omega_J}$. Consequently, the bandwidth of the charge detection is not limited by the transistor but rather by the device used to measure the transistor current.

In experiment 2, we have detected the response of the transistor to a sudden variation $\Delta n_g = 0.1$ of its reduced gate charge n_g (Figure 2.10). This response indicates that the

electrometer has a bandwidth of 1 MHz, probably limited by the filtering of the input lines feeding the SQUID array. The noise level corresponds to a sensitivity of 3.10^{-4} e/$\sqrt{\text{Hz}}$.

Further details about this experiment can be found in Appendix 2.B.5 *and in the article* [25] *which is reproduced at the end of this chapter*

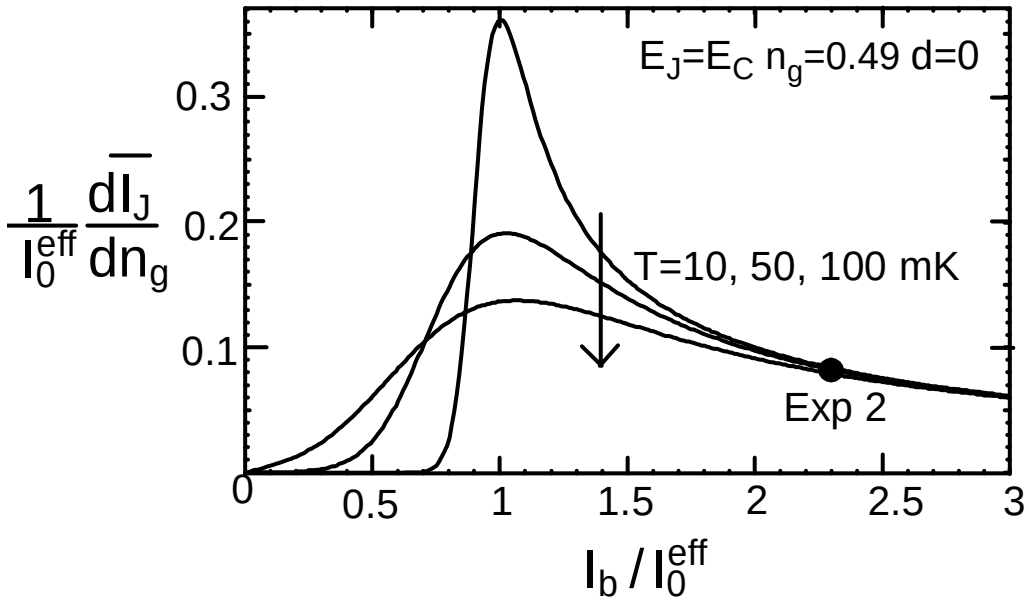

Figure 2.8: *Calculated charge current tranduction coefficient* β *for the continuously driven Cooper pair transistor as a function of the bias current* I_b*, at* $n_g = 0.49$*. The dot corresponds to experiment 2. We have not operated the transistor at the optimal point* $I_b = I_0^{eff}$ *in order to have a transduction coefficient* β *independent of temperature.*

.

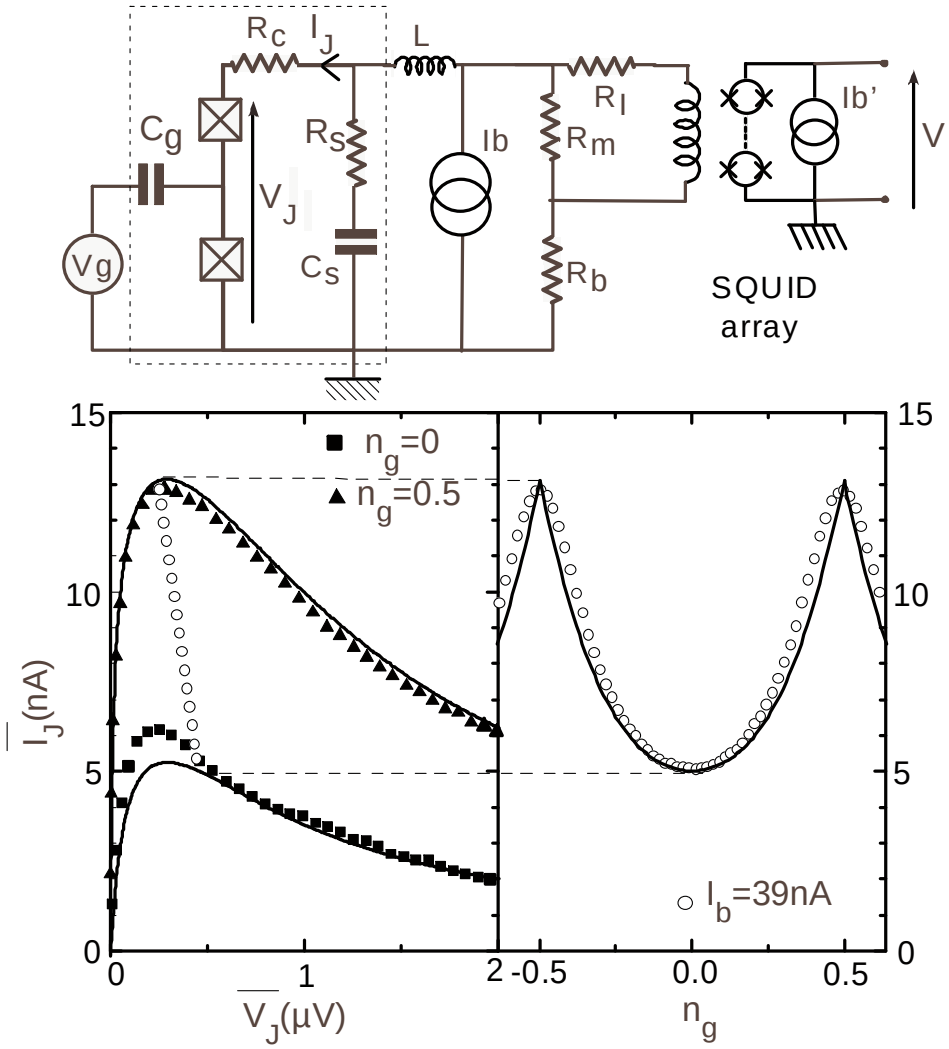

Figure 2.9: *Top panel: Circuit used for the measurement of the DC shunted transistor. The chip is delimited by the dotted square. The elements* $R_b = 10\ \Omega$, $R_s = 11.8\ \Omega$, $C_s = 100$ pF, $R_m = 10\ \Omega$, *and* $R_I = 10\ \Omega$ *are Surface Mounted Components. The contact resistance* $R_c = 10.75\ \Omega$ *results from the transistor fabrication process. The inductance* L *is that of the connections between the on-chip and the off-chip circuitry. One third of the current passing through the shunt resistor is derived in the input coil of a SQUID array. Bottom panel: Comparison between the* $\overline{I_J} - \overline{V_J}$ *and* $\overline{I_J} - n_g$ *characteristics measured at* $T = 40$ mK *(symbols) and the calculated ones (lines) using (2.10) with* $E_J = 2$ k$_b$K, $E_C = 2.2$ k$_b$K, $d = 0$, $R = 38\ \Omega$ *and* $T = 200$ mK.

.

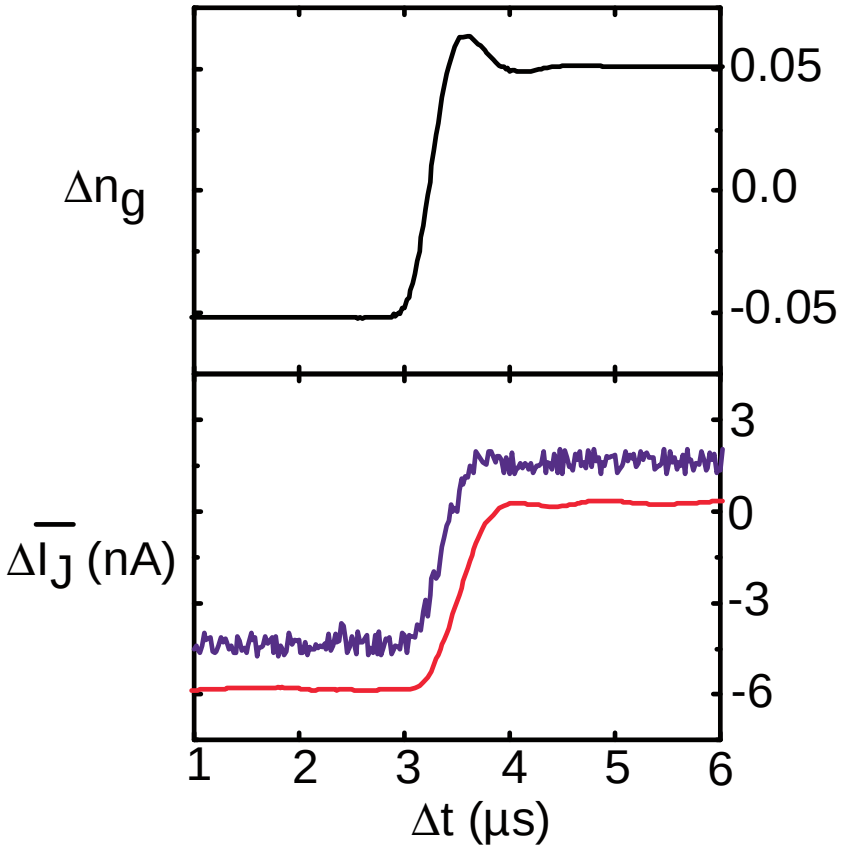

Figure 2.10: *Detection of* 10% *of* $2e$ *in* 1 μs, *with the DC shunted transistor tuned at* $I_b = 39$ nA, *and* n_g *just below* 0.5. *Top panel: Applied charge step at the gate of the transistor. Bottom panel: Transistor response, averaged over* 4000 *curves and measured in a bandwidth of* 10 MHz *(upper curve) and* 1 MHz *(lower curve). (curves offset for clarity).*

2.3.2 AC shunted Cooper pair transistor (Experiment 3)

Principle and design of the experiment

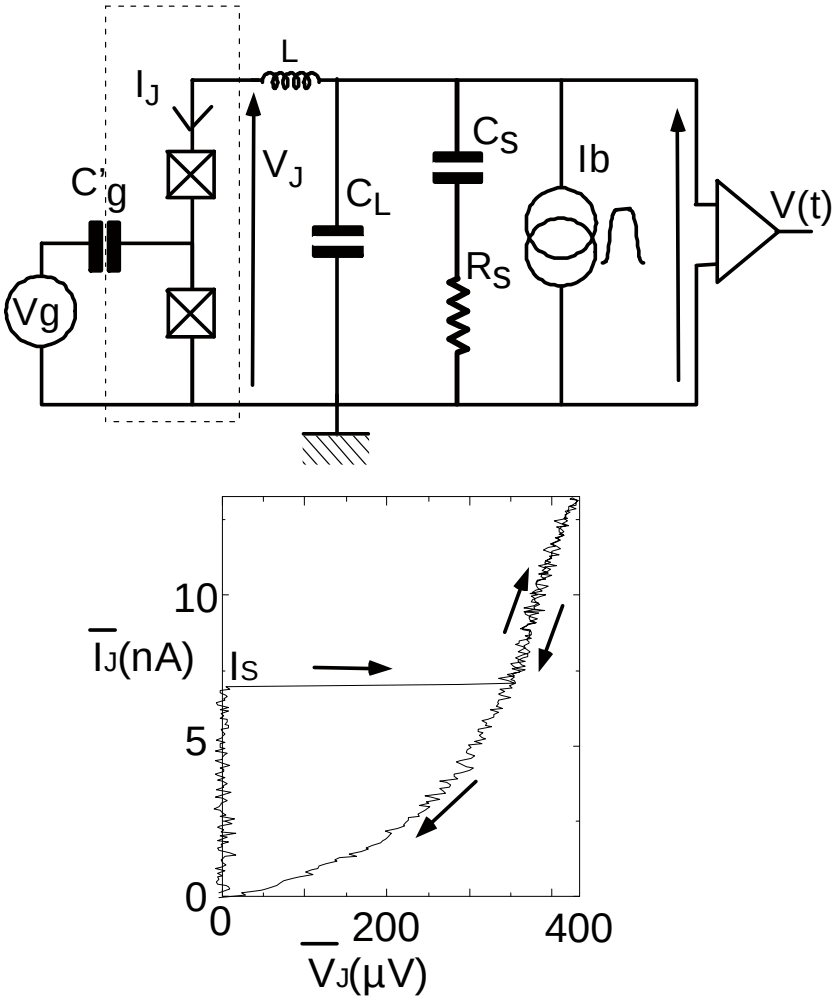

Figure 2.11: *Top panel: Circuit used for the measurement of the AC shunted transistor. The chip is delimited by the dashed rectangle. The elements* $R_s = 400\ \Omega$ *and* $C_s = 180$ pF *are Surface Mounted Components. The parasitic capacitance* $C_L = 0.75$ pF *and the inductance* L *are due to the fact the the RC environment has been implemented off-chip. Bottom panel: Single shot current voltage characteristic of the transistor for a bias current ramp with speed* $v_I = dI_b/dt = 690$ nA/s. *The transistor jumps to a non-zero voltage state at a switching current* I_s *which varies randomly within a statistical distribution.*

The second Cooper pair transistor circuit we have operated is represented in Figure 2.11. In this circuit, the transistor switches to the voltage-state at a rate $\Gamma_s(I_b,n_g)$ [42, 26]. In contrast with the circuit of Figure 2.5, all the electrical components are placed off-chip in order to have a more flexible design. This makes larger the inductance L of the connection between the sample and these components, and the capacitance C_L of these connections to ground.

For fast electrometry purposes, one has to optimise the value of the shunt. We have thus performed numerical simulations of the transistor phase dynamics and determined that $R_s = 400\ \Omega$, $C_s = 180$ pF would allow a good trade-off between the sensitivity and the speed of the measurement. Note that for these values, the zero junction capacitance approximation done by P. Joyez et al. in [26] is not valid.

Gate modulation curves and switching probabilities

In order to study the switching dynamics of the circuit, bias current "square" pulses with a variable amplitude I_p and with a duration τ have been used. The switching probability during the pulses is:

$$P_s(I_p, \tau, n_g) = 1 - \exp(-\Gamma_s(I_p, n_g)\tau) \ ,$$

with $\Gamma_s(I_b, n_g)$ the switching rate at a bias current I_b . The bias current pulses used in practice (Figure 2.12) are not perfectly square, but the rate varies so sharply with I_p that the finite rising time has no importance. The variations of the switching fraction with the different parameters of the experiment have been measured. Figure 2.13 (left panel) shows the gate modulation of the amplitude I_p of the bias current pulses that give 50% switching events in 2 μs . In order to analyse these data, we have performed numerical simulations of the dynamics of δ and u altogether, by taking into account the exact form of $I_0^{eff}(n_g)$. We have fitted the data with $E_C = 4.48$ k$_b$K, $E_J = 1.92$ k$_b$K, $d = 0$ and $T = 50$ mK, without taking into account the stray capacitance C_L .

The experimental variations of P_s with the amplitude I_p are shown in Figure 2.13 (right panel) for different values of n_g . We have used these data to reconstruct the experimental gate variation of P_s with n_g for a given pulse amplitude (Figure 2.14), which determines the sensitivity of the electrometer. We have simulated the phase dynamics in order to explain the slopes of these latter curves, which are less sharp than expected, and found necessary to take into account the finite value $C_L = 0.75$ pF of the stray capacitance of the connections between the sample and the SMC components. This does not change the fitting parameters E_C and E_J for the gate modulation curves.

Electrometry performances

The AC shunted Cooper pair transistor can be used to discriminate two charges $2en_1$ and $2en_0$ coupled capacitively to the transistor island. Let's consider that these charges induce variations of the transistor gate charge $\varkappa n_1$ and $\varkappa n_0$ respectively, where $\varkappa$ is a coupling constant. The discriminating power of the readout, for a bias-current pulse with duration τ, can be defined as:

$$\alpha(\tau) = \max_{I_p, n_g}[P_s(I_p, \tau, n_g + \varkappa n_1) - P_s(I_p, \tau, n_g + \varkappa n_0)] \ . \qquad (2.15)$$

The optimal sensitivity of the electrometer is reached for $I_p = 13.6$ nA (Figure 2.14). Supposing $n_1 - n_0 = 2e$, and $\varkappa = 2\%$, one obtains:

$$\alpha(\tau = 2\ \mu\text{s}) = 0.95\ . \tag{2.16}$$

A slow two level charge fluctuator of 4% of $2e$ was present on the sample during a part of the run. In order to test the electrometer, we have applied a current ramp with speed $v_I = dI_b/dt = 2$ nA.s^{-1}, and determined the switching time $T_s = I_s/v_I$ at which the switching occurred. The distribution histogram of T_s shows two peaks well separated, which proves that this electrometer perfectly discriminates 4% of $2e$ in 2 μs (Figure 2.15).

The capacitance C_L , which reduces the slope of the $P_s(I_p, \tau, n_g)$ curves with n_g, reduces the electrometry performances of the transistor. However, in a quantum bit experiment, this capacitance becomes essential because it reduces the back-action of the transistor onto the box at high frequency (see chapter 3).

Further details about this experiment can be found in Appendix 2.B.6 *and in the article* [27] *which is reproduced at the end of this chapter.*

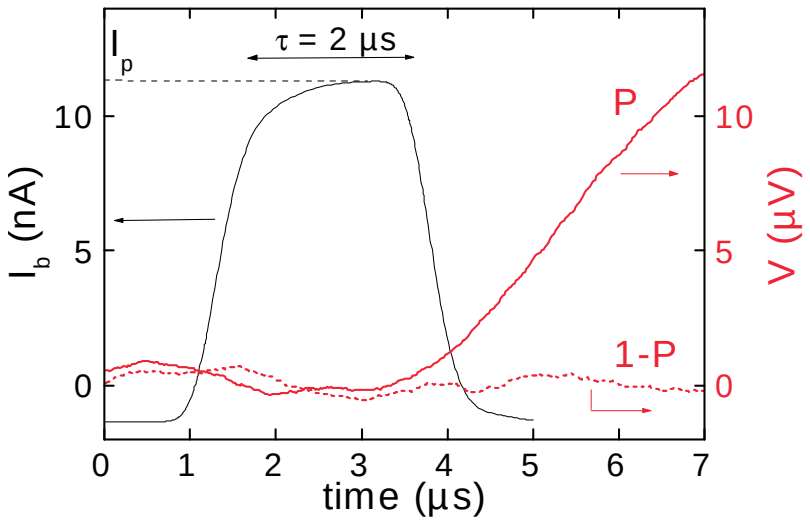

Figure 2.12: *Bias current pulse applied to the transistor, and voltage at the input of the amplifier in case of switching (solid line) and in absence of switching (dotted line).*

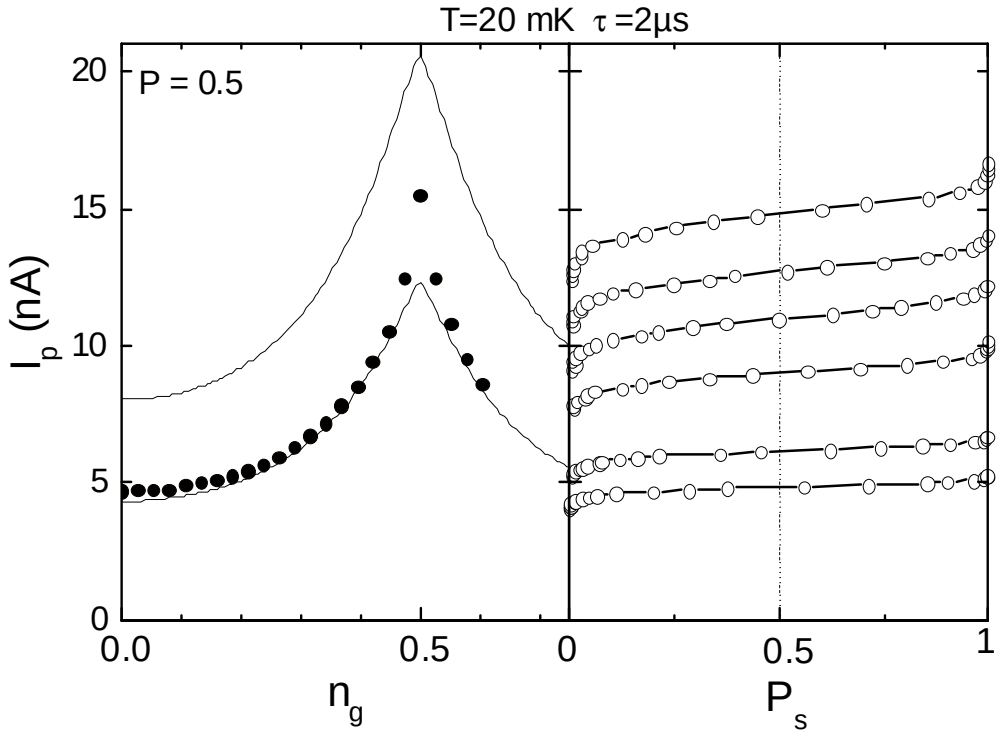

Figure 2.13: *Left panel: Gate modulation of a transistor with* $E_C = 4.48$ $\mathrm{k_bK}$, $E_J = 1.92$ $\mathrm{k_bK}$ *and* $d = 0$. *The curves plotted correspond to the critical current* I_0^{eff} *(top curve), to the experimentally determined current* I_p *such that* $P_s(I_p, \tau = 0.5\ \mu\mathrm{s}, n_g) = 0.5$ *(dots) and to numerical simulations of* I_p *(bottom curve). Right panel: Experimental variation of the switching fraction* $P_s(I_p, \tau = 0.5\ \mu\mathrm{s}, n_g)$ *with the amplitude* I_p *of the current pulses for* $n_g = 0.15$, 0.56, 0.82, 0.91, 0.95 *and* 0.98 *from bottom to top respectively. Each point is averaged over* 5000 *pulses.*

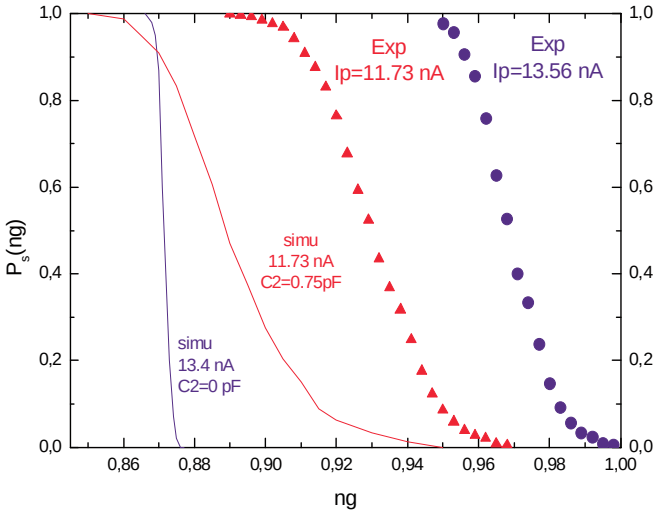

Figure 2.14: *Symbols: Gate variation of* $P_s(I_p, \tau = 0.5\ \mu\text{s}, n_g)$ *with* $I_p = 11.7$ nA *and* $I_p = 13.56$ nA, *reconstructed from the data of Figure 2.13. Lines: Theoretical predictions made by simulating numerically the phase dynamics. The slope of* P_s *is only explained when one takes into account the stray capacitance* C_L *of the connections between the transistor and its shunting components. The slight current shift between the experimental data and simulations can be attributed to the inaccuracy of the experimental calibration.*

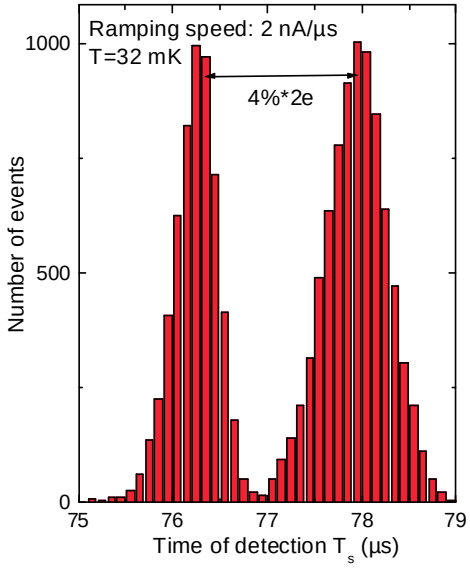

Figure 2.15: *Double peaked switching histogram of the time of detection* T_s *due to a slow two level charge fluctuator with amplitude* $0.08e$, *measured with a bias current ramp rate* $v_I = 2$ nA/ μs. *These data prove that the transistor of experiment 2 can fully discriminate* 4% *of* $2e$ *in* 2 μs.

2.3.3 Conclusion

Table 2.17 compares the sensitivity of the two electrometers we have operated with the sensitivity of the best electrometer implemented so far, namely the RF-SET [21, 62].

	Experiment 2	Experiment 3	RF-SET
Bandwidth	1 MHz	1 MHz	10 MHz
Equivalent sensitivity	$3\ 10^{-4}\ e/\sqrt{Hz}$	$2\ 10^{-5}\ e/\sqrt{Hz}$	$3\ 10^{-6}\ e/\sqrt{Hz}$

(2.17)

At the beginning of this thesis, the issue at stake was to find a readout device in order to implement a quantum bit experiment with a Cooper pair box. A measurement apparatus used to read a quantum bit must satisfy different requirements. First, it must be able to discriminate the quantum states $|0\rangle$ and $|1\rangle$. Secondly the back-action of the measurement apparatus on the quantum system must be low. Indeed, the measurement apparatus must not destroy the coherence of the quantum system when no measurement is being performed. The quantum information must also not be destroyed before the end of the measurement. The sensitivity and the back-action of the measuring apparatus being antagonist, one has to find a trade-off. The interest of the electrometers of experiments 2 and 3 for implementing a quantum bit depends on their sensitivity but also on the back-action they would have on a Cooper pair box. Since these electrometers are based on the modulation of a supercurrent, without shot noise, their back-action is expected to be very different from that of a RF-SET. This back-action is estimated in the next chapter.

Appendix 2-A: Fabrication techniques

We have seen in previous chapters that the physics of a Cooper pair box or transistor depends on two energy scales, the charging energy E_C of the island and the Josephson energy E_J of the junctions, which set an upper limit for the operating temperature of the experiment. Having E_C and E_J of the order of 1 k_bK requires to fabricate devices with a micron-size island and submicron-size junctions. These circuits are fabricated using e-beam lithography (EBL) techniques. We have typically fabricated Al/AlO_2/Al Josephson junctions with a surface of 100 nm$\times$100 nm and aluminum islands with a surface of 1 μm$\times$100 nm . This results in C_g of the order of 10 aF and C_J of the order of 1 fF . Hence $E_C \simeq (2e)^2/(2C_J)$ is of the order of 1 k_bK . The Josephson energy E_J is controlled independently with the oxidation of the junctions and is of the same order as E_C for the experiments we have performed.

2-A-1 Nanofabrication techniques for Cooper pair boxes

Electron beam lithography

Electron beam lithography (EBL) (Figure 2.16) makes use of a focused electron beam, emitted by the gun of an electron microscope, to locally alter a polymer resist. The beam position is controlled by a computer in such a way that a precise irradiation dose is delivered on the sample inside the scanned pattern. In our laboratory, we use a 25 keV electron beam generated by a commercial Philips SFEG scanning electron microscope. Between two area exposures, the beam is shifted away from the sample by an electrostatic beam blanker. After exposure is completed, the sample is removed from the microscope and placed in a specific solvent with a great solubility difference between exposed and non-exposed areas. The resolution reached by EBL is neither limited by the electron beam size nor by diffraction but by the backscattering of electrons inside the resist and substrate, resulting in a partial exposure of the resist near the exposed pattern. This broadening effect is important near large exposed areas. Small details in their vicinity must consequently be underexposed according to a position-dependent dose correction. This is the case for the island of a box, which is placed close to the much larger gate electrodes. The exposed areas are removed by the solvent while the non-exposed ones remain unaffected. Thin layers of material are then deposited through the mask. A final lift-off is performed by dipping the chip in a solvent.

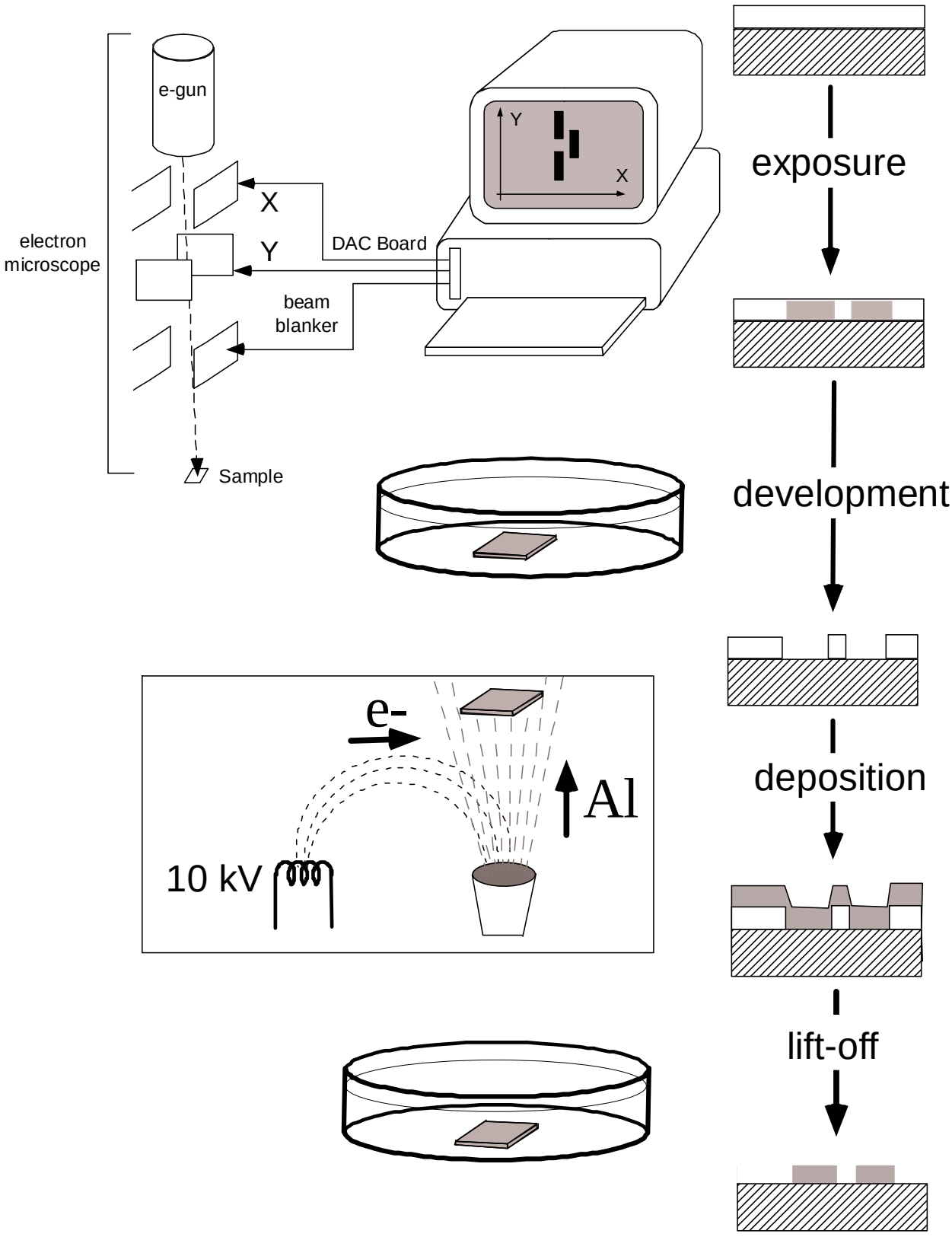

Figure 2.16: *The different steps of electron beam lithography: electronic exposure of the sample covered with a polymer resist, development of the mask in a solvent bath, metallic thin film deposition(s) and mask lift-off.*

The suspended shadow mask technique

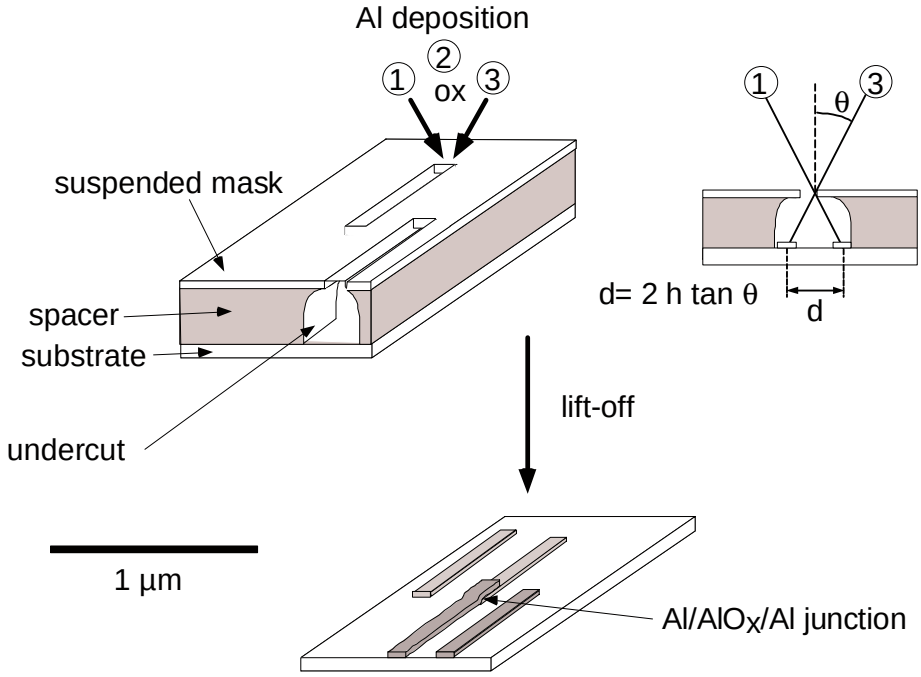

Figure 2.17: *Fabrication of a Josephson junction with the suspended shadow mask technique. The pattern of the junction corresponds to two separated slits. The first deposited metallic layer is oxidized before the deposition of a second metallic layer. The angle of deposition of this second evaporation is adjusted so that a metallic track of the second layer overlaps an oxidized track of the first evaporated layer. The overlap zone corresponds to the Josephson junction.*

The shadow mask technique [63, 64] used for the fabrication of Cooper pair boxes ensures a good self-alignment of the electrodes for junction fabrication (Figure 2.17). It consists in exposing a substrate previously covered with two different layers of polymer resist. Since the upper layer is more soluble in the developer bath, the development creates a cavity below the mask, thus allowing angle evaporations. If the evaporation angle is changed between different layer depositions, the mask shadow is shifted: a single slit in the mask leads to separate projected electrodes. The angles are adjusted in such a way that two deposited electrodes overlap over a small area. A tunnel junction is obtained by oxidizing the first deposited layer of metal before deposition of the counterelectrode. The junction capacitance and tunnel resistance can be controlled independently by varying the overlap area and oxidation parameters respectively. (For an example of shadow mask used in this thesis work, see Figure 4.31, left)

Fabrication of on-chip electromagnetic environments

The Josephson junctions, the Cooper pair boxes and Cooper pair transistors must be embedded in an appropriate electrical circuit with the following elements:

• Normal metal leads close to the superconducting Al reservoirs of the box to suppress spurious out of equilibrium quasiparticles.

• Capacitors and resistors in order to control the high frequency environment of the device.

• Connection pads to connect the sample to the outside electrical lines (Figure 2.18).

Different strategies can be adopted to implement these elements. The first possibility is to fabricate them together with the Josephson junction at the EBL stage. (example: contact pads in experiment 3, represented in Figure 2.18). This method is time consuming because electron beam lithography is a "serial" fabrication technique, in which the beam scans all the exposed zones. It is however possible to accelerate the fabrication of large elements using a resist more sensitive to electrons than the commonly used PMMA resist, namely UV3, in order to pattern several tens of chips on a single wafer (example: capacitor C_d of experiment 4 and 5, represented in Picture 2.19). Furthermore, whereas the box requires the best resolution provided by e-beam lithography, the leads and connecting circuitry have less critical resolution requirements. Hence, it is possible to fabricate the close electromagnetic environment of the box using standard ultra-violet optical lithography which has the great advantage of processing many samples on a single silicon wafer "in parallel". (Example: R_s and C_s in experiments 1 and 2, see section 2-B-3).

Alignment of the box with the on-chip environment

When the electromagnetic environment of the circuit is fabricated first, the circuit must be aligned on it with an accuracy of about 100 nm . Alignment marks (picture 2.20) are designed on the sample during the fabrication of the environment to allow the alignment without exposing the places where the circuit will be patterned. The alignment procedure can be automated with the software "Elphy Quantum" (by Raith) driving the Philips microscope.

Before the deposition of a Cooper pair box or transistor on a preexisting environment, it is preferable to clean the metallic surface previously fabricated by Argon ion milling to ensure a good contact between the two layers.

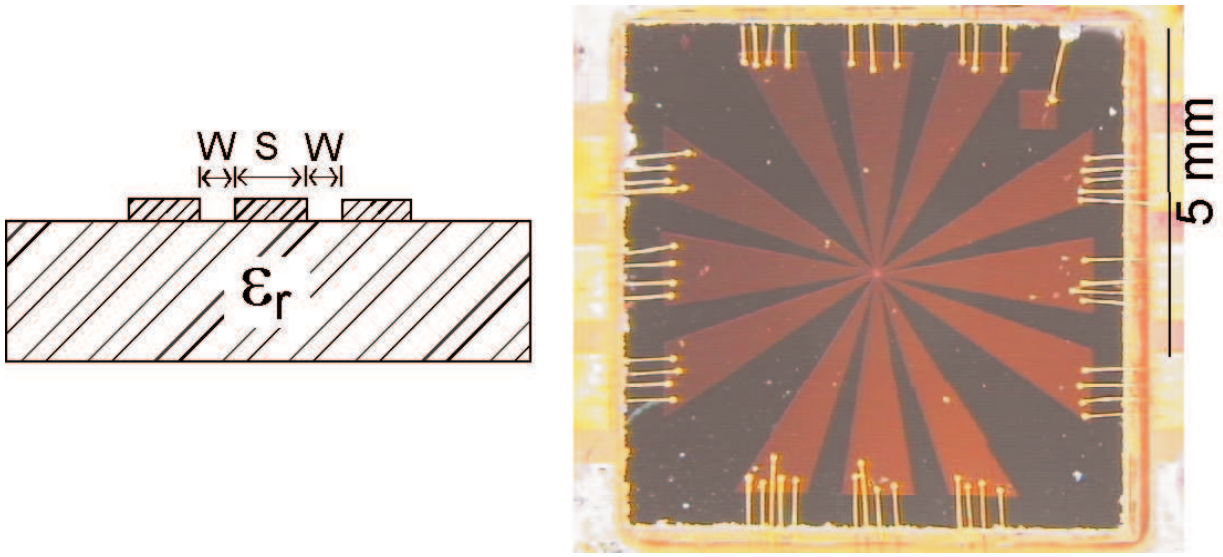

Figure 2.18: *Example of contact pads. In order to conduct microwave signals without reflections, it is necessary to use coplanar waveguides with a constant impedance. A coplanar waveguide consists of a center strip with width S, with 2 ground planes located parallel on the same substrate at a distance of W from the center strip (left panel). The characteristic impedance of the central strip is determined by the relative permittivity ϵ_r of the substrate and the ratio S/W* [65]*. In order to have an impedance of 50 Ω on the silicon substrate we use, and which has a relative permittivity $\epsilon_r = 11$, the width S of the center strip must be twice the gap W . In experiment* 3*, four coplanar waveguides with $W/S = 2$ were implemented on the same chip (right panel).*

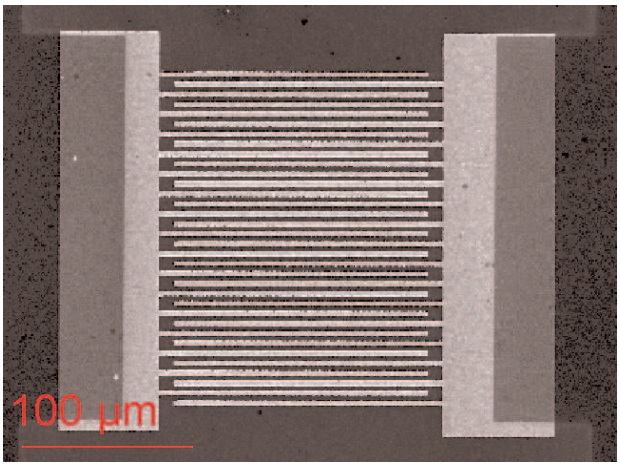

Figure 2.19: *Example of electrical component fabricated on chip: one* 0.25 pF *section of the capacitor* C_L *of experiment* 5.

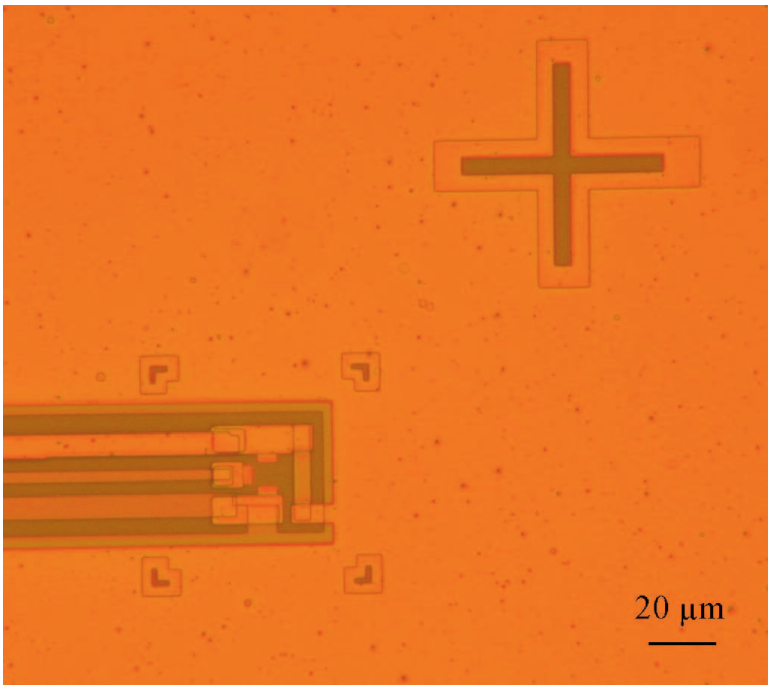

Figure 2.20: *Micrograph of the alignments marks used in experiment 3 to align the Cooper pair transistor with the optically fabricated environment. In this experiment, the alignment procedure had two steps, a first rough alignment on the big cross visible at top right of this picture, followed by a second accurate alignment on the 4 smaller marks shown at the bottom left of this picture. The transistor must be placed at the center of these 4 marks.*

Technical data for the EBL Bilayer process

These data are given here for the experiment 5.

Polymer resists:

Bottom layer : copolymer meta-acrylate acid/methyl-meta-acrylate (PMMA/MAA) diluted at 8.5% in ethylactate.

Top layer : copolymer poly-methyl-meta-acrylate PMMA (molecular weight 950 K) diluted at 3% in Anisole.

Resist deposition:

For the Quantronium, the PMMA top resist layer must be particularly thick because the fabrication of the big Josephson junction requires to pattern a long PMMA/MAA bridge

Bottom layer:

Spin at 2200 tr.min^{-1} during 60 s.

Dry at 165°C on a hot plate for 120 s, gives a 700 nm thickness.

Top layer:

Spin at 4800 tr.min^{-1} during 60 s .

Dry at 170°C on a hot plate for 1800 s, gives a 95 nm thickness.

Electron beam exposure

Electrons accelerated by a voltage of 25 kV, standard dose 250 mC/cm^2.

Development

Develop for typically 40 s at room temperature in a solution of MIBK (methyl-isobutyl-ketone) diluted at 25% vol. in propanol-2

Rinse in propanol-2.

Deposition of metallic films

Deposition of 25 nm of aluminum, oxidation during 240 s under a pressure of 20 mb of a mixture of O_2 (25% mol.) and of Ar (75% mol.), deposition of 30 nm of aluminum.

Lift-off

Acetone heated at 50°, with ultrasonic bath when necessary.

Appendix 2-B: Electrical wirings of the experiments

2-B-1 The different elements composing the electrical lines

In all experiments reported in this thesis, the sample is mounted in a copper sample holder thermally anchored to the mixing chamber of a dilution refrigerator. The sample is connected to room temperature electronics by electrical lines which have to be carefully engineered in order to stop thermal and external electromagnetic fluctuations. This appendix presents the different components appearing in the connection lines of experiments 1 to 5.

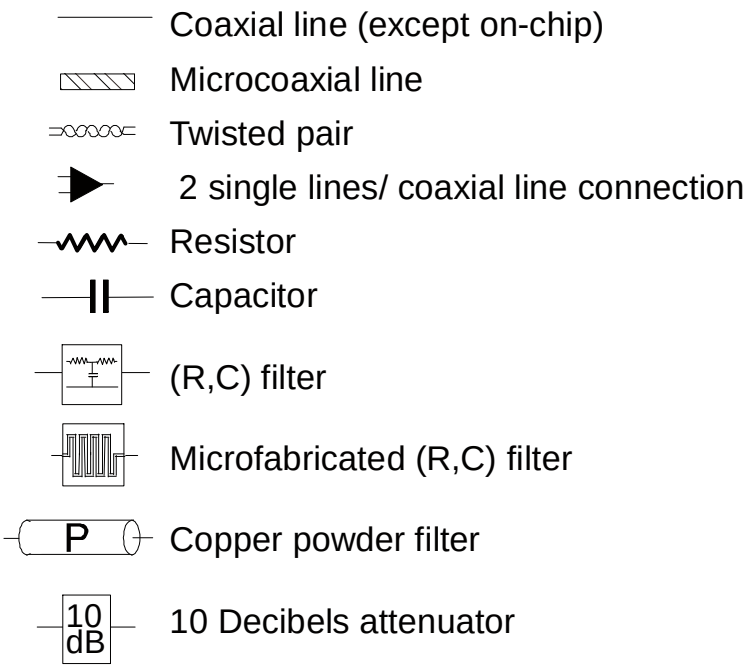

Figure 2.21: *Legend of the symbols used in the electrical schemes of this thesis.*

The electrical lines connected to the sample holder generally consist of coaxial lines, except the measurement line, which is very often a twisted pair cable. Twisted pair cables have the

interest of avoiding the pick up of parasitic magnetic fields. Different filters are used to stop the noise at high frequencies: discrete (R,C) filters, home made microfabricated (R,C) filters [66] and home made copper powder filters [67]. A microfabricated (R,C) filter consist of a microlithographied meander line circulating on top of a ground plane, with a resistance of about 1.5 kΩ and a capacitance of about 70 pF. It provides more than 120 dB of attenuation above 0.1 GHz. A copper powder filter consists of a manganin wire spiraling in a box filled with copper powder, which provides skin depth losses. It has an attenuation better than 60 dB above 1 GHz. The microcoaxial lines used in experiments 4 and 5 also act as distributed (R,C) filters. The resistors are special resistors adapted to low temperatures. Resistors and capacitors which are inside the sample holder are surface mounted components (SMC) which can be placed very close to the sample.

2-B-2 The DC SQUID array

The array of 100 DC SQUIDs used in experiment 1 and 2 has been fabricated at the NIST laboratory in Boulder [23, 60] (Figure 2.23). A DC SQUID consists of a superconducting loop enclosing two resistively shunted Josephson junctions with critical current I_0, threaded by a magnetic flux Φ_{squid} . Each SQUID behaves as a tunable Josephson junction with an effective critical current $I_0^{squid} = 2I_0 \cos(2\Phi_{squid}/\varphi_0)$ (See [40, 51]). When the array is current biased, the voltage V_{array} across the series of SQUID is modulated by the flux Φ_{squid} . Since there are 100 SQUIDs, the voltage V_{array} is large enough to be measured with room temperature amplifiers. The measured V_{array}-Φ_{squid} characteristic present irregularities due to phenomenons of mutual inductance between the SQUIDs (Figure 2.22, bottom). Since the sensitivity $dV_{array}/d\Phi_{squid}$ depends on Φ_{squid}, on I_b, and on the number of flux quanta trapped in the SQUIDs, it is preferable to operate the SQUID array in a feed-back mode using a feed back coil (Figure 2.22, top). In practice, the SQUID array is placed in its own shielding sample holder, next to the sample holder containing the measured device.

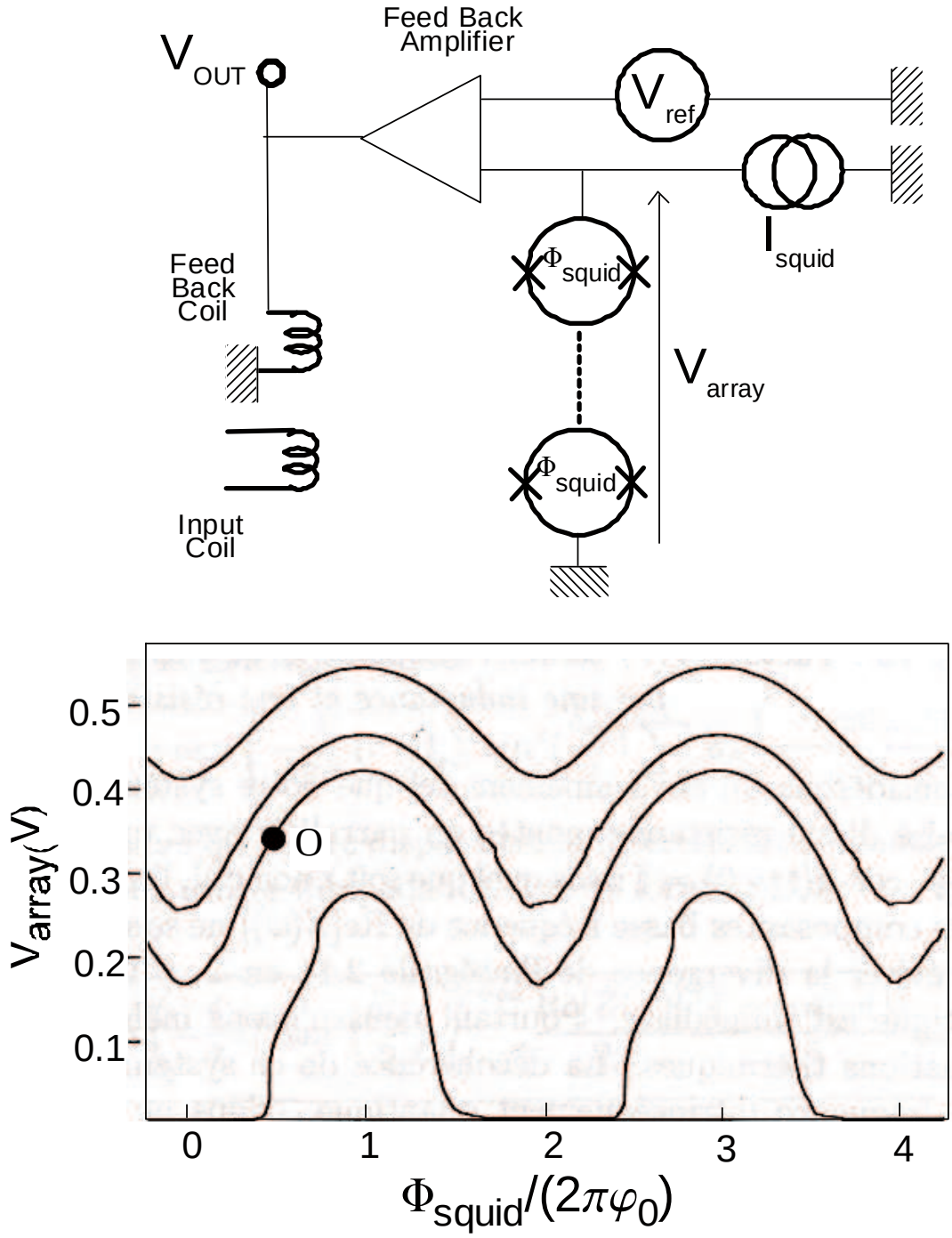

Figure 2.22: *Top panel: Scheme of the feed-back loop in which the array of DC SQUIDs is embedded. The series of SQUIDs is biased by a current I_{squid}. The voltage V_{array} across the array, which depends on the flux Φ_{squid} through the squids, is measured using an amplifier. In the feed-back mode, this voltage is maintained at a fixed value V_{ref}. Bottom panel: Measured V_{array}-Φ_{squid} characteristic for 4 different values of I_{squid}. The irregularities in the characteristic are due to mutual inductance phenomena between the SQUIDs. The feed-back amplifier gain is tuned so that the flux sent by the feed-back coil maintains the SQUID array at a constant working point like O. The output of the measurement is the output signal of the feed-back amplifier.*

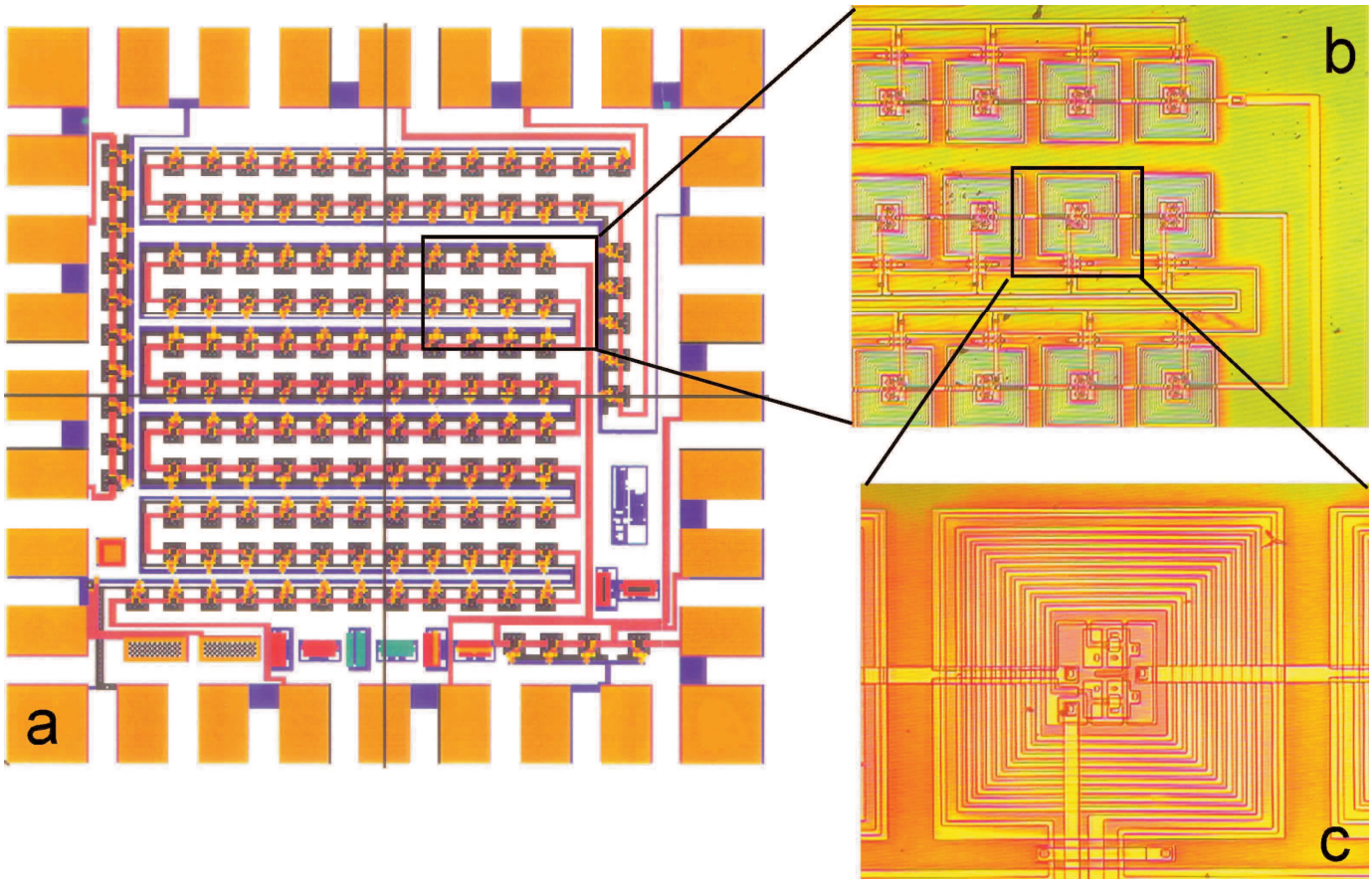

↑Figure 2.23 ↓Figure 2.24

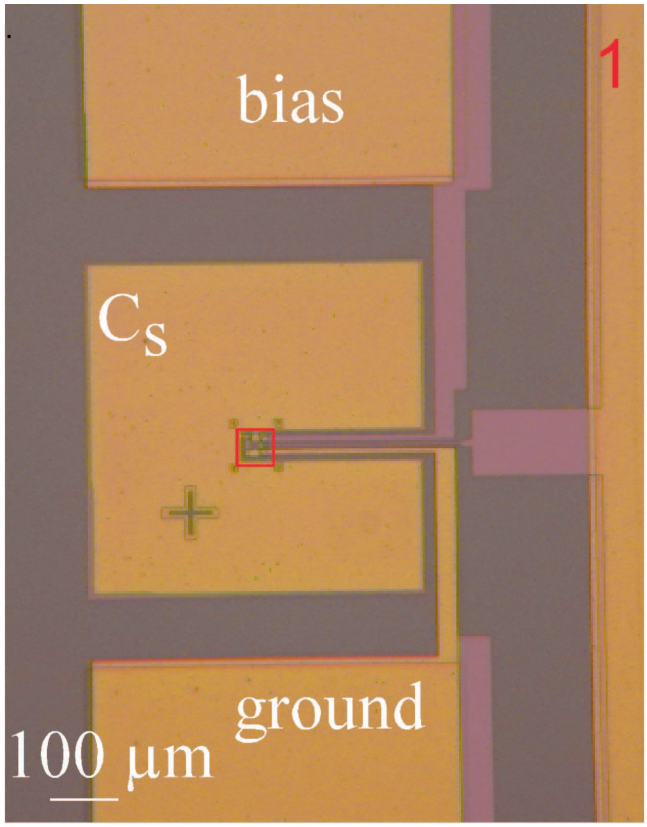

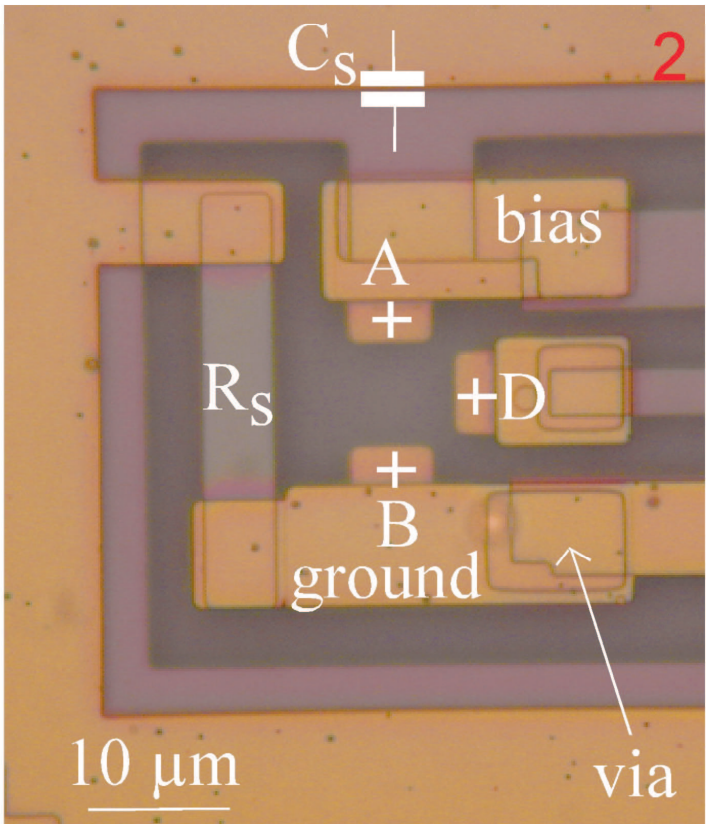

2-B-3 On chip $(R_s + C_s)$ environment used in experiments 1 and 2

The electromagnetic environment of the junction or transistor of the experiments 1 and 2 was microfabricated by A. Steinbach at the NIST laboratory of Boulder using optical lithography. The substrate is a silicon chip covered with 200 nm of thermally grown SiO_2 . The 10 Ω resistor R_s indicated in Picture 2.24, 2 is made of AuPd. The marks A, B and C indicate Au pads used to contact the junction or transistor fabricated afterwards with EBL. The capacitor $C_s = 100$ pF surrounds this central area everywhere except on the right where the leads exit. The bottom capacitor electrode is Nb grown using a Plasma Enhanced Chemical Vapor Deposition Process (PECVD), and the top capacitor electrode is Au. The leads connected to A and B, used to current bias the sample, go to large contact pads shown in top and bottom of Picture 2.24, 1. The contact D is designed for the transistor gate of experiment 2. Contacts to the Nb capacitor electrode and to the Au electrodes are established by via structures which are etched through the PECVD SiO_2

Previous page:

- *Top: Figure 2.23. Global scheme of the SQUID array (picture a) and micrographs of a group of 12 SQUID (picture b) and of a single SQUID (picture c).*
- *Bottom: Figure 2.24. Micrographs of the $(R_s + C_s)$ environment of experiments 1 and 2. A and B are the connecting pads for the device. D is a gate pad. The red square in picture 1 indicates the area zoomed in picture 2.*

.

2-B-4 Implementation of experiment 1

In experiment 1, the Josephson junction was fabricated with the EBL technique in the electromagnetic environment ($R_s + C_s$) previously described. Figure 2.25 presents a global schematics of the electrical wiring of experiment 1, from the sample to the room temperature amplifiers. The R_c resistor is a contact resistor resulting from the transistor fabrication process. The R_b and R_m resistors are SMC components connected to the chip with indium pads and isolated from the sample holder by a Kapton film. The SQUID array used to probe the sample behaviour is described in 2-B-2. The input lines of the SQUID array are filtered with copper powder filters and capacitors. All these elements, which are thermally anchored to the mixing chamber of the dilution refrigerator, are grouped inside a lead shield in order to avoid the pick-up of electromagnetic noise by the SQUID array. The bias current I_b is delivered by a voltage source V_b in series with a resistor R_b

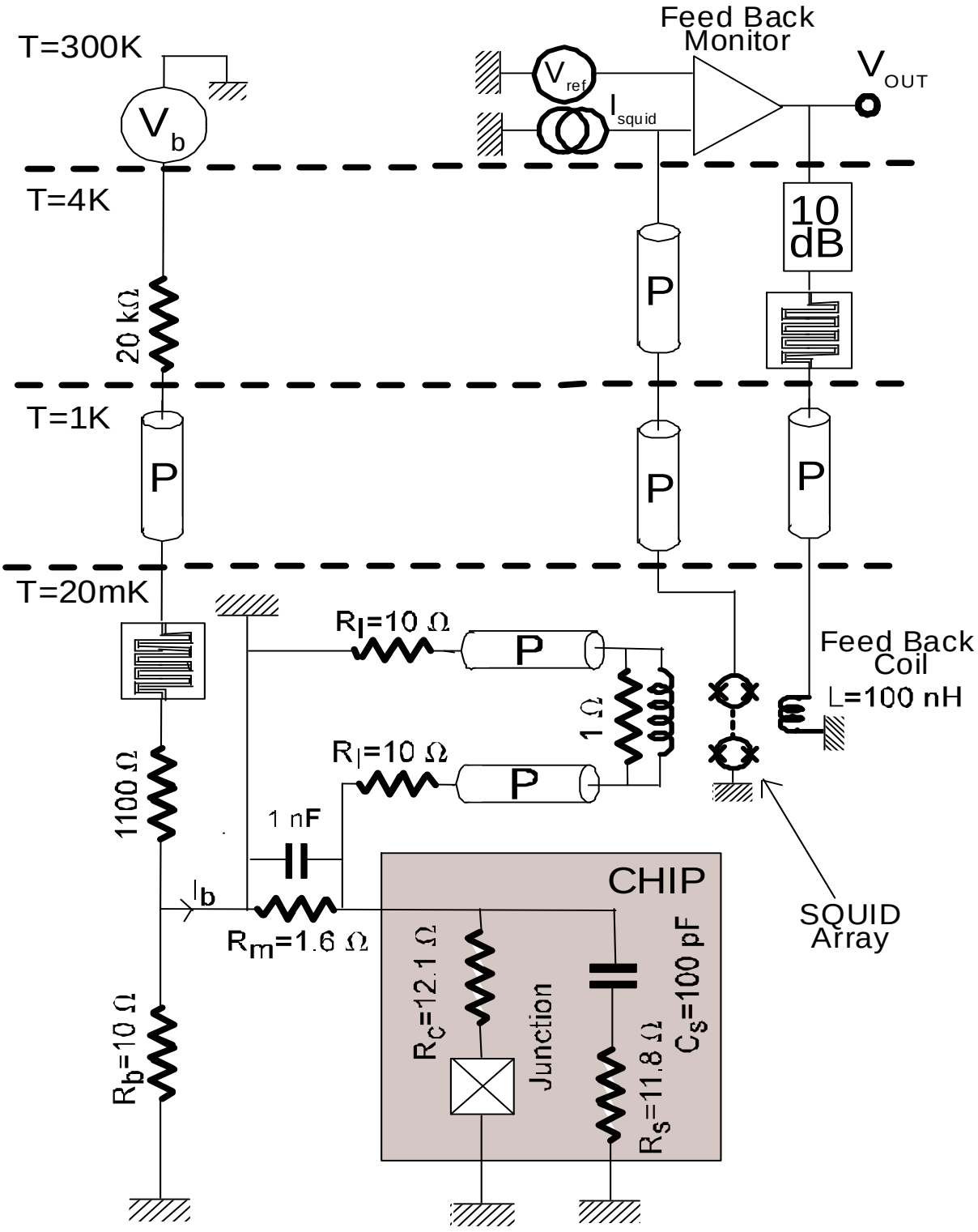

Figure 2.25: *Global schematics of the electrical circuitry of experiment 1 (The symbols used are defined in Figure* 2.21*).*

2-B-5 Implementation of experiment 2

In experiment 2, the Cooper pair transistor was fabricated with the EBL technique in the same electromagnetic environment ($R_s + C_s$) as in the previous experiment (picture 2.26, 1). The gold quasiparticle filters have been fabricated at the same time as the transistor during the e-beam lithography stage (picture 2.26, 2). Figure 2.27 presents a global schematics of the electrical wiring of experiment 2, from the sample to the room temperature amplifiers. The R_c resistor is a contact resistor resulting from the transistor fabrication process. The R_1, R_b and R_m resistors are SMC components connected to the chip with indium pads and isolated from the ground of the sample holder with a Kapton film. The SQUID array used is the same as in experiment 1 (Appendix 2-B-2), but its input line is now only filtered with copper powder filters.

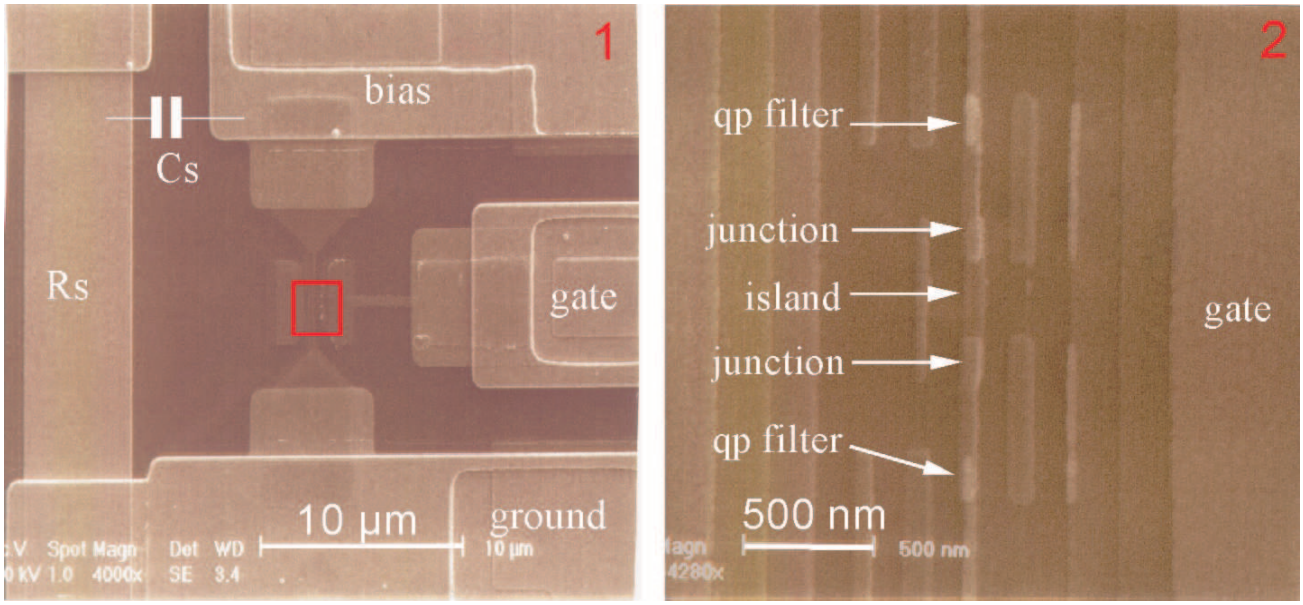

Figure 2.26: *Micrographs of the Cooper pair transistor (picture 2), embedded in an on-chip electromagnetic environment ($R_s + C_s$) (picture 1). The red square in the left picture indicates the area zoomed in the right picture.*

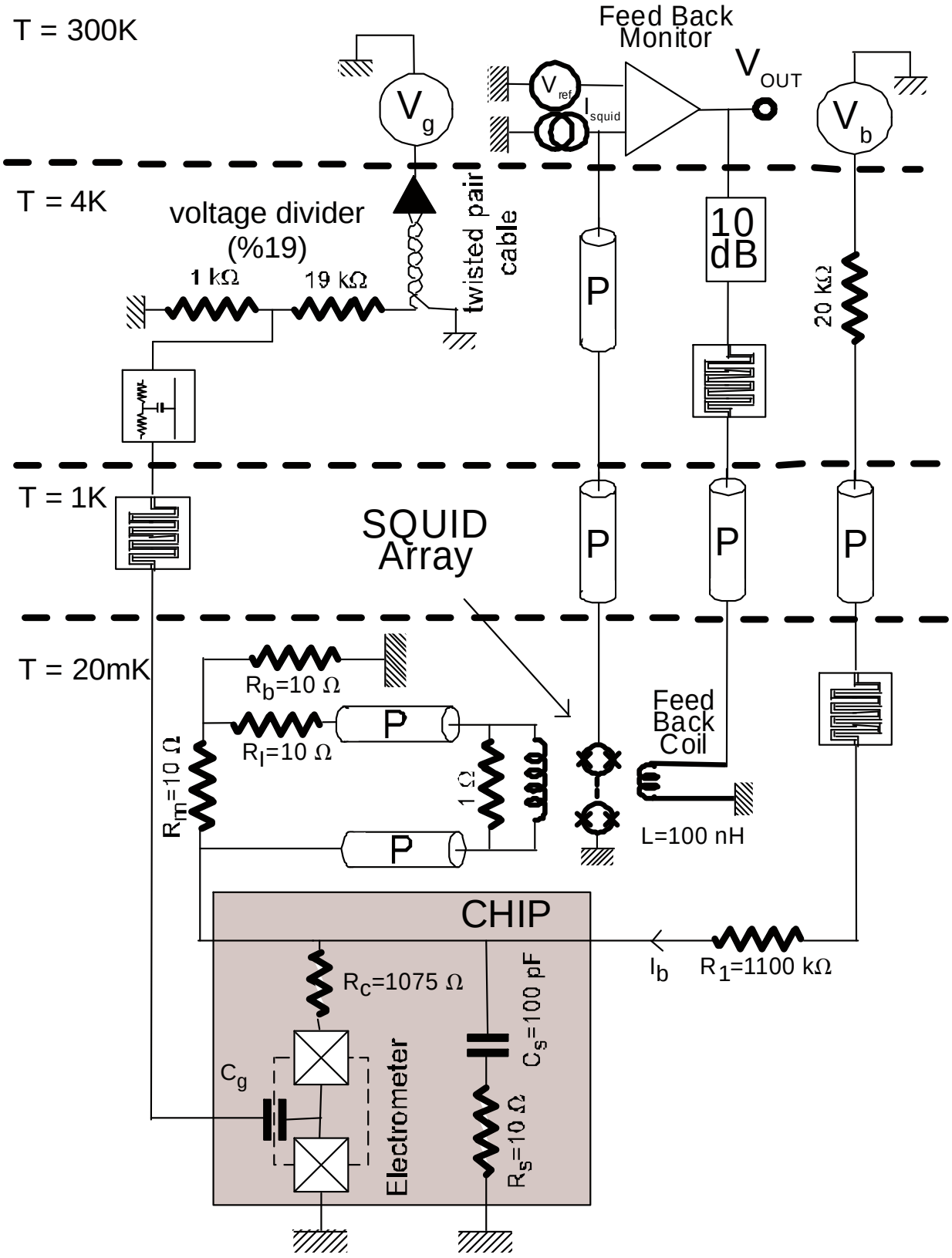

Figure 2.27: *Global schematics of the wiring of experiment 2 (The symbols used are defined in Figure 2.21).*

2-B-6 Implementation of experiment 3

In experiment 3, the on-chip gate and bias connection pads placed on-chip have a coplanar waveguide geometry specially designed to avoid reflections of the microwave signals (Figure 2.18, right). Figure 2.30 presents a global schematics of the electrical wiring of experiment 3, from the sample to the room temperature amplifiers. No electrical components is placed on-chip in order to improve the flexibility of the experiment. This results in a stray capacitance $C_L = 0.75$ pF and a stray inductance L, due to the connection between the sample and the electrical components, . In order to make these connections, we have used a miniature Printed Circuit Board (PCB) which wears the SMC components R_s, C_s, R_1, and R_2 (see Picture 2.28, 2 and Figure 2.29). The connecting pads of the PCB are contacted to the sample connecting pads using gold wire bonding. The PCB is also connected through carefully filtered electrical lines to the room temperature electronics. The sample current bias I_b is implemented by a voltage source V_b in series with a resistor R_b.

Next page:

- *Top: Figure 2.28. Four micrographs of the Cooper pair transistor (Picture 4 and 3), whose chip is placed at the center of a PCB (Picture 2) itself mounted in the sample holder (Picture 1). The bright zones in pictures 3 and 4 correspond to the gold layer evaporated on top of the aluminium layers. The green rectangles in picture 2 are the SMC components. The chip includes 2 transistors, but only one of them was effectively used in the experiment (Its connections can been seen at the left of Picture 2). The red rectangle in a photograph indicates the zone zoomed in the next picture.*
- *Bottom:Figure 2.29. Sketch of the PCB chip (white and yellow) which allows to connect the SMC components R_1, R_2 and R_3 (in pink) and C_d (in blue) to the sample (in light blue). The yellow areas are the gold tapes of the PCB and the gold bondings*

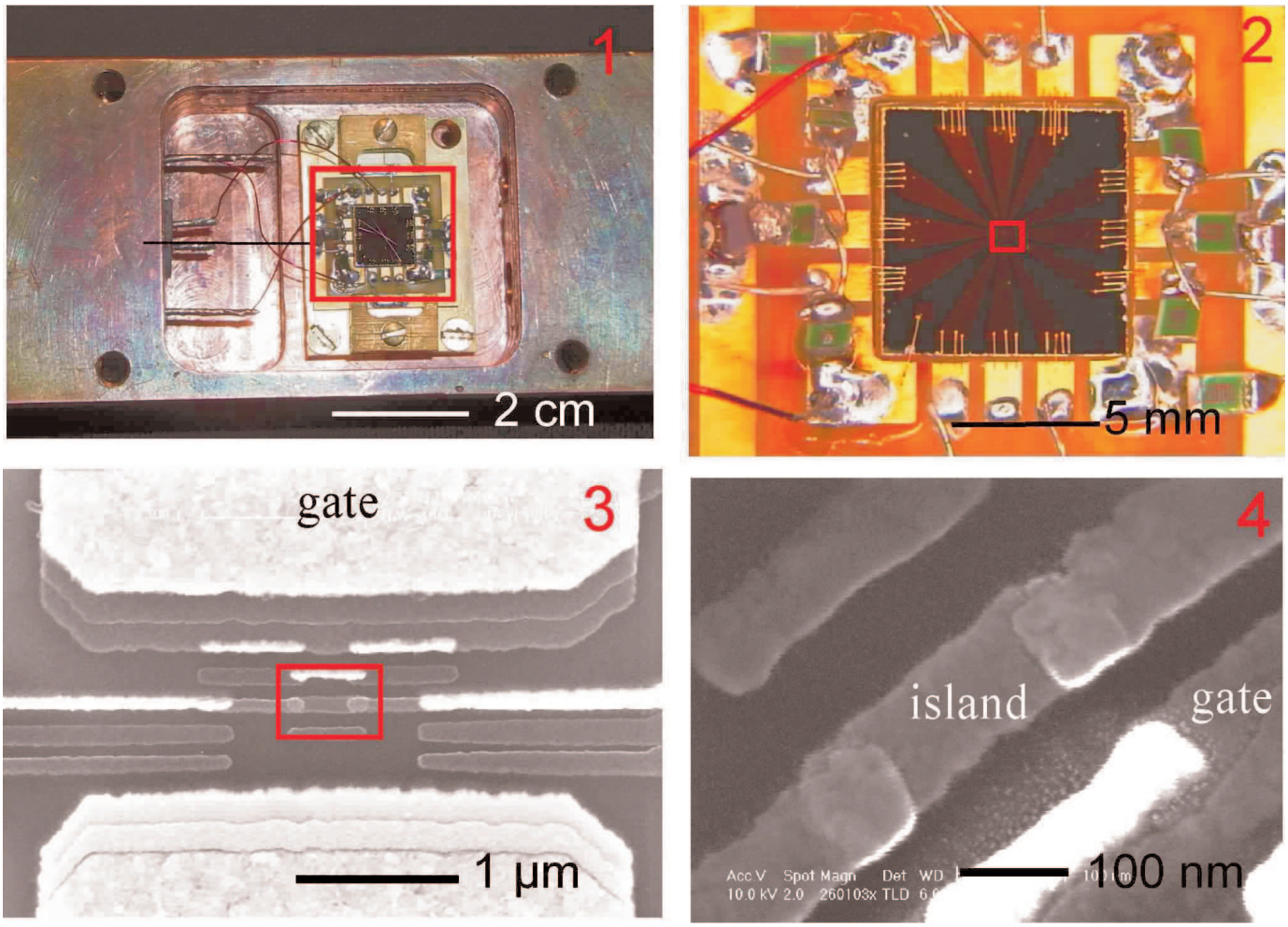

↑Figure 2.28 ↓Figure 2.29

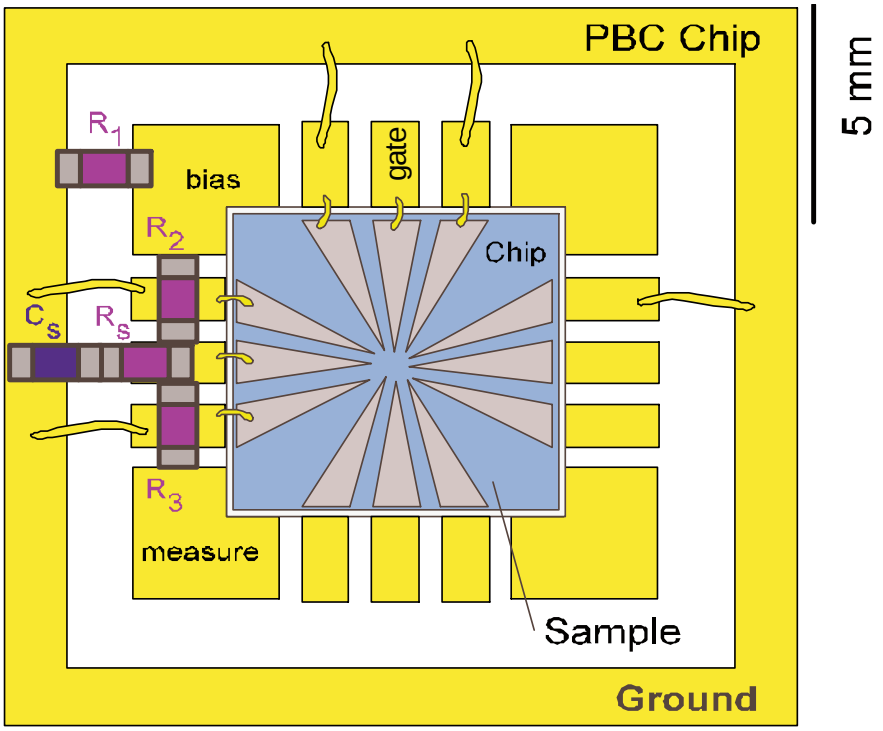

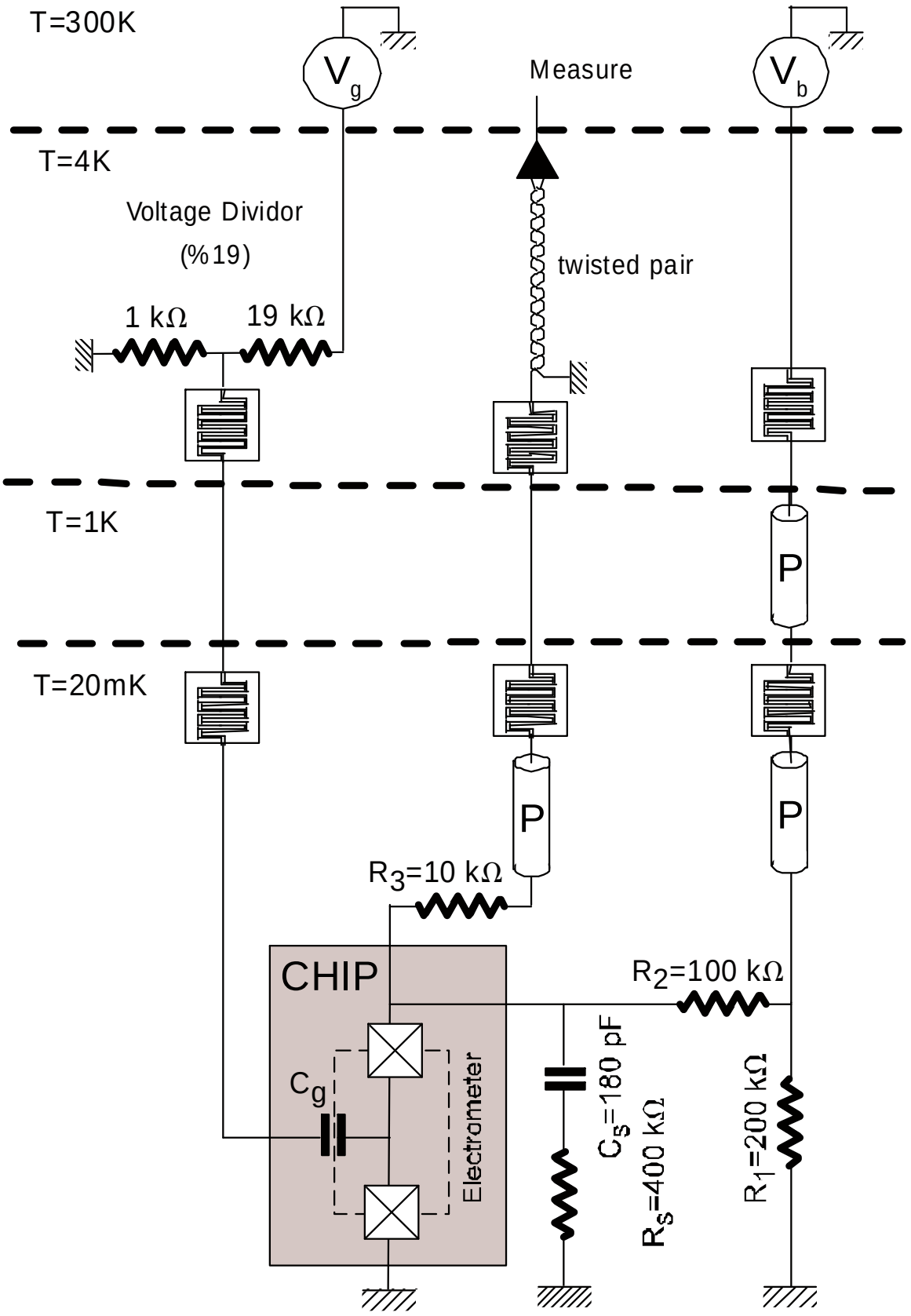

Figure 2.30: *Global schematics of the wiring of experiment 3 (The symbols used are defined in Figure* 2.21*).*

Appendix 2-C: Articles reporting the experiments of chapter 2

The articles reproduced here are:

[24] A.H. Steinbach, P. Joyez, A. Cottet, D. Esteve, M.H. Devoret, M.E. Huber and J.M. Martinis, *Direct Measurement of the Josephson Supercurrent in an Ultrasmall Josephson Junction* Phys. Rev. Lett. **87**, 137003 (2001).

[25] A. Cottet, A.H. Steinbach, P. Joyez, D. Vion, H. Pothier, D. Esteve, and M.E. Huber, *Superconducting Electrometer for Measuring the Single Cooper pair box,* in "*Macroscopic Quantum Coherence and Quantum Computing*", D.V. Averin , B. Ruggiero, and P. Silvestrini eds., Kluwer Academic, Plenum Publishers, New York (2001), p111.

[27] A. Cottet, D. Vion, P. Joyez, D. Esteve, and M.H. Devoret, *A Hysteretic Single Cooper pair transistor for Single-Shot Reading of a Charge-Qubit,* in "*International Workshop on Superconducting Nano-electronic Devices*", J. Pekola, B. Ruggiero, and P. Silvestrini eds., Kluwer Academic, Plenum Publishers, New York (2002), p. 73.

Beware that in these articles, the definitions used for E_C and E_J are different from those used in the body of the thesis.

Direct Measurement of the Josephson Supercurrent in an Ultrasmall Josephson Junction

A. Steinbach,[1] P. Joyez,[1] A. Cottet,[1] D. Esteve,[1] M. H. Devoret,[1] M. E. Huber,[2] and John M. Martinis[3]

[1]*Service de Physique de l'Etat Condensé, CEA-Saclay, F-91191 Gif-sur-Yvette, France*

[2]*Department of Physics, University of Colorado at Denver, Denver, Colorado 80217*

[3]*National Institute of Standards and Technology, Boulder, Colorado 80303*

(Received 10 April 2001; published 10 September 2001)

We have measured the supercurrent flowing through a nonhysteretic, ultrasmall, voltage-biased Josephson junction. In contrast with experiments performed so far on hysteretic Josephson junctions, we find a supercurrent peak whose maximum $I_{s\max}$ increases as the temperature T decreases. The asymptotic $T = 0$ value of $I_{s\max}$ agrees with the junction Ambegaokar-Baratoff critical current, as predicted by theory.

DOI: 10.1103/PhysRevLett.87.137003 PACS numbers: 74.50.+r, 73.23.–b, 73.40.Gk

A Josephson tunnel junction between two superconducting electrodes is a basic quantum nonlinear system [1,2]. For excitation energies much smaller than the superconducting gap Δ, it can be modeled by the Josephson Hamiltonian $\hat{H} = -E_J \cos\hat{\delta}$ where $\hat{\delta}$ is the gauge-invariant phase-difference operator, a purely electrodynamic quantity which is $2e/\hbar$ times the space and time integral of the electric field across the junction [2]. The Josephson energy E_J is a macroscopic parameter, which, for BCS superconductors at temperatures $T \ll \Delta/k_B$ and for sufficiently opaque junctions, depends only on the junction tunnel resistance R_t and Δ through $E_J = \frac{h}{8e^2}\Delta/R_t$ [3]. The supercurrent flowing through the junction is given by the Josephson relation $I_S = (2e/\hbar)\langle \partial\hat{H}/\partial\hat{\delta}\rangle = (2eE_J/\hbar)\langle\sin\hat{\delta}\rangle$, the average $\langle\cdots\rangle$ being performed on the degrees of freedom of the electrodynamic environment of the junction. Thus, the highest supercurrent that the junction can sustain is given by the so-called Ambekaokar-Baratoff critical current $I_0 = \frac{\pi}{2e}\Delta/R_t$ corresponding to an environment for which $\langle\sin\hat{\delta}\rangle = 1$. This critical current is easily observed for junctions with a small Coulomb energy $E_C = 2e^2/C_0 \ll E_J$ where C_0 is the intrinsic capacitance of the junction [4]. For these junctions, the phase behaves as a good quantum number δ which can be driven to the critical value $\delta = \pi/2$. However, for the so-called "ultrasmall" junctions characterized by $E_C \gtrsim E_J$, which are considered for applications in quantum information processing [5], the highest supercurrent has always been found experimentally well below the expected value I_0 [6–9]. Several untested hypotheses have been formulated to explain these results. The average $\langle\sin\hat{\delta}\rangle$ may not reach the value 1 because of uncontrolled quantum or thermal fluctuations. Failure of the Josephson Hamiltonian model for ultrasmall junctions could also explain the results, even if it is not directly expected from theory. Note that, experimentally, one cannot simply shunt the two leads of the junction by a small superconducting inductance to impose the phase difference, since it then becomes impossible to check the junction parameters by measuring its quasiparticle current.

The aim of the experiment reported in this Letter was to test the validity of the Josephson Hamiltonian model and the Josephson relation for an ultrasmall junction embedded in a controlled environment which should suppress phase fluctuations.

The principle of our experiment is shown schematically in Fig. 1a: an ultrasmall Josephson junction with critical current I_0 and intrinsic capacitance C_0 is biased by a circuit equivalent to a capacitor C_B in parallel with an ideal voltage source V_B in series with a resistance R_B. This bias circuit is also equivalent to a current source $I_B = V_B/R_B$ in parallel with R_B and C_B (Thévenin theorem). The average current I through the junction is measured by a current meter in series with the junction. The impedance of the meter is made negligible in comparison with the impedance of the bias circuit. The system is analogous to a damped quantum particle with mass $C(\hbar/2e)^2$, where $C = C_0 + C_B$, placed in a tilted washboard potential $U(\hat{\delta}) = -E_J\cos\hat{\delta} - I_B(\hbar/2e)\hat{\delta}$. The damping due to the resistance R_B, assumed to be in thermal equilibrium at temperature T, manifests itself also as a fluctuating force acting on the particle [2]. We consider only the overdamped regime $R_B \ll \sqrt{\hbar/(2eCI_0)}$, for which the particle mass can be neglected. In this regime, all quantum fluctuations of the phase are suppressed, provided that $R_B \ll h/(2e)^2$ [10]. Previous experiments have tried to implement this idealized circuit and determine the supercurrent maximum $I_{S\max} = \max[I_S(V_B)]$ which should tend to I_0 as $T \to 0$. However, instead of the pure R_B and C_B combination, all of them had a strongly frequency-dependent and often ill-characterized impedance $Z(\omega)$. This difficulty arose because the measuring setups involved high input impedance field-effect transistor amplifiers and the dc value of Z had to be made large in order to resolve the contribution of the junction quasiparticle current to the $I(V)$ characteristics. In practice, the condition for hysteresis $Z(\omega = 0) \gg \sqrt{\hbar/(2eC_0I_0)}$ was inevitable. The zero-voltage state, in which the supercurrent is measurable, was therefore metastable and was switching to the nonzero voltage state at $I_B = I_{\rm sw} < I_{S\max}$ [11]. This switching

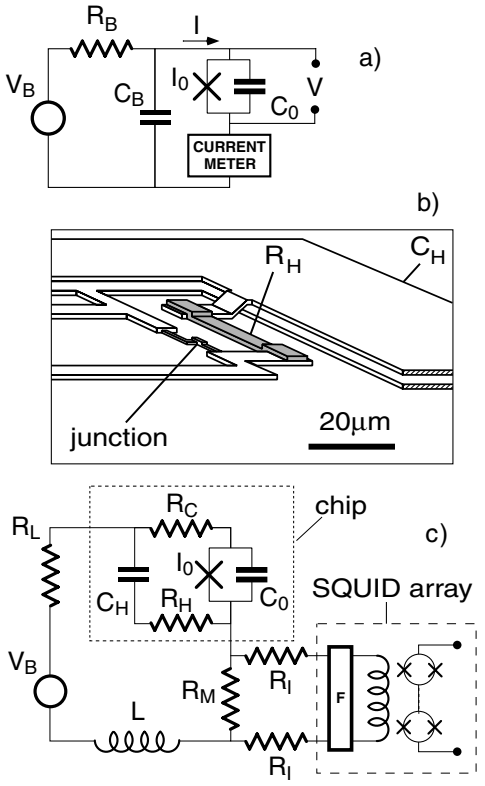

FIG. 1. (a) Idealized circuit for measurement of supercurrent of Josephson junction. The junction consists of a Josephson element (cross) in parallel with a capacitor. (b) On-chip high-frequency circuitry contributing to electrodynamic damping of Josephson junction. For clarity, metallic thin films only are represented. (c) Measurement setup schematics including both on-chip circuitry (box in dotted line) and off-chip circuitry. A known fraction of the current through the junction is coupled to a SQUID array (box in dashed line). The backaction noise of the SQUID array is attenuated by filter F.

transition is affected by thermal and quantum fluctuations, and $I_{\rm sw}$ is characterized by a probability distribution. The average $\bar{I}_{\rm sw}$ obtained so far for ultrasmall junctions showed various degrees of reduction compared to I_0 [6], ranging from around $10^{-3}I_0$ to $0.65I_0$, this largest value having been obtained using an on-chip impedance [9].

In the present experiment, we have circumvented these problems and measured the current through a junction in the nonhysteretic regime using as the current meter a recently developed SQUID series array with 100 dc SQUIDs [12]. The impedance of the current-measuring circuit is so low that we can afford to overdamp conservatively the junction at all frequencies, thereby ensuring that the measurement finds the junction in a fully stable state with a controlled absence of quantum fluctuations. The total impedance seen by the junction is equivalent to a pure resistor $R_B = 24 \pm 1\ \Omega$ in parallel with a reactive element which behaves as a capacitor $C_B = 200 \pm 20$ fF above a few tens of MHz. In conventional measuring setups, such heavy damping would make the junction current hardly distinguishable from the current through the shunt resistor.

The actual measurement setup implementing the idealized Fig. 1a circuit is shown in Figs. 1b and 1c. It has been designed to minimize deviations of the environmental impedance from the ideal limit $Z(\omega)^{-1} = R_B^{-1} + jC_B\omega$ while maintaining dissipative elements in thermal equilibrium at a controlled temperature T, as well as imposing an accurate bias current. In order to meet, in a frequency range spanning 10 orders of magnitude, these conflicting requirements, we have engineered an environment which consists of both microscopic on-chip (Fig. 1b) and macroscopic off-chip components (see outside of dotted line box in Fig. 1c). The on-chip components contribute mainly to the high-frequency values of the environmental impedance, which include the junction bare plasma frequency $\sqrt{2eI_0/(\hbar C_0)}$ in the tens of GHz range, while the off-chip components contribute mostly to the low-frequency values, which includes possible Josephson resonances in the hundreds of MHz range, as well as the measurement frequencies below a few kHz. The on-chip circuitry consists of a resistance $R_H = 11.8\ \Omega$ in series with a capacitance $C_H \simeq 100$ pF, which were fabricated using a five-layer optical lithography process. The resistor R_H was made from 150 nm thick AuPd with a width and length of approximately 5 μm by 25 μm. This small resistor was in good electrical contact with a large Au pad that served as a thermal reservoir. A single Al-AlO_x-Al Josephson junction was fabricated by e-beam lithography and double angle shadow mask evaporation [13]. We estimate the capacitance $C_0 = 1$ fF from the junction area. The contact resistance resulting from the junction fabrication process was $R_C = 12.1\ \Omega$. The off-chip components $R_M = 1.67\ \Omega$, $R_I = 10\ \Omega$, and $R_L = 10.1\ \Omega$ were surface mounted resistors for microwave circuits placed within 5 mm of the junction to minimize the stray inductance $L \simeq 4$ nH of the connection between the off-chip and on-chip circuitry. The role of R_M and the two R_I's is to provide a current divider for minimizing the backaction of the Josephson oscillations inside the SQUID array on the measured junction. A microwave copper-powder filter [14] placed in series with the R_I resistors provides further attenuation at high frequency. Only about 8% of the junction supercurrent was thus coupled to the SQUID array. The biasing circuitry at high temperature was connected to the resistor R_L through coaxial lines filtered by a combination of copper-powder filters and miniature cryogenic filters [15], and its action is equivalent to a voltage source V_B in series with R_L. The sum of R_L, R_M, and R_C determines the dc value of the environmental impedance, while the sum of R_H and R_C determines its high-frequency value (inductor L blocks high-frequency currents). The sample and the low temperature bias circuitry were thermally anchored inside a copper box bolted to the mixing chamber of a dilution refrigerator.

The junction $I(V)$ characteristic is shown in Fig. 2a for $T = 34$ mK. The superconducting gap is directly measured to be $\Delta = 200 \pm 2\ \mu$V and the junction normal

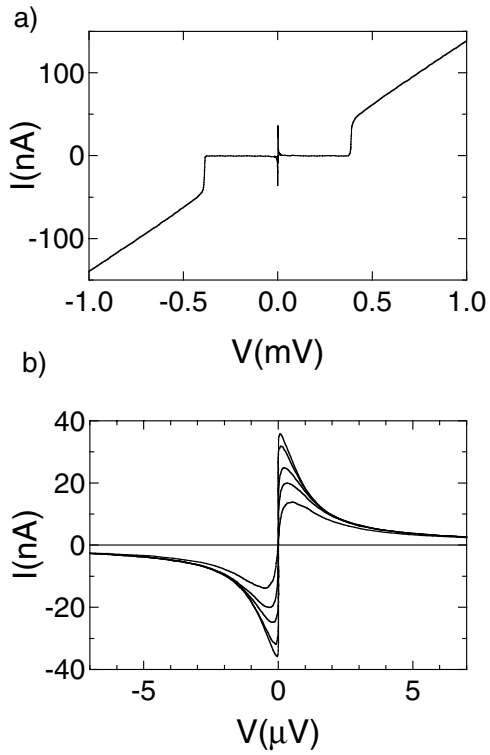

FIG. 2. (a) Large-scale $I(V)$ characteristic of the ultrasmall Josephson junction of Figs. 1b and 1c at $T = 34$ mK. (b) Josephson supercurrent peak shown on an expanded voltage scale, at different temperatures. From top to bottom: $T = 34, 98, 245, 400, 622$ mK, respectively.

state resistance approaches the asymptotic value $R_N = 6.99\ \mathrm{k}\Omega$ at voltages many times $2\Delta/e$. The critical current is then calculated to be $I_0 = 44.9 \pm 0.5$ nA. On first inspection, the $I(V)$ of Fig. 2a appears conventional, with the Josephson current manifesting itself as a vertical line at zero voltage. However, because of the low impedance of our biasing circuit, there is no hysteresis and all points on the $I(V)$ characteristic are stable, in contrast with the usual current-bias ramp method giving access only to the positive differential conductance part of the $I(V)$ in the best cases. Thus, it is worth stressing that in our experiment, a *supercurrent peak,* as opposed to a supercurrent branch, is measured for the first time. The detailed structure of the supercurrent peak is shown for several temperatures in Fig. 2b. The higher temperature data show a finite slope around zero bias which is due to phase diffusion in the tilted washboard potential [16]. The full $I(V)$ characteristic in the pure Ohmic damping case was first calculated by Ivanchenko and Zil'berman [17]:

$$I(V_B) = I_0\,\mathrm{Im}\left[\frac{I_{1-2i\beta eV_B/\hbar R_B}(\beta E_J)}{I_{-2i\beta eV_B/\hbar R_B}(\beta E_J)}\right], \qquad (1)$$

where $I_\nu(z)$ is the modified Bessel function, $\beta = 1/k_BT$, $V_B = V + R_BI$. The more general approach [18], developed to solve the steady-state Fokker-Planck equation for the phase distribution in a tilted washboardlike potential, has been proved to yield equivalent results [19]. The expression (1) predicts a supercurrent peak with a maximum which tends to I_0 in the zero temperature limit. A detailed comparison between the $I(V)$ characteristics measured at three temperatures and the theoretical predictions are shown in Fig. 3 with no adjustable parameters. The close agreement between theory and experiment around the peak maximum shows that the temperature of the electromagnetic environment which drives the phase dynamics is indeed equal to the experimental refrigerator temperature. The agreement over the whole voltage range, without any spurious resonances, confirms that the impedance of the junction environment is indeed almost constant over the corresponding range of Josephson frequencies. As a check, we have simulated the classical dynamics of a small junction for the exact circuit of Fig. 1b, including the effect of thermal fluctuations. The theoretical $I(V)$ curves so obtained are negligibly different from those obtained with expression (1) with $R_B = 24\ \Omega$, which indicates that our experiment implements the ideal bias case satisfactorily. As a further check of the influence of the off-chip bias circuitry on the $I(V)$, we have increased L to a value of order 100 nH and observed that the $I(V)$ then developed two metastable branches predicted by our numerical simulations and corresponding to chaotic Josephson oscillations in the hundreds of MHz range [20].

In Fig. 4, we compare the measured supercurrent peak height $I_{S\,\max}$ with the values predicted from (1) over a large temperature range [21]. The peak height $I_{S\,\max}$ increases as the temperature is lowered down to 26 mK, in agreement with the classical theory. However, the agreement between theory and experiment below 200 mK was attained only after the filtering at the input of the SQUID array, as described in Fig. 1c, had been installed. This indicates the magnitude of the backaction noise produced by this type of amplifier. We do not have a fully convincing explanation for the deviations between experiment and theory at

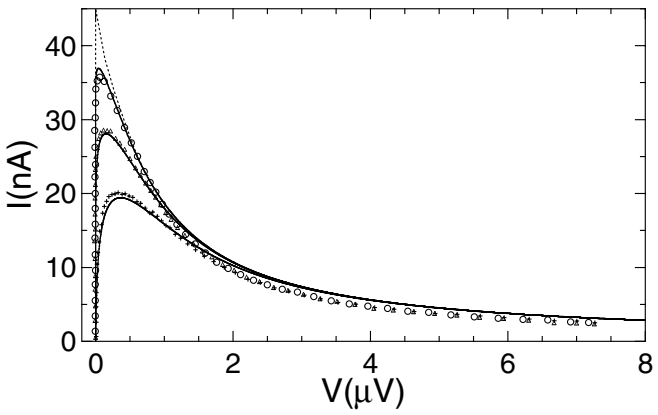

FIG. 3. Comparison between the $I(V)$ characteristics measured at different temperatures (symbols) and the calculated ones (full lines) using Eq. (1) and $I_0 = 44.9$ nA and $R = 24\ \Omega$. From top to bottom: $T = 34$, 157, and 400 mK, respectively. Dashed line represents the $I(V)$ predicted at $T = 0$.

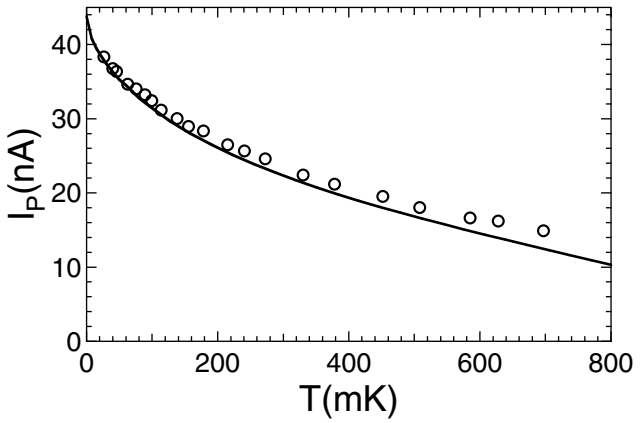

FIG. 4. Comparison between the measured temperature dependence of the maximum supercurrent (open circles) and the predicted one (full line).

the highest temperatures, but the contribution of the quasiparticle current to the damping of the junction, which we neglect in our analysis, may play a role in this regime.

Our experiment thus provides strong experimental evidence that the commonly observed reduction of the maximum supercurrent in an ultrasmall junction is not an intrinsic junction property, but is due to its electrodynamic environment. When the environment is engineered to place the junction in the overdamped regime in a controlled manner, the Ambegaokar-Baratoff critical current I_0 can be reached at low temperature, thereby showing the validity of the Josephson Hamiltonian for ultrasmall junctions. A control of the environment impedance similar to that of our experiment, but with higher resistances, would allow the observation of the strong reduction of the maximum supercurrent by quantum fluctuations, which has been recently predicted by Ingold and Grabert [22] in the case of a resistive environment with $R \sim R_Q$.

Our work also provides ground for the application of the single Cooper pair transistor (SCPT) [7] to electrometry. This device consists of two small Josephson junctions in series. At low temperature, it is equivalent to a single junction whose Josephson energy is modulated with a $2e$ period by the gate charge coupled to the island formed between the two junctions. This modulation can be exploited for low-noise-temperature electrometry [23], provided that the device supercurrent is measured like in the present experiment. The SCPT could operate at high frequencies since intrinsic bandwidths up to 120 and 250 MHz have been demonstrated for arrays with 100 and 30 SQUIDs, respectively [24]. Further work is needed to know how this new type of electrometer competes in fast electrometry with the recently developed RF-SET [25].

We gratefully acknowledge discussions with J. Imry, G.-L. Ingold, and H. Grabert. This work was partly supported by the European Union through Contract No. IST-10673 SQUBIT and by the Bureau National de la Métrologie.

[1] B. D. Josephson, in *Superconductivity,* edited by R. D. Parks (Marcel Dekker, New York, 1969).
[2] A. O. Caldeira and A. J. Leggett, Ann. Phys. (N.Y.) **149**, 374 (1983).
[3] V. Ambegaokar and A. Baratoff, Phys. Rev. Lett. **10**, 486 (1963).
[4] A. Barone and G. Paternò, *Physics and Applications of the Josephson Effect* (Wiley, New York, 1982).
[5] M. F. Bocko, A. M. Herr, and M. F. Feldman, IEEE Trans. Appl. Supercond. **7**, 3638 (1997); J. E. Mooij *et al.,* Science **285**, 1036 (1999); D. V. Averin, Solid State Commun. **105**, 659 (1998); Yu. Makhlin, G. Schoen, and A. Shnirman, Nature (London) **398**, 305 (1999); Y. Nakamura, Yu. A. Pashkin, and J. S. Tsai, Nature (London) **398**, 786 (1999).
[6] M. Tinkham, in *Single Charge Tunneling,* edited by H. Grabert and M. Devoret (Plenum Press, New York, 1992).
[7] P. Joyez *et al.,* Phys. Rev. Lett. **72**, 2458 (1994).
[8] W. J. Elion *et al.,* Nature (London) **371**, 594 (1994).
[9] D. Vion *et al.,* Phys. Rev. Lett. **77**, 3435 (1996); P. Joyez *et al.,* J. Supercond. **12**, 757 (1999).
[10] H. Grabert, G.-L. Ingold, and B. Paul, [Europhys. Lett. **44**, 360 (1998)], have established that for the circuit shown in Fig. 1a, and in the limit $R_B \ll R_Q = h/(2e)^2$, the junction dynamics is the same as if the phase was a classical variable, but with a renormalized E_J depending on both R_B and $C = C_B + C_0$. According to this theory, the quantum corrections to the bare E_J are negligible for our experiment (note that both R_B and C_B contribute to driving the junction into the classical phase regime).
[11] T. A. Fulton and L. N. Dunkleberger, Phys. Rev. B **9**, 4760 (1974).
[12] R. P. Welty and J. M. Martinis, IEEE Trans. Magn. **27**, 2924 (1991); M. E. Huber *et al.,* Appl. Supercond. **5**, 425 (1998).
[13] G. J. Dolan and J. H. Dunsmuir, Physica (Amsterdam) **152B**, 7 (1988).
[14] J. M. Martinis, M. H. Devoret, and J. Clarke, Phys. Rev. B **35**, 4682 (1987).
[15] D. Vion *et al.,* J. Appl. Phys. **77**, 2519 (1995).
[16] J. M. Martinis and R. L. Kautz, Phys. Rev. Lett. **63**, 1507 (1989); R. L. Kautz and J. M. Martinis, Phys. Rev. B **42**, 9903 (1990).
[17] Yu. M. Ivanchenko and L. A. Zil'berman, Sov. Phys. JETP **28**, 1272 (1969).
[18] V. Ambegaokar and B. I. Halperin, Phys. Rev. Lett. **22**, 1364 (1969).
[19] W. T. Coffey, Yu. P. Kalmykov, and J. T. Waldron, *The Langevin Equation* (World Scientific, Singapore, 1996).
[20] K. K. Likharev, *Dynamics of Josephson Junctions and Circuits* (Gordon and Beach, New York, 1986), pp. 177–180.
[21] Small corrections to the Josephson relation have been applied for temperatures above 600 mK following Ref. [3].
[22] G.-L. Ingold and H. Grabert, Phys. Rev. Lett. **83**, 3721 (1999).
[23] A. B. Zorin *et al.,* J. Supercond. **12**, 747 (1999).
[24] M. Huber *et al.,* IEEE Trans. Appl. Supercond. **11**, 1251 (2001).
[25] R. J. Schoelkopf *et al.,* Science **280**, 1238 (1998); A. Aassime, G. Johansson, G. Wendin, R. J. Schoelkopf, and P. Delsing, Phys. Rev. Lett. **86**, 3376 (2001).

Superconducting Electrometer for Measuring the Single Cooper Pair Box

A. Cottet[1], A. Steinbach[1], P. Joyez[1], D. Vion[1],
H. Pothier[1], D. Esteve[1], and M. E. Huber[2]
[1]Service de Physique de l'Etat Condensé, CEA-Saclay, F-91191
Gif-sur-Yvette, France
[2] Department of Physics, University of Colorado at Denver,
Denver, CO 80217, USA

Date: June 8, 2001

Abstract

We discuss for the single Cooper pair box the contributions to relaxation and to decoherence of the electromagnetic environment, of the offset charge noise, and of a measuring Single Electron Transistor. We show that a single Cooper pair transistor can also be used for that purpose. Experimentally, we have operated such a device by measuring the variations of its critical supercurrent with the gate voltage using a SQUID series array amplifier. We describe the characteristics of this new electrometer and compare different schemes for measuring the critical current.

0.1 Introduction

The giant leap that quantum mechanics could bring to computing science[1] motivates an intense research of systems suitable for implementing quantum bits (qubits) and quantum algorithms. The requirements are formidable: the quantum states of the elementary qubits should be manipulable at will without significant loss of coherence over times much longer than the duration

of elementary transformations, the couplings between qubits should be fully controllable, and the state of a qubit should be readable reliably. Furthermore, the implementation of the error correcting codes necessary to fight the unavoidable residual decoherence would require to perform measurements on some qubits during the computation process in order to perform adequate correction manipulations[2]. At the present time, quantum entanglement up to four qubits[3] and operation of elementary quantum gates[4] have already been demonstrated in quantum-optics based systems. Although less developped, microfabricated solid state systems are more appealing because they could be integrated on a large scale far more easily. The most advanced results reported so far with solid state systems have been obtained on qubits based on flux-states of small superconducting loops[5], and on charge states of small superconducting islands[6, 7]. In particular, Rabi precession between the two states of a charge qubit has been demonstrated in the single Cooper pair box over a few tens of oscillations[7], and longer coherence times are expected. The understanding of all decoherence sources which limit the duration of coherent oscillations in this system is thus an important issue. In this work, we discuss the influence on the single Cooper pair box of the residual dissipation in the box circuit, of the offset charge noise, and of the measuring system. In order to reduce the back-action of the measuring apparatus, we consider a new type of electrometer based on the superconducting version of the single electron transistor[8]. Finally, we report the first electrometry measurements performed with such an electrometer, and we discuss the different possible measuring set-ups.

0.2 Description of the single Cooper pair box

The single Cooper pair box[6], described in Fig. 1, consists of a single superconducting island connected to a voltage source U through a small capacitor C_g on one side and through a small Josephson junction[9], with capacitance C_J and Josephson energy E_J, on the other side. When the superconducting gap Δ in the junction electrodes is larger than the charging energy $E_c = e^2/2C_\Sigma$ (with $C_\Sigma = C_J + C_g$), two charge states $|n\rangle$ and $|n+1\rangle$ differing by one Cooper pair in the island form, close to their electrostatic energy degeneracy point, a two-level-system well decoupled from other degrees of

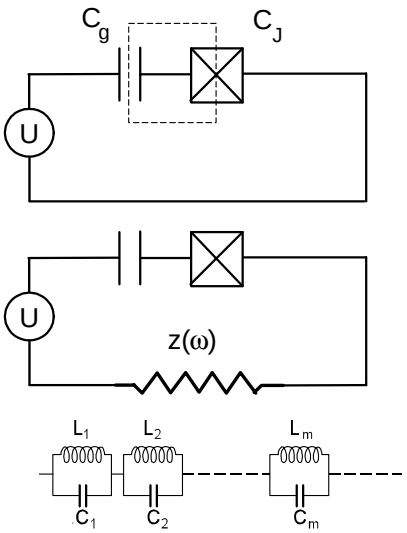

Figure 1: Top: schematic circuit of the single Cooper pair box. The dashed line encloses the box island. Middle: realistic circuit with a residual series impedance. Bottom: representation of the electromagnetic modes coupled to the box.

freedom. The effective spin 1/2 hamiltonian of this two-level system writes:

$$H_0 = -\frac{1}{2}\vec{B}.\vec{\sigma} \tag{1}$$

where $\vec{\sigma}$ is a vector of Pauli operators, and $\vec{B}$ a fictitious field with components $\{E_J, 0, 4E_c(1-n_g)\}$, with $n_g = C_g U/e$ (see Fig. 2). The ground and excited states of the above hamiltonian, $|\sigma_B = 1\rangle$ and $|\sigma_B = -1\rangle$, are the two states of the qubit. Their energy difference is $\hbar\Omega = E_J/\sin\theta$, where θ is the angle between $\vec{B}$ and the z axis. This description is however oversimplified, and the qubit is coupled to other degrees of freedom, both at thermal equilibrium and out of thermal equilibrium. We will consider in this work the effect of residual electromagnetic dissipation in the Cooper pair box circuit, the effect of moving charges in the neighborhood of the box island, and the effect of an electrometer measuring the state of the qubit from the electrostatic potential of the box island.

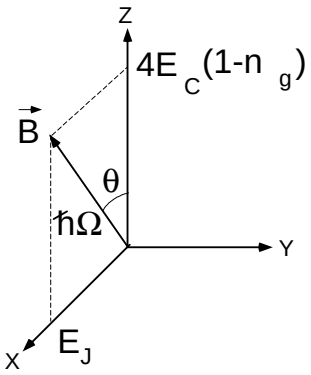

Figure 2: Fictitious spin 1/2 representation of the Cooper pair box. The vector $\overrightarrow{B}$ is the effective field acting on the spin.

0.3 Relaxation and decoherence induced by the electromagnetic environment

The electromagnetic degrees of freedom of the box circuit can be modeled by inserting a small series impedance $z(\omega)$, as shown in Fig. 1. This impedance

incorporates the effect of the voltage source and wiring impedances. Its effect is to couple the box to a set of bosonic electromagnetic modes with frequencies $\{\omega_j\}$ through the hamiltonian:

$$h = -\sqrt{\pi} \sum_j \hbar\omega_j \sqrt{\frac{Z_j}{R_K}} i(b_j - b_j^\dagger)\sigma_z \ , \tag{2}$$

where Z_j, b_j and $b_j^\dagger$ are the impedance, the annihilation and creation operators of mode j, respectively, and $R_K = h/e^2$ is the resistance quantum. These modes, which form the electromagnetic environment of the charge qubit, are assumed at thermal equilibrium. Any summation $\sum_j f(\omega_j)Z_j$ over the set of modes is performed in the following way[10]:

$$\sum_j f(\omega_j)Z_j = \frac{2}{\pi}\int_0^\infty f(\omega)\,\mathrm{Re}\,Z(\omega)\ \ \frac{d\omega}{\omega} \ , \tag{3}$$

with, in the weak coupling regime $\kappa = C_g/(C_J + C_g) \ll 1$ relevant for the experiments, $\mathrm{Re}\,Z(\omega) = \kappa^2\,\mathrm{Re}\,z(\omega)$. The coupling hamiltonien (2) induces transitions between the box and the modes of the environment. The standard second order perturbation theory yields for the downward and upward transition rates $\Gamma_\downarrow$ and $\Gamma_\uparrow$ between the excited state and the ground state of the box:

$$\Gamma_{\downarrow(\uparrow)} = \frac{(2\pi)^2 \sin^2\theta\ S(+(-)\Omega)}{\hbar R_K} \ , \tag{4}$$

where $S(\omega)$ is the spectrum of the voltage fluctuations across the effective impedance $Z(\omega)$:

$$S(\omega) = \frac{\hbar\,|\omega|}{2\pi}\left[\coth(\frac{\hbar\omega}{2k_BT}) + 1\right]\mathrm{Re}\,Z(\omega) \ . \tag{5}$$

The total relaxation rate $\Gamma_1^{ENV} = \Gamma_\downarrow + \Gamma_\uparrow$ is the decay rate of the diagonal part of qubit matrix density. In the low temperature regime $T \ll \hbar\Omega/k_B$, one has $\Gamma_\uparrow \simeq 0$, and the total relaxation rate is simply:

$$\Gamma_1^{ENV} \simeq 4\pi\Omega\sin^2\theta\ \kappa^2\,\mathrm{Re}\,z(\Omega)/R_K \ . \tag{6}$$

Numerically, one gets $\Gamma_1^{ENV} = 50$ kHz for the box parameters $\Omega/2\pi = 10$ GHz ($\hbar\Omega/k_B \simeq 0.5$ K) , $\kappa = 2.5\%, \mathrm{Re}\,z(\Omega) = r = 5\ \Omega$, and $\theta = \pi/4$.

We now discuss the decay of the coherence amplitude $\langle X' \mid X'(t)\rangle$ of a state prepared at $t = 0$ as $\mid X'\rangle = 1/\sqrt{2}\,(|\sigma_B = 1\rangle + |\sigma_B = -1\rangle)$. Although on-resonance modes exchanging energy with the box contribute to the decay of coherence, out-of-resonance oscillators also contribute because they get entangled with the box. The coherence amplitude $\langle X' \mid X'(t)\rangle$ picks an extra decay factor[11] :

$$A(t) = \exp\left(4\cos^2\theta.\,\mathrm{Re}[J(t)]\right) \tag{7}$$

where $J(t)$ is the phase correlation function which appears in the theory of Coulomb blockade[12] :

$$J(t) = 2\int_0^\infty \frac{d\omega}{\omega}\frac{\mathrm{Re}\,Z(\omega)}{R_K}\frac{\exp(-i\omega t)-1}{1-\exp(-\hbar\omega/k_BT)} \tag{8}$$

In the simple case when $z(\omega) = r$, the function $J(t)$ can be calculated exactly. The long time behavior of $\mathrm{Re}\,J(t)$ is:

- At zero temperature: $\mathrm{Re}\,J(t) \sim -2\frac{\kappa^2 r}{R_K}(\gamma + \ln(t/\kappa r C_J))$

- At finite temperature: $\mathrm{Re}\,J(t) \sim -2\frac{\pi\kappa^2 r}{R_K}(k_BTt/\hbar)$

At zero temperature, $A(t)$ follows a power-law with a small exponent, and decoherence is weak. At temperatures $T > 10$ mK, the classical regime is almost reached, and $A(t)$ decays exponentially at a rate Γ_2^{ENV} :

$$\Gamma_2^{ENV} = 8\pi\left(\frac{k_BT}{\hbar}\right)\frac{\kappa^2 r}{R_K}\cos^2\theta\ . \tag{9}$$

This result can be easily retrieved by performing the following semi-classical average:

$$A(t) = \left\langle \exp i\int_0^t \left(\Omega(t') - \bar{\Omega}\right)\ dt' \right\rangle \tag{10}$$

where $\Omega(t)$ is now the time dependent transition frequency modulated by the thermal fluctuations of the voltage across the impedance $z(\omega)$. In the classical regime, this entanglement is dominated by a random phase factor between the two states of the coherent superposition. It is worth noticing that the entanglement between the qubit and its environment is not an irreversible process by itself, and that one could in principle recover to some extent the loss of coherence due to low frequency modes using echo or even more sophisticated pulse techniques, analogous to those developped in nuclear magnetic

resonance (NMR). If the impedance $z(\omega)$ is frequency independent, the ratio between the relaxation rate and the decoherence rate due to thermally excited oscillators reduces to:

$$\frac{\Gamma_1^{ENV}}{\Gamma_2^{ENV}} = \frac{\hbar\Omega}{2k_BT}\tan^2\theta \ . \tag{11}$$

Since the experiments are performed in the low temperature regime $k_BT \ll \hbar\Omega$, one has $\Gamma_1^{ENV}/\Gamma_2^{ENV} \gg 1$ in practice. In this case, the electromagnetic environment of the qubit relaxes the whole qubit density matrix at the rate Γ_1^{ENV}.

0.4 Relaxation and decoherence induced by the offset charge noise

It is well known that the island of a Single Electron Transistor (SET) [13] is subject to an offset charge noise with a $1/f$ spectrum[14]. This noise is attributed to a set of charges randomly fluctuating between two positions in the junction barriers and/or in the insulators close to the SET island. Occasionnaly, slow two-level fluctuators (TLF) have been directly observed over long times. The $1/f$ character of this TLF noise has been probed up to about 10 MHz. Its typical intensity is $S_q(f) = e^2B/f$, with $B \approx 10^{-7}$. Like the electromagnetic environment, the charge noise induces relaxation and decoherence on the box quantum states. Although the spectral density of the charge noise has only been measured at frequencies much smaller than Ω, recent experiments on the single electron pump[15] have provided experimental evidence that the charge noise extends up to 100 GHz, i.e. well above Ω. Amazingly, the spectral density estimated from the measured transition rate of otherwise forbidden transitions falls rather close to the extrapolated value of the $1/f$ spectrum, with $B' \approx 10^{-8}$. This noise should result in upward as well as downward transitions at a rate Γ_1^{TLF}:

$$\Gamma_1^{TLF} = \frac{2\pi B'}{\Omega}\left(\frac{E_c}{\hbar}\right)^2 \sin^2\theta \ . \tag{12}$$

The estimated value is about $\left(1 \times \sin^2\theta\right)$ MHz, significantly larger than the estimated contribution of the box circuit electromagnetic environment.

The decay rate of the coherence amplitude picks an extra contribution from the low-frequency offset charge fluctuations. Because of divergences inherent to the $1/f$ spectrum, the experimental protocol has to be precisely defined. When a measurement, performed during a short time τ, is averaged over a time $t_{av} \gg \tau$, the transition frequency has drifted away from its initial value and one finds for the decay function:

$$A'(\tau) \simeq \exp - \left[8B \cos^2 \theta \ \left(E_c \tau / \hbar \right)^2 \ln(t_{av}/\tau) \right] \ . \tag{13}$$

The contributions of low frequency TLF to the decay of a coherence signal can be suppressed using an echo pulse sequence similar to those used in NMR to compensate for inhomogeneous line-broadening. In this case, the decay function does not depend on the averaging time and writes:

$$A'(\tau) \simeq \exp - \left[8B \cos^2 \theta \ \left(E_c \tau / \hbar \right)^2 \frac{\log(2)}{2} \right] \ . \tag{14}$$

The decay is still fast, and coherence is lost after a time $\sim (20/\cos\theta)$ ns for $B = 10^{-7}$, $E_c = 0.5\ k_B$K. The $1/f$ noise is thus a serious limitation, and its reduction to a level significantly smaller than commonly achieved is an important issue.

0.5 Relaxation and decoherence induced by a measuring SET electrometer

The state of the box can be measured either by measuring the electrostatic potential of the island[6], or by connecting it to an extra small probing tunnel junction which directly exchanges electrons with it[7]. Whereas this latter method results in a destructive measurement of the qubit state, the first one discussed here could in principle allow quantum non demolition (QND) measurements. For that purpose, the measuring electrometer should be able to distinguish both states of the qubit without inducing transitions between them. Repeated measurements of the qubit state should then give the same answer. An important characteristic of any measuring electrometer is thus the amount of information it can provide before irreversible transitions induced by the measuring system or by other relaxation mechanisms occur. Figure 3 shows a measuring set-up with a SET electrometer capacitively coupled through C_c to the box island, a set-up which has been used

to measure the island potential in the box ground state[6]. The measuring process has been theoretically investigated in great detail for this set-up[16]. The back-action of the SET results from the fluctuations of the electrostatic

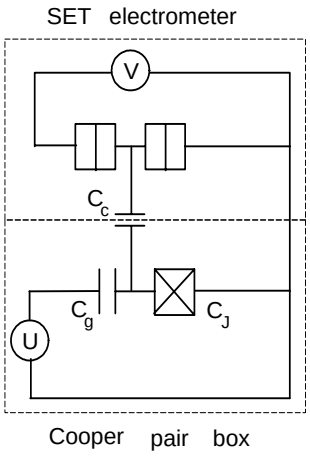

Figure 3: Schematic circuit of a single Cooper pair box electrostatically coupled to a measuring SET. The SET measures the potential of the box island. The voltage fluctuations of its island produce a back-action noise on the box, which induces relaxation and decoherence.

potential of its own island while the current is flowing. When one electron enters or exits the island, the voltage varies by $\delta V = e/C_{SET}$, where C_{SET} is the capacitance of the SET island. Typically, δV is a few hundreds of microvolts. At a practical working point, the correlation time of these voltage fluctuations is $\tau_c \approx 1/R_{SET}C_{SET} \approx e/I$, where R_{SET} is the tunnel resistance of the SET junctions, and I is the average current. The spectrum is thus lorentzian with a cut-off frequency τ_c^{-1}. Its detailed form depends on the biasing point, and is precisely known for SETs with junction resistances larger than R_K [17]. Low frequency fluctuations result in decoherence, and a SET at the threshold can reach the quantum limit in the sense that the qubit state is decohered just on the time scale needed to measure it[16]. However, fluctuations at the qubit transition frequency Ω induce transitions at a significant rate when $\Omega\tau_c < 1$. In this regime, the induced relaxation rate follows from Eq. (4) using the spectral density of the SET island voltage and the relevant

coupling factor $\kappa_{SET} = C_c/C_J \ll 1$ between the box and the SET :

$$\Gamma_1^{SET} \simeq \frac{(2\pi)^2 \sin^2\theta \ \kappa_{SET}^2 \ (\delta V/2)^2 \ \tau_c}{\hbar R_K} \ . \tag{15}$$

More precise estimates can be obtained to take into account the precise working point of the SET and the effect of the rf drive in the case of an rf-SET[18]. The question thus arises if a SET is able to measure the box state before the induced relaxation has destroyed the qubit. A figure of merit can be defined as $f^{SET} = 1/\left(\Gamma_1^{SET}.\tau_m\right)$, τ_m being the minimum time necessary to perform a measurement of the box state. Assuming that the measurement accuracy is solely limited by the SET intrinsic noise and not by the electronic amplifiers measuring the SET current, one finds $f^{SET} \approx \cot^2\theta$. A usual SET can thus perform a single measurement of the qubit[16], but not by a large margin. Note that a SET operated in the strong tunneling regime could possibly achieve a better performance. From the experimental point of view, the sensitivity of the best rf-SET is still presently limited by the noise of the microwave amplifier at the carrier frequency but the intrinsic limit is not beyond reach. In the following, we examine another type of electrometer based on the superconducting version of the SET, the SSET.

0.6 The superconducting SET electrometer

The SSET is almost equivalent to a single small Josephson junction whose critical current $I_c(n_g)$ is periodically modulated by the gate charge[8]. The only difference with a single junction is that the current-phase is not strictly sinusoidal, and that higher energy states can be excited. In the case when the gate charge is modulated at frequencies smaller than the band gap, the adiabatic approximation holds, and the SSET behaves as a tunable junction. The modulation pattern is determined by the ratio E_c/E'_J, where $E'_J = I_0\hbar/2e$ is the Josephson energy of each junction with critical current I_0. For practical values $E_c/E'_J \sim 1$, the maximum critical current of a SSET, obtained for a reduced gate charge $n_g = 1 \ [\mathrm{mod}\, 2]$, is of the order of $I_0/2$, and the slope dI_c/dn_g is of the order of I_0 at practical working points. The predicted critical current for a SSET is compared in Fig. 4 with the average maximum supercurrent measured in a current-biased set-up[8]. In this case, the current-voltage $I-V$ characteristic is hysteretic and, upon ramping the bias current, the junction switches out of the zero-voltage-state at a switching

current I_S. The values of I_S are distributed with an histogram whose average value and width depend on the electromagnetic impedance as seen from the SSET[19]. The average value is smaller than the critical current but almost scales with the predicted variations for $I_c(n_g)$. Depending on the biasing circuitry impedance, the critical current of a SSET can be measured in two different ways, which yields to two very different types of electrometers.

Straight line: predicted variations for the critical current of a SSET with $E_c = 0.66\ k_B$K and $E'_J = 0.50\ k_B$K. Dots: Measured average switching current I_S for this SSET in a moderate damping circuit at $T = 20$ mK. Dashed line: theoretical predictions.

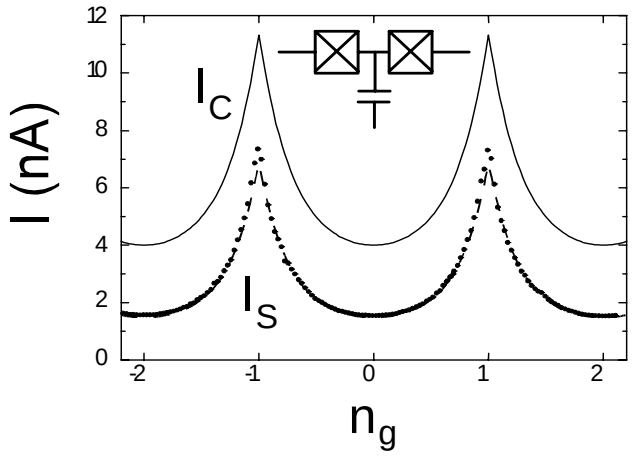

Figure 4: Straight line: predicted variations for the critical current of a SSET with $E_c = 0.66\ k_B$K and $E'_J = 0.50\ k_B$K. Dots: Measured average switching current I_S for this SSET in a moderate damping circuit at $T = 20$ mK. Dashed line: theoretical predictions.

0.6.1 electrometry based on the switching of an ac-shunted SSET

The variations of the average switching current with the gate charge can be used for electrometry. The obtention of narrow switching histograms suitable for electrometry requires to damp the dynamics of the phase across the junction. Switching histograms with an average close to the critical current and

a relative width smaller than 10^{-3} have been obtained in the case of a single junction using an RC ac-shunting circuit[19]. However, the bias current ramp-rate required for measuring a box is larger than used in the previous experiment[19], and we have found that histograms get wider when the ramp rate increases. Experimentally, we have measured switching histograms of an RC-shunted SSET using ramping speeds up to $0.2 \times I_S/\mu$s. Preliminary results show switching histograms narrow enough to discriminate the two box states within a measuring time of 1 μs.

0.6.2 electrometry based on the dc-shunted SSET

When a Josephson junction is shunted by a small enough resistor, its $I-V$ characteristic is no longer hysteretic. However, its measurement is far more difficult than in the unshunted case because the voltage across the junction is too small to be measured using room temperature amplifiers. Recently, our group has used the SQUID series array amplifiers developped at NIST-Boulder[20] to measure the full $I-V$ characteristic of a small Josephson junction. The array we have used consists of 100 dc-SQUIDs in series, and delivers a signal large enough to be amplified by room temperature amplifiers without degradation[21]. Closed loop operation of the arrays is possible within a few MHz bandwidth. The experimental results on single junctions[22], in excellent agreement with the calculated $I-V$ characteristics[26], show that the classical regime for the phase dynamics was indeed reached. This result made possible the design of an electrometer based on the measurement of a shunted SSET[23]. For that purpose, we have implemented the set-up schematically described in Fig. 5, in order to measure the current I_R through the shunting resistance R_s of a SSET. More precisely, a fraction of this current flows in the input coil of a SQUID array amplifier. In order to avoid any high frequency resonance, an extra ac-shunt has been placed on-chip across the SSET, but careful mounting of discrete components should however be sufficient to obtain an adequate environment.

sensitivity and bandwidth The sensitivity of the electrometer is set by the intrinsic SSET sensitivity $dI_c/dn_g \approx I_0$, by the ratio $dI_R/dI_c \lesssim 1$ at the bias point of the device, and by the noise of the SQUID array referred to its input $S_I \simeq 3$ pA/$\sqrt{\text{Hz}}$. The intrinsic noise floor which results from the thermal fluctuations of I_R is much smaller and will be considered later

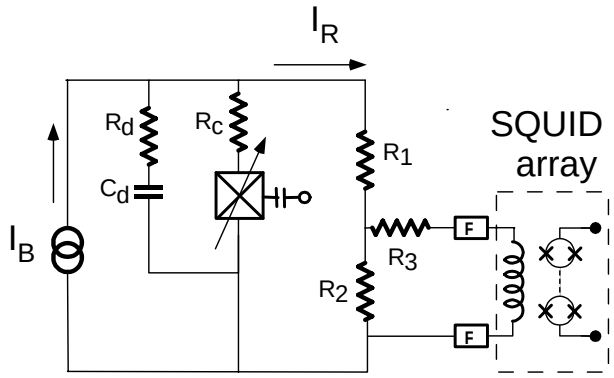

Figure 5: Schematic circuit of a SSET electrometer. The SSET is displayed as a tunable junction. A fraction $\sim 1/3$ of the dc-current in the shunt resistance passes in the input coil of a 100 SQUID series array. R_d and C_d form an on-chip damping circuit, R_c is a contact resistance, and R_1, R_2 and R_3 are surface-mounted components. The low-pass filters F prevent the Josephson oscillations in the SQUIDs from disturbing the SSET.

on. The sensitivity, expressed in $e/\sqrt{\text{Hz}}$, is thus $s \approx S_I/I_0$. Although a larger critical current I_0 should result in better sensitivity, too large values of I_0 result in a strong renormalisation of the island charging energy due to virtual quasiparticle tunneling and correlatively to a strong reduction of the modulation depth of the critical current. In practice, we have found that the optimal value of I_0 is in the range $20 - 40$ nA, which would result in a sensitivity $s \approx 10^{-4} e/\sqrt{\text{Hz}}$ for a maximal coupling between the SSET and the array. This figure is significantly worse than the sensitivity $s \approx 7\ 10^{-6} e/\sqrt{\text{Hz}}$ already achieved with the rf-SET, but two-stage SQUID amplifiers might allow to improve the present sensitivity by about one order of magnitude. In this design, the SSET is connected to the input coil of a single dc-SQUID, which is itself in series with the input coil of a SQUID array. The bandwidth is limited by the input circuit and by the electronics backing the array. As seen from the array input coil, the SSET behaves as a source with a resistive impedance which is of the order of the series resistance in the input coil circuitry, 10 Ω in our case. For an input coil inductance of 200 nH, the resulting bandwidth is about10 MHz, but can be made larger if needed.

experimental results We have fabricated SSETs using 3 angle deposition through a shadow mask[24]. The two first aluminum layers form the junction electrodes, and the third gold layer forms normal wires which help eliminating spurious quasiparticles in the superconducting electrodes, and connect the SSET to an on-chip RC damping circuit fabricated by optical lithography. The SSET junction have an area of 80×130 nm^2 and a tunnel resistance of 7.5 kΩ. The samples were mounted in a shielded box fitted with coaxial connections to the SQUID series array box, and microfabricated RC filters[25] were installed on the bias and gate lines of the electrometer. As shown in Fig. 6 for a series of bias current values, the current through the shunt resistor of the SSET is modulated by the gate voltage, with a measured period corresponding to $2e$. At larger bias currents, the modulation depth decreases progressively. We have also determined the IV characteristic of the SSET for different gate voltages. The extremal IVs, obtained for $n_g = 0$ and $n_g = 1$, are shown in Fig. 7. The overall agreement between the experimental results and the theoretical predictions[26] for a tunable Josephson junction is satisfactory. The parameters are $Ec = 0.55\ k_B K$, and $I_0 = 40$ nA which are in good agreement with the values estimated from the area and tunnel resistance

of the junctions, and from the superconducting gap $\Delta = 180\ \mu eV$. This corresponds to a ratio $Ec/E'_J = 0.55$. The damping resistance as seen from the SSET is $R_{eff} = 38\ \Omega$, larger than the estimated value 25 Ω taking into account all components in the circuit. The effective temperature of 200 mK needed to fit the data is larger than the fridge temperature 40 mK because filtering between the SQUID array and the SSET has been greatly reduced compared to previous experiments on a single junction. This excess noise temperature is however tolerable for electrometry applications, and can be reduced if needed.We have also applied to the SSET gate a $0.2e$ step and

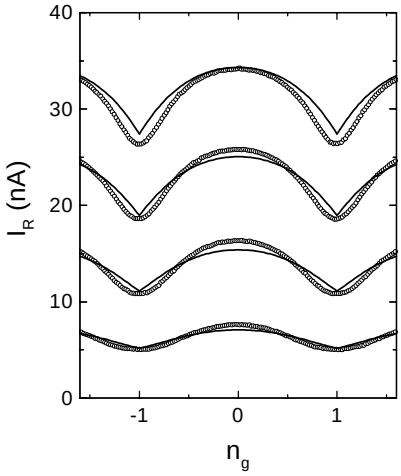

Figure 6: Open symbols: variations of the current through the shunt resistor I_R with the gate charge n_g at $T = 40$ mK and for bias currents $I = 11, 21, 31, 40$ nA, from bottom to top. Full lines: theoretical predictions at $T = 200$ mK based on the effective junction model.

recorded the response of the electrometer. In order to be sure that the measured signal originates from the SSET and not from a direct coupling to the SQUID electronics, we have substracted the traces with the SSET

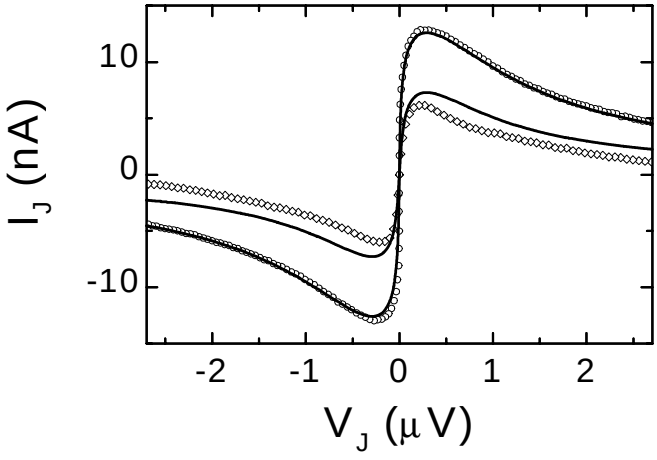

Figure 7: Open symbols: extremal $I-V$ characteristics of the SSET obtained for $n_g = 0$ and $n_g = 1$, at $T = 40$ mK. Full lines: theoretical predictions at $T = 200$ mK.

on and off. The applied step is compared in Fig. 8 with the electrometer response for two different output bandwidths, averaged over 4000 traces. The results demonstrate that the overall system has a bandwidth of about 1 MHz, probably limited by the extra filtering installed on the SQUID array lines. The noise level corresponds to the estimated one of $3.10^{-4}e/\sqrt{\text{Hz}}$, taking into account that only a fraction of the modulated current goes through the array input coil, and numerical factors. Although a faster response would be convenient, it would be of little use for measuring the state of a Cooper pair box if the sensitivity is not improved. Indeed, with the achieved noise level, one would need a typical time of a few μs to perform a measurement of the box state, assuming a coupling factor $\kappa_{SSET} = 2.5\%$. Improving the sensitivity is thus mandatory, and two stage SQUID amplifiers will be tested in the future for that purpose.

back-action noise The fluctuations of the island voltage V are very different from those in the SET because the SSET island is not sequentially charged and discharged. Since the island voltage varies periodically with the superconducting phase across the SSET, the island voltage fluctuations fol-

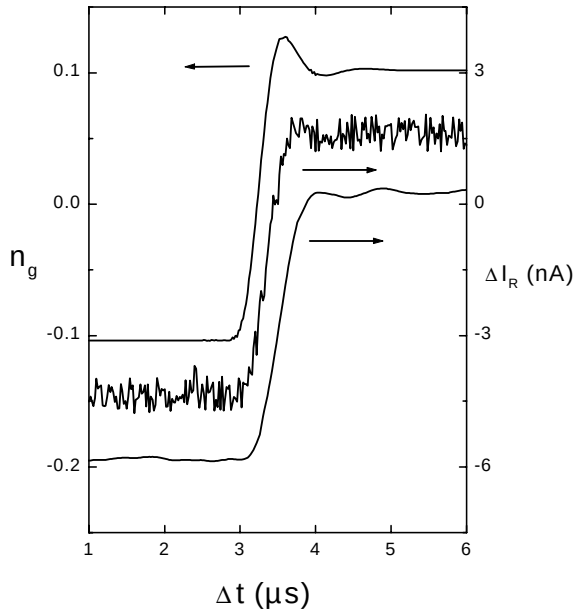

Figure 8: From top to bottom: applied charge step at the gate of the SSET electrometer; electrometer response averaged over 4000 steps and measured within 10 MHz and 1 MHz bandwidths, respectively. Curves have been offsetted for clarity.

low the phase fluctuations. Assuming that the box transition frequency is lower than the SSET band gap, the dynamics of the SSET can be calculated using an adiabatic approximation, and we find for the relaxation rate Γ_1^{SSET} due to the measuring SSET:

$$\Gamma_1^{SSET} \sim \frac{R_s I_c^2}{\hbar\Omega}\ \kappa_{SSET}^2 \sin^2\theta. \tag{16}$$

For the electrometer we have operated, this rate would be of the order of 1 MHz, assuming again $\kappa_{SSET} = 2.5\%$. The charge sensitivity of the SSET as an electrometer is limited by the thermal fluctuations of the voltage at the working point[27, 23]. The intrinsic figure of merit of the shunted SSET for the measurement of the box is:

$$f^{SSET} = \frac{1}{\Gamma_1^{SSET}\tau_m} \sim \frac{\hbar\Omega}{k_B T}\cot^2\theta, \tag{17}$$

where τ_m is again the minimum time needed to discriminate the two states of the box. Although the factor $\hbar\Omega/k_B T$ can be large, the practical figure of merit of the present electrometer would be smaller than one because the measuring time would be limited by the SQUID array and not by the intrinsic noise of the shunted SSET.

The decoherence results from the low frequency fluctuations of the island voltage. Although the spectrum of the phase fluctuations is known[27], the complicated relation between the phase across the SSET and the voltage in the island does not allow to deduce the island voltage fluctuation spectrum except in some limits. In the non-running state, the fluctuations of the phase are small, and a perturbative calculation of around the average value leads to:

$$\Gamma_2^{SSET} = \frac{4k_B T}{h}\frac{\kappa_{SSET}^2\ R_K}{r}\left(\frac{E_C}{E_J}\right)^2\ g^2\cos^2\theta, \tag{18}$$

where

$$g = \frac{I_c}{\sqrt{I_c^2 - I_{SSET}^2}}\frac{\partial\left(C_{SSET}V/e\right)}{\partial\left(\arcsin\left(I_{SSET}/I_c\right)\right)} \tag{19}$$

is an increasing function of the dc current $I_{SSET} < I_c$ with $g(0) = 0$. For our electrometer biased at $I_{SSET} = I_c/2$, the decoherence rate of a box coupled to it with $\kappa_{SSET} = 2.5\%$ would be of the order of a few MHz. This implies that, for a SSET used in the switching mode, the bias current has to be

reduced close to zero during box manipulations. When the ratio Ec/E'_J is larger than one, the variations of the island voltage are almost proportional to $\cos(\delta)$, and the spectrum can be calculated numerically along the lines of refs.[27] in all regimes. We find that the spectrum of the island voltage fluctuations has a peak at the Josephson frequency, and that the induced decoherence rate is the largest when the current through the electrometer is close to its maximum value. Quantitatively, the SSET we have operated would result in a decoherence rate $\Gamma_2^{SSET} \approx 0.3$ MHz at the working point used for electrometry.

alternate high bandwidth set-up using a SQUID array In the shunted SSET set-up, the bandwidth is ultimately limited by the time constant of the RL circuit at the input of the array. This limitation is not mandatory, and an alternate high bandwidth set-up is possible. For that purpose, a SSET, directly connected in parallel with the input coil of a SQUID, is current biased well below its critical current. Due to the residual resistance in the coil wiring, the dc bias current flows through the SSET only, and the phase difference accross the SSET adjusts to accomodate it. When the critical current of the SSET is ac-modulated, its effective inductance is varied accordingly, and the distribution of the bias current between the SSET and the SQUID input coil is modulated. In this set-up, the SSET behaves as a charge to current transducer, and the sensitivity, bandwidth and back-action are entirely determined by the current measuring stage.

0.7 Conclusions

We have evaluated in the single Cooper pair box the relaxation and decoherence rates due to electromagnetic dissipation in the box circuit itself and to external charges moving in the neighborhood of the box. The offset charge noise is likely the dominant source of relaxation and of decoherence, which rises an important problem. We have also evaluated the relaxation and decoherence rates due to a measuring electrometer coupled to the box island, and discussed in particular set-ups based on unshunted or shunted SSETs. Experimentally, we have operated an electrometer based on the continuous measurement of a shunted SSET with a SQUID series array. The sensitivity achieved by this system was about $3.10^{-4}e/\sqrt{\text{Hz}}$, limited by the SQUID array noise, within a few MHz bandwidth. Such an electrometer would be

useful in Cooper pair box experiments only if its sensitivity is significantly improved. Other measuring strategies can however be used for that purpose. In particular, the switching of an unshunted SSET is a simple one because it does not require a cold amplifier and is well suited for pulsed operation.

Acknowledgments: We thank Michel Devoret for stimulating discussions on quantum limited measurements.

References

[1] P. W. Shor, in *Proceedings of the Symposium on the Foundations of Computer Science* (IEEE Computer Society Press, New-York, 1994); L. K. Grover, Phys. Rev. Lett. **79**, 325 (1997).

[2] P. Shor, Phys. Rev. A 52, R2493 (1995); A. M. Steane Nature, **399**, 124 (1999).

[3] W. Lange and H. J. Kimble, Phys. Rev. A **61**, 63817 (2000); C. A. Sackett, D. Kielpinski, B. E. King, C. Langer, V. Meyer, C. J. Myatt, M. Rowe, Q. A. Turchette, W. M. Itano, D. J. Wineland, and C. Monroe, Nature **404**, 256 (2000).

[4] C. Monroe, D.M. Meekhof, B.E. King, W.M. Itano, and D.J. Wineland, Phys. Rev. Lett. **75**, 4714 (1995).

[5] C. H. van der Wal, A. C. ter Haar, F. K. Wilhelm, R. N. Schouten, C. J. P. M. Harmans, T. P. Orlando, Seth Lloyd, and J. E. Mooij, to be published.

[6] : V. Bouchiat, D. Vion, P. Joyez, D. Esteve, and M. H. Devoret, Physica-Scripta **76**, 165 (1998) and J. of Superconductivity **12**, 789, (1999).

[7] Y. Nakamura, Y. A. Pashkin, and J. S. Tsai, Physica-B **280**, 405 (2000) and this book; Y. Nakamura, J. S. Tsai, J. of Superconductivity, **12**, 799 (1999) and J. Low. Temp. Phys. **118**,765 (2000).

[8] P. Joyez, P. Lafarge, A. Filipe, D. Esteve and M. H. Devoret, Phys. Rev. Lett. **72**, 2548 (1994).

[9] A. Barone and G. Paternò, *Physics and Applications of the Josephson Effect* (Wiley, New York, 1992).

[10] A. J. Leggett, in *Chance and Matter* (North-Holland, Amsterdam, 1987).

[11] A. Cottet *et al.*, unpublished.

[12] G. Ingold and Yu. V. Nazarov, in *Single Charge Tunneling*, edited by H. Grabert and M. H. Devoret (Plenum Press, New York, 1992).

[13] T.A. Fulton and G.J. Dolan, Phys. Rev. Lett. **59**, 109 (1987).

[14] A. B. Zorin, F. J. Ahlers, J. Niemeyer, T. Weimann, H. Wolf, V. A. Krupenin, and S. V. Lotkhov, Phys. Rev. B **53**,13682 (1996); V. A. Krupenin, D. E. Presnov, M. N. Savvateev, H. Scherer, A. B. Zorin, and J. Niemeyer, Conference on Precision Electromagnetic Measurements Digest, IEEE, **140** (1998).

[15] M. Covington, Mark W. Keller, R. L. Kautz, and John M. Martinis, Phys. Rev. Lett. **84**, 5192 (2000).

[16] A. Shnirman and G. Schon, Phys. Rev.B **57**,15400 (1998) ; Y. Makhlin, G. Schon, and A.Shnirman, Physica-B **280**, 410 (2000).

[17] B. Starmark, T. Henning, T. Claeson, P. Delsing, A. N. Korotkov, Journal-of-Applied-Physics. **86**, 2132 (1999).D. Averin, this book.

[18] R. J. Schoelkopf, P. Wahlgren, A. A. Kozhevnikov, P. Delsing and D. E. Prober, Science **280**, 1238 (1998).

[19] D. Vion, M. Gotz, P. Joyez, D. Esteve, and M. H. Devoret, Phys. Rev. Lett. **77**, 3435 (1996); P. Joyez, D. Vion, M. Gotz, M. H. Devoret, and D. Esteve, J. of Superconductivity **12**, 757 (1999).

[20] R. P. Welty and J. M. Martinis, IEEE Trans. Mag. **27**, 2924 (1991).

[21] M. E. Huber *et al.*, Applied Superconductivity **5**, 425 (1998).

[22] A. Steinbach, P. Joyez, D. Esteve, M. H. Devoret and M. E. Huber, to be published.

[23] A. B. Zorin, Phys. Rev. Lett. 76, 4408 (1996); A. B. Zorin et al., J. of Superconductivity **12**, 747 (1999).

[24] G. J. Dolan and J. H. Dunsmuir, Physica B **152**, 7 (1988).

[25] D. Vion, P. F. Orfila, P. Joyez, D. Esteve, and M. H. Devoret, J. Appl. Phys. **77**, 2519 (1995).

[26] Yu. M. Ivanchenko and L. A. Zil'berman, Soviet Phys. JETP **28**, 1272, (1969); V. Ambegaokar and B. I. Halperin, Phys. Rev. Lett. **22**, 1364 (1969).

[27] A. V. Vystavkin, V. N. Gubankov, L. S. Kuzmin, K. K. Likharev, V.V. Migulin, and V. K. Semenov, Rev. Phys. Appl. **9**, 79 (1974); W. T. Coffey, Yu. P. Kalmykov, and J. T. Waldron, *The Langevin Equation* (World Scientific, 1996).

A HYSTERETIC SINGLE COOPER PAIR TRANSISTOR FOR SINGLE SHOT READING OF A CHARGE-QUBIT

Audrey Cottet, Denis Vion, Philippe Joyez, Daniel Esteve, and Michel H. Devoret*

1. INTRODUCTION

Superconducting nano-electronic devices are appealing candidates for implementing quantum-bits[1] (qubit) because they can be fabricated in parallel using lithography techniques. At the present time, the most advanced qubits are the single Cooper pair box[2] (CPB), which involves charge states of a small superconducting island, the RF-SQUID[3] and the 3-junction SQUID[4]. Recently, Nakamura[5] *et al*. demonstrated temporal coherence of quantum superpositions of qubit states in the CPB. The decay of Cooper pairs into quasiparticles used in this experiment for measuring the CPB is far from providing a single shot readout, and severely limits the coherence time of the superposition of states. Achieving single shot determination of the qubit energy eigenstate while preserving the coherence prior to measurement is a central issue. Recently, fast electrometers[6,7,8,9] have been developed for measuring the charge of the CPB island, and the sensitivity necessary for such single-shot readout has already been reached by an electrometer based on the radio-frequency Single Electron Transistor. In this work, we present a new readout scheme based on the single Cooper Pair Transistor[10,11,12] (CPT). In this superconducting device, the supercurrent is modulated by the charge coupled to the transistor island. We have measured the charge resolution of such an electrometer, and evaluated the back-action it would have on a CPB.

* All authors, Service de Physique de l'Etat Condensé, CEA-Saclay, F91191 Gif-sur-Yvette, France

2. PRINCIPLE OF THE READOUT

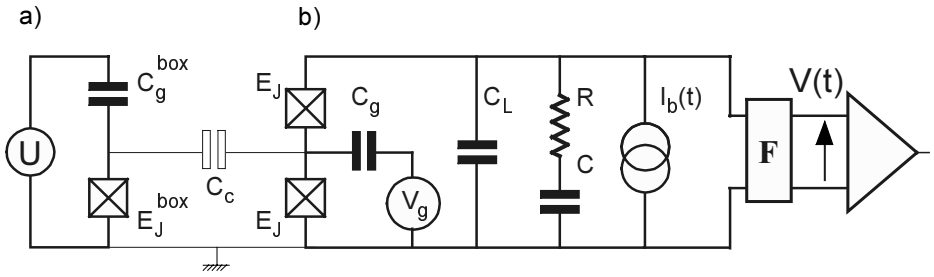

Figure 1. The single Cooper pair box (a) is a charge qubit. A natural readout scheme is to couple it to an electrometer through a capacitor C_c. The electrometer (b) tested in this work is a Cooper pair transistor (CPT). The transistor is current biased and damped only at AC frequencies.

2.1 The Cooper Pair Box as a Charge Qubit

The CPB[2] is schematically represented on Fig. 1a. It consists of a superconducting island coupled to a voltage source U through a Josephson junction with capacitance C_J^{box} and Josephson energy E_J^{box}, and through a small capacitance C_g^{box}. When the superconducting gap is larger than the charging energy $E_c^{box} = e^2 / 2C_\Sigma^{box}$, where C_Σ^{box} is the total capacitance of the island, the two lowest energy states of the CPB are superpositions of charge states $|n\rangle$, where n is an even number of electrons in the island. When the reduced gate charge $n_g^{box} = C_g^{box} U / e$ is close to an odd integer n_0, and if E_J^{box} / E_c^{box} is small, the system behaves at low energy like an effective two level system. In the subspace spanned by $(|n = n_0 - 1\rangle, |n = n_0 + 1\rangle)$, the Hamiltonian is that of a spin ½ in an effective field:

$$H_{box} = -\frac{1}{2}\vec{B}.\vec{\sigma}\,, \tag{1}$$

where $\vec{\sigma} = [\sigma_x, \sigma_y, \sigma_z]$ is the Pauli matrices vector, and $\vec{B} = [E_J^{box}, 0, 4E_c^{box}(1 - n_g^{box})]$. The ground and excited eigenstates of this Hamiltonian are the two states $|qb0\rangle$ and $|qb1\rangle$ of the qubit, indexed by 0 and 1 in this paper. The energy difference is $\hbar\Omega = E_J^{box} / \sin\theta$, and the charge difference obeys $\Delta n_{01} = \langle n \rangle_1 - \langle n \rangle_0 = 2\cos\theta$, where θ is the angle between $\vec{B}$ and $\vec{z}$. Ideally, when the island charge of a generic state $\alpha|qb0\rangle + \beta|qb1\rangle$ is measured, the state is projected on $|qb0\rangle$ or $|qb1\rangle$ with the probabilities $|\alpha|^2$ and $|\beta|^2$.

2.2 The Single Cooper Pair Transistor as an Electrometer

A schematic representation of the CPT and of the bias circuitry we have implemented in our experiment is shown in Fig. 1b. The CPT[10,12,12] itself consists of a superconducting island coupled to two superconducting reservoirs through two nominally identical small Josephson junctions with capacitance C_J and Josephson energy E_J, and coupled to a gate voltage source V_g through a small capacitance C_g. Its charging energy is $E_c = e^2/2C_\Sigma$, where C_Σ is the total capacitance of its island. Nominally, the CPT has two dimensionless control parameters: the gate charge $n_g = C_g V_g / e$ and the superconducting phase difference $\phi = \int v dt/\varphi_0$, where v is the voltage across the transistor and $\varphi_0 = \hbar/2e$. The energy spectrum of the CPT is that of a CPB with effective Josephson energy $2E\ |\cos(\phi/2)|$. In the ground state with energy $E_0(n_g,\phi)$, the electrical potential of the island with respect to ground (see Fig. 1) is $V_I(n_g,\phi) = (1/e)\partial E_0/\partial n_g$, and the supercurrent through the CPT is $I(n_g,\phi) = (1/\varphi_0)\partial E_0/\partial\phi$. These quantities are both $2e$ periodic in n_g and 2π periodic in ϕ.

The CPT can be seen as an effective Josephson junction whose critical current $I_c(n_g) = \mathrm{Max}_\phi[I(n_g,\phi)]$ is periodically modulated by the gate charge, and whose current-phase relation $I = I_c(n_g) f(n_g,\phi)$ is not strictly sinusoidal. This charge-induced variation of I is used for electrometry. It can be characterized by the dimensionless "gains" $g(n_g,\phi) = \partial\ln(I)/\partial n_g$ and $g_0(n_g) = \partial\ln(I_c)/\partial n_g$. These gains are maximal close to $n_g = 1[\mathrm{mod}\,2]$. The optimal sensitivity is obtained when $E_c \approx E_J$, with a gate modulation of I_c larger than 50% and $g_0 \approx 2$.

The CPT is a transducer obeying the reciprocity relation linking the phase dependence of the island potential and the gate charge dependence of the current:

$$\frac{\partial V_I}{\partial\phi} = \frac{R_k}{4\pi}\frac{\partial I}{\partial n_g}, \tag{2}$$

where $R_k = h/e^2$ is the resistance quantum.

In order to turn this transducer into an electrometer, it has to be embedded in a circuit which will perform a measurement of the supercurrent I. In a previous experiment, the CPT was voltage biased with a small shunt resistor, and the supercurrent measured with a SQUID array amplifier[8]. For this scheme, the sensitivity was limited by the SQUID amplifier to about $3.\ 10^{-4}$ e/Hz$^{1/2}$, within a 10 MHz bandwidth. In the present experiment, we use a current-biasing scheme like in conventional measurement setups,

for which the zero-voltage branch of the characteristics is metastable. The working principle of our electrometer is to determine the gate dependent current required to induce the switching transition out of the zero-voltage state, during a given measuring time and with a given probability.

2.3 Switching of the CPT during a Current Pulse

Like in the case of a Josephson junction, the dynamics of the phase across a current-biased CPT is that of a particle in a tilted washboard potential, and subject to friction due to the impedance across the transistor. The mass of the particle and its velocity are proportional to the capacitance and the voltage, respectively. At $s(n_g) = I_b / I_c(n_g) < 1$, the potential has metastable minima from which the particle escapes by thermal activation. Note that here, an escape event does not always trigger the switching to the voltage state. The key point is that dissipation, which governs whether the particle will be retrapped in the next well or not, depends here strongly on the velocity. Switching occurs when the particle reaches a critical velocity which is determined by the difference between the actual tilt $s(n_g)$ and a critical tilt $s_{\max} < 1$: This process corresponds to an activation above a "dissipation barrier"[13] as the greater the dissipation, the greater $s_{\max}$ is. We introduce the switching rate $\Gamma[s(n_g), s_{\max}]$ which depends on the impedance and temperature.

The measurement of Γ at a given tilt is performed directly by applying a square bias-current pulse with amplitude $s(n_g)$ and duration t_{meas}. The probability that the system switches to the voltage-state is $p[s(n_g), s_{\max}, t_{meas}] = 1 - \exp[-\Gamma t_{meas}]$. We operate the device with I_b and n_g chosen such that $p[s(n_{g0}), s_{\max}, t_{meas}] = 0.5$. We exploit the steepness of p with respect to n_g: Depending whether n_g is above or below n_{g0}, the device will essentially switch or not. The CPT is thus here a threshold charge detector.

2.4 Theoretical Sensitivity

The charge resolution defined as $\Delta n_g(t_{meas}) = (dp / dn_g)^{-1}_{n_{g0}}$ is given by:

$$\Delta n_g(t_{meas}) = \frac{2}{\ln 2} \frac{1}{g_0(n_{g0})} \frac{1}{s(n_{g0}) \partial \ln(\Gamma) / \partial s}. \qquad (3)$$

We estimate the associated error probability $er = p(n_{g0} - \Delta n_g / 2)$ to be 0.15. Note that the resolution Δn_g does not improve with the measurement time as $\sqrt{t_{meas}}$, like in the case of linear amplifiers. Nevertheless, for the sake of comparison, one can define an equivalent sensitivity as the input noise spectral density $S_{n_g} = 0.47\,\Delta n_g{}^2\, t_{meas}$ of a linear amplifier, which would result in the same error probability for the same measuring time.

Optimizing the CPT sensitivity requires maximizing $s(n_{g0})\partial \ln(\Gamma)/\partial s$. In a previous work[13], we have shown that both the reduced switching current s and the logarithmic derivative $\partial \ln(\Gamma)/\partial s$ of a small effective Josephson junction can be maximized by damping the dynamics of the phase at ac frequencies with an RC circuit in parallel with the junction, as shown in Fig. 2. The charge resolution can be as small as desired by increasing the damping, but this gain is done at the expense of increased measuring time and back-action.

2.5 Numerical Simulations

In the case of a small Josephson junction, the switching rate Γ is analytically calculable in some limit cases, and approximate expressions are available[13,14]. In the case of the CPT, one has to rely on numerical simulations of the system dynamics to determine the sensitivity. The dynamics of the phase across the CPT is governed by the system of Langevin equations[13]:

$$\begin{cases} \dot{\phi} = u_L = u + \alpha\,\dot{u} + \eta \\ s - f(n_g, \phi) = \alpha\left(\dot{u} + \varepsilon\,\dot{u}_L\right) \end{cases}, \tag{4}$$

where u and u_L are the voltages across C and C_L in units of RI_c, $\alpha = R^2 C I_c / \varphi_0$ and $\varepsilon = C_L / C$; $\dot{x}$ denotes the derivative of x with respect to the reduced time $\tau = RI_c t / \varphi_0$, and η is the reduced Johnson voltage noise across resistor R, which verifies $\langle \eta(0)\eta(\tau)\rangle = (2k_B T / \varphi_0 I_c)\delta(\tau)$. We have numerically integrated Eqs. (4) for bias-current linear ramps and square pulses. In the case of a linear ramp, s is increased starting from a small value until u exceeds a threshold value u_{th}, the last s defining the reduced switching current I_s / I_c. In the case of a pulse, s is kept constant and the system is considered as having switched if u exceeds u_{th} before the end of the pulse. The result of these numerical experiments does not depend on the exact value chosen for

u_{th} since the acceleration during the switching is very fast. The simulation determines the average switching current $\langle I_s \rangle$ for linear ramps, or directly the switching probability for bias-current pulses.

3. EXPERIMENT

3.1 Experimental Setup

We have fabricated a CPT on a thermally oxidized Si chip using 3-angle evaporation through a shadow mask[15]. The two first layers form the aluminum CPT, and the third layer forms the gold connecting leads. These non-superconducting leads provide dumps for out-of-equilibrium quasiparticles present in the superconducting electrodes. The leads, with estimated total parasitic capacitance to ground $C_L \approx 0.75\,\mathrm{pF}$, are wire-bonded to a printed circuit board. Surface mounted components implementing the AC shunt ($R = 400\Omega$ and $C = 180pF$) of Fig. 2 are fitted onto this PCB. The CPT junctions have an area of 70x90 nm^2, the asymmetry being smaller than 10%. The circuit was mounted in a shielded box fitted with SMA coaxial connectors. The bias, gate and measuring lines ending at these connectors were carefully filtered with copper powder and microfabricated RC filters[16]. The sample was current biased through a 100 kΩ resistor placed on the PCB, and its voltage was measured using a room temperature low noise amplifier. The gap voltage of the aluminum electrodes $\Delta = 170 \pm 5\,\mu eV$, and the total CPT tunnel resistance $2R_T = 15.3 \pm 0.1 k\Omega$ were deduced from large-scale I-V characteristics. The Josephson energy $E_J = 0.82\,k_B.K$ of each junction was calculated from the Ambegaokar-Baratoff's relation assuming no asymmetry between the junctions.

3.2 Input and Output Signals

An arbitrary waveform voltage source was connected to the bias-current line. The frequency dependent transmission of the bias-current line was carefully calibrated, and the pulses were adjusted so as to provide a shape of the bias-current pulse as close as possible to a square wave. Figure 2 shows the bias-current pulses resulting from this adjustment. Switching always occurs when the bias-current is within to 10% of the maximum value I_P, and we can take $t_{meas} = 1 - 2\,\mu s$. Figure 2 also shows the time evolution of the voltage V for events where the CPT switches or does not. The observed

voltage rise is well explained by the total capacitance of the measuring line including filters (represented by F in Fig. 1b), which is about 0.8 nF. The threshold voltage (see dashed line on Fig. 2) used to discriminate a switching event from a non-switching one was chosen sufficiently larger than the voltage noise to avoid false switching events while minimizing heating. The pulses were repeated with a frequency of 40 kHz, which corresponds to a duty cycle of 2/25.

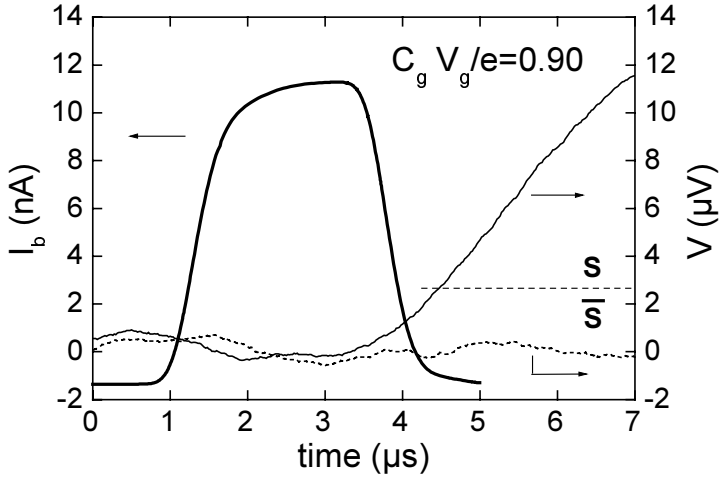

Figure 2. Bias-current pulse applied to the CPT, and voltage at the input of the amplifier for events where the transistor switches (solid line) or does not (dotted line). The dashed line indicates the threshold voltage used to discriminate the two types of events.

3.3 Gate Modulation

The gate modulation of the switching current was first measured by the standard bias-current ramp technique[17]. An experimental modulation pattern $\langle I_s \rangle(n_g)$ is shown in Fig. 3, together with the predicted critical current $I_c(n_g)$, and the corresponding $\langle I \rangle(n_g)$ curve determined by simulation. The single fitting parameter is $E_c = 1.12 k_B K$, for which the experimental and simulated $\langle I_s \rangle$ coincide at $n_g = 0$ (a renormalization of the bare Josephson energy[18] up to $E_J^* = 0.96\, k_B K$ by charging effects has been taken into account). The E_c value agrees with the capacitance estimated from scanning electron micrographs. The experimental and simulated modulation curves agree quantitatively except in a narrow region around $n_g = 1$, where the simulated $< I_s >$ is 17 % lower than the experimental one. This discrepancy is not fully understood yet.

For measurements using the pulse technique, a digital feedback loop was used to vary the peak value I_P of the pulses to maintain the switching probability at 50%. The resulting gate modulation $I_P(n_g, p = 0.5)$ is also shown on Fig. 3.

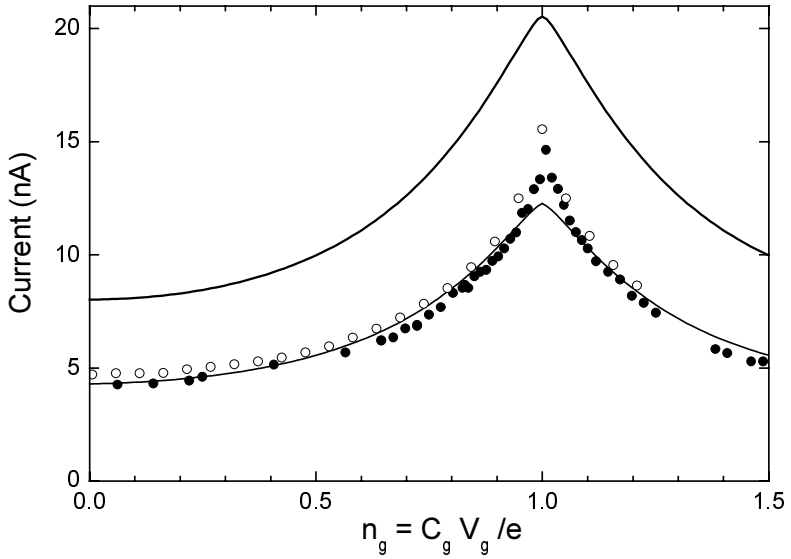

Figure 3. Gate modulation of the supercurrent of a CPT with E_c=1.12 k_BK and E_J* = 0.96 k_BK. Solid symbols: average switching current measured at T = 45 mK by the ramp technique with dI_b/dt = 87 pA/µs and 14000 events per data point; bottom curve: average switching current predicted from numerical simulations for the same parameters. Open symbols: Current pulse height I_p resulting at 20 mK in a 50% switching probability for pulses with the same duration as that shown in Fig. 2, and 5000 events per point. Top curve: Theoretical critical current I_c.

3.4 Sensitivity

Experimental and simulated $p(n_g)$ curves obtained for different I_P corresponding to n_{g0} values close to 1, for which the sensitivity is maximal, are shown in Fig. 4. The best experimental sensitivity was obtained at $n_g = 0.97$ with $I_P = 13.5\,nA$ (triangles on Fig. 4). In these conditions, according to the definitions of section 2.3, $\Delta n_g = 0.021$ and $S_{n_g}{}^{1/2} \approx 2.10^{-5}\, e\,/\,\mathrm{Hz}^{1/2}$. Apart from a slight offset, the numerical simulation well reproduces the experimental curve $p(n_g)$ at $I_P = 11.7\,\mathrm{nA}$. This shows that the sensitivity of the device is indeed limited by thermally activated switching and not by noise. The achieved sensitivity is not the ultimate value, and can still be improved by

increasing the damping. A gain in sensitivity by a factor 5 could be reached by implementing the RC shunt directly on chip, so that the parasitic capacitance C_L is almost suppressed (simulation not shown). However, for the purpose of qubit readout, sensitivity and back-action have to be optimized jointly. When back-action is taken into account, the capacitor C_L is found necessary, as shown in the following section.

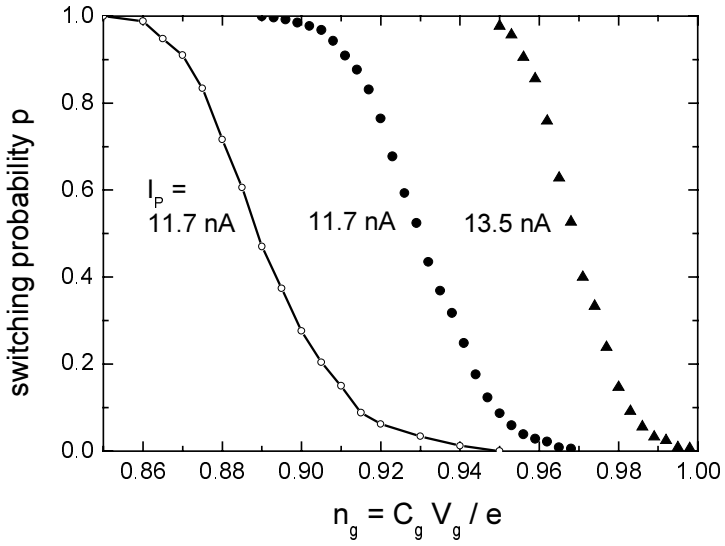

Figure 4. Experimental (solid symbols) and numerically simulated (open symbols) gate variation of the switching probability obtained with bias-current pulses as shown in Fig. 2. Peak currents are indicated for each data set. Each point is the result of an average over 500 (simulation) or 5000 (experiment) pulses. The steepest experimental gate variation (triangles) is obtained around n_g=0.97 and leads to an experimental charge sensitivity of 2.10^{-5} e/Hz$^{1/2}$.

In order to measure a CPB, the transistor island has to be connected to the box island by a coupling capacitor C_c (see Fig.1). The charge difference which has to be discriminated corresponds to $\kappa_1 \Delta n_{01}(\theta)$, where $\kappa_1 = C_c / C_\Sigma$ is the coupling factor between the CPT and the CPB. The condition for a single shot readout, i.e. readout with an error probability lower than our standard 15% (see above), is thus:

$$\kappa_1 \;>\; \kappa_{1\,\min} \;=\; \Delta n_g(t_{meas}) / 2\cos\theta \;. \qquad (5)$$

For instance, a coupling κ_1 of 2% would be enough to measure a CPB with $\theta = \pi/4$ with one 2µs long pulse.

4. Back-action onto a Charge Qubit

A readout amplifier induces decoherence of the measured qubit. In the case where an explicit Hamiltonian of the system {qubit + readout} can be handled, this phenomenon can be described by computing the time evolution of the density matrix[19]. However, in the case of a CPB coupled to an electrometer, it is possible to follow a simpler approach. When the temperature is above 10 mK, it can be shown[8] that decoherence is dominated only by dephasing induced by the thermal noise of its environment. Moreover, when the qubit environment is at low temperature, relaxation of the qubit from its excited state is much more probable than the opposite excitation[8]. The back-action of the readout is thus characterized by only 4 characteristic times T_φ^{OFF}, T_1^{OFF}, T_φ^{ON}, and T_1^{ON} describing dephasing and relaxation, in the OFF and ON states of the readout, respectively. These times have to fulfill several requirements for qubit manipulation and readout. Both T_φ^O and T_1^O should be long enough to allow coherent evolution prior to measurement, and T_1^{ON} should be longer than the measuring time t_{meas}, so that the information is not lost before the measurement is completed. The value of T_φ^{ON} is less important since quantum mechanics imposes anyway full decoherence in a projective measurement. The comparison of T_φ^{ON} with t_{meas} provides nevertheless an estimate of the readout ideality.

4.1 Dephasing due to Readout Back-action Noise

In the same way as the CPB island potential acts on the CPT supercurrent, the electrical potential $V_I(n\ ,\phi)$ of the CPT island reacts on the CPB as a perturbing gate charge. Due to the Johnson noise in the resistor R, the phase ϕ across the CPT fluctuates according to Eqs. (4), and the CPT converts this phase fluctuation into a fluctuation δV_I of its island potential. The box gate charge fluctuates by $\delta n_g^{box} = \kappa_2 \delta v_I$, where $\kappa_2 = C_c / C_\Sigma^{box}$ and $\delta v_I = C_\Sigma \delta V_I / e$, inducing fluctuations of the CPB transition frequency. A coherent superposition of qubit states would thus accumulate a random phase at a rate $d\Delta\varphi / dt = A\,\delta v_I$, with $A = 4\kappa_2 E_c^{box} \cos\theta / \hbar$. If the fluctuating voltage δv_I is gaussian, the coherence factor $\left\langle e^{i\Delta\varphi(t)} \right\rangle$ at time t is given by:

$$\left\langle \mathrm{e}^{i\Delta\varphi(t)} \right\rangle = \mathrm{e}^{-\frac{\left\langle \Delta\varphi(t)^2 \right\rangle}{2}},$$

$$\text{with } \left\langle \Delta\varphi(t)^2 \right\rangle = A^2\, \mathrm{t}^2 \int_0^\infty \mathrm{S}_{v_I}(\omega)\, \mathrm{sinc}^2(\omega t/2)\, d\omega\,. \tag{6}$$

Here, $\mathrm{S}_{v_I}(\omega)$ is the spectral density* of the CPT island voltage fluctuations. The time dependence of the coherence factor is exponential at long times only when the spectral density is constant below some characteristic frequency ω_c. At times longer than ω_c^{-1}, the dephasing time T_φ^{ON} is given by:

$$T_\varphi^{ON} = \frac{2}{\pi A^2 S_{v_I}(\omega = 0)}. \tag{7}$$

When the readout is OFF ($I_b << I_P$), the phase ϕ fluctuates in the vicinity of one of the minima of the washboard potential, located at $\phi_0 = \arcsin I_b / I_c \ [\mathrm{mod}\, 2\pi]$, and Eqs. (4) can be linearized around ϕ_0. Using Eq. (2), one obtains for the spectral density:

$$S_{v_I}{}^{OFF}(\omega) \approx \frac{2}{\pi}\left(\frac{\hbar}{4E_c}\frac{g}{l}\right)^2 \frac{k_B T}{\mathrm{R}\, e^2} \frac{1}{1+\dfrac{1}{(RC\omega)^2}}\ , \tag{8}$$

where $l = \partial \ln(f)/\partial\phi$. Using Eq. (6), one gets:

$$\frac{\left\langle \Delta\varphi(t)^2 \right\rangle^{OFF}}{2} = \frac{t}{\tau_\varphi{}^{OFF}} \frac{1-\mathrm{e}^{-t/RC}}{t/RC}, \tag{9}$$

where

$$\tau_\varphi{}^{OFF\ -1} = \left(\kappa_2 \cos\theta \frac{E_c^{box}}{E_c}\frac{g}{l}\right)^2 \frac{k_B T}{Re^2}\ . \tag{10}$$

Since the spectral density is zero at zero frequency, decoherence stays finite. The coherence factor thus saturates at a value $\left\langle e^{i\Delta\varphi(t)} \right\rangle = e^{-RC/\tau_\varphi^{OFF}}$ for times longer than *RC*. For the parameters we consider, $RC << \tau_\varphi^{OFF}$. Dephasing due to the CPT in the OFF state is thus negligible.

When the readout is ON, the excursions of the phase ϕ are no longer bounded. The spectral density $\mathrm{S}_{v_I}(\omega)$ can be obtained from simulations, using the constitutive relation $V_I(n_g, \phi)$. It is constant at low frequency, which leads to an exponential decay for the coherence factor with a time constant $T_\varphi{}^{ON}$.

* We use here only "engineer" spectral densities corresponding to the power density at a positive pulsation.

Table 1 treats the case of a CPB with $E_J^{box} = E_c^{box} = 0.5 k_B K$, coupled to the readout with $\kappa_2 \approx \kappa_{1\,\min}/2 = 1\%$ and displays T_φ^{ON} and t_{meas} calculated from Eqs. (9)-(10). Since $t_{meas}/T_\varphi^{ON} \sim 20$, the readout is far from reaching the ideal quantum measurement limit. Although we have only considered here the contribution of the CPT to dephasing, one should not forget that the dominant dephasing source in the CPB is the offset charge noise, which is due to the random motion of charges at the microscopic level.

Table 1. Estimated coherence time T_φ and relaxation time T_1 of a CPB ($E \quad = E \quad = 0.5k\ K$) if it were coupled to the readout of our experiment with $\kappa_2 \approx 1\%$. Decoherence sources other than the readout have not been considered. Operating conditions are indicated on the first line. The measurement time t_{meas} is given for comparison.

	OFF State		**ON State**
	$s = 0$ $\theta = \pi/2$	$s = 0.5$ $\theta = \pi/4$	$s = I_P/I_C \approx 0.7$ $\theta = \pi/4$
T_φ	∞	non-exponential decay $\tau_\varphi \sim 500$ µs (see text)	~ 100 ns
T_1	∞	~ 200 ms	~ 60 µs
t_{meas}	-	-	< 2 µs

4.2 Relaxation

We now discuss the relaxation of the CPB from $|qb1\rangle$ towards $|qb0\rangle$ at low temperature, accompanied by an energy transfer $\hbar\Omega$ into an electromagnetic mode Ω of the circuit. We assume here that the bandgap of the CPT is sufficiently higher than $\Omega/2\pi$, so that it stays in its ground state, and can be treated adiabatically. Within this framework, the CPT and its bias circuitry are equivalent to an effective impedance $Z_{eff}(\omega)$ connected to the CPB island. This impedance is given by:

$$Z_{eff}(\omega) = \frac{1}{jC_c\omega}\left(1 - \frac{\kappa_1}{2E_C}\left(\frac{\partial^2 E_0}{\partial n_g^2} - \frac{\varphi_0 g^2 I}{l}\frac{1}{1 + \frac{j\omega\varphi_0 Y(\omega)}{l\,I}}\right)\right)^{-1}, \qquad (11)$$

where $Y(\omega)$ is the admittance in parallel with the CPT. The relaxation rate is then obtained from $Z_{eff}(\omega)$ using Fermi's golden rule:

$$\Gamma_1 = 4\pi\,\Omega\sin^2\theta\,\kappa_2^{\,2}\,\frac{\mathrm{Re}\left[Z_{eff}(\Omega)\right]}{R_k}. \qquad (12)$$

At $\phi = 0$, $g = 0$, $\mathrm{Re}\left[Z_{eff}(\Omega)\right] = 0$, and no relaxation occurs at the lowest order. At $\phi \neq 0$, and for the external admittance $Y(\omega) = iC_L\omega + (iC\omega + R^{-1})^{-1}$ we consider, one has:

$$\frac{\mathrm{Re}[Z_{eff}(\Omega)]}{R_K} = \frac{R_K}{R}\left(\frac{g}{4\pi\,l}\right)^2 \frac{1}{\left[\left(\frac{\Omega}{\omega_{c1}}\right)^2 - 1\right]^2 + \left[\frac{\Omega}{\omega_{c1}}\right]^2}, \qquad (13)$$

where $\omega_{c1} = \sqrt{\frac{\partial I/\partial\phi}{\varphi_0\,C_L}}$ and $\omega_{c2} = R\frac{\partial I/\partial\phi}{\varphi_0}$ are cutoff angular frequencies of the system.

These expressions give an instantaneous rate depending on ϕ and n_g. They can be used directly to obtain the relaxation time $T_1(\phi) = 1/\Gamma_1$ when the readout is OFF, when the phase excursions are small. When the readout is ON, the system experiences a variable relaxation rate as the phase ϕ turns but an average can be performed, assuming equiprobability of ϕ. The resulting T_1^{ON} is displayed in Table 1 and verifies $T_1^{ON}/t_{meas} \sim 30$, what is compatible with a non-destructive measurement of the CPB. We have found that this relaxation time depends strongly on the external admittance. In particular, the capacitor $C_L = 0.75\,\mathrm{pF}$ provides a high frequency shunt that diminishes relaxation by a factor of about 10^3. An improved design of the microwave impedance would probably allow a better sensitivity while keeping the relaxation time T_1^{ON} longer than t_{meas}.

5. CONCLUSION

We have fabricated and operated a new threshold charge detector based on the Cooper pair transistor. The best equivalent sensitivity we have obtained is 2.10^{-5} e/Hz$^{1/2}$ in a 1MHz bandwidth. This detector, which is of the latching type and only requires simple room temperature electronics, could provide an efficient readout for a charge qubit. We have shown that, by proper engineering of the impedance in parallel with the Cooper pair transistor, this system meets the criteria for qubit operation and readout: dephasing and relaxation are negligible prior to readout, and relaxation during readout is small enough to allow discrimination of qubit states with signal to noise ratio of order 1.

6. REFERENCES

1. M. Nielsen and I. Chuang, *Quantum Computation and Quantum Information* (Cambridge University Press, Cambridge, 2000).
2. V. Bouchiat et al, *Physica-Scripta*, **76**, 165 (1998).
3. Siyuan-Han, R. Rouse, and J.E. Lukens, *Phys. Rev. Lett.*, **84**, 1300 (2000).
4. C.H. van der Wal et al., *Science*, **290**, 773 (2000).
5. Y. Nakamura, Y.A. Pashkin, and J.S. Tsai, *Nature*, **398**, 786 (1999) ; *Physica-B* **280**, 405(2000).
6. R.J. Schoelkopf et al., *Science*, **280**, 1238 (1998).
7. A. Aassime et al, *Phys. Rev. Lett.*, **86**, 15 (2001).
8. A. Cottet et al, in : *Macroscopic Quantum Coherence and Quantum Computing*, edited by D. Averin, B.Ruggiero, and P. Silvestrini (Kluwer Academic/Plenum Publisher , New York 2001), pp 111-125.
9. A.B. Zorin in this book.
10. T.A. Fulton and G.J. Dolan, *Phys. Rev. Lett.*, **59**, 109 (1987).
11. P. Joyez et al, *Phys. Rev. Lett.*, **72**, 2548 (1994).
12. A. B. Zorin, *Phys. Rev. Lett.*, **76**, 4408 (1996).
13. D. Vion et al, *Phys. Rev. Lett.*, **77**, 3435 (1996) ; P. Joyez et al, *J. of Superconductivity.* 12, 757 (1999).
14. The theoretical sensitivity corresponding to very short current square pulses above $s_{\max}$ will be published elsewhere.
15. G.J. Dolan and J.H. Dunsmuir, *Physica B*, **152**, 7 (1988).
16. D. Vion et al, *J. Appl. Phys.*, **77**, 2519 (1995).
17. T.A. Fulton and L.N. Dunkleberger, *Phys. Rev. B*, **9**, 4760 (1974).
18. P. Joyez, *Thesis*, Paris VI University, (1995).
19. A. Schnirman and G. Schön, *Phys Rev.*, *B* **57**, 15400 (1998).

Chapter 3

Decoherence in Cooper pair boxes

This chapter is devoted to the analysis of decoherence mechanisms in Cooper pair box devices. We first consider a Cooper pair box embedded in an electromagnetic circuit at thermal equilibrium, a case which can be mapped on the spin-boson problem. Then, we consider the decoherence due to the back-action of a measuring apparatus on the Cooper pair box, stressing the importance of the absence of dephasing when the measuring apparatus is off, and the absence of relaxation when the measuring apparatus is on. We also estimate the dephasing due to the charge-noise acting on the box island, and show that this decoherence mechanism severely limits quantum coherence in the Cooper pair box. We provide numerical estimates of the decoherence rate in the Cooper pair box for the different setups considered in this thesis.

The quantum coherence of a Cooper pair box is limited by its interactions with the degrees of freedom of its environment, including the measuring circuit [68, 69, 70]. Although these interactions yield in principle to a complex entanglement between the box and the external degrees of freedom, their effect on the box can be described in simple terms in the weak coupling regime[1]. As described in Fig.3.1, interactions induce in this case dephasing, relaxation and excitation of the box [71]. Dephasing processes randomly modify the relative phase between the components of a superposition of the box states $|0\rangle$ and $|1\rangle$, whereas relaxation and excitation, which can be grouped under the more general term of depolarisation, describe respectively downward and upward transitions of the box. As it will be shown, the dephasing, relaxation and excitation rates depend on the generalised spectral density of the external field coupled to the box.

The environment of the box includes different types of degrees of freedom. At the microscopic level, the box is subject to the charge noise induced by randomly moving charges in the insulating material close to the island [20]. This noise mainly induces dephasing because its spectral density is peaked at low frequency. In the case of the split box, moving vortices in

[1] A more global calculation of decoherence, based on diagramatic techniques, has been performed by A. Shnirman and G. Schön in the case of a Cooper pair box coupled to a single electron transistor [72].

the superconducting films may also result in flux-noise which also induces dephasing. The degrees of freedom involved in these charge and flux noise sources cannot be assumed at thermal equilibrium.

At the macroscopic level, the box is coupled to the electromagnetic degrees of freedom of the biasing circuit, and to the measuring system. When the measuring system is turned off, and if all lines are properly filtered down to the sample temperature, the whole external circuit can be treated as a collection of electromagnetic modes in thermal equilibrium with the sample. In this case, the generic model of a two-level system linearly coupled to a bosonic bath can be used to describe the interaction between the box and these modes.

When the measuring system is turned on, its back-action induces dephasing, relaxation and excitation. Whereas dephasing is needed for performing the measurement, relaxation and excitation are detrimental effects which have to be kept at a low enough level. In this respect, different measuring strategies can lead to very different decoherence processes. Those which allow to control separately dephasing and depolarisation have a clear advantage.

In this chapter, we discuss the general case of a box linearly coupled to a source of decoherence, before evaluating decoherence in different possible setups.

3.1 Generic model of a Cooper pair box linearly coupled to a noise source

In the absence of decoherence sources, the effective field $\overrightarrow{h}$ seen by a (split) Cooper pair box is determined by the control parameters n_g (and δ), generically called here λ. The "free" hamiltonian of the box writes:

$$\widehat{H} = -\frac{1}{2}\overrightarrow{\sigma} \cdot \overrightarrow{h}(\lambda) \ , \tag{3.1}$$

with $\overrightarrow{h}$ the "free" field seen by box. When a noise source is coupled to the box, the parameter λ is shifted by a quantity $\widehat{\Delta\lambda}$. In the linear coupling approximation, the coupling hamiltonian between the box and the noise source writes:

$$\widehat{H}_c = -\frac{1}{2}\left(\overrightarrow{\sigma} \cdot \overrightarrow{D}_\lambda\right)\widehat{\Delta\lambda} \ , \tag{3.2}$$

where $\overrightarrow{D}_\lambda$ is the representative vector of the restriction of $\partial\widehat{H}/\partial\lambda$ to the subspace $\{|0\rangle, |1\rangle\}$. (Beware that $\overrightarrow{D}_\lambda$ can be obtained from the derivative of the vector $\overrightarrow{h}$ with respect to λ only in the case $E_J \ll E_C$) . Dephasing can be attributed to the $\widehat{\sigma}_z$ component of $\widehat{H}_c$. It can be treated in two different ways, depending on whether the noise source can be considered as classical or quantum. Depolarisation is due to the $\widehat{\sigma}_x$ and $\widehat{\sigma}_y$ components of $\widehat{H}_c$, and must be treated quantically.

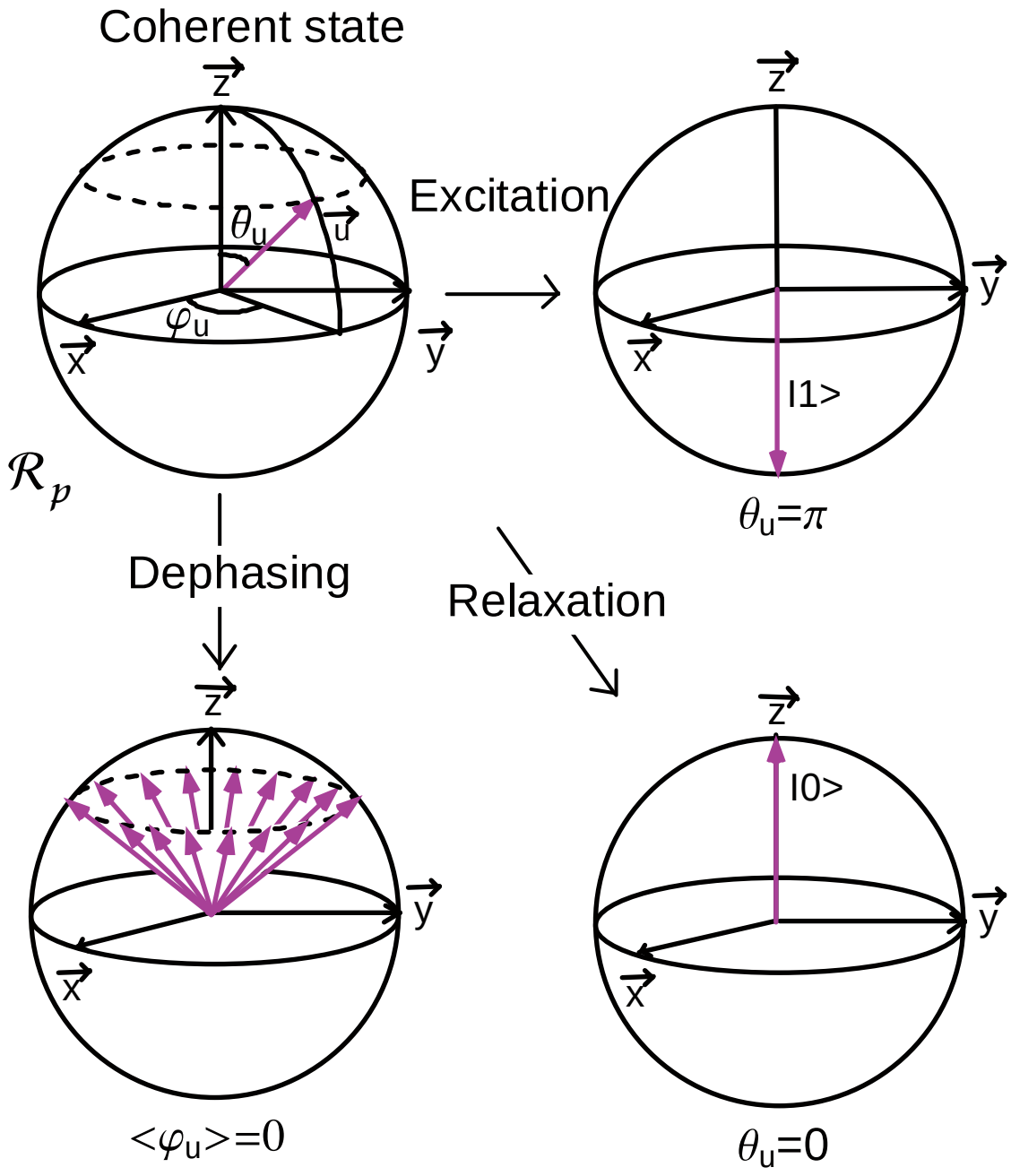

Figure 3.1: *For a two level system in the weak coupling regime, the decoherence of an initially coherent state (top left) can be decomposed into three different processes, dephasing, relaxation and excitation. In the rotating Bloch sphere frame* $\mathcal{R}_p$ (see 1.3.2)*, dephasing corresponds to a diffusion of the representative vector* $\vec{u}$ *of the two level system around the direction* $\vec{z}$ *of its free hamiltonian representative vector (bottom left). Relaxation corresponds to a transition to* $\vec{z}$ *(bottom right panel), and excitation to a transition to* $-\vec{z}$ *(top right).*

3.1.1 Dephasing due to a noise source treated classically

A first simple approach of dephasing consists in considering $\widehat{\Delta\lambda}$ as a classical noise $\Delta\lambda(t)$ [68]. Within this approximation, dephasing can be seen as the diffusion of the representative vector $\overrightarrow{u}$ of the box state due to the fluctuating field $\overrightarrow{D}_\lambda \Delta\lambda$. Let us consider that at $t = 0$, the box is prepared in the pure initial state i:

$$|u(t=0)\rangle = \cos\left(\frac{\theta_u^i}{2}\right)\exp\left(-\mathbf{i}\frac{\varphi_u^i}{2}\right)|0\rangle + \sin\left(\frac{\theta_u^i}{2}\right)\exp\left(\mathbf{i}\frac{\varphi_u^i}{2}\right)|1\rangle \ . \tag{3.3}$$

The box state thus evolves as:

$$|u(t)\rangle = \cos\left(\frac{\theta_u^i}{2}\right)\exp\left(-\mathbf{i}\frac{\varphi_u(t)}{2}\right)|0\rangle + \sin\left(\frac{\theta_u^i}{2}\right)\exp\left(\mathbf{i}\frac{\varphi_u(t)}{2}\right)|1\rangle \ , \tag{3.4}$$

where:

$$\varphi_u(t) = \varphi_u^i + \Omega_{01}\, t + \Delta\varphi_u(t) \ . \tag{3.5}$$

The phase term $\Omega_{01}\, t$ arises from the free field $\overrightarrow{h}(\lambda)$. The random phase shift

$$\Delta\varphi_u(t) = \frac{1}{\hbar} D_{\lambda,z} \int_0^t \Delta\lambda(t')dt' \ , \tag{3.6}$$

with

$$D_{\lambda,z} = \overrightarrow{D}_\lambda . \overrightarrow{z} \ ,$$

is due to the fluctuating field $\overrightarrow{D}_\lambda \Delta\lambda$. One can introduce the dephasing factor

$$f_\varphi(t) = \langle \cos\left[\Delta\varphi_u(t)\right]\rangle \ , \tag{3.7}$$

where $\langle\ \rangle$ is a statistical ensemble average. It ranges from 1 when the box is perfectly coherent to 0 when dephasing is complete. When $\Delta\varphi_u(t)$ is close to a gaussian signal, $f_\varphi(t)$ can be recast in the form

$$f_\varphi(t) = \exp(-\frac{\langle\Delta\varphi_u^2(t)\rangle}{2}) \ , \tag{3.8}$$

where $\langle\Delta\varphi_u^2(t)\rangle$ is the variance of the random phase. This variance is related to the classical noise power spectrum

$$S_\lambda^{cl}(\omega) = \frac{1}{2\pi}\int_{-\infty}^{+\infty} d\tau\, \langle\Delta\lambda(t)\Delta\lambda(t+\tau)\rangle \exp(-\mathbf{i}\omega\tau)$$

of the fluctuations of $\lambda(t)$ (definition (3.94) of Appendix 3-B):

$$\left\langle\Delta\varphi_u^2(t)\right\rangle = \left(\frac{tD_{\lambda,z}}{\hbar}\right)^2 \int_{-\infty}^{+\infty} d\omega\ S_\lambda^{cl}(\omega)\mathrm{sinc}^2(\frac{\omega t}{2}) \ . \tag{3.9}$$

Therefore, one has:

$$\boxed{f_\varphi(t) = \exp\left[-\tfrac{1}{2}\left(\tfrac{D_{\lambda,z}\ t}{\hbar}\right)^2 \int_{-\infty}^{+\infty} d\omega\ S_\lambda^{cl}(\omega)\ \mathrm{sinc}^2(\tfrac{\omega t}{2})\right] \ ,} \tag{3.10}$$

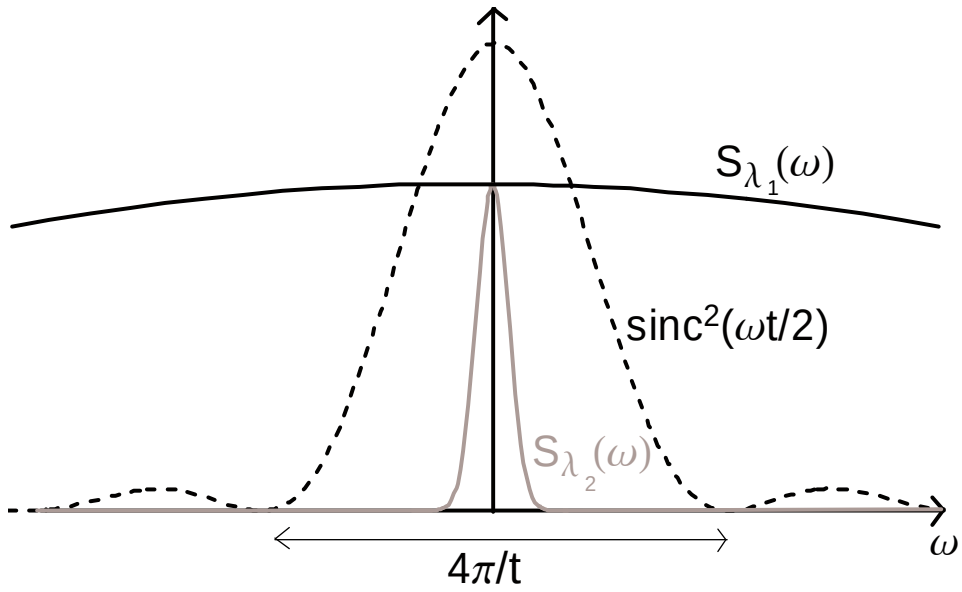

Figure 3.2: *The two limits of broad band (black line) and low frequency (grey line) noises for calculating at time t the dephasing induced by a classical noise source. The dotted curve is the function* $\mathrm{sinc}^2(\omega t/2)$.

Two limit cases can be made explicit (see Figure 3.2). First, when $S_\lambda^{cl}(\omega)$ is constant at frequencies lower than $1/t$, Formula (3.9) leads to the exponential decay law

$$f_\varphi(t) = \exp(-\Gamma_\varphi t) \tag{3.11}$$

at the rate

$$\boxed{\Gamma_\varphi = \pi \left(\frac{D_{\lambda,z}}{\hbar}\right)^2 S_\lambda^{cl}(\omega = 0)\ .} \tag{3.12}$$

Secondly, when $S_\lambda^{cl}(\omega)$ falls off on a range much smaller than $1/t$, the dephasing factor is gaussian:

$$f_\varphi(t) = \exp\left[-\frac{1}{2}\left(\frac{D_{\lambda,z}}{\hbar}\right)^2 t^2 S_\lambda^{tot}\right]\ , \tag{3.13}$$

with $S_\lambda^{tot} = \int_{-\infty}^{+\infty} d\omega\ S_\lambda^{cl}(\omega)$ the total noise power.

3.1.2 Dephasing and depolarisation within the spin-boson model

Coupling hamiltonian

A more rigorous approach of decoherence in the Cooper pair box consists in using the generic model of a two-level system coupled linearly to a bosonic bath, namely the spin-boson model [68, 69]. Here, we only consider the weak coupling regime, for which a direct approach is readily

implemented. One considers that the control parameter λ is shifted by a quantity linear in the bosonic operators:

$$\widehat{\Delta\lambda} = \sum_{p\in\mathbb{N}^*} \left(\mu_p^* \widehat{c}_p^+ + \mu_p \widehat{c}_p\right) \tag{3.14}$$

where $\widehat{c}_p$ and $\widehat{c}_p^+$ are the creation and annihilation operators associated to the bosonic mode p with hamiltonian:

$$\widehat{h}_p = \hbar\omega_p(\widehat{c}_p^+\widehat{c}_p + \frac{1}{2}) \ ,$$

with

$$\left[\widehat{c}_{p'}, \widehat{c}_p^+\right] = \delta_{p,p'} \ ,$$

and where $\mathbb{N}^* = \mathbb{N} - \{0\}$ is the space of the nonzero integers. In practice, the shift coefficient μ_p, which characterises the coupling between the spin and the bosonic mode p, depends on the physical system studied. The spin-boson model allows to evaluate both dephasing and depolarization processes.

Dephasing

The $\widehat{\sigma}_z$ component of $\widehat{H}_c$ is:

$$\widehat{H}_{c,z} = -\frac{1}{2}\left[\sum_{p\in\mathbb{N}^*} \left(\mu_p^* \widehat{c}_p^+ + \mu_p \widehat{c}_p\right)\right] D_{\lambda,z}\widehat{\sigma}_z \ .$$

The evolution operators $\widehat{U}$ and $\widehat{U}_p$ of the isolated spin and of the isolated oscillator p are

$$\begin{aligned} \widehat{U}(t) &= \exp(-\mathbf{i}\frac{\widehat{H}t}{\hbar}) \\ \widehat{U}_p(t) &= \exp(-\mathbf{i}\frac{\widehat{h}_p t}{\hbar}) \ . \end{aligned}$$

In the interaction representation, $\widehat{H}_{c,z}$ becomes

$$\widehat{H}_\varphi(t) = \left(\prod_{p\in\mathbb{N}^*} \widehat{U}_p^*(t)\right) \widehat{U}^*(t)\widehat{H}_{c,z}\widehat{U}(t) \left(\prod_{p\in\mathbb{N}^*} \widehat{U}_p(t)\right) = -\frac{1}{2}\widehat{\sigma}_z\widehat{h}_\varphi(t) \ , \tag{3.15}$$

with

$$\widehat{h}_\varphi(t) = D_{\lambda,z} \sum_{p\in\mathbb{N}^*} \left(\mu_p^*\widehat{c}_p^+ \exp(\mathbf{i}\omega_p t) + \mu_p \widehat{c}_p \exp(-\mathbf{i}\omega_p t)\right) \ . \tag{3.16}$$

The field $\widehat{h}_\varphi(t)$ induces a change $\widehat{\Delta\varphi_u}(t)$ of the phase φ_u:

$$\widehat{\Delta\varphi_u}(t) = -\frac{1}{\hbar}\int_0^t \widehat{h}_\varphi(t)dt \ . \tag{3.17}$$

More explicitly,

$$\widehat{\Delta\varphi_u}(t) = \frac{D_{\lambda,z}}{\mathbf{i}} \sum_{p\in\mathbb{N}^*} \left(\frac{1-\exp(\mathbf{i}\omega_p t)}{\hbar\omega_p} \mu_p^* \widehat{c}_p^+ - \frac{1-\exp(-\mathbf{i}\omega_p t)}{\hbar\omega_p} \mu_p \widehat{c}_p \right) . \tag{3.18}$$

The phase shift $\widehat{\Delta\varphi_u}(t)$ is now a quantum operator which describes the entanglement of the spin with the oscillators. The dephasing factor $f_\varphi(t)$ can be calculated by replacing the classical statistical average of formula (3.8) with a quantum statistical average on the state of the oscillators. The Glauber formula at finite temperature [73] allows to calculate the average value of any operator of the type $\exp\left[i\left(q_p\widehat{c}_p - q_p^*\widehat{c}_p^+\right)\right]$:

$$\left\langle \exp(i\left(q_p\widehat{c}_p - q_p^*\widehat{c}_p^+\right)\right\rangle = \exp\left[-\frac{1}{2}\left|q_p\right|^2 \coth(\frac{\hbar\omega_p}{2kT})\right] . \tag{3.19}$$

One thus obtains:

$$f_\varphi(t) = \exp\left[\left(\frac{D_{\lambda,z}}{\hbar}\right)^2 \mathrm{Re}\,\mathbf{J}(t)\right] . \tag{3.20}$$

where the function $\mathbf{J}(t)$ is the following sum over the oscillators:

$$\mathbf{J}(t) = \sum_{p\in\mathbb{N}^*} \frac{\left|\mu_p\right|^2}{\omega_p^2} \coth(\frac{\hbar\omega_p}{2kT}) \left[\exp(\mathbf{i}\omega_p t) - 1\right] . \tag{3.21}$$

This function is analogous to the function $J(t)$ introduced in the context of Coulomb blockade of tunneling [75]. It can be related to a physical quantity, the generalised noise spectrum $S_\lambda(\omega)$ of λ [see (3.101)]:

$$S_\lambda(\omega) = \frac{1}{2\pi}\int_{-\infty}^{+\infty} d\tau \left\langle \widehat{\Delta\lambda}(t)\widehat{\Delta\lambda}(t+\tau)\right\rangle \exp(-\mathbf{i}\omega\tau) \tag{3.22}$$

From (3.14), for a bath of harmonic oscillators, the generalised correlation function of $\widehat{\Delta\lambda}(t)$ writes [74]

$$\left\langle \widehat{\Delta\lambda}(t).\widehat{\Delta\lambda}(0)\right\rangle = \sum_{p\in\mathbb{N}^*} \left|\mu_p\right|^2 \left[\exp\left(+\mathbf{i}\omega_p t\right) n_{\omega_p} + \exp\left(-\mathbf{i}\omega_p t\right)\left(1+n_{\omega_p}\right)\right] , \tag{3.23}$$

where:

$$n_\omega = \frac{1}{\exp(\frac{\hbar\omega}{k_b T}) - 1} = \frac{1}{2}\left(\coth(\frac{\hbar\omega}{2kT}) - 1\right)$$

is the average quanta number in the mode ω . Using the definition (3.22) of the generalised noise spectrum, one obtains:

$$S_\lambda(\omega) = \sum_{p\in\mathbb{N}^*} \left|\mu_p\right|^2 \left[\left(1+n_{\omega_p}\right)\delta(\omega-\omega_p) + n_{\omega_p}\delta(\omega+\omega_p)\right] . \tag{3.24}$$

The odd and even parts of the spectrum are respectively:

$$S_\lambda^{even}(\omega) = \sum_{p\in\mathbb{N}^*} \frac{\left|\mu_p\right|^2}{2} \coth(\frac{\hbar\omega_p}{2kT}) \ \left[\delta(\omega-\omega_p) + \ \delta(\omega+\omega_p)\right] \tag{3.25}$$

and:

$$S_\lambda^{odd}(\omega) = \sum_{p\in\mathbb{N}^*} \frac{\left|\mu_p\right|^2}{2} \left[\delta(\omega-\omega_p) - \delta(\omega+\omega_p)\right] . \tag{3.26}$$

Using equations (3.21) and (3.25), the real part of $\mathbf{J}(t)$ can be written in the following forms:

$$\mathrm{Re}\,\mathbf{J}(t) = -\,t^2 \int_0^{+\infty} d\omega\; S_\lambda^{even}(\omega)\; \mathrm{sinc}^2(\frac{\omega t}{2}) = -\frac{1}{2}t^2 \int_{-\infty}^{+\infty} d\omega\; S_\lambda(\omega)\; \mathrm{sinc}^2(\frac{\omega t}{2}) . \tag{3.27}$$

The expression (3.20) can thus be written as

$$f_\varphi(t) = \exp\left[-\frac{1}{2}\left(\frac{D_{\lambda,z}\;t}{\hbar}\right)^2 \int_{-\infty}^{+\infty} d\omega\; S_\lambda(\omega)\; \mathrm{sinc}^2(\frac{\omega t}{2})\right] , \tag{3.28}$$

which takes the same form as the semi-classical prediction (3.10), but with the full quantum spectrum $S_\lambda(\omega)$ in place of the classical one. At long times, the integral entering in Expression (3.27) is dominated by the spectral density $S_\lambda(\omega)$ at low frequencies, for which the classical and quantum spectral densities are equal. In this regime, the quantum calculation and the semi-classical model thus predict the same decay, with an exponential tail $f_\varphi(t) = \exp\left[-\pi\,(D_{\lambda,z}/\hbar)^2\, S_\lambda(\omega=0)\; t\right]$, and the entanglement between the spin and the environment can be figured as a random dephasing of the spin due to low frequency fluctuations of its transition frequency. The quantum behavior only shows up in the zero temperature limit, for which the semi-classical model predicts no decay. It can be pictured as arising from the zero-point fluctuations of the oscillators.

Depolarisation

The $\widehat{\sigma}_x$ and $\widehat{\sigma}_y$ terms of $\widehat{H}_c$ couple the states $|1\rangle$ and $|0\rangle$ of the spin. Relaxation and excitation proceed by exchange of an energy $\hbar\Omega_{01}$ between the spin and the oscillator with pulsation $\omega_p = \Omega_{01}$. From the Fermi golden rule, the relaxation and excitation rates Γ_R and Γ_E of such processes are

$$\Gamma_R \;=\; \frac{\pi}{2}\left(\frac{D_{\lambda,\perp}}{\hbar}\right)^2 \; S_\lambda(\Omega_{01}), \tag{3.29}$$

$$\Gamma_E \;=\; \frac{\pi}{2}\left(\frac{D_{\lambda,\perp}}{\hbar}\right)^2 \; S_\lambda(-\,\Omega_{01}) . \tag{3.30}$$

where:

$$D_{\lambda,\perp} = \left\| \overrightarrow{D_\lambda} - D_{\lambda,z}\,\overrightarrow{z} \right\|$$

These rates verify the detailed balance:

$$\frac{\Gamma_E}{\Gamma_R} = \exp(-\frac{\hbar\Omega_{01}}{k_b T}) .$$

3.1.3 Case of a bosonic bath described by an impedance function

In the case where the bosonic bath coupled to a Cooper pair box consists of a dissipative impedance $Z(\omega)$, the expression (3.24) of the spectral density $S_\lambda(\omega)$ can always be related to the spectrum $S_{u_Z}(\omega)$ of the voltage fluctuations (3.102) across this impedance by a circuit-dependent transfer function $g(\omega)$ defined by the following relation :

$$S_\lambda(\omega) = g(\omega)\ S_{u_Z}(\omega)\ . \tag{3.31}$$

The transfer function $g(\omega)$ can also be found from the coupling coefficient μ_p:

$$g(\omega_p) = \frac{2\left|\mu_p\right|^2}{\hbar\omega_p^2\,\mathrm{Re}\left(Z(\omega_p)\right)}\ . \tag{3.32}$$

Note that the function $g(\omega)$ is even.

Dephasing

From the formula (3.102) of Appendix 3-B, the function $\mathrm{Re}\,\mathbf{J}(t)$ (3.27) can then be recast in the form:

$$\mathrm{Re}\,\mathbf{J}(t) = -\frac{\hbar}{4\pi}\ t^2 \int_{-\infty}^{+\infty} d\omega\ \omega\ g(\omega)\,\mathrm{Re}\left[Z(\omega)\right]\coth(\frac{\hbar\omega}{2kT})\ \mathrm{sinc}^2(\frac{\omega t}{2})\ . \tag{3.33}$$

The time dependence of $\mathrm{Re}\,\mathbf{J}(t)$ is not universal except in the semi-classical regime at long times. The cross-over between the quantum and semi-classical regimes can be determined when the function $\mathrm{Re}\,Z(\omega)g(\omega)$ is a lorentzian :

$$g(\omega)\,\mathrm{Re}\,Z(\omega) = \frac{R\ g_a}{(1+\omega^2 t_a^2)}\ , \tag{3.34}$$

with t_a a correlation time. The following approximation [76]

$$\mathrm{Re}\,\mathbf{J}(t) \simeq -\frac{\hbar R g_a}{\pi}\left(\gamma + \frac{t}{t_T} + \ln(\frac{t}{t_a})\right)$$

with

$$t_T = \frac{\hbar}{\pi k_b T} \tag{3.35}$$

yields to the result:

$$f_\varphi(t) \simeq \exp -\left[A\left(\gamma + \frac{t}{t_T}\right)\right]\left(\frac{t}{t_a}\right)^{-A}\ , \tag{3.36}$$

where $\gamma \simeq 0.577$ is the Euler constant, and A an exponent equal to:

$$A = \frac{D_{\lambda,z}^2\ R\ g_a}{\pi\hbar}\ .$$

When the factor A is small and the correlation time t_a larger than the thermal time t_T, the semi-classical regime applies at all times larger than t_a. The decay of $f_\varphi(t)$ is exponential with a rate (3.12) proportional to temperature:

$$\Gamma_\varphi = k_b T\ \left(\frac{D_{\lambda,z}}{\hbar}\right)^2 R\ g_a\ . \tag{3.37}$$

Depolarisation

Using (3.31) and (3.102), the expressions (3.29) and (3.30) can be written as:

$$\begin{aligned}\Gamma_R &= \tfrac{\hbar\Omega_{01}}{4}\left(\tfrac{D_{\lambda,\perp}}{\hbar}\right)^2 \mathrm{Re}\left[Z(\Omega_{01})\right] g(\Omega_{01})\left(1+\coth(\tfrac{\hbar\Omega_{01}}{2k_bT})\right) \ , \\ \Gamma_E &= \tfrac{\hbar\Omega_{01}}{4}\left(\tfrac{D_{\lambda,\perp}}{\hbar}\right)^2 \mathrm{Re}\left[Z(\Omega_{01})\right] g(\Omega_{01})\left(1-\coth(\tfrac{\hbar\Omega_{01}}{2k_bT})\right) \ .\end{aligned} \tag{3.38}$$

The total depolarisation rate is

$$\Gamma_1 = \frac{\hbar\Omega_{01}}{2}\left(\frac{D_{\lambda,\perp}}{\hbar}\right)^2 \mathrm{Re}\, Z(\Omega_{01})\ g(\Omega_{01}) \ .$$

3.1.4 Decoherence due to a measuring apparatus

Let us consider a measuring apparatus weakly coupled to the two level system and measuring the variable $\widehat{X} = \partial\widehat{H}/\partial\lambda$. The measuring apparatus induces fluctuations of λ with a spectral density $S_{\lambda\ meas}(\omega)$. These fluctuations cause dephasing, relaxation and excitation on the measured two level system, with respective rates $\Gamma^{off}_{\varphi\ meas}$ (or $\Gamma^{on}_{\varphi\ meas}$), $\Gamma^{off}_{R\ meas}$ (or $\Gamma^{on}_{R\ meas}$), $\Gamma^{off}_{E\ meas}$ (or $\Gamma^{on}_{E\ meas}$) when the measuring apparatus is off (or on). In the exponential decay limit, these rates, calculated along the same lines as in the semi-classical approach, are:

$$\Gamma^{off/on}_{\varphi\ meas} = \left[\pi\left(\frac{D_{\lambda,z}}{\hbar}\right)^2 S_{\lambda\ meas}(\omega=0)\right]^{off/on} \tag{3.39}$$

$$\Gamma^{off/on}_{R\ meas} = \left[\frac{\pi}{2}\left(\frac{D_{\lambda,\perp}}{\hbar}\right)^2 S_{\lambda\ meas}(\omega=+\Omega_{01})\right]^{off/on} \ , \tag{3.40}$$

$$\Gamma^{off/on}_{E\ meas} = \left[\frac{\pi}{2}\left(\frac{D_{\lambda,\perp}}{\hbar}\right)^2 S_{\lambda\ meas}(\omega=-\Omega_{01})\right]^{off/on} \ , \tag{3.41}$$

Let's suppose that $\Gamma^{on}_{\varphi\ meas} \gg \Gamma^{on}_{1\ meas} = \Gamma^{on}_{R\ meas} + \Gamma^{on}_{E\ meas}$. Since the measurement of the two level system state requires a time t_{meas} in order to resolve the signal

$$\Delta X^{on}_{01} = \langle 1\left|\widehat{X}\right|1\rangle^{on} - \langle 0\left|\widehat{X}\right|0\rangle^{on} = D^{on}_{\lambda,z} \ , \tag{3.42}$$

it can be reliably performed only if the following inequality holds:

$$t_{meas} \ll \frac{1}{\Gamma^{on}_{1\ meas}}.$$

The overall efficiency of the measurement is then given by the product $\Gamma^{on}_{\varphi\ meas} t_{meas} < 1$, the upper limit corresponding to a perfect measuring apparatus with minimal back-action. In this case, full dephasing occurs in just the time needed for the measurement [69, 71].

3.2 Decoherence in a basic Cooper pair box

3.2.1 Decoherence due to a series impedance

The general results of the previous section can be applied to the case a basic Cooper pair box connected in series with an impedance $Z(\omega)$ (Figure 3.3, left). The control parameter which fluctuates is here $\lambda = n_g$.

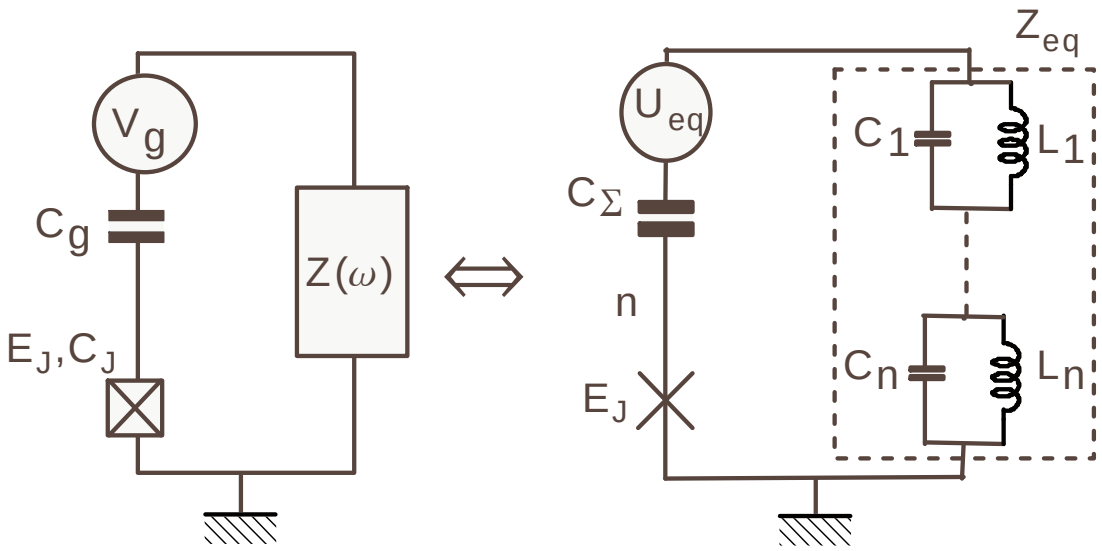

Figure 3.3: *Left panel: Electrical scheme of a basic Cooper pair box coupled to an impedance. Right panel: Model used for a quantum description of decoherence effects.*

It is easier to work on the equivalent circuit of Figure 3.3, right, where the capacitance C_J of the Josephson junction is included in the equivalent impedance Z_{eq} seen by the pure Josephson element E_J :

$$Z_{eq}(\omega) = \frac{1}{\mathbf{i}C_\Sigma\omega} + \frac{\kappa_g^2 Z(\omega)}{1 + \mathbf{i}\kappa_g(1-\kappa_g)C_\Sigma\omega Z(\omega)} \ , \tag{3.43}$$

with:

$$\kappa_g = \frac{C_g}{C_\Sigma} \ .$$

In this description, the equivalent Cooper pair box, formed by the series combination of a pure Josephson element E_J and of the total capacitance C_Σ of the real box, is biased by an equivalent voltage source:

$$U_{eq} = \kappa_g V_g \ .$$

The transfer function $g(\omega)$ which transforms voltage fluctuations across the impedance $Z_{eq}(\omega)$ into fluctuations of n_g is simply

$$g(\omega) = \left(\frac{C_\Sigma}{2e}\right)^2 \ . \tag{3.44}$$

The coupling hamiltonian between the box and the gate charge fluctuations is:

$$\widehat{H}_c = \frac{\partial \widehat{H}}{\partial n_g}\ \Delta n_g(t)\ ,$$

with:

$$\frac{\partial \widehat{H}}{\partial n_g} = -2E_C(\widehat{\mathbf{n}} - n_g) = -\frac{1}{2}\overrightarrow{\sigma}\cdot\overrightarrow{D}_{n_g}(n_g)\ ,$$

$$D_{n_g,z}(n_g) = -2E_C\ \Delta n_{01}(n_g)\ , \tag{3.45}$$

$$D_{n_g,\perp} = 4E_C\ \ |\langle 0\,|\widehat{\mathbf{n}}|\,1\rangle|\ \ , \tag{3.46}$$

and:

$$\Delta n_{01}(n_g) = \langle 1\,|\widehat{n}|\,1\rangle - \langle 0\,|\widehat{n}|\,0\rangle\ \ . \tag{3.47}$$

Note that in the limit $E_J \ll E_C$, from (1.54), $\overrightarrow{D}_{n_g}$ takes the simple form:

$$\overrightarrow{D}_{n_g} = -2E_C\ \overrightarrow{z}\ . \tag{3.48}$$

For the sake of completeness, the explicit coupling to the set of harmonic oscillators corresponding to this model is detailed below. The impedance $Z_{eq}(\omega)$ can be modeled with a series of oscillators (L_p,C_p) [Figure 3.3, right panel, and Appendix 3-A]. The voltage difference $\left(\sum_{p\in\mathbb{N}^*}\widehat{Q_p^c}/C_p\right)$ across the series of oscillators is determined by the charges $\widehat{Q_p^c}$ of the capacitors C_p, and shifts the parameter n_g of the box by a quantity:

$$\widehat{\Delta n_g} = \frac{C_\Sigma}{2e}\left(\sum_{p\in\mathbb{N}^*}\frac{\widehat{Q_p^c}}{C_p}\right)\ .$$

Using the bosonic operators $\widehat{c_p^+}$ and $\widehat{c_p}$ associated to the charge $\widehat{Q_p^c}$ and the flux $\widehat{\varphi_p^c}$ of each oscillator [formulas (3.91)], one obtains for the coefficients μ_p of the coupling hamiltonian (3.14):

$$\mu_p = \frac{\mathbf{i}\sqrt{\pi}}{E_C}\hbar\sqrt{\frac{Z_p}{R_k}}\omega_p \text{ with } Z_p = \sqrt{\frac{L_p}{C_p}}. \tag{3.49}$$

Dephasing

When the impedance $Z(\omega)$ is a pure resistor R, $\mathrm{Re}[Z_{eq}(\omega)]$ is lorentzian :

$$g(\omega)\,\mathrm{Re}[Z_{eq}(\omega)] \simeq \left(\frac{C_\Sigma}{2e}\right)^2\frac{\kappa_g^2\ R}{1+\omega^2/\omega_c^2}\ , \tag{3.50}$$

where $\omega_c = [\kappa_g(1-\kappa_g)RC_\Sigma]^{-1}$ is a cut-off frequency. The dephasing factor $f_\varphi(t)$ then follows the law (3.36) with

$$A = \frac{D_{\lambda,z}^2\ \kappa_g^2\ R\ g_a}{\pi\hbar} = 8\ \Delta n_{01}^2\ \kappa_g^2\frac{R}{R_K}$$

In the semi-classical regime, the exponential tail occurs at a rate Γ_φ (3.37):

$$\Gamma_\varphi = 8\pi\Delta n_{01}^2 \frac{k_B T}{\hbar}\ \kappa_g^2 \frac{R}{R_K}\ . \tag{3.51}$$

In the limit $E_J \ll E_C$, using Eq. (3.48), the expression (3.51) reduces to (Formula (9) of [25]):

$$\Gamma_\varphi = 8\pi \cos^2\theta \frac{k_B T}{\hbar} \kappa_g^2 \frac{R}{R_K}\ . \tag{3.52}$$

Depolarisation

In qubit experiments, one has to reach the low temperature regime $k_b T \ll \hbar\ \Omega_{01}$. In this case, the excitation rate due to an impedance at thermal equilibrium can be neglected ($\Gamma_E \ll \Gamma_R \simeq \Gamma_1$). The relations (3.38) and (3.50) allow to calculate the relaxation rate Γ_R. The result can be further simplified in the weak coupling limit $\kappa_g \ll 1$

$$\Gamma_R = \pi\kappa_g^2 \left(\frac{D_{n_g,\perp}}{E_C}\right)^2 \frac{\mathrm{Re}[Z(\Omega_{01})]}{R_k}\Omega_{01}\ . \tag{3.53}$$

In the limit ($E_J \ll E_C$, $T = 0$), using (3.48), this expression reduces to (Formula (6) of [25]):

$$\Gamma_R = 4\pi\kappa_g^2 \sin^2\theta \frac{\mathrm{Re}[Z(\Omega_{01})]}{R_k}\Omega_{01}\ . \tag{3.54}$$

Conclusion

In all the above expressions of the rates, a κ_g^2 factor ensures that dephasing and relaxation disappear when the gate capacitance vanishes. In Cooper pair box experiments, the gate capacitance can be made quite small ($\kappa_g \ll 1$), so that dephasing and relaxation due to the impedance of the gate charge bias-line are not a serious problem. Let's suppose that $\hbar\Omega_{01}$ ~ 1 k$_b$K, $T \sim 10$ mK, $C_g \sim 10$ aF, $\kappa \sim 1\%$ and $\mathrm{Re}[Z(\omega)] \sim 10\ \Omega$. In this case, the cross-over to the semiclassical regime of dephasing occurs at the thermal time $t_T = \hbar/(\pi k_B T) \sim 2$ ns$\gg$ $1/\omega_c \sim 10^{-18}$ s. The corresponding exponential decay occurs at a rate $\Gamma_\varphi \simeq \cos^2\theta/80$ MHz. Concerning relaxation, one finds $\Gamma_R \simeq \cos^2\theta/20$ MHz. The excitation of the box is negligible: $\Gamma_E \simeq 0$. The situation is different when an active measuring apparatus is connected to the box island. In this case, the back-action of the measuring apparatus on the box can be excitation as well as relaxation or dephasing, as discussed in the next section.

3.2.2 Decoherence due to a measuring Cooper pair transistor

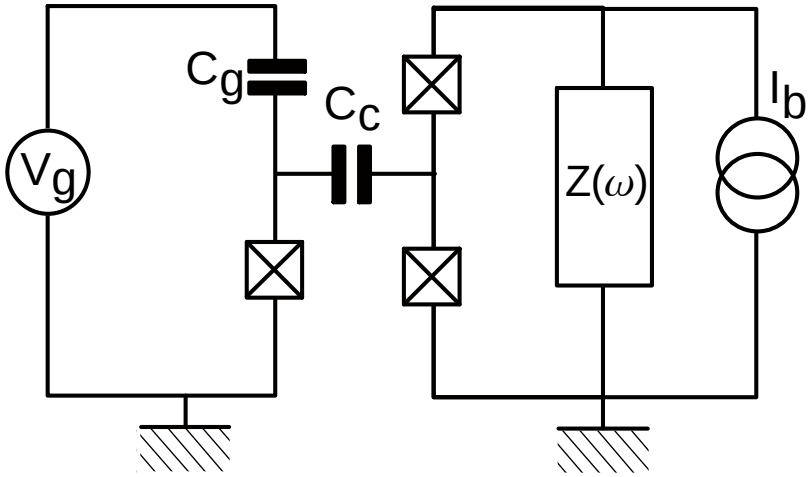

Figure 3.4: *Electrical scheme of a Cooper pair box capacitively coupled to a Cooper pair transistor. The impedance $Z(\omega)$ placed in parallel with the transistor induces decoherence on the box.*

The state of a basic Cooper pair box can be measured by using a Cooper pair transistor capacitively coupled to the box island (see chapter 2). This measurement requires the transistor to be shunted with dissipative elements. These elements cause fluctuations of the transistor island potential which induce decoherence. This back-action is present even when the transistor is not measuring the box, i.e. when its bias current is zero. In order to compute the relaxation rates $\Gamma^{off/on}_{R\ meas}$, the excitation rates $\Gamma^{off/on}_{E\ meas}$, and the dephasing rates $\Gamma^{off/on}_{\varphi\ meas}$ due to the off/on transistor, one can generalize the previous approach by replacing the term $S_{n_g}(\omega)$ in the expression of the rates by $\left[C_g C/\left(2eC_J\right)\right]^2 S_{V'}^{off\ /on}(\omega)$, where $S_{V'}^{off\ /on}(\omega)$ refers to the spectral density of the noise in the transistor island voltage V'. From (3.12) and (3.38), one finds

$$\Gamma^{off/on}_{\varphi\ meas} = \pi\kappa^2_{\rm SCPT}\left(\frac{D_{n_g,z}}{\hbar}\frac{C_g}{2e}\right)^2 S_{V'}^{off/on}(0)\ , \tag{3.55}$$

$$\Gamma^{off/on}_{R\ meas} = \frac{\pi}{2}\kappa^2_{\rm SCPT}\left(\frac{D_{n_g,\perp}}{\hbar}\frac{C_g}{2e}\right)^2 S_{V'}^{off\ /on}(+\Omega_{01})\ , \tag{3.56}$$

$$\Gamma^{off/on}_{E\ meas} = \frac{\pi}{2}\kappa^2_{\rm SCPT}\left(\frac{D_{n_g,\perp}}{\hbar}\frac{C_g}{2e}\right)^2 S_{V'}^{off/on}(-\Omega_{01})\ , \tag{3.57}$$

where

$$\kappa_{\rm SCPT} = \frac{C_c}{C_J}$$

is the coupling constant between the box and the transistor (and C_J is the capacitance of the box junction).

Calculating the spectral density $S_{V'}^{on\ /off}(\omega)$ requires to know the dynamics of the measuring circuit. When the transistor is off, the fluctuations of the phase difference across it are small.

Assuming that a transition from the ground state band of the transistor to its first band cannot occur, each band state of the transistor corresponds to an effective impedance for which the previous results can be applied. Therefore, assuming $k_bT \ll \hbar\,\Omega_{01,}$ one finds $\Gamma^{off}_{E\,meas} \ll \Gamma^{off}_{R\,meas}$. When the transistor is on, the spectral density $S_{V'}(\omega)$ cannot be calculated analytically. The low frequency part of $S^{on}_{V'}(\omega)$, which determines dephasing, is obtained from numerical simulations of the transistor dynamics. Its high frequency part is estimated by averaging over the phase dynamics the value calculated using an effective impedance model [27, 28]. For that purpose, the transistor in its lowest band is treated as an inductor whose value varies with the phase across the transistor. The relaxation and excitation rates are then calculated for the corresponding effective impedance seen from the Cooper pair box, and averaged over the phase dynamics. Care must be taken for the temperature of the effective impedance because of dissipation in the transistor circuit.

3.3 Split Cooper pair box coupled to an impedance

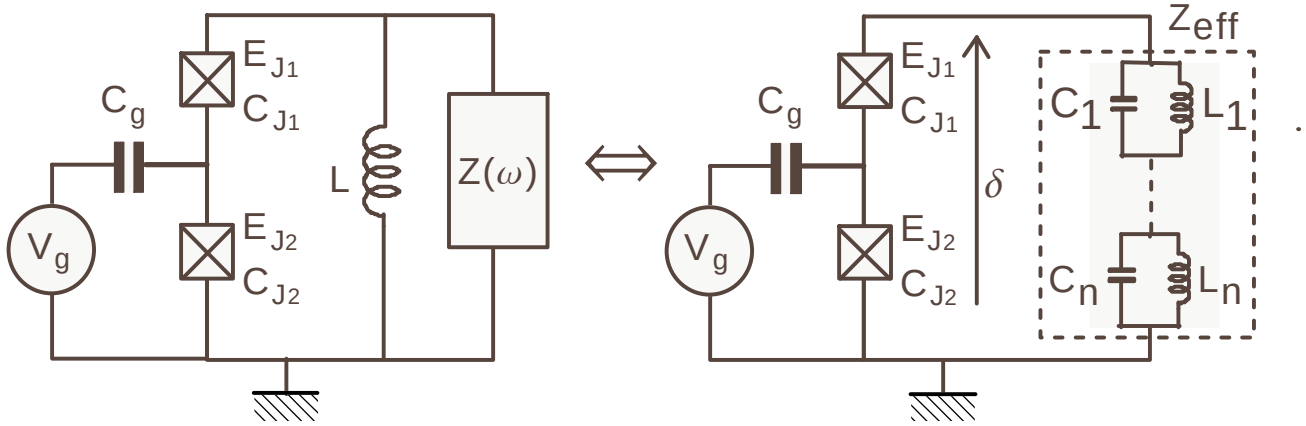

Figure 3.5: *Left panel: Electrical scheme of a split Cooper pair box whose loop is coupled to an impedance. Right panel: Model used for a quantum description of decoherence effects in this circuit.*

In the case of a split box, decoherence is conveyed by two control variables: the gate charge n_g and the phase difference δ . The decoherence due to an impedance in the gate circuit can be calculated as indicated previously. This section focuses on the case of an impedance in the box loop. The Figure 3.5 (left) represents a split box whose loop is loaded with a dissipative impedance $Z(\omega)$ placed in parallel with a superconducting inductor L . We assume here that[2]:

$$L \ll I_0^{eff}/\varphi_0 \ . \tag{3.58}$$

[2]In the experiment 5 reported in chapter 4, the split box is shunted with a large Josephson junction with energy E_J^d which plays the role of this inductance.

In the circuit of Figure 3.5, the total impedance seen by the series combination of the two Josephson junctions of the box is:

$$Z_{eff}(\omega) = \frac{1}{\frac{1}{Z(\omega)} + \frac{1}{\mathbf{i}L\omega}} \ .$$

The electromagnetic fluctuations of $Z_{eff}(\omega)$ induce fluctuations of the parameter δ, which plays the role of the parameter λ used in the generic case:

$$\lambda = \delta \ .$$

The transfer function $g(\omega)$ associated to this circuit is :

$$g(\omega) = \frac{1}{\varphi_0^2 \ \omega^2} \ . \tag{3.59}$$

The linear coupling term between the box and these fluctuations is:

$$\widehat{H}_c = \frac{\partial \widehat{H}}{\partial \delta} \widehat{\Delta\delta} \ ,$$

with:

$$\frac{\partial \widehat{H}}{\partial \delta} = \varphi_0 \widehat{I} \ = -\frac{1}{2} \overrightarrow{\sigma} \cdot \overrightarrow{D}_\delta \ ,$$
$$D_{\delta,z} = -\varphi_0 \Delta i_{01}(n_g, \delta) \ ,$$
$$D_{\delta,\perp} = 2\varphi_0 \left| \left\langle 0 \left| \widehat{I} \right| 1 \right\rangle \right| \ ,$$

and

$$\Delta i_{01}(n_g, \delta) = i_1 - i_0|_{n_g,\delta} \ .$$

Note that in the limit $E_J \ll E_C$, from (1.54),

$$\overrightarrow{D}_\delta = -\frac{E_J}{2} \sin(\frac{\delta}{2}) \overrightarrow{x'} + d\frac{E_J}{2} \cos(\frac{\delta}{2}) \overrightarrow{y'} \ .$$

The impedance $Z_{eff}(\omega)$ can again be modeled with a discrete series of harmonic oscillators (L_p,C_p) [Figure 3.5, right and Appendix 3-A]. The total phase difference δ across the series combination of the box Josephson junctions is shifted by the sum:

$$\widehat{\Delta\delta} = \sum_{p \in \mathbb{N}^*} \widehat{\varphi_p^l}/\varphi_0 \tag{3.60}$$

where $\widehat{\varphi_p^l}$ is the phase across the inductances L_p . Due to the hypothesis (3.58), the phase fluctuations of δ are small and one can use the first order coupling theory. In order to describe the oscillators, one can use the bosonic operators $\widehat{c}_p^+$ and $\widehat{c}_p$ associated to the charge operator $\widehat{Q_p^c}$ and the flux operator $\widehat{\varphi_p^c}$ of C_p [formulas (3.91)]. In that picture, the shift coefficients characterizing $\widehat{\Delta\delta}$ are:

$$\mu_p = 2\sqrt{\frac{\pi Z_p}{R_k}} \ . \tag{3.61}$$

Dephasing

When the impedance $Z(\omega)$ is a pure resistor R, the product $g(\omega)\,\mathrm{Re}\,Z_{eff}(\omega)$ has the lorentzian form:

$$g(\omega)\,\mathrm{Re}\,Z_{eff}(\omega) \simeq \frac{L^2}{\varphi_0^2\ R}\frac{1}{(1+\omega^2 t_L^2)}\ . \tag{3.62}$$

with

$$t_L = \frac{L}{R}\ ,$$

and $f_\varphi(t)$ follows the law (3.36) with

$$A = \frac{\kappa_L^2}{8\pi^2}\left(\frac{D_{\delta,z}}{E_J}\right)^2\frac{R_K}{R}\ .$$

where

$$\kappa_L = \frac{E_J L}{\varphi_0^2} \tag{3.63}$$

is a dimensionless coupling coefficient, analogous to the coupling factor κ_g entering in the expression (3.51). From (3.58), the inductance L is small compared to the junction inductance φ_0^2/E_J, and κ_L is small. In the exponential regime, the dephasing rate is :

$$\Gamma_\varphi = \frac{\kappa_L^2}{8\pi}\left(\frac{\varphi_0\Delta i_{01}}{E_J}\right)^2\frac{R_K}{R}\frac{k_bT}{\hbar}\ .$$

When the impedance $Z(\omega)$ varies only slowly at low frequency, this dephasing rate can be generalised as:

$$\Gamma_\varphi = \frac{\kappa_L^2}{8\pi}\left(\frac{\varphi_0\Delta i_{01}}{E_J}\right)^2\frac{R_K}{Z(0)}\frac{k_bT}{\hbar}\ . \tag{3.64}$$

Note that in the limit $E_J \ll E_C$, from (1.54), this expression becomes:

$$\Gamma_\varphi = \frac{\kappa_L^2}{32\pi}\frac{R_K}{Z(0)}\frac{k_bT}{\hbar}\sin^2\theta\left[\sin^2(\delta/2)+d^2\cos^2(\delta/2)\right]\ . \tag{3.65}$$

Depolarisation

In our experiments, one has $k_bT \ll \hbar\,\Omega_{01}$, therefore $\Gamma_E \ll \Gamma_R \simeq \Gamma_1$ and the excitation due to an impedance can be neglected. One can insert (3.59) in the general formula (3.38) in order to obtain the relaxation rate due to an impedance:

$$\Gamma_R = 4\pi D_{\delta,\perp}^2\frac{\mathrm{Re}[Z_{eff}(\Omega_{01})]}{R_k}\frac{1}{\hbar^2\Omega_{01}}\ . \tag{3.66}$$

In the limit ($E_J \ll E_C$,$T=0$), this rate becomes[3]:

$$\Gamma_R = \frac{\pi E_J^2}{\hbar^2\Omega_{01}}\frac{\mathrm{Re}[Z_{eff}(\Omega_{01})]}{R_k}\left[\cos^2\theta\left[\sin^2(\delta/2)+d^2\cos^2(\delta/2)\right]+\frac{d^2E_J^2}{\hbar^2\Omega_{01}^2}\right]\ . \tag{3.67}$$

[3]Formula (3.67) was published in a slightly different form, for the case $n_g = \frac{1}{2}$ and $\delta = 0$, as formula (7) of article [28] .

For the sake of simplicity, let us consider that $Z(\omega) = R$, so that $Z_{eff}(\omega) = R/\left[1 + 1/\left(\omega^2 t_L^2\right)\right]$. Two limit cases are possible. When $\Omega_{01} < 1/t_L$, $\mathrm{Re}[Z_{eff}(\Omega_{01})] \simeq \Omega_{01}^2 L^2/R$ is attenuated because Ω_{01} falls in the low frequency cutoff provided by the inductance. The relaxation rate Γ_R has thus a form analog to the dephasing rate (3.64):

$$\Gamma_R = \frac{\kappa_L^2}{16\pi}\left(\frac{D_{\delta,\perp}}{E_J}\right)^2 \frac{R_k}{R}\Omega_{01} \ .$$

On the contrary case, when $\Omega_{01} > 1/t_L$,

$$\Gamma_R = 4\pi D_{\delta,\perp}^2 \frac{R}{R_k}\frac{1}{\hbar^2\Omega_{01}} \ , \tag{3.68}$$

and one must choose a low value for R in order to limit relaxation.

Conclusion

In the experiments related in this thesis, one has typically $E_J \sim E_C \sim 1$ k$_b$K, $T \sim 10$ mK, $C_g \sim 10$ aF. Let's also consider that $Z(0) = 500\ \Omega$, $d = 0.1$ and $L_J \simeq 1$ nH. One has $\kappa_L \sim 1\%$, so that $t_L \simeq 0.2\ \mu\mathrm{s} \gg t_T$. At $\theta = 0$, no dephasing is predicted at first order in the fluctuations. At $\theta = \pi/4$, for $t > 0.2\ \mu$s, one finds that the semi-classical regime applies, with a dephasing rate $\Gamma_\varphi \simeq 0.22$ MHz. Considering in addition $\mathrm{Re}\, Z_{eff}(\Omega_{01}) = 2\ \Omega$, the relaxation rate is $\Gamma_R \simeq 0.5$ MHz. The introduction of a phase port thus opens a decoherence way due to the loop impedance, but the decoherence rate can be controlled by a proper tailoring of the impedance $Z_{eff}(\omega)$ .The split Cooper pair box setup is discussed more in detail in the following chapter.

3.4 Effect of charge noise on a Cooper pair box

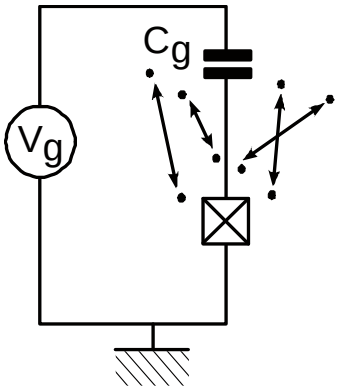

Figure 3.6: Symbolic representation of a Cooper pair box close to two level charge flutuators

The island of a box or a transistor is subject to the 1/f charge noise resulting from the random motion of microscopic charges in its vicinity [20]. This noise, ubiquitous in charging devices, has a spectral density of the form:

$$S_q^{cl}(\omega) = \frac{e^2 B}{2\,|\omega|} \text{ for } \omega \in \,]-\infty, +\infty[\tag{3.69}$$

where $B \sim 10^{-7}$ has been directly measured up to 10 MHz, which is larger than the frequency range relevant for dephasing. The spectrum has not been directly measured at higher frequencies.

3.4.1 Dephasing

In order to calculate the dephasing due to a 1/f noise, one can use a special procedure described in Appendix 3-B-2, which consists in working in a discretised frequency space. According to this procedure, the resonance pulsation Ω_{01} of the box, which fluctuates with time, can be written as

$$\Omega_{01}(t) = 2\int_0^\infty \sqrt{d\omega\ S_{\Omega_{01}}^{cl}(\omega)}\cos(\omega t + \varphi_\omega)\ ,$$

where $S_{\Omega_{01}}(\omega)$ is the noise spectrum of $\Omega_{01}(t)$, where φ_ω is a random phase factor, and where $\sqrt{d\omega\ S_{\Omega_{01}}(\omega)}$ is a symbolic notation defined in Appendix 3-B-2. The spectrum $S_{\Omega_{01}}(\omega)$ can calculated as:

$$S_{\Omega_{01}}^{cl}(\omega) = \left(\frac{\partial\Omega_{01}}{\partial n_g}\right)^2 \frac{1}{(2e)^2} S_q(\omega)\ ,$$

which gives:

$$S_{\Omega_{01}}^{cl}(\omega) = \frac{A}{|\omega|}$$

with

$$A = \left(\frac{D_{n_g,z}}{\hbar}\right)^2 \frac{B}{4} .$$

Following the same procedure, the phase shift acquired between t and t' is noted[4]:

$$\Delta\varphi(t,t') = \int_t^{t'} \Omega_{01}(\tau)d\tau = 2(t'-t)\int_0^\infty \sqrt{d\omega\frac{A}{|\omega|}}\mathrm{sinc}\left[\frac{\omega(t'-t)}{2}\right]\cos\left[\frac{\omega\,(t'+t)}{2}+\varphi_\omega\right] . \quad (3.70)$$

where $\mathrm{sinc}[x] = \sin[x]/x$. Due to the 1/f structure of the noise, the resonance pulsation Ω_{01} can have sudden and strong time variations, and thus $\Delta\varphi(t,t')$ diverges. In order to perform a measurement on this system in spite of the $1/f$ noise, a strict experimental protocol must be defined. The temporal structure of this experimental protocol determine the statistical properties of the results.

The protocol considered here can be divided into different steps with controlled durations. The first stage is a preliminary evaluation of the average precession speed $\overline{\Omega_{01}}$, from $t = -t_1$ to $t = 0$. This evaluation is made by leaving the box in the ground state $|0\rangle$ and by measuring the mean charge or mean loop current of the box. experimentally, when the dependence of these quantities with n_g has been previously measured, this allows to determine the value of n_g and thus $\overline{\Omega_{01}}$. The box is then left at rest from $t = 0$ to $t = t_2 - \tau/2$. At $t = t_2 - \tau/2$, the box is prepared in a superposition of $|0\rangle$ and $|1\rangle$ in a time considered as instantaneous compared to the duration of the other steps of the experiment. The box is then left to evolve freely from $t = t_2 - \tau/2$ to $t = t_2 + \tau/2$ and its state is measured at $t = t_2 + \tau/2$. In order to evaluate the decoherence acquired during that time because of charge noise, one can define the phase shift $D\varphi$ as the difference between the true phase shift due to $\Omega_{01}(t)$ and the phase shift that one can expect knowing $\overline{\Omega_{01}}$:

$$D\varphi = \Delta\varphi(t_2 - \frac{\tau}{2}, t_2 + \frac{\tau}{2}) - \tau\overline{\Omega_{01}} . \quad (3.71)$$

with:

$$\overline{\Omega_{01}} = \frac{\Delta\varphi(-t_1, 0)}{t_1}$$

We choose $t_1 = 2t_2 = \Upsilon$. This choice is arbitrary and allows to simplify the analytical expression of $D\varphi$. From (3.70), one obtains for the variance $\langle D\varphi^2\rangle$ of $D\varphi$ a regular expression:

$$\left\langle D\varphi^2\right\rangle = \tau^2\int_0^\infty \frac{A}{\omega}\left(\mathrm{sinc}^2\left[\frac{\omega\Upsilon}{2}\right] + \mathrm{sinc}^2\left[\frac{\omega\tau}{2}\right] - 2\mathrm{sinc}\left[\frac{\omega\Upsilon}{2}\right]\mathrm{sinc}\left[\frac{\omega\tau}{2}\right]\cos\left[\frac{\omega\Upsilon}{2}\right]\right)d\omega . \quad (3.72)$$

A first order development of $\langle D\varphi^2\rangle$ in τ/Υ then gives the dephasing factor:

$$f_\varphi(\tau) = \exp\left[-\frac{\langle D\varphi^2\rangle}{2}\right] \simeq \exp\left\{-\left[\frac{D_{n_g,z}}{\hbar}\right]^2\frac{B}{8}\tau^2\ln(\frac{\Upsilon}{\tau})\right\} . \quad (3.73)$$

[4]Note that the calculation made here does not take into account the exact microscopic structure of the charge fluctuators causing the 1/f noise. A microscopic approach of decoherence due to charge noise in Josephson qubits has been peformed by E.Paladino [47].

In the case $E_J \ll E_C$, one finds:

$$f_\varphi(\tau) \simeq \exp\left\{-\frac{1}{2}\cos^2(\theta)\left[\frac{E_c\tau}{\hbar}\right]^2 B\ln(\frac{\Upsilon}{\tau})\right\} . \tag{3.74}$$

In a repeated experiment, the waiting time Υ is of the order of the total measuring time. The averaging procedure thus degrades progressively when the data recording time increases.

3.4.2 Compensating the dephasing with echo techniques

In order to compensate the effect of charge noise, it is possible to perform echo experiments [48]. The first stage consists in letting the qubit evolve freely around a given field $\overrightarrow{h}$ from $t = -\tau/2$ to $t = 0$. The second stage consists in applying to the box a radiofrequency pulse with a duration much shorter than τ in order to reverse the phase shift acquired previously. The last stage consists in letting the box evolve from $t \simeq 0$ to $t = \tau/2$. The total phase drift $D\varphi$ acquired at the end of the experiment is:

$$D\varphi = -\Delta\varphi(-\tau/2, 0) + \Delta\varphi(0, \tau/2) .$$

Using (3.70) and the fact that $\int_0^\infty dx \sin^4(x)/(x^2\,|x|) = \log(2)$, the dephasing factor $f_\varphi(\tau)$ can be calculated exactly as:

$$f_\varphi(\tau) \simeq \exp\left\{-\left[\frac{D_{n_g,z}}{\hbar}\right]^2 \frac{B}{8}\tau^2\ln(2)\right\} . \tag{3.75}$$

In the case $E_J \ll E_C$, this gives:

$$f_\varphi(\tau) \simeq \exp\left\{-\cos^2(\theta)\left[\frac{E_c\tau}{\hbar}\right]^2 B\frac{\ln(2)}{2}\right\} . \tag{3.76}$$

The divergences due to the 1/f charge noise are suppressed by the echo technique and a preliminary measurement of the precession speed is now useless. However, the coherence time is not significantly enhanced. For $E_J \ll E_C = 0.5$ k_bK, in an echo experiment, coherence is lost after $\tau = 20/\cos\theta$ ns . The 1/f charge noise thus severely limits the coherence time, except at the symmetry points where $D_{n_g,\,z} = 0$. Considering that the gate charge n_g cannot be tuned perfectly at this point, one has to choose a ratio E_J/E_C as large as possible, so that the sensitivity to charge noise around the points $D_{n_g,\,z} = 0$ is lowered, as discussed in chapter 2.

3.5 Searching for the best qubit setup

Using a Cooper pair box as a quantum bit is possible provided the box and the measurement apparatus fulfill some criterions. First, the manipulation of the box state must not be perturbed by the measuring apparatus:

$$\Gamma_\varphi^{off} \ll 1/t_{manip}$$

and:

$$\Gamma_1^{off} \ll 1/t_{manip} \ ,$$

where t_{manip} is the duration of this manipulation. Then, when the measuring apparatus is on, it should project the box on the states $|0\rangle$ or $|1\rangle$, and discriminate a physical quantity related to these energy eigenstates before relaxation occurs. This second criterion requires to fulfill the extra inequality:

$$\Gamma_1^{on} \ll 1/t_{meas} \ ,$$

where t_{meas} is the time needed to perform a discriminating measurement. The pages 178-179 presents the evaluation of the dephasing and relaxation rates for three different qubit setups which can be implemented with single Cooper pair devices. The results are given in terms of the relaxation and dephasing times[5] $T_R^{off\ (on)} = 1/\Gamma_R^{off\ (on)}$ and $T_\varphi^{off\ (on)} = 1/\Gamma_\varphi^{off\ (on)}$. For the purpose of comparing the different circuits, when $f_\varphi(t)$ has not the exponential form, the characteristic dephasing time $T_\varphi^\#$ such as $f_\varphi(T_\varphi^\#) = 1/e$ is indicated. Note that other setups have been proposed and evaluated [78, 79].

3.5.1 Setup A: Box coupled to a DC shunted transistor

In setup A represented in p.178, the Cooper pair box island is connected to the island of a Cooper pair transistor with a coupling capacitor C_c. The sources of decoherence are the resistance r of the box gate line, the 1/f charge noise, and the transistor together with its biasing circuitry. The decoherence rates of this setup are estimated for the parameters indicated in p.179. (For the transistor, these parameters are those of experiment 2; R_{eff} is the effective resistance seen by the transistor). In order to minimize dephasing during the manipulation of the box state, the box gate charge n_g must be tuned to $n_g \simeq 1/2$ and the bias current I_b of the transistor to $I_b = 0$. (For the calculations, we have assumed that we cannot tune n_g with an accuracy better than 0.01). For the measurement, n_g must be taken away from 1/2 and I_b switched on to a value $I_b > I_0^{eff}$ (see Figure 2.8), so that the transistor current reveals the box state.

The dephasing and relaxation rates due to r have been calculated using formulas (3.51) and (3.53). The dephasing rate due to the charge noise has been estimated for an echo experiment with formula (3.75). The relaxation and dephasing rates due to the transistor have been calculated with formulas (3.55), (3.56) and (3.57), after a determination of the voltage spectrum $S_{V''}(\omega)$ of the transistor island voltage V' (see section 3.2.2).When the readout is off, this spectrum has a cutoff at low frequencies, which limits the decay of the dephasing factor. It also falls off before Ω_{01}, which makes relaxation negligible. When the readout is on, the phase excursions are not bounded anymore. The spectrum obtained is constant at low frequency and exhibits a peak at the Josephson frequency Ω_J, but falls off below Ω_{01} .

[5]Since the experiments are performed at $k_bT \ll \hbar\nu_{01}$, we expect $T_R^{off\ (on)} \ll T_E^{off\ (on)}$. That is why the excitation times are not indicated in p.179.

Conclusion

This setup is too much perturbed by 1/f noise. Moreover, even if this 1/f noise was not present, the readout device would not be sensitive enough to read the box state before it relaxes ($t_{meas} > T_1^{on}$)

3.5.2 Setup B: Box coupled to an AC shunted transistor

In the setup B represented in p.178, the Cooper pair box island is still connected to the island of a Cooper pair transistor with a capacitor C_c, but the Cooper pair transistor is now hysteretic like in experiment 3. Decoherence is evaluated for the parameters indicated in p.179. For the measurement, n_g must be taken away from 1/2 and the amplitude of the bias pulse I_b tuned so that the transistor switches if the box is in the state $|1\rangle$ but not in the state $|0\rangle$.

The relaxation and dephasing rates due to the gate line resistance r, the 1/f noise and the transistor have been estimated using the same methods as for setup A. The rates during measurement have been calculated just before the switching of the transistor at $\overline{I_s} \simeq 0.76\ I_0^{eff}$.

Conclusion

Setup B is more efficient than setup A, but it is still quite sensitive to charge noise.

3.5.3 Setup C: Quantronium

For the sake of comparison, decoherence for the setup C that will be discussed in chapter 4 is also indicated here. In setup C, an AC shunted Josephson junction is inserted in the loop of a split Cooper pair box (Figure p. 178). In order to minimize dephasing during the manipulation of the box state, the box gate charge must be tuned to $n_g = 1/2$ and the superconducting phase through the box to $\delta = 0$. The readout is performed by applying a pulse of bias current I_b . In principle, it is possible to tune the amplitude of this pulse so that the readout junction switches when the box is in the state $|1\rangle$ but not in the state $|0\rangle$.

The expected sources of decoherence are the resistor r in the gate line, the 1/f noise and the shunting impedance of the detection junction. We have calculated their effect for the parameters indicated in p.179. The relaxation and dephasing rates due to the impedance of the gate line and to the charge noise have been calculated using the same methods as for setup A. A Cooper pair box with a E_J/E_C ratio larger than that of setup A and B can be used,

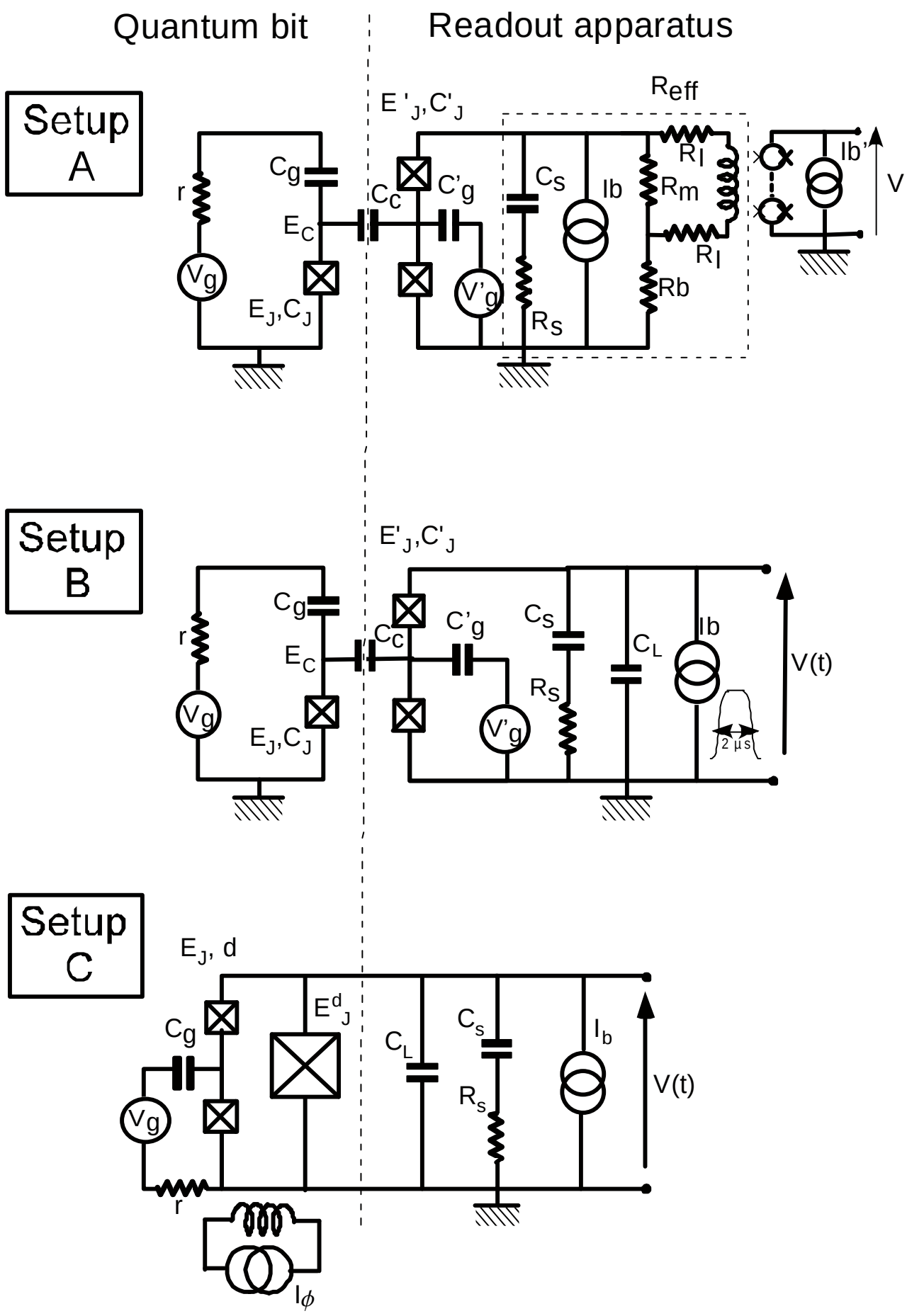

Readout Off Readout On

$n_g = 0.49\ (\theta = \pi/2),\ I_b = 0$

	r	readout	charge noise
T_R^{off}	62 μs	∞	unknown
T_φ^{off}	∞	∞	0.5 μs

$t_{meas} = \infty$

$n_g = 0.325\ (\theta \simeq \pi/4),\ I_b = 2I_0^{eff}$

	r	readout	charge noise
T_R^{on}	107 μs	1 μs	unknown
T_φ^{on}	463 μs	$<$ 10 ns	30 ns

$t_{meas} = 36\ \mu$s

parameters used: $T = 50$ mK, $E_c = 2E_J = 2$ k$_b$K, $r = 5\ \Omega$, $E_c' = 2.2$ k$_b$K, $E_J' = 2$ k$_b$K, $R_{eff} = 38\ \Omega$, $\kappa_g = C_g/(C_g + C_J) = 1$ %, $\kappa_{\rm SCPT} = C_c/C_J' = 2.5$ %

$n_g = 0.49\ (\theta = \pi/2),\ I_b = 0$

	r	readout	charge noise
T_R^{off}	62 μs	∞	unknown
T_φ^{off}	∞	∞	0.5 μs

$t_{meas} = \infty$

$n_g = 0.325\ (\theta \simeq \pi/4),\ I_b = 0.76I_0^{eff}$

	r	readout	charge noise
T_R^{on}	107 μs	60 μs	unknown
T_φ^{on}	463 μs	$<$ 100 ns	30 ns

$t_{meas} = 2\ \mu$s

parameters used: $T = 50$ mK, $E_c = 2E_J = 2$ k$_b$K, $r = 5\ \Omega$, $E_C' = 2E_J' = 4$ k$_b$K, $R_s = 400\ \Omega$, $C_s = 180$ pF, $C_L = 0.75$ pf, $\kappa_g = C_g/(C_g + C_J) = 1$ %, $\kappa_{\rm SCPT} = C_c/C_J' = 1$ %.

$n_g = 0.49\ (\theta = \pi/2),\ \delta = 0$

noise source	r	readout	$c.n$
T_R^{off}	68 μs	2.5 μs	unknown
T_φ^{off}	∞	∞	1.3 μs

$t_{meas} = \infty$

$n_g = 0.49,\ I_b = 0.97I_0^d\ (\delta \simeq \pi/2)$

noise source	r	readout	$c.n$
T_R^{on}	100 μs	2.5 μs	unknown
T_φ^{on}	∞	30 ns	2.7 μs

$t_{meas} = 0.1\ \mu$s

parameters used: $T = 50$ mK, $E_J = 0.86$ k$_b$K, $E_C = 0.68$ k$_b$K, $d = 0.1$, $r = 5\ \Omega$, $I_J^d = 0.77\ \mu$A$\Leftrightarrow E_J^d = 18.3$ k$_b$K$\Rightarrow \kappa_d = E_j/E_J^d = 4.7$ %, $R_s = 500\ \Omega$, $C = C_L + C_J = 0.5$ pf, $C_s = 10$ pf,$\kappa_g = C_g/(C_g + C_J) = 1$ %

leading to a reduced sensitivity to charge noise. In order to evaluate the decoherence due to the readout line, we have considered that before the switching, the phase fluctuations through the readout junction are small, so that it behaves as an effective inductance:

$$L_J^d = \frac{\varphi_0^2}{E_J^d \cos(\delta)}$$

with

$$\delta \simeq \arcsin s \ .$$

and

$$s = \frac{\varphi_0 I_b}{E_J^d}$$

For instance, with the parameters of p.179, at $\delta = 0$, one has $L_J^d = 0.43$ nH . From (3.64), the dephasing time due to the readout line is:

$$T_\varphi = 8\pi \frac{R_s}{R_k} \frac{\hbar}{k_b T} \frac{E_J^d \cos^2(\delta)}{\varphi_0^2 \left(i_1 - i_0\right)^2} \ . \tag{3.77}$$

Note that when $s = 0$, one has $L_J^d = 0$, so that the box is decoupled from the readout circuit and there is no dephasing at first order. The time T_φ decreases with s (Figure 3.8), which enables the full dephasing of the box state necessary when one increases s to perform a projective measurement[6] on the states $|0\rangle$ and $|1\rangle$. From (3.66), the relaxation time is:

$$T_R = \frac{\hbar}{16\pi} \frac{R_k}{\mathrm{Re}[Z_{eff}(2\pi\nu_{01})]} \frac{h\nu_{01}}{\varphi_0^2 \left| \left\langle 0 \left| \widehat{I} \right| 1 \right\rangle \right|^2} \ , \tag{3.78}$$

where

$$Z_{eff}(\omega) \simeq \frac{1}{1/R_s + 1/(\mathbf{i} L_J^d \omega) + \mathbf{i} C \omega}$$

is the effective impedance seen by the split box, where

$$C = C_J + C_L$$

is the total capacitance seen by the readout junction. Note that the value of $\mathrm{Re}[Z_{eff}(\Omega_{01})]$, which determines the relaxation time T_R, is difficult to control in practice because it varies significantly with C_L (See Figure 3.7). The time T_R is minimum for $s = 0$ (Figure 3.9) and decreases strongly with d (Figure 3.10).

Conclusion

This setup seems more favorable for a quantum bit experiment, since it allows to use a larger E_J/E_C ratio and thus enhances the immunity to charge noise[7]. Its implementation is detailed in chapter 4.

[6] Note that the numerical estimate of (3.77) given in p.178 implies that in experiment 5, the quantronium is fully dephased much before the switching of the readout junction.

[7] We have presented here numerical estimates for parameters close to those of experiment 4 and 5, in order to allow a comparison with the experimental results. However, theoretically, larger values of E_J/E_C would lead

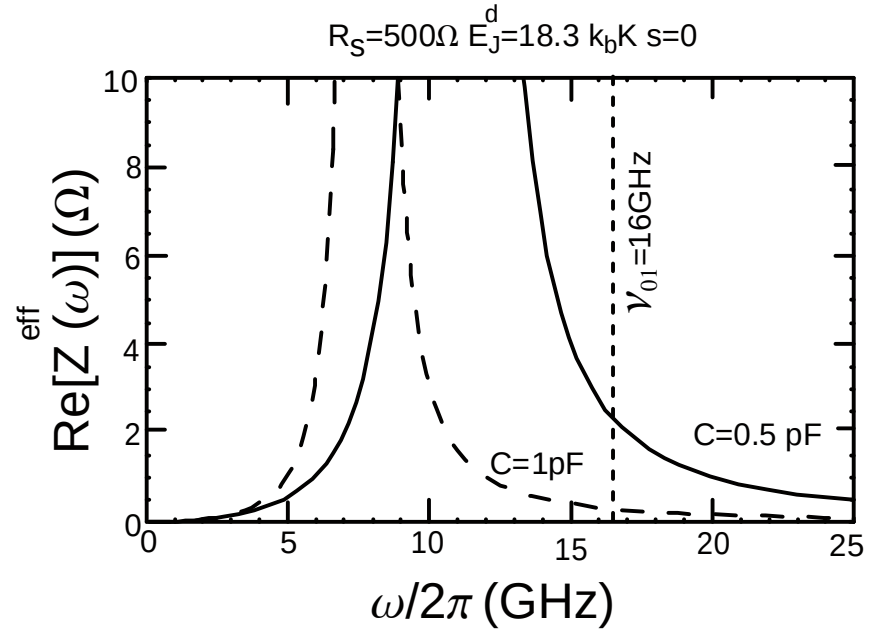

Figure 3.7: *Frequency dependence of* $\mathrm{Re}[Z^{eff}(\omega)]$ *for* $R_s = 500\ \Omega$, $E_J^d = 18.3\ \mathrm{k}_b\mathrm{K}$ *(parameters of experiment 5), and two different values of* C. *The dashed line corresponds to* $C = 1$ pF, *value that we wanted to implement originally for experiment 5. The full line corresponds to* $C = 0.5$ pF, *the value reached in practice in experiment 4. Note that* $\mathrm{Re}[Z^{eff}(\omega)]$ *presents a peak at the plasma resonance of the readout junction.*

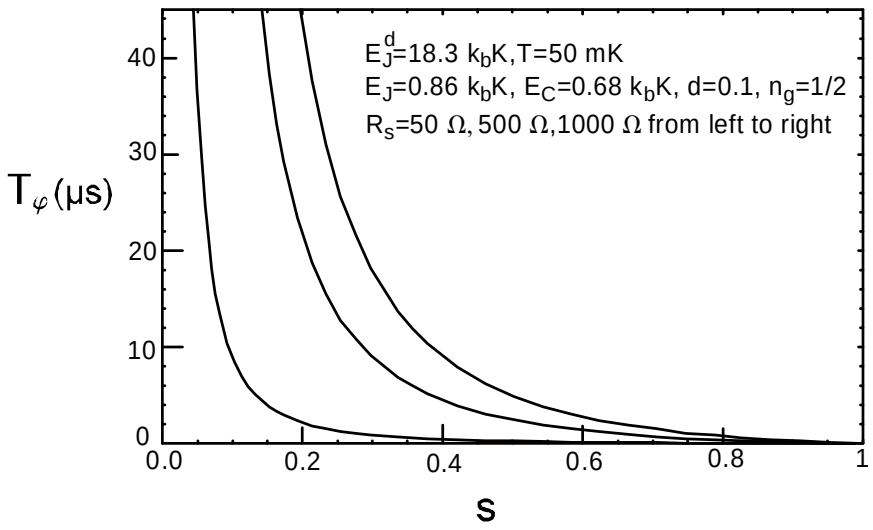

Figure 3.8: *Variations of the dephasing time* T_φ *of the quantronium with the reduced bias current* s, *for different values of* R_s. *The parameters used here are those of experiment 5.*

to an even larger immunity to charge noise. By choosing a ratio $E_J/E_C = 4$ instead of the ratio $E_J/E_C = 1.3$ used here, the value of T_φ^{off} indicated in the bottom table of p.179 would be 230 times higher.

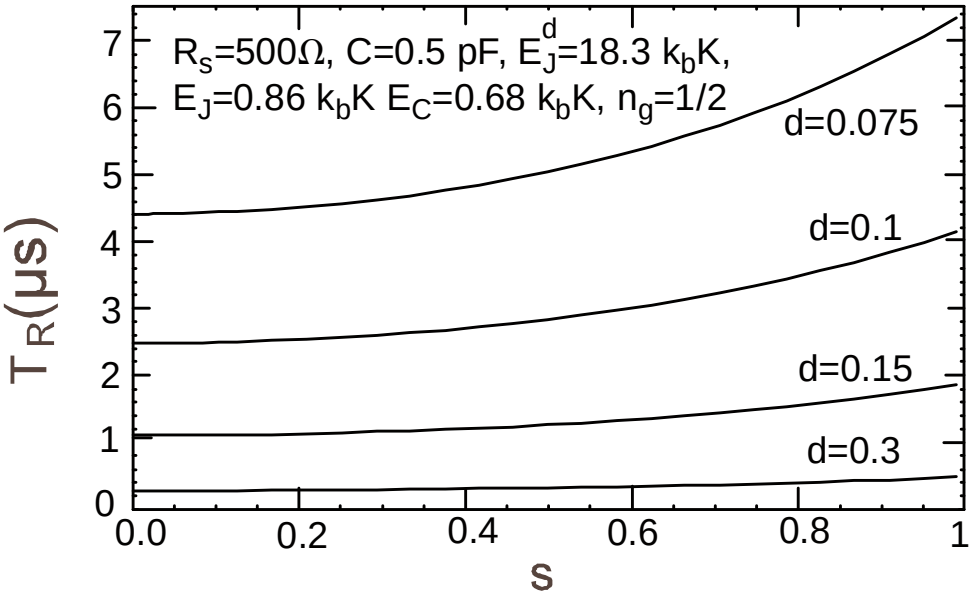

Figure 3.9: *Variations of the relaxation time T_R of the quantronium with the reduced bias current s, for different values of the asymmetry d of the split box.*

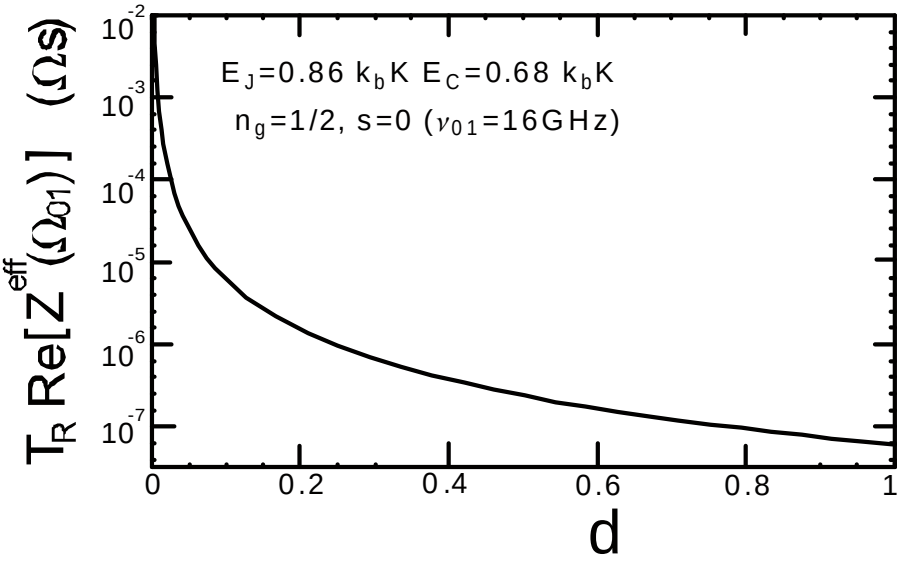

Figure 3.10: *Variations of $T_R \mathrm{Re}[Z_{eff}(\Omega_{01})]$ with the asymmetry d of the split box. The parameters E_J and E_C used here are those of experiment 5 (See chapter 4)*

Appendix 3-A: Quantum description of dissipative dipoles

The true internal structure of a dissipative impedance $Z(\omega)$ is not relevant to describe its decoherence effects on a quantum circuit. It is enough to model $Z(\omega)$ as an infinite series of discrete resonant circuits $\{(L_p, C_p),\ p \in \mathbb{N}\}$. The present appendix describes the procedure used to do so.

3-A-1 Impedance of a dipole

The voltage $v(t)$ across a dipole can be expressed as a function of the current $i(t)$ flowing through it and of a nucleus $\widetilde{Z}(t')$:

$$v(t) = \int_0^{+\infty} dt' \widetilde{Z}(t') i(t - t') \ ,$$

where the kernel real function $\widetilde{Z}(t)$ is the voltage response of the dipole to a current pulse $i(t) = \delta(t)$. The response $\widetilde{Z}(t)$ is zero at negative times.

3.5.4 Impedance of a dissipative dipole

The impedance $Z(\omega)$ is the Fourier transform of $\widetilde{Z}(t)$:

$$Z(\omega) = \int_{-\infty}^{+\infty} dt \widetilde{Z}(t') \exp(\mathbf{i}\omega t) \ . \tag{3.79}$$

In the case of a dissipative dipole, the response $\widetilde{Z}(t)$ vanishes at long times, and the above integral is convergent. Note that $\mathrm{Re}[Z(\omega)]$ is even, and $\mathrm{Im}[Z(\omega)]$ is odd.

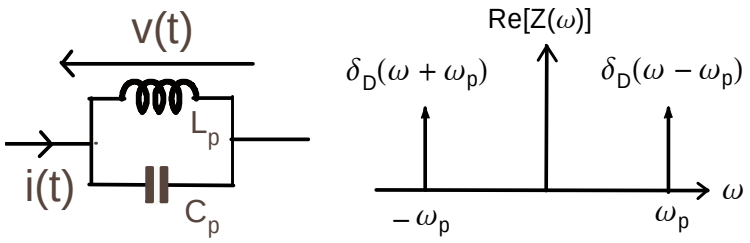

Figure 3.11: *Scheme of a (L_p, C_p) resonant dipole (left panel) and representation of the real part of its impedance (right panel), which is a sum of two Dirac functions.*

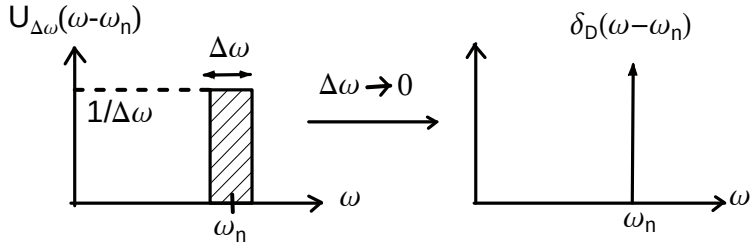

Figure 3.12: *The square function $U_{\Delta\omega}(\omega)$ (left panel) tends towards the Dirac function $\delta_D(\omega)$ (right panel) when $\Delta\omega$ tends towards zero.*

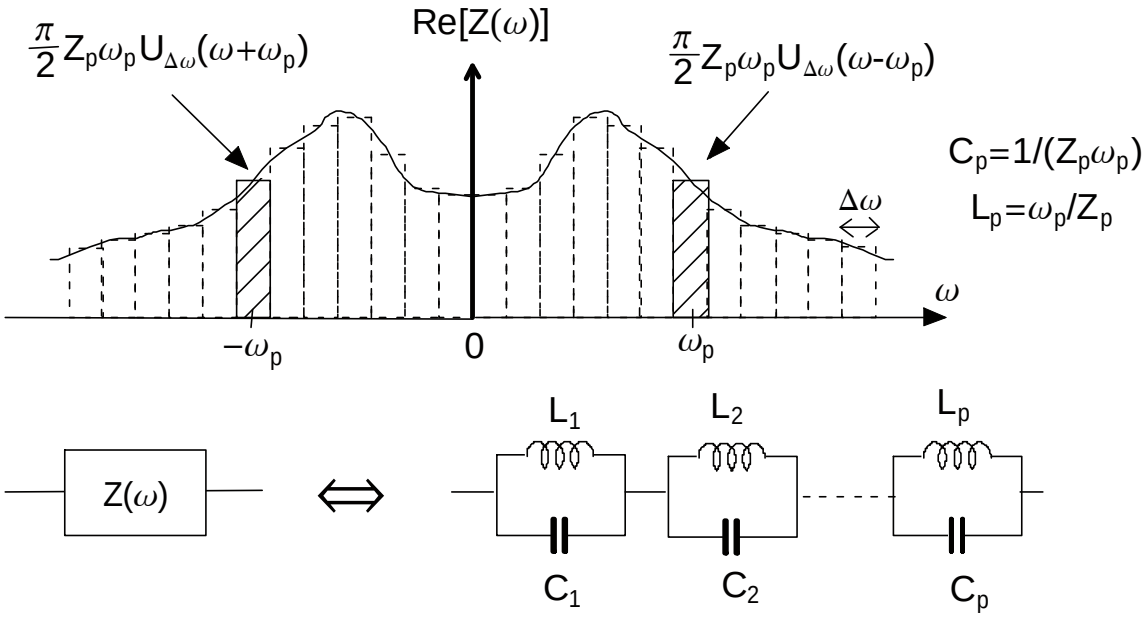

Figure 3.13: *Top*: *Decomposition of* $\mathrm{Re}(Z(\omega))$ *into a staircase function with $\Delta\omega$ wide steps. Bottom: Modelisation of a dissipative element (left panel) by a discrete set of (L_p, C_p) circuits (right panel).*

Impedance of a non dissipative dipole

For non dissipative dipoles, the integral (3.79) does not converge and needs to be regularised:

$$Z(\omega) = \lim_{\epsilon \to 0^+} \int_{-\infty}^{+\infty} \widetilde{Z}(t) \exp(\mathbf{i}\omega t - \epsilon t) dt \ . \tag{3.80}$$

Impedance of a resonant dipole

From (3.80), the impedance $Z(\omega)$ of a resonant dipole consisting of a capacitor C_p in parallel with an inductor L_p (Figure 3.11) is such that:

$$\mathrm{Re}[Z(\omega)] = \frac{\pi}{2} Z_p \omega_p \delta_D(\omega - \omega_p) + \frac{\pi}{2} Z_p \omega_p \delta_D(\omega + \omega_p) \ , \tag{3.81}$$

where:

$$\omega_p = \frac{1}{\sqrt{L_p C_p}} \tag{3.82}$$

is the resonance pulsation of the dipole, and

$$Z_p = \sqrt{\frac{L_p}{C_p}} \tag{3.83}$$

is its characteristic impedance, and where δ_D is the Dirac delta function.

Modeling a dissipative dipole

Any dissipative dipole can be decomposed into a series of resonant dipoles [3]. In order to demonstrate this property, let us define the rectangular function $U_{\Delta\omega}$ (Figure 3.12, left) such that:

$$U_{\Delta\omega}(\omega) = \begin{cases} 1/\Delta\omega \text{ if } |\omega| < \frac{\Delta\omega}{2} \\ \\ 0 \text{ if } |\omega| > \frac{\Delta\omega}{2} \end{cases} \ .$$

Note that:

$$\lim_{\Delta\omega \to 0} U_{\Delta\omega}(\omega - \omega_p) = \delta_D(\omega) \ . \tag{3.84}$$

The real part of an impedance $Z(\omega)$ can be seen as the limit of a staircase function (Figure 3.13, top):

$$\mathrm{Re}[Z(\omega)] = \lim_{\Delta\omega \to 0} \sum_{p \in \mathbb{N}^*} \mathrm{Re}[Z(\omega_p)] \Delta\omega \left[U_{\Delta\omega}(\omega - \omega_p) + U_{\Delta\omega}(\omega + \omega_p) \right] \ , \tag{3.85}$$

where $\Delta\omega$ is a small pulsation interval, and for any $p \in \mathbb{N}^*$, the frequency ω_p is:

$$\omega_p = \Delta\omega \left(p - \frac{1}{2} \right) \ .$$

For each frequency ω_p, there exists a resonant dipole (L_p,C_p) such that:

$$\mathrm{Re}[Z(\omega_p)]\Delta\omega = \frac{\pi}{2} Z_p \omega_p \ , \tag{3.86}$$

with ω_p and Z_p defined in (3.82) and (3.83). Since $\mathrm{Re}[Z(\omega)]$ is even with ω, the expression (3.85) can be recast in the form:

$$\mathrm{Re}[Z(\omega)] = \lim_{\Delta\omega\to 0} \sum_{p\in\mathbb{N}^*} \frac{\pi}{2} Z_p \omega_p [U_{\Delta\omega}(\omega-\omega_p) + U_{\Delta\omega}(\omega+\omega_p)] \ . \tag{3.87}$$

From the Kramers-Kronig relations, for a causal device, the real part of the impedance determines the whole impedance. Hence, in order to determine an equivalent model of $Z(\omega)$, the expression (3.87) of $\mathrm{Re}[Z(\omega)]$ is sufficient. From (3.81), (3.84) and (3.87), the impedance $Z(\omega)$ can be modeled by the ensemble of the resonant dipoles (L_p,C_p) connected in series (Figure 3.13, bottom). At the end of a calculation using this model, the arbitrary discretisation into the (L_p,C_p) elements can be eliminated by setting $\Delta\omega \to 0$. All the results which appear as a sum of the values of a function $f(\omega)$ taken at the oscillator frequencies, and weighted by their impedance take a simple form in this limit:

$$\lim_{\Delta\omega\to 0} \sum_{p\in\mathbb{N}^*} Z_p f(\omega_p) = \frac{2}{\pi} \int_0^{+\infty} \mathrm{Re}[Z(\omega)] \frac{f(\omega)}{\omega} d\omega \ . \tag{3.88}$$

This expression can be derived by multiplying the two sides of (3.86) by $\frac{f(\omega_p)}{\omega_p}$ and by summing the resulting expressions.

3-A-2 Hamiltonian modeling a dissipative element

Hamiltonian of a resonant dipole

In order to make the quantum description of a resonant dipole (L_p,C_p), one can chose different sets of variables. A possible choice is to work with the charge $\widehat{Q_p^c}$ through the capacitor C_p and its conjugate flux $\widehat{\varphi_p^c}$. Since the magnetic flux through the loop between L_p and C_p is arbitrary and irrelevant, one can assert:

$$\widehat{\varphi_p^c} = \widehat{\varphi_p^l} \ . \tag{3.89}$$

where $\widehat{\varphi_p^l}$ is the flux through L_p . Consequently, the hamiltonian $\widehat{h}_p$ of the resonant circuit at frequency ω_p writes as:

$$\widehat{h}_p = \frac{\widehat{Q_p^c}^2}{2C_p} + \frac{\widehat{\varphi_p^c}^2}{2L_p} \ . \tag{3.90}$$

The bosonic operators $\widehat{c}_p$ and $\widehat{c}_p^+$ related to $\widehat{Q_p^c}$ and $\widehat{\varphi_p^c}$ are:

$$\widehat{c}_p = \sqrt{\frac{1}{2\hbar Z_p}}\widehat{\varphi_p^c} + \mathbf{i}\sqrt{\frac{2Z_p}{\hbar}}\widehat{Q_p^c} \ , \qquad \widehat{c}_p^+ = \sqrt{\frac{1}{2\hbar Z_p}}\widehat{\varphi_p^c} - \mathbf{i}\sqrt{\frac{2Z_p}{\hbar}}\widehat{Q_p^c} \ , \tag{3.91}$$

with:

$$Z_p = \sqrt{\frac{L_p}{C_p}} \ , \qquad \omega_p = \frac{1}{\sqrt{L_p C_p}} \ ,$$

and:

$$\left[\widehat{c}_{p'}, \widehat{c}_p^{+}, \right] = \delta_{p,p'} \ .$$

so that:

$$\widehat{h}_p = \hbar\omega_p(\widehat{c}_p^{+}\widehat{c}_p + \frac{1}{2}) \ . \tag{3.92}$$

Quantum description of a dissipative dipole

An hamiltonian treatment of the dissipative dipole is possible once this element is modeled it with a discrete series of resonant circuits (L_p,C_p). Following (3.92), each resonant circuit p is described by an hamiltonian $\widehat{h}_p$. The hamiltonian $\widehat{H}_{env}$ of the impedance is thus:

$$\widehat{H}_{env} = \sum_{p\in\mathbb{N}} \widehat{h}_p \ . \tag{3.93}$$

The infinite number of oscillator accounts for dissipation and leads to the irreversible destruction of the coherent states coupled to the impedance. After the calculation, one must get rid of the arbitrary discretisation into the (L_p,C_p) elements by using the formula (3.88).

Appendix 3-B: Spectral description of noises

3-B-1 Classical definition of noise power

In this thesis, the classical noise power spectrum $S_A^{cl}(\omega)$ of the classical time varying signal $A(t)$, is defined for $\omega \in \mathbb{R}$, as:

$$S_A^{cl}(\omega) = \frac{1}{2\pi} \int_{-\infty}^{+\infty} d\tau \, \langle \Delta A(t) \Delta A(t+\tau) \rangle \exp(-\mathbf{i}\omega\tau) \ . \tag{3.94}$$

where $\langle\rangle$ is a statistical average and where

$$\Delta A(t) = A(t) - \langle A \rangle$$

refers to the fluctuations of $A(t)$ away from its average value $\langle A \rangle$. Note that this power spectrum obeys the Wiener-Kintchine theorem:

$$\langle A(t) A(t+\tau) \rangle = \int_{-\infty}^{+\infty} d\omega S_A^{cl}(\omega) \exp(\mathbf{i}\omega\tau) \ . \tag{3.95}$$

The Parseval theorem giving the total power of the noise is just (3.95) taken for $\tau = 0$:

$$\left\langle A^2 \right\rangle = \int_{-\infty}^{+\infty} d\omega S_A^{cl}(\omega) \ . \tag{3.96}$$

3-B-2 Reconstruction of the temporal signal from the spectrum

Since the classical noise spectrum $S_A^{cl}(\omega)$ is even with ω, $A(t)$ can be approximated by the limit of a Fourier series:

$$A(t) = \langle A \rangle + \lim_{\Lambda \to 0} \sum_{p \in \mathbb{N}} A_p \cos(p\Lambda t + \gamma_{p\Lambda}) \ , \tag{3.97}$$

where Λ is small frequency interval, and where $\gamma_{p\Lambda}$ is a random phase defined for each frequency $p\Lambda$. From (3.97), the total noise power of $A(t)$ writes, in this representation:

$$\left\langle A^2 \right\rangle = \sum_{p \in \mathbb{N}} \frac{A_p^2}{2} \ . \tag{3.98}$$

On the other hand, from (3.96), one has:

$$\left\langle A^2 \right\rangle = \sum_{p\in\mathbb{N}} 2\Lambda S_A^{cl}(p\Lambda) \ . \tag{3.99}$$

where the factor two stems from the fact that one has to take into account both positive and negative pulsations. Equations (3.98) and (3.99) imply that:

$$A_p^2 = 4\Lambda S_A^{cl}(p\Lambda) \ ,$$

Therefore, this Fourier series representation can be written symbolically as:

$$A(t) \text{ " = " } 2\int_0^\infty \sqrt{d\omega \ S_A^{cl}(\omega)}\cos(\omega t + \gamma_\omega) \ . \tag{3.100}$$

At the end of the calculation, the random phase γ_ω must be eliminated by using a statistical average over it. This trick allows to correctly obtain all physical quantities linear in the noise spectrum.

3-B-1 Generalised definition of noise power

For a quantum variable $\widehat{A}(t)$, one can define the generalised noise power spectrum as:

$$S_A(\omega) = \frac{1}{2\pi}\int_{-\infty}^{+\infty} d\tau \left\langle \widehat{A}(t)\widehat{A}(t+\tau) - \left\langle \widehat{A} \right\rangle^2 \right\rangle \exp(-\mathbf{i}\omega\tau) \tag{3.101}$$

for any $\omega \in \mathbb{R}$.

3-B-3 Noise Spectrum of a dissipative impedance

The noise due to a dissipative impedance $Z(\omega)$ can be taken into account by considering an equivalent voltage noise source $u_Z(t)$ in series with $Z(\omega)$ or an equivalent current noise source $i_Z(t)$ in parallel with $Z(\omega)$ (Figure 3.14). From the quantum fluctuation-dissipation theorem, the generalised noise power (3.101) are, for $u_Z(t)$ and $i_Z(t)$,

$$S_{u_Z}(\omega) = \frac{\hbar\omega}{2\pi}\left(\coth(\frac{\hbar\omega}{2kT}) + 1\right)\mathrm{Re}\left(Z(\omega)\right) \tag{3.102}$$

$$S_{i_Z}(\omega) = \frac{\hbar\omega}{2\pi}\left(\coth(\frac{\hbar\omega}{2kT}) + 1\right)\mathrm{Re}\left(1/Z(\omega)\right) \tag{3.103}$$

The low and high frequency limits of these expressions are:

ω domain	$S_{u_Z}(\omega)$	$S_{i_Z}(\omega)$
$\lvert\hbar\omega\rvert \ll kT$	$kT\,\mathrm{Re}[Z(\omega)]/\pi$	$kT\,\mathrm{Re}[1/Z(\omega)]/\pi$
$\hbar\omega \gg kT$	$\hbar\omega\,\mathrm{Re}[Z(\omega)]/\pi$	$\hbar\omega\,\mathrm{Re}[1/Z(\omega)]/\pi$
$\hbar\omega \ll -kT$	0	0

. (3.104)

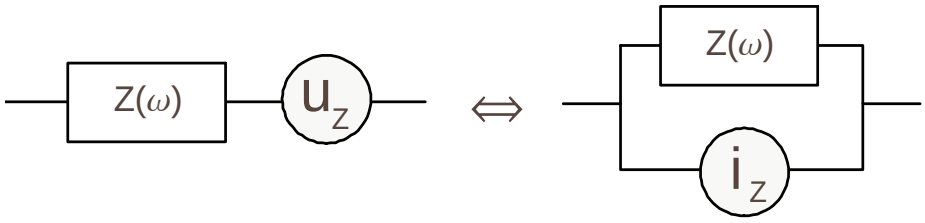

Figure 3.14: *Impedance $Z(\omega)$ in series with its equivalent voltage noise generator (top), or in parallel with its equivalent Johnson noise sourve (bottom).*

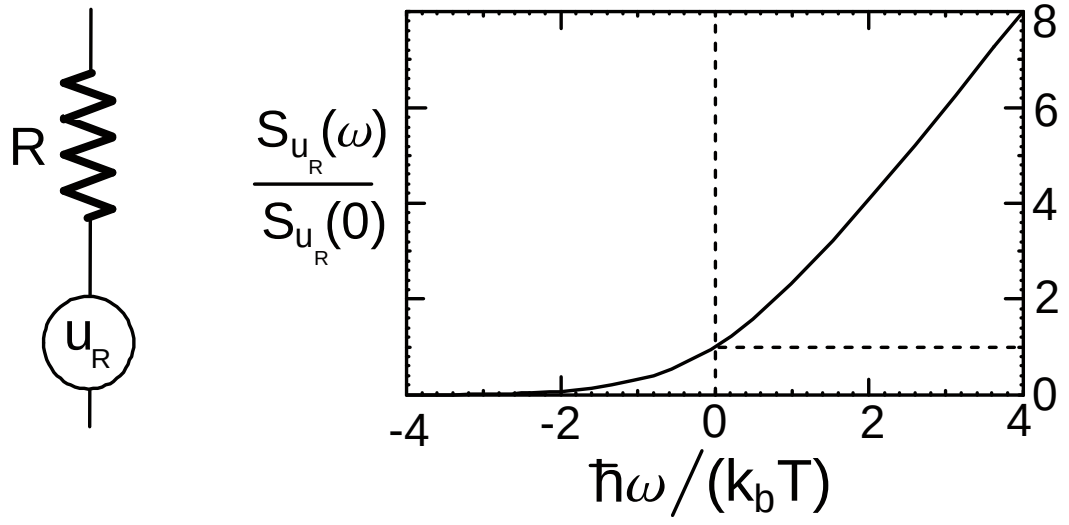

Figure 3.15: *Left panel: Pure resistor R in series with its equivalent voltage generator $u_R(t)$. Right panel: reduced voltage spectral density $S_{u_R}(\omega)/S_{u_R}(0)$ of $u_R(t)$.*

As an example, the equivalent spectrum of voltage noise $S_{u_R}(\omega)$ of a resistor R is plotted in Figure 3.15. This spectrum corresponds to a one dimensional black body, as expected from the equivalence between a resistor R and an infinite length transmission line with characteristic impedance R. For $|\hbar\omega| \gg kT$, the asymmetry of S_{u_R} reveals the asymmetry between spontaneous emission and absorption processes. The impedance can absorb energy at any frequency, but its emitting power falls off at frequencies $\omega > k_b T/\hbar$.

Chapter 4

The quantronium

The major source of decoherence in a Cooper pair box is the 1/f charge noise coupled to its gate. In order to use the Cooper pair box as a quantum bit, one must choose a strategy which minimizes the influence of this noise. At the beginning of this thesis work, we intended to develop electrometers as readout devices for a quantum bit based on the Cooper pair box. As explained in chapters 1 and 2, this strategy requires a box with a ratio $E_J/E_C \leq 0.5$ in order to have a sufficiently large charge signal. We have shown in the previous chapters that such an experiment would be too sensitive to the $1/f$ charge noise both in the Cooper pair box and the electrometer. We have also shown that another readout strategy, based on the measurement of the loop current in a split Cooper pair box, would allow to use larger values of E_J/E_C, and thus would make the experiment more immune to the $1/f$ charge noise. The operation of the quantronium circuit that we have developed by following this second strategy is described in this chapter.

4.1 Operating principle of the quantronium

4.1.1 The quantronium circuit

The quantronium consists of a split box which includes in its superconducting loop an extra Josephson junction with energy $E_J^d \gg E_J$, called the readout junction (Figure 4.1). When the box loop is biased with a magnetic flux $\varphi_0\delta_m$, the superconducting phase difference across the series combination of the two junctions of the box is:

$$\delta = \delta_m + \gamma \ ,$$

where γ is the phase difference across the readout junction. The readout junction is AC shunted, so that it can switch to the voltage state when the bias current I_b approaches its critical current

$I_0^d = E_J^d/\varphi_0$. As discussed in chapter 3, when $I_b \ll I_0^d$, the readout junction behaves below its plasma frequency as a small inductance which provides a good decoupling of the Cooper pair box from the readout circuit at low frequency. The immunity to 1/f noise is achieved by choosing a large ratio E_J/E_C, which is compatible with measuring the loop current of the split box, and by setting $n_g = 1/2$.

Next page: Figure 4.1, Principle of the quantronium experiment

- *Top: Electrical scheme of the quantronium, showing the different functional blocks. The circuit is based on a split box with Josephson energy E_J and charging energy E_C. The box state manipulation is achieved by applying radiofrequency pulses on the box gate with the source U_{RF}. For the purpose of readout, the superconducting loop of the box includes a readout Josephson junction with energy E_J^d. This readout junction is AC shunted with a capacitor C_L connected in parallel with the series combination of a resistor R_s and of a capacitor C_s. Therefore, the junction can switch to a high voltage state with a rate $\Gamma_u(I_b, n_g, \delta_m)$ which depends on the bias current I_b and on the state $|u\rangle$ of the box just before the measurement. The control of the box transition frequency ν_{01} is achieved with the gate voltage source V_g and with the magnetic phase δ_m applied through the box loop. The magnetic phase δ_m shifts the superconducting phase $\delta = \gamma + \delta_m$ across the series combination of the two box junctions from the phase γ across the readout junction.*

- *Bottom: The signals involved in the quantronium manipulation and readout. Top: Radiofrequency pulses are applied to the gate for state manipulation. Middle: A readout current pulse I_b is applied to the parallel combination of the split box and of the detection junction a time t_d after the last microwave pulse. Bottom: Voltage $V(t)$ across the junction in the cases when the junction switches or not. Ideally, the probability to observe a pulse is the weight of $|1\rangle$ in the quantum state $|u\rangle$ of the box just before the measurement. A discriminator with threshold V_{th} converts $V(t)$ into a boolean 0/1.*

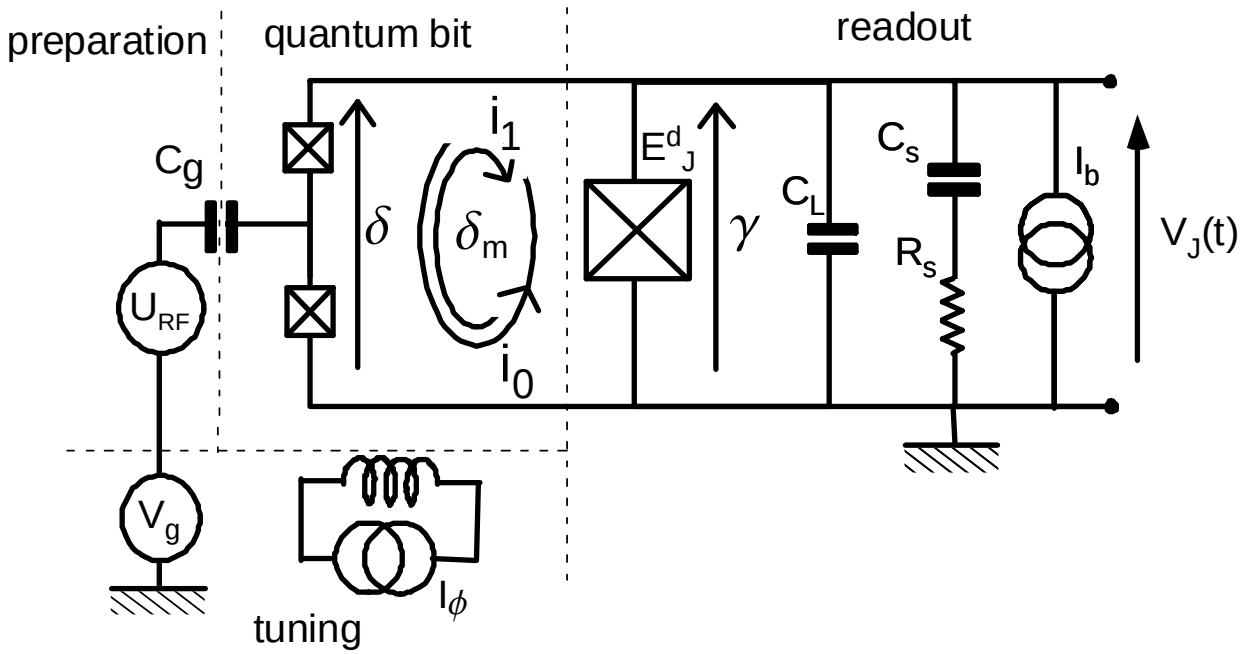

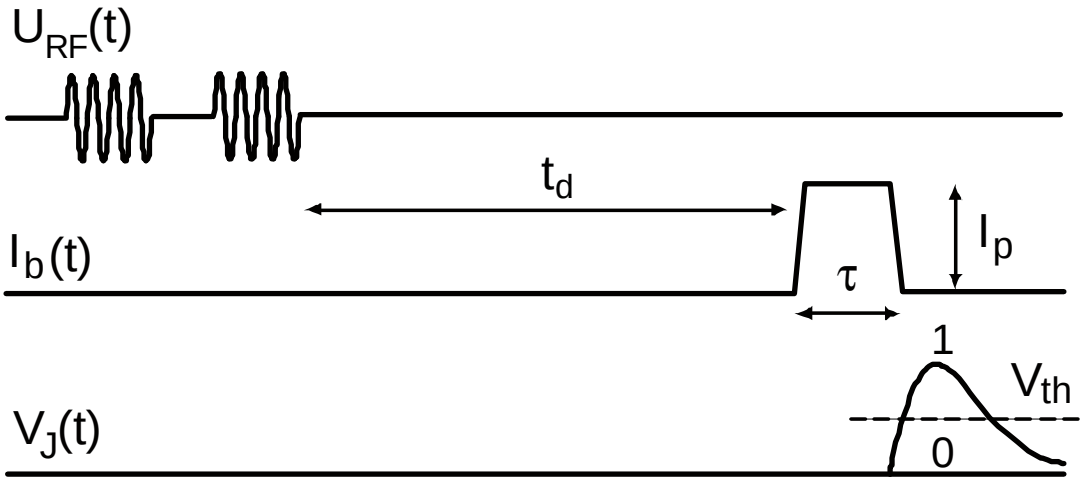

Figure 4.1

4.1.2 Manipulation and readout principle

The manipulation of the quantronium state can be achieved by applying to its gate radiofrequency pulses with frequency $\nu_{RF} \simeq \nu_{01}$ and amplitude U_{RF} (see Figure 4.1, bottom and section 1.3.2). Ideally, after the pulse sequence, the quantronium is in a pure state:

$$|u\rangle = \cos(\theta_u/2)\exp(-\mathbf{i}\varphi_u/2)\,|0\rangle + \sin(\theta_u/2)\exp(\mathbf{i}\varphi_u/2)\,|1\rangle \ .$$

The readout is triggered by a bias current pulse with amplitude I_p and with duration τ applied to the parallel combination of the two small junctions, of the large junction and of its shunting impedance. Under the influence of this pulse, the superconducting phase $\delta = \gamma + \delta_m$ is shifted and the dephasing rate of the box strongly increases. As a consequence, the box state is projected on the state $|0\rangle$ with a probability:

$$p_0 = \cos^2(\theta_u/2) \ ,$$

or on the state $|1\rangle$ with a probability $p_1 = 1 - p_0$. The current passing through the readout junction after the projection of the box on the state $|k\rangle$, with $k \in \{0,1\}$ is $I_b - i_k(n_g, \delta = \gamma + \delta_m)$, where i_k is the average loop current associated to the state $|k\rangle$. If the box is in the state $|u\rangle$ just before the measurement, the switching probability of the readout junction is thus:

$$P_u(I_p, \tau, n_g, \delta_m) = p_0 P_0(I_p, \tau, n_g, \delta_m) + p_1 P_1(I_p, \tau, n_g, \delta_m) \ ,$$

where the switching probability in the state $|k\rangle$,

$$P_k(I_p, \tau, n_g, \delta_m) = 1 - \exp(-\Gamma_k(I_p, n_g, \delta_m)\tau) \ ,$$

with $k \in \{0, 1\}$, depends on the switching rate $\Gamma_k(I_p, n_g, \delta_m)$ in the state $|k\rangle$. The readout is optimal if I_p can be tuned so that the readout junction switches with a large probability P_1 for state $|1\rangle$ and a small probability P_0 for state $|0\rangle$. A switching event then corresponds to the detection of the state $|1\rangle$.

4.2 Current discrimination using an AC shunted Josephson junction

4.2.1 Principle

The dynamics of an underdamped AC shunted Josephson junction

Part 2.1.5 focuses on the dynamics of a hysteretic Josephson junction in the case when its capacitance C_J can be neglected (overdamped regime). The readout junction of the circuit of Figure 4.2 can easily be placed in the opposite regime, namely the underdamped regime. This

junction is connected to a capacitor C_L and to a dipole $(R_s + C_s)$. The total impedance seen by the pure Josephson element E_J^d is then:

$$Z(\omega) = \left(\frac{1}{\mathbf{i}\omega C} + \frac{1}{R_s + 1/\left(\mathbf{i}\omega C_s\right)} \right)^{-1} , \tag{4.1}$$

where the total capacitance:

$$C = C_J + C_L$$

seen by the junction is artificially increased by the capacitor C_L . When the tilt coefficient $s = I_b/I_0$ of $\mathcal{U}$ is close to 1, the frequency of the oscillations of the phase γ at the bottom of the wells is well approximated by:

$$\frac{\omega_p}{2\pi} \simeq \frac{\omega_0}{2\pi}(2-2s)^{1/4} , \tag{4.2}$$

with

$$\frac{\omega_0}{2\pi} = \sqrt{\frac{I_C}{\varphi_0 C}} .$$

The quality factor of these oscillations is:

$$Q \simeq \frac{C\omega_p}{\mathrm{Re}[1/Z(\omega_p)]} .$$

The escape of the fictive particle representing the state of the readout junction (see chapter 2) out of a potential well triggers its run-away down the washboard potential and the subsequent development of a finite voltage across the junction. The escape rate describing this process depends on the potential barrier height:

$$\Delta U(I_b) \simeq \frac{4\sqrt{2}}{3} E_J^d (1-s)^{3/2} .$$

In the underdamped regime $Q \gg 1$, below the cross-over temperature defined by:

$$k_B T_{CO} = \frac{\hbar\omega_p}{2\pi} , \tag{4.3}$$

quantum fluctuations of the phase dominate thermal fluctuations and the particle escapes by quantum tunneling through the barrier at a rate [3]:

$$\Gamma_s(I_b) = 52\sqrt{\frac{\Delta U}{\hbar\omega_P}}\frac{\omega_p}{2\pi}\exp\left(-7.2\frac{\Delta U}{\hbar\omega_p}\right) . \tag{4.4}$$

At high temperature, the phase γ is an almost classical variable and the switching occurs mainly by thermal activation up to the top of the energy barrier ΔU, at a rate:

$$\Gamma_s(I_b) = a\frac{\omega_p}{2\pi}\exp\left(-\frac{\Delta U}{k_B T}\right) , \tag{4.5}$$

with a prefactor $a \simeq 1$ [80, 81]. It is useful to define an effective escape temperature T_{esc} by the relation:

$$\Gamma_s = \frac{\omega_p}{2\pi}\exp\left(-\frac{\Delta U}{k_B T_{esc}}\right) . \tag{4.6}$$

The theoretical predictions [82] for a junction in the regime $Q \geq 1$ are $T_{esc} \simeq T$ for T above T_{CO}, and $T_{esc} \simeq \hbar\omega_p/7.2k_B$ below.

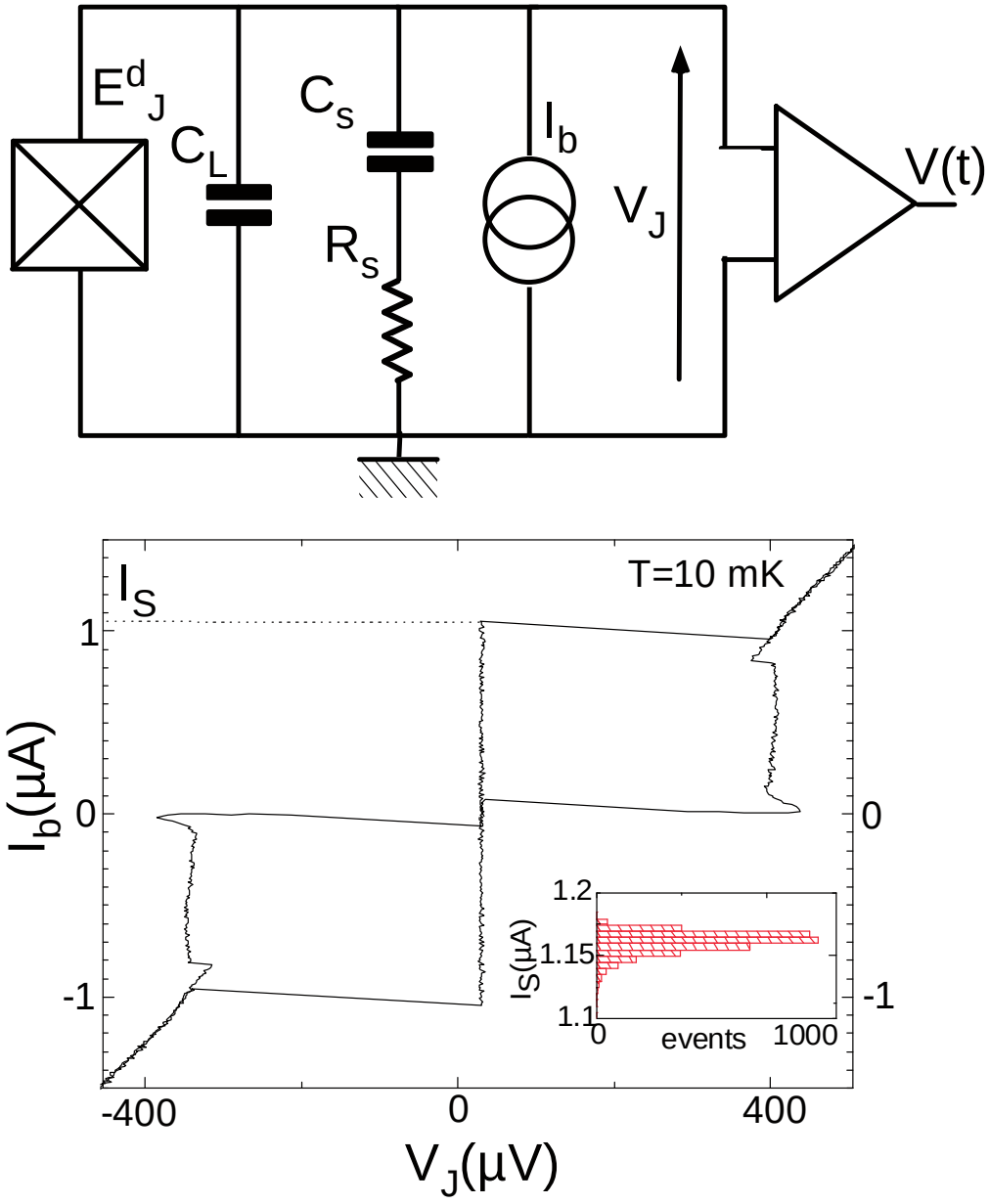

Figure 4.2: *Top panel: Circuit used for the measurement of the AC shunted Josephson junction in experiment 4. The capacitor* $C_L \approx 1$ pf *is implemented on-chip. The capacitance* $C_s = 10$ pf *is that of the connection between the sample and the bias lign. The component* $R_s = 500\ \Omega$ *is a surface mounted component. Bottom panel: Large scale* $I_b - \overline{V_J}$ *characteristic of the circuit measured at* $T = 10$ mK. *The junction jumps to the high voltage state when the bias current* I_b *reaches a switching current* I_s, *distributed according to a switching histogram shown in the inset (Note that this switching histogram was taken for* $dI_b/dt = 12.8$ nA/μs, *but the* $I_b - \overline{V_J}$ *characteristic was taken at a slower bias current ramp rate).*

Phase dynamics of the full quantronium circuit

We consider again the case of the full quantronium circuit[1] (Figure 4.1, top). The switching rate $\Gamma_k(I_b,n_g,\delta_m)$, $k \in \{0,1\}$ of the large junction now depends on the bias current I_b, on the reduced bias flux δ_m and on the state $|k\rangle$ on which the box has been projected at the beginning of the measurement. An approximate calculation of the switching rate $\Gamma_k(I_b,\delta_m)$ can be obtained within the framework of the Born-Oppenheimer hypothesis, assuming that the dynamics of the phase γ is slow compared to that of the Cooper pair box. This is justified when the Cooper pair box transition frequency ν_{01} is always much larger than the plasma frequency of the readout junction. In this case, the dynamics of the readout junction is that of a junction in a modified potential (see Figure 4.3):

$$U_k(I_b,n_g,\gamma) = E_k(n_g,\delta=\delta_m+\gamma) - E_J^d\cos\gamma - I_b\gamma\varphi_0 \ .$$

For $E_J^d \gg E_J$, one can consider that the switching angle of the readout junction is independent from n_g and δ_m :

$$\gamma \simeq \arcsin s$$

Following this approximation, for $\delta_m < |\pi/2|$, the potential U_k is close to that calculated assuming that the readout junction imposes the phase $\delta = \delta_m + \gamma$ to the split box:

$$\widetilde{U_k}(I_b,n_g,\gamma) = -E_J^d\cos(\gamma) - [I_b - i_k(n_g,\delta_m+\gamma)]\gamma\varphi_0 \ .$$

The loop current-phase characteristic of the split box can thus be obtained by measuring the bias current I_b at constant $\Gamma_k(I_b,n_g,\delta_m)$.

In the experiment 5, at the moment of the switching, s is close to 1, so that one can consider that the phase of the detection junction at the moment of the switching is $\gamma^s \simeq \frac{\pi}{2}$. For $\delta_m \approx \frac{\pi}{2}$, the transistor frequency falls to zero in the phase range probed by the switching :$\delta^s = \delta_m + \gamma^s \simeq \frac{\pi}{2}+\frac{\pi}{2} = \pi$, so that the Born-Oppenheimer approximation is not valid anymore. In this case, the calculation of the switching rate requires to treat the full system quantum mechanically [83].

Discriminating power of the quantronium readout junction

The discriminating power of the readout for a bias-current pulse of duration τ is defined at the optimal point as:

$$\alpha(\tau) = \max_{I_p}[P_1(I_p,\tau,n_g=\frac{1}{2},\delta_m=-\frac{\pi}{2}) - P_0(I_p,\tau,n_g=\frac{1}{2},\delta_m=-\frac{\pi}{2})] \ . \qquad (4.7)$$

[1] Note that our readout method could be used to measure the phase-current characteristic $i(\delta)$ through any dipole based on the tunneling of the Cooper pairs. (atomic contacts, small Josephson junction arrays...)

Perfect single shot readout corresponds to $\alpha = 1$. The relations (4.4) and (4.5) show that α is limited by thermal and quantum fluctuations, which decrease the derivative $d\Gamma_s/dI$. Assuming that the temperature is lower than T_{CO}, one can enhance significantly α by adding a capacitor C_L to the circuit in order to decrease artificially the readout junction plasma frequency ω_p. Finally, the time resolution will be limited by the readout pulse duration, provided the readout junction stays at thermal equilibrium in one of its metastable potential wells while the bias current is raised. For that purpose, its Q factor must not be too large. For the parameters:

$$\begin{aligned} E_J &= E_C = 0.8 \text{ k}_b\text{K}, \, d = 0.1, \delta_m = 0 \Rightarrow \Delta i_{01}(n_g = 1/2, \delta = \pi/2) = 10.68 \text{ nA} \\ I_J^d &= 0.8 \ \mu\text{A}, \ C = 1 \text{ pF} \Rightarrow \omega_0/2\pi = 7.8 \text{ GHz}, \ \min\left[T_{esc}\right] = 60 \text{ mK} \, . \end{aligned}$$

the expected discriminating power is:

$$\alpha(\tau = 0.5 \ \mu\text{s}) = 0.95 \, .$$

Next page:

- *Top: Figure 4.3. Comparison between the exact escape potentials U_0 and U_1 seen by the phase γ of the readout junction in the cases where the box is in the state $|0\rangle$ (blue line) and in the state $|1\rangle$ (red line), and the potentials $\widetilde{U}_0$ and $\widetilde{U}_1$ that the readout junction alone would see if its bias current I_b was shifted by the box loop currents i_0 or i_1 (dashed lines). These potentials are shown for increasing values of δ_m from top to bottom. They are furthermore offsetted in order to allow a comparison between them. When $\delta_m < \pi/2$, the switching dynamics governed by these two models are equivalent. When δ_m exceeds $\pi/2$, the two potentials become very different and approximating U_k with $\widetilde{U}_k$ is not valid anymore.*

- *Bottom: Figure 4.4. Experimental signals in a switching experiment. A trapezoidal bias current pulse with amplitude I_p and with duration τ is applied (green trace). The junction can either switch to the voltage state (red trace) or not (blue trace). When the junction switches to the voltage state, the voltage pulse is detected with a threshold discriminator. The data shown here have been taken in experiment 5 for pulses with duration $\tau = 0.1$ μs. In experiment 4 (data not shown), the duration of the pulses was rather $\tau = 0.5$ μs.*

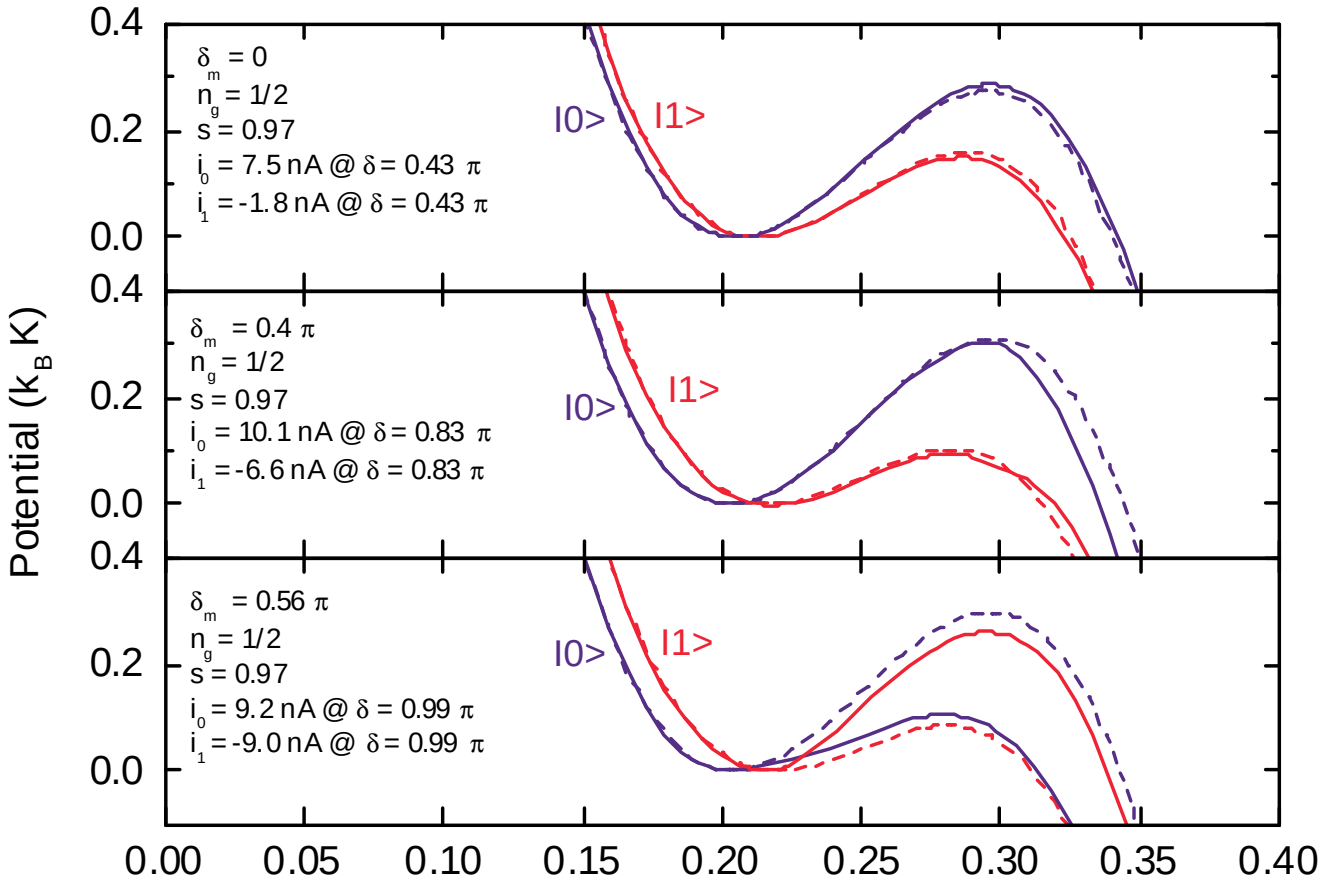

↑Figure 4.3 ↓Figure 4.4

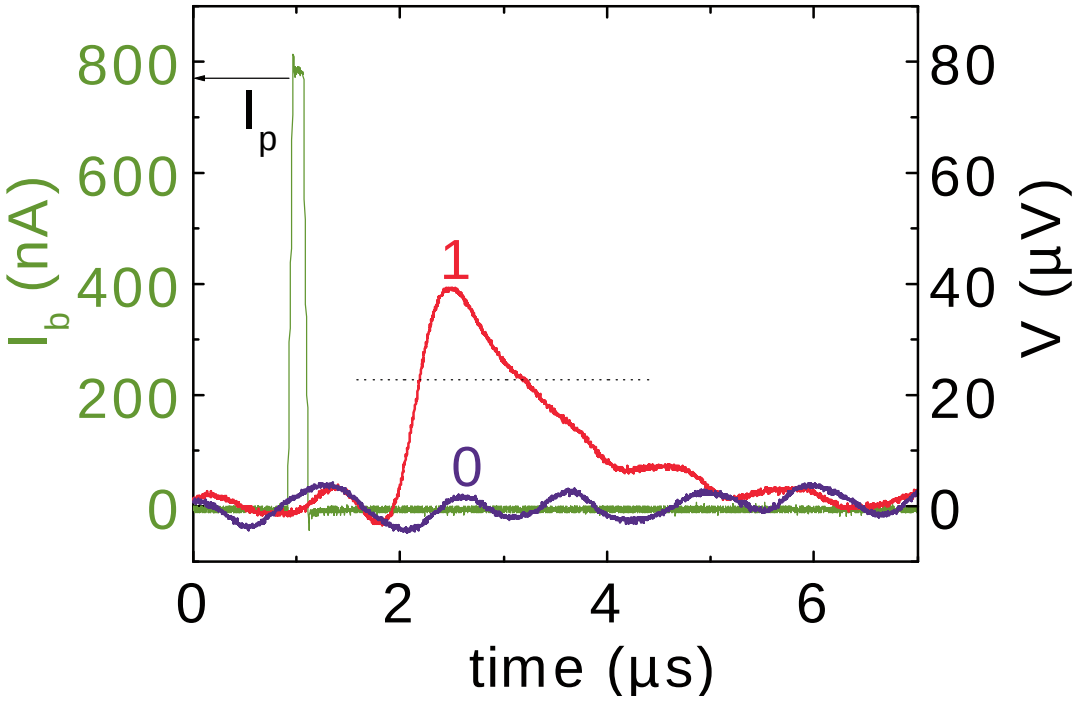

4.2.2 Characterisation of the readout circuit alone (Experiment 4)

Switching experiment

We have first implemented the experiment with the split box disconnected on purpose, in order to evaluate the discriminating power of the readout junction (see appendix 4-A and the publication [28] for further details). The capacitor C_L is implemented on-chip. The capacitance $C_s = 10$ pf intervening in the impedance (4.1) is provided by the cable connecting the bias line to the sample (see Figure 4.35). The resistor $R_s = 500\ \Omega$ is a CMS component. Typical switching and non switching signals are shown in Figure 4.4. In experiment 4, when the switching of the junction occurs, the voltage on the measuring line with capacitance $C_M \approx 1$ nF rises at a rate $I_C/C_M \approx 1$ mV/μs . The switching is detected by monitoring the voltage with a low-noise amplifier with a sensitivity of 1.4 nV/$\sqrt{\text{Hz}}$ in a 1 MHz bandwidth.

Switching probabilities

We have measured the switching probability $P_s(I_p,\tau) = 1 - \exp(-\Gamma_s(I_p)\tau)$ of the readout junction alone when a bias current pulse with duration $\tau = 0.5$ μs and with adjustable height I_p is applied, at different temperatures (Figure 4.5). The maximum slope, obtained at the lowest temperature, would correspond to a discriminating power:

$$\alpha(\tau = 0.5\ \mu\text{s}) = 0.58$$

if this readout junction was used to measured a split box with $\Delta i_{01}(n_g = 1/2,\ \delta = \pi/2) = 10.7$ nA .

Switching rates and escape temperatures

We have deduced the switching rates $\Gamma_s(I_b)$ from the measured probabilities $P_s(I_p,\tau)$ (Figure 4.6). The escape temperatures calculated from the fit of these rates with:

$$I_c = 1.17\ \mu\text{A}$$

and

$$\omega_0/2\pi = 12\ \text{GHz}$$

are plotted in Figure 4.7 (The fitting method is described in detail in [4]). The lowest escape temperature found is about $\min[T_{esc}] = 90$ mK ,which is stronger than the expected value of 60 mK . This discrepancy can be attributed to two effects. First the effective value of the capacitor C may be smaller than expected ($\omega_0/2\pi = 12$ GHz corresponds to $C \approx 0.6$ pF). Secondly, due to the large bandwidth of the biasing lines (about 200 MHz), radiofrequency noise could reach the device and heat the sample.

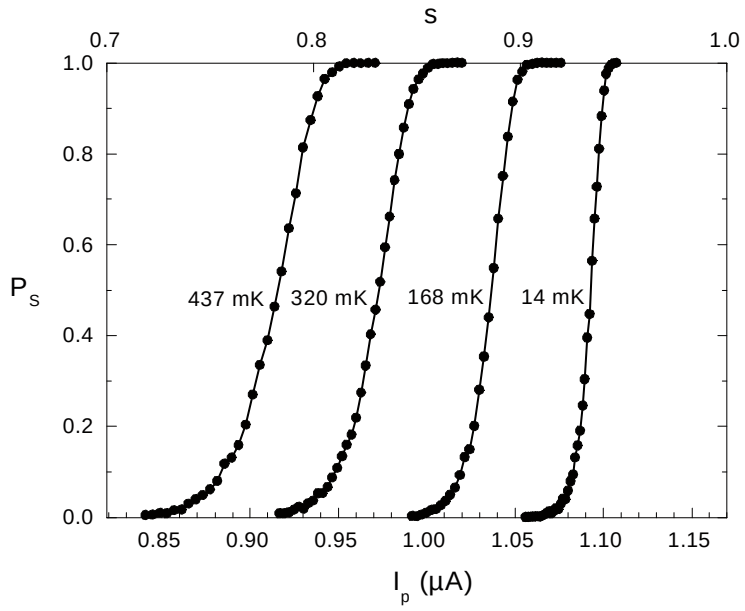

Figure 4.5: *Switching probability P_s of the readout junction when* 0.5 μs *long trapezoidal pulses with variable amplitude I_p are applied, for $T =$* 437, 320, 168 *and* 14 mK (*from left to right). The sharpest step, obtained at the lowest temperature, would correspond to a discriminating power $\alpha(\tau = 0.5\ \mu\text{s}) = 0.58$ for the readout of a quantronium with $\Delta i_{01} = 10.7$ nA.*

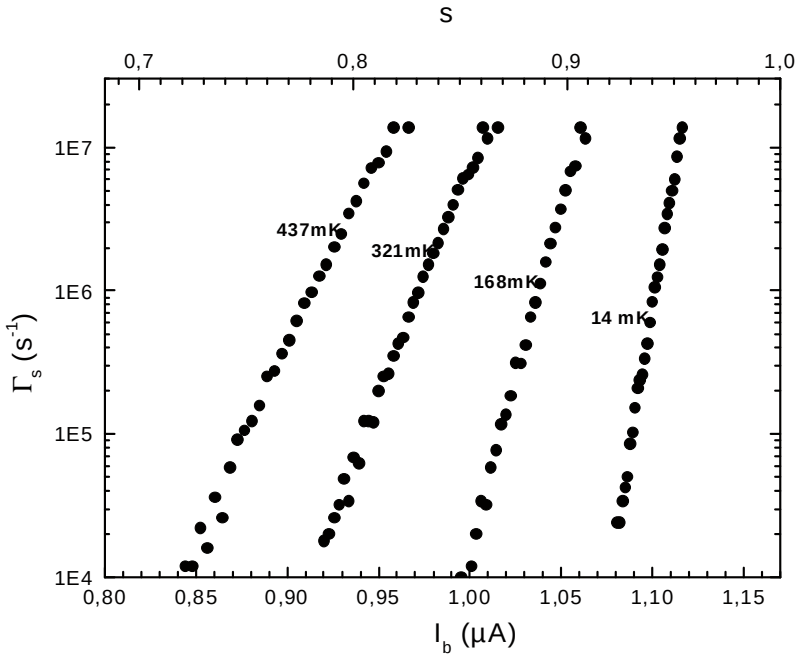

Figure 4.6: *Switching rate Γ_s of the readout junction as a function of the bias current I_b at different temperatures, calculated from the switching probabilities of Figure* 4.5.

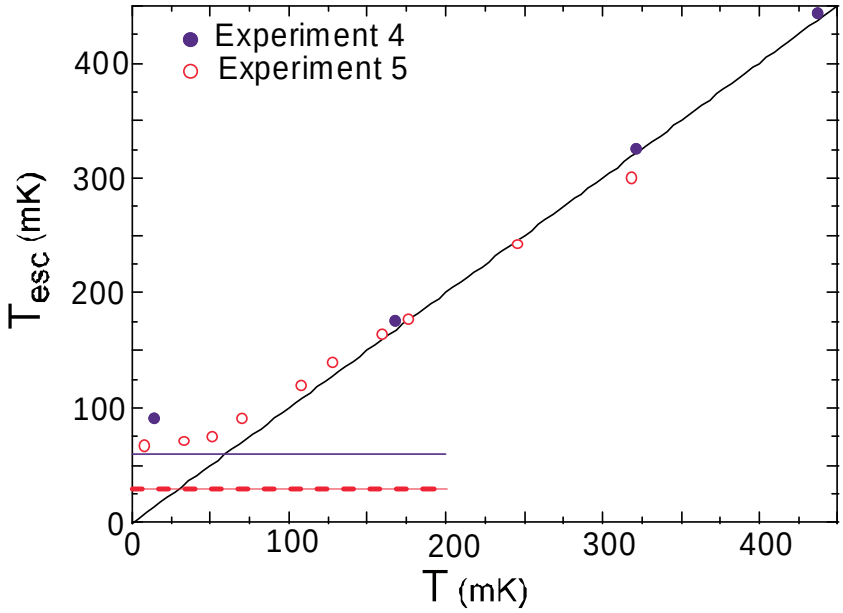

Figure 4.7: *Escape temperature calculated from the experimental switching rates, for experiment 4 (solid dots) and by anticipation for experiment 5 (open dots), compared to the predicted quantum escape temperature for experiment 4 (solid line), and experiment 5 (dashed line). The black line represents the classical law* $T = T_{esc}$.

Conclusion

In summary, experiment 4 shows that the readout strategy based on the switching of an auxiliary junction inserted in the split box loop can approach the current resolution necessary for single shot readout.

4.3 Operation of a quantronium circuit (Experiment 5)

4.3.1 Switching probabilities in the ground state

In experiment 5, we have implemented the full circuit of Figure 4.1 (see Appendix 4-A and the appended publications [28, 29]). The different electrical components represented in this scheme have been implemented in the same way as for experiment 4. We have increased C_L in order to reduce the escape temperature which was higher than expected in experiment 4. We have determined from the experimental switching rates (see section 4.3.4):

$$I_0^d = 0.77\ \mu\text{A} \Leftrightarrow E_J^d = 18.4\ \text{k}_b\text{K}$$

and

$$\omega_0/2\pi = 8\ \text{GHz}\ .$$

which corresponds to:

$$C = 0.9 \text{ pF}$$

The lowest escape temperature in the experiment 5 is $\min[T_{esc}] = 70$ mK (see Figure 4.7). The discriminating power of the readout junction of experiment 5 is thus better than that of experiment 4. Indeed, for $\Delta i_{01} = 10.7$ nA, we have reached the same discriminating power as in experiment 4, but in a measurement time 5 times shorter (Figure 4.8):

$$\alpha(\tau = 0.1\ \mu\text{s}) = 0.54\ . \tag{4.8}$$

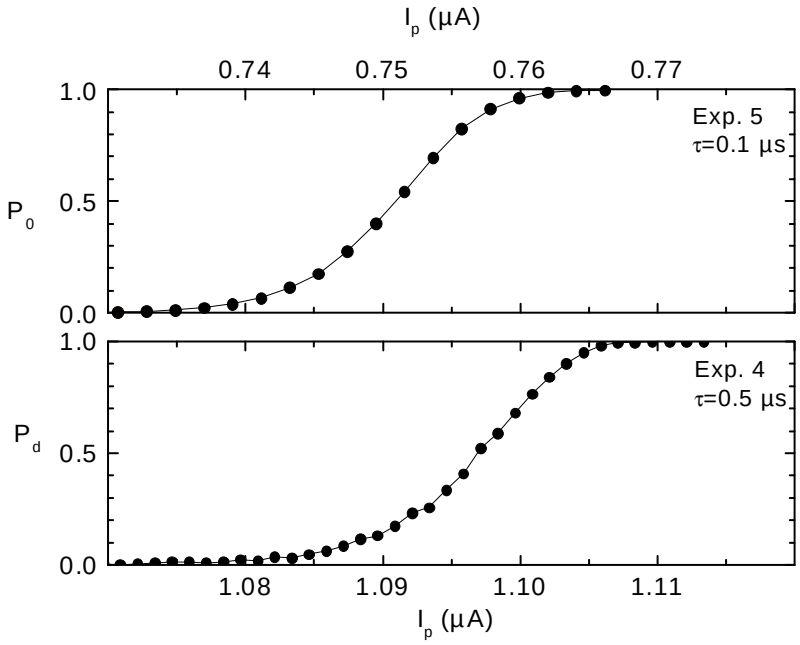

Figure 4.8: *Comparison between the switching probability* $P_0(I_p - i_0, \tau = 0.1\ \mu\text{s}, n_g = constant, \delta_m = 0)$ *obtained in experiment 5 for the readout junction of the quantronium in state* $|0\rangle$ *(top panel, data processing explained in Figure* 4.22*) and the switching probability curve* $P_s(I_p, \tau = 0.5\ \mu\text{s})$ *of the isolated junction of experiment 4. Although the duration* τ *is different for the two experiments, the discriminating power reached is the same.*

4.3.2 Current measurements

When the box is in the state $|k\rangle$ just before the measurement, the switching probability of the readout junction is P_k . According to the section 4.2.1, for $|\delta_m| < \pi/2$, this switching probability is related to the switching probability P_s of the isolated readout junction:

$$P_k(I_p, \tau, n_g, \delta_m) = P_s(I_J(I_p, n_g, \delta_m, k), \tau)\ ,$$

where the current passing through the junction is::

$$I_J(I_p, n_g, \delta_m, k) \approx I_p - i_k(n_g, \delta = \delta_m + \gamma^s)\ ,$$

and where γ^s is the phase of the readout junction at the moment of the switching (γ^s can be considered as constant). In practice, the critical current I_0^d of the readout junction is modulated by the flux $a\delta_m$ which penetrates its barrier [40]:

$$I_0^d(\delta_m) = I_0^d \left|\mathrm{sinc}(a\delta_m/\varphi_0)\right| \ .$$

with $a < 1$. This modulation contributes to the variations of the bias current amplitude I_p^r giving a constant switching probability r, that is:

$$P_k(I_p^r, \tau, n_g, \delta_m) = r \ .$$

The difference:

$$\Delta I_p^r(n_g, \delta = \delta_m + \gamma^s) = I_p^r(n_g, \delta = \delta_m + \gamma^s) - \left|I_0^d(\delta_m)\right|$$

identifies with $i_k(n_g, \delta = \delta_m + \gamma^s)$ for $|\delta_m| < \pi/2$. This allows to measure the phase dependence of $i_0(n_g,\delta)$.

We have performed the measurement of $I_p^{0.61}$ for $k = 0$ (quantronium at thermal equilibrium) and $\tau = 0.5$ μs (Figure 4.9). We have determined the curve $\left|I_0^d(\delta_m)\right|$ best matching the experimental $I_p^{0.61}$ in order to extract the experimental $\Delta I_p^{0.61}$. For $|\delta_m| < \pi/2$, the shape of the variations of $\Delta I_p^{0.61}$ is close to that of the predicted i_0 (Figures 4.11 and 4.12, left). However, the gate modulations disappear for $\delta_m > \pi/2$ and the flux modulations have less amplitude than expected.

In order to explain these data for any value of δ_m, we have calculated $\Delta I_p^{0.61}$ (Figure 4.12, right panel) defined as the current amplitude such that the wells of the exact potential $U_k(n_g,\gamma,I_p^{0.61})$ have a constant depth, using $E_J = 0.8$ k$_b$K,$E_C = 0.68$ k$_b$K (fitting parameters taken from the spectroscopic measurements in section 4.3.3) and $d = 0$. As shown in Figure 4.12, the variations of our calculated $\Delta I_p^{0.61}$ are close to that of i_0 for any δ, thus this calculation does not explain the disappearance of the gate modulations in the experimental signal for $\pi/2 < \delta_m < 3\pi/2$. This effect can rather be attributed to the breakdown of the Born-Hoppenheimer approximation. Indeed, when the box levels $|0\rangle$ and $|1\rangle$ become degenerate, Zener transitions might affect the escape rate [83].

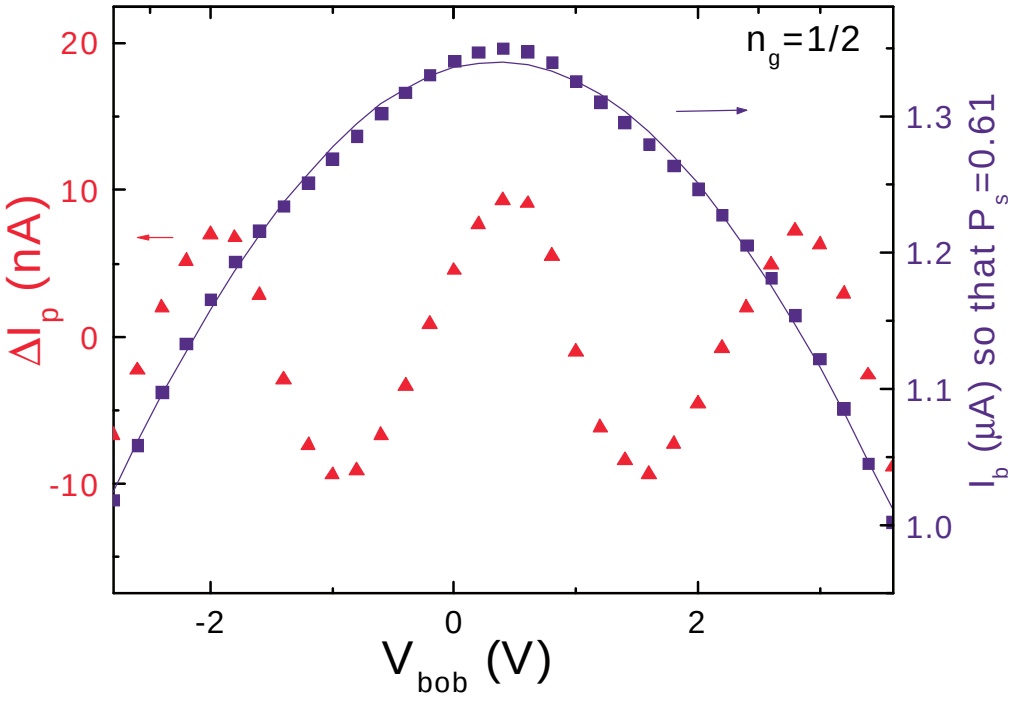

Figure 4.9: *The critical current $I_0^d(\delta_m)$ (line) of the readout junction is substracted from the current $I_p^{0.61}$ (squares) in order to get $\Delta I_p^{0.61}$ (triangles) which should identify with the average loop current of the box for $|\delta_m| < \pi/2$. Note that the flux is expressed here in terms of the voltage V_{bob} used to feed the circuit of the flux coil. These data have been obtained using an averaging on 50000 points. Beware that they have been obtained during a first run in which the phase modulations of $\Delta I_p^{0.61}$ were larger than the modulations measured in the second run, due to the thermal cycling of the sample. All the data shown in the following are related to this second run and are thus consistent with one another.*

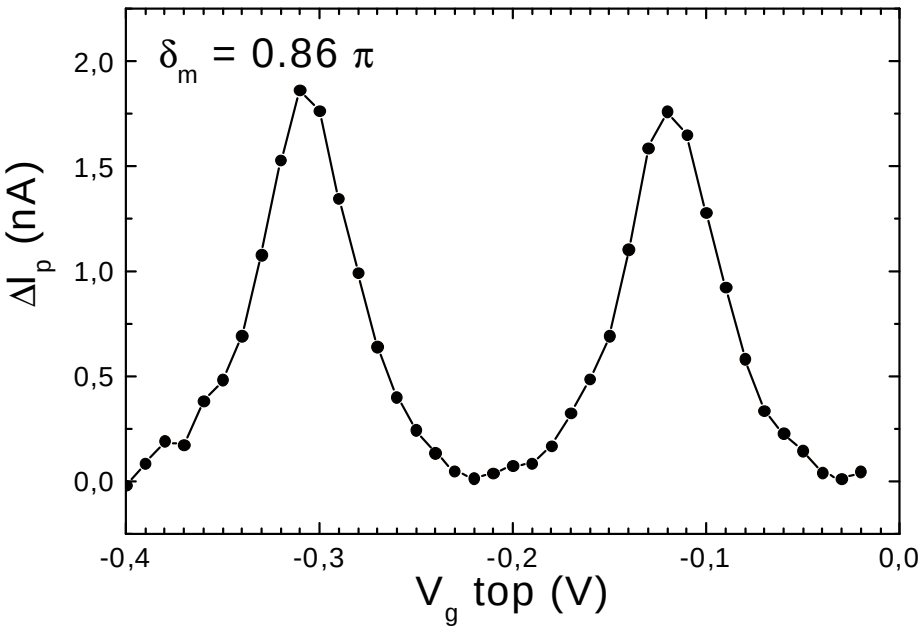

Figure 4.10: *Experimental gate voltage modulations of the current* $\Delta I_p^{0.61}$. *The gate control voltage periodicity is used to calibrate the gate capacitance* $C_g \simeq 32$ aF.

Next page:

- *Top: Figure 4.11. Experimental gate and flux modulations of the current* $\Delta I_p^{0.61}$ *when the quantronium is not excited. The gate modulation amplitude for* $\pi/2 < \delta < 3\pi/2$ *is smaller than for* $-\pi/2 < \delta < \pi/2$.

- *Middle: Figure 4.12. Left panel: Predicted variations of the loop current* i_0 *in the state* $|0\rangle$ *for* $E_J = 0.86\ \mathrm{k_bK}$ *and* $E_C = 0.68\ \mathrm{k_bK}$. *Right panel: Predicted variations of the current* $\Delta I_p^{0.61}$ *corresponding to a switching probability of* 61%, *using the exact expression of the potential* $\mathcal{U}$ *seen by the ensemble of the readout junction plus the split box.*

- *Bottom: Figure 4.13. Calculated transition frequency* ν_{01} *as a function of* n_g *and* δ *for* $E_J = 0.86$ K, $E_C = 0.68$ K and $d = 0$. *The spectroscopic data were recorded in the following along* $n_g = 1/2$ *(blue line) and along* $\delta = 0$ *(red line). The saddle point at the intersection of these two lines is the optimal point where the quantronium is immune to fluctuations of the control parameters at first order*

.

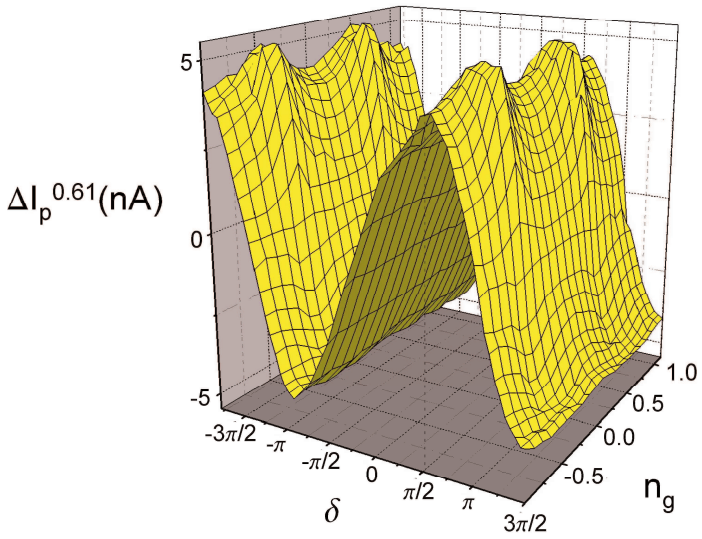

↖Figure 4.11

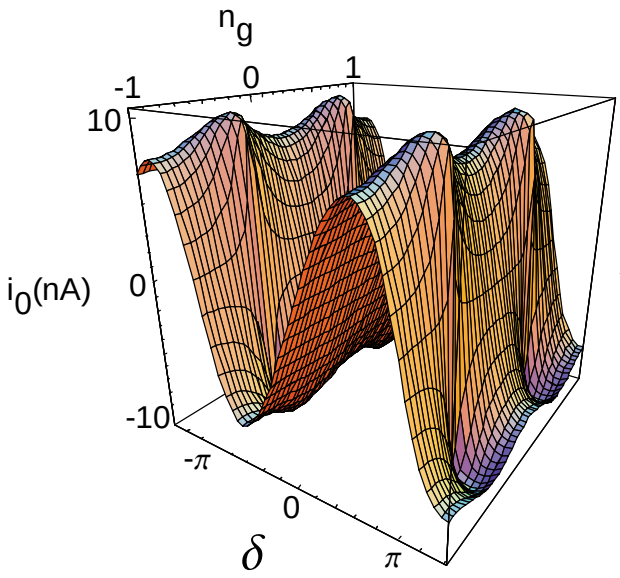

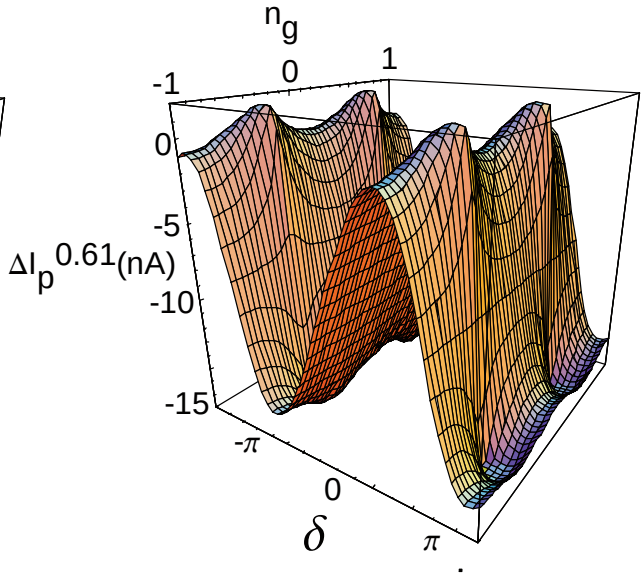

↑Figure 4.12 ↓Figure 4.13

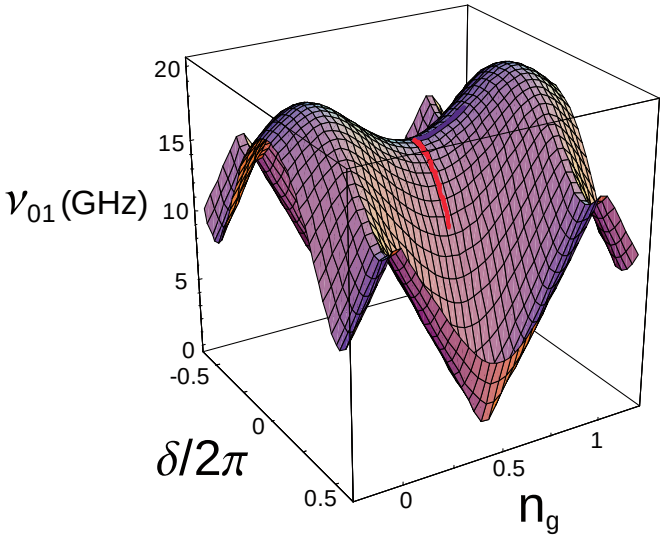

4.3.3 Spectroscopy of the quantronium

Determination of the split box parameters

In order to characterise precisely the quantronium, we have performed spectroscopic measurements along the two lines $n_g = 1/2$ and $\delta = 0$ (Figure 4.13). We have measured the resonant increase of the switching probability when a continuous radiofrequency signal with a small amplitude is applied at the resonance frequency ν_{01} just before the readout. The fit of the experimental results, obtained with $s = 0.97$, $\tau = 0.1$ μs and $t_d < 100$ ns (Figures 4.14, 4.15, and 4.16) gives the box parameters:

$$\boxed{E_J = 0.86 \text{ k}_b\text{K}, \; E_C = 0.68 \text{ k}_b\text{K}} \tag{4.9}$$

It was not possible to determine d from these data because the spectroscopy could not be performed close to $\delta = \pi$, the only domain where the asymmetry has a sizeable influence on the transition frequency.

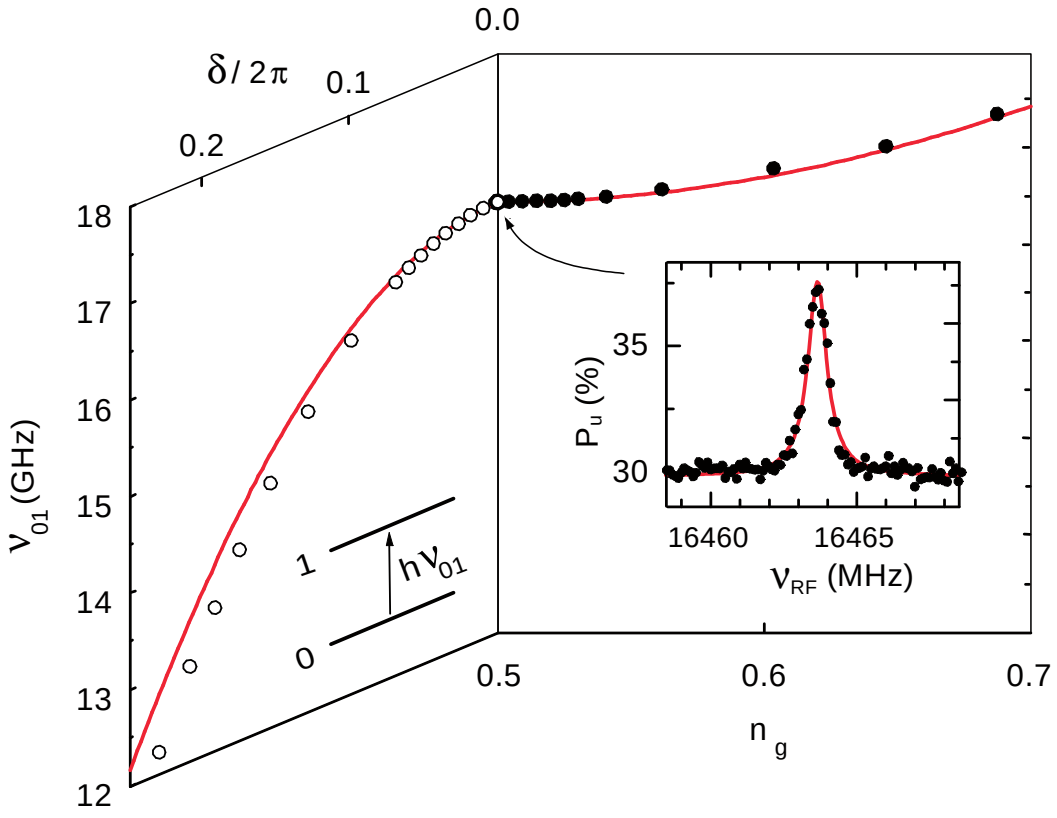

Figure 4.14: *Resonance frequency ν_{01} measured at $T = 15$ mK (dots) for $n_g = 0.5$ (left panel) or $\delta = 0$ (right panel) and fit with $E_J = 0.86$ K, $E_C = 0.68$ K, and $d = 0$ (line). Inset: Resonance lineshape at the optimal point.*

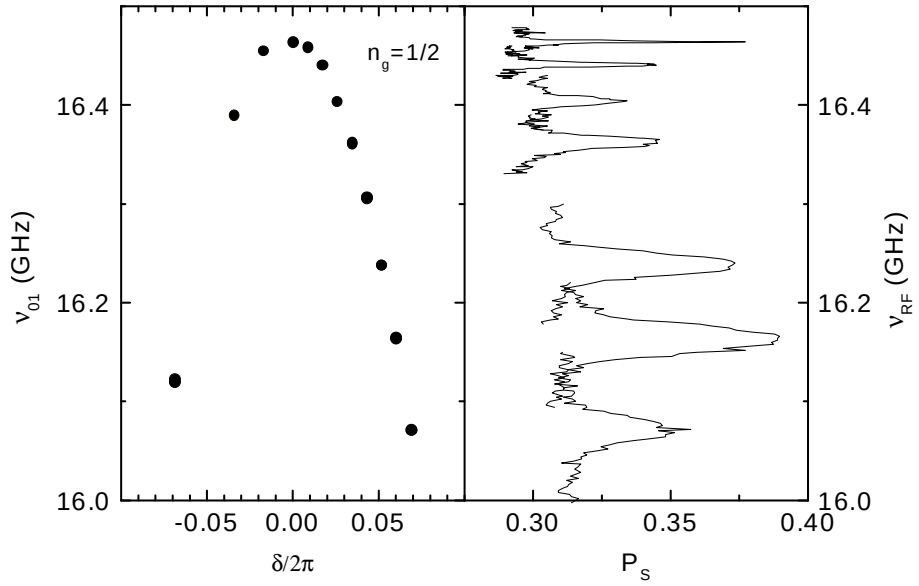

Figure 4.15: *Left panel: Resonance frequency ν_{01} measured at $T = 15$ mK (dots) for $n_g = 0.5$ and different values of δ. Right panel: Lineshapes corresponding to a few values of δ. The resonance gets sharper when δ approaches* 0.

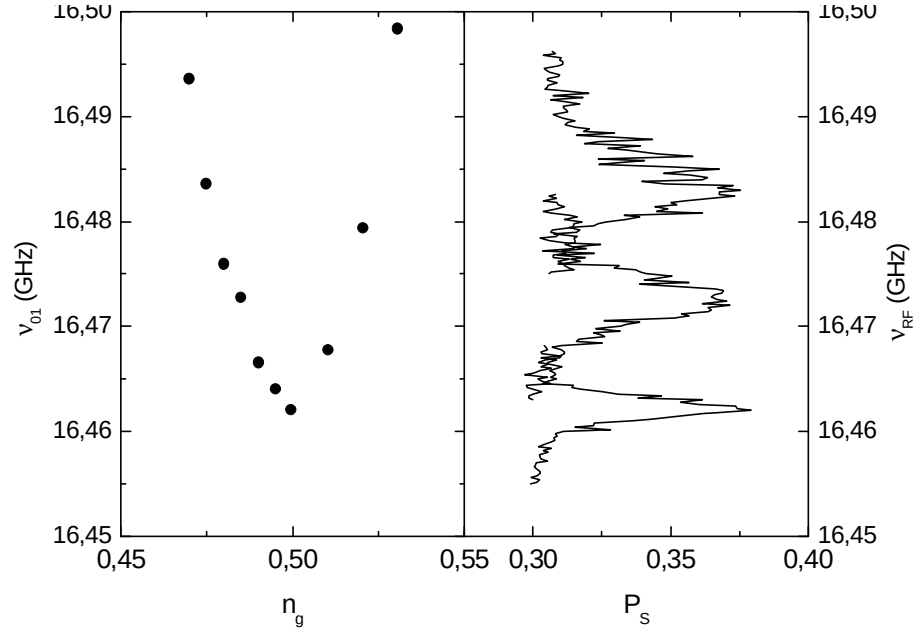

Figure 4.16: *Left panel: Resonance frequency ν_{01} measured at $T = 15$ mK (dots) for $\delta = 0$ and different values of n_g. Right panel: Lineshapes corresponding to a few values of n_g. The resonance gets sharper when n_g approaches* $1/2$.

Resonance linewidth at the optimal point

As expected, the linewidth of the resonances gets sharper when the bias point gets closer to the optimal point ($n_g = 0.5$, $\delta = 0$) where the resonance frequency is stationary with respect to both control parameters (Figures 4.15, 4.16). These resonances can be characterised by their quality factor:

$$Q = \frac{\nu_{01}}{\Delta\nu_{01}} \ , \tag{4.10}$$

where $\Delta\nu_{01}$ is the full linewidth at half-maximum. At the optimal point (Figure 4.17), we have measured the transition frequency:

$$\nu_{01} = 16463.5 \text{ MHz} \ ,$$

with a width $\Delta\nu_{01} = 0.80$ MHz, which corresponds to a quality factor :

$$Q^{opt} = 2.0\ 10^4 \ .$$

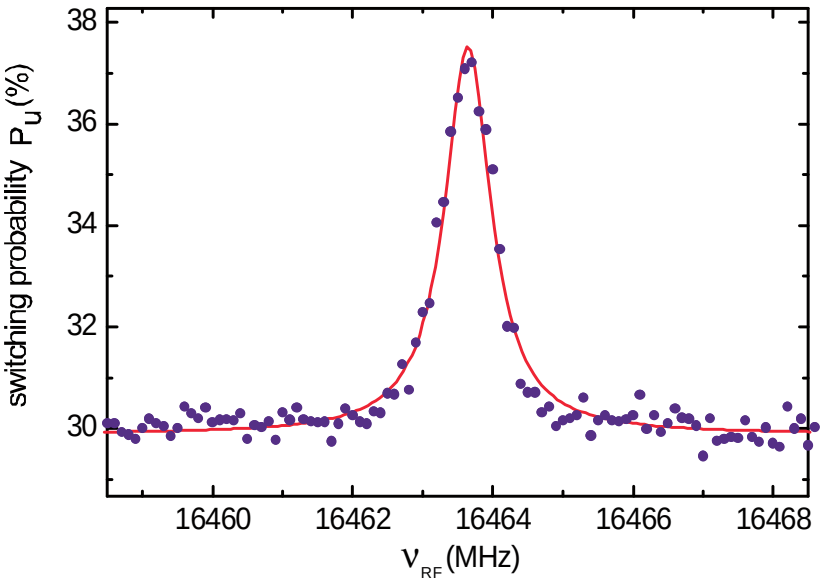

Figure 4.17: *Lineshape measured at the optimal working point* $\delta = 0$ *and* $n_g = 1/2$ *(dots), and Lorentzian fit with a full width at half maximum* $\Delta\nu_{01} = 0.8$ MHz.

Amplitude of the noise seen by the quantronium

The lifetime

$$\frac{1}{T_2} = \frac{1}{2T_1} + \frac{1}{T_\varphi} \tag{4.11}$$

of a coherent superposition of $|0\rangle$ and $|1\rangle$ can be related to the quality factor Q (4.10) of the spectroscopic resonance:

$$T_2 = \frac{Q}{\pi\nu_{01}} \tag{4.12}$$

At the optimal point, the quality factor $Q^{opt} = 2.10^4$ corresponds to:

$$T_2^{opt} \simeq 0.4\ \mu\text{s}\ . \tag{4.13}$$

Although these resonance data do not allow to distinguish whether T_2 can be attributed to relaxation or to dephasing, the dependence of the linewidth $\Delta\nu_{01}$ of the resonant peak with n_g and δ can provide informations about the noise sources which limit coherence (Figure 4.18). As expected, $\Delta\nu_{01}$ increases when departing from the optimal point $(n_g = 1/2, \delta = 0)$. For $n_g = 1/2$ and $\delta/2\pi < 0.07$, the dependency of $\Delta\nu_{01}$ with δ is linear, which indicates that the phase noise inducing decoherence could be a low frequency noise (See 3.1.1). The lineshapes obtained when n_g is taken away from 1/2 at $\delta = 0$ are not reproducible, probably due to a low frequency charge noise that produces slight shifts of the resonance frequency during the measurement. The slope of the lines determining the lower bounds of $\Delta\nu_{01}$ are:

$$\frac{\partial\nu_{01}}{\partial n_g} \simeq 250\ \text{MHz / Cooper pair}$$

and:

$$\frac{\partial\nu_{01}}{\partial\delta} \simeq 310\ \text{MHz /tour}\ .$$

In a rough approximation, these dependences correspond to r.m.s. deviations $\Delta n_g \simeq 0.004$ and $\Delta\delta/2\pi \simeq 0.002$ during the time needed to record the resonance. The amplitude Δn_g of charge noise found here is in agreement with measurements of the 1/f charge noise usually reported in the literature [20]. The amplitude of the phase noise is unusually large [84] and could possibly be improved by protecting the sample with a magnetic shielding.

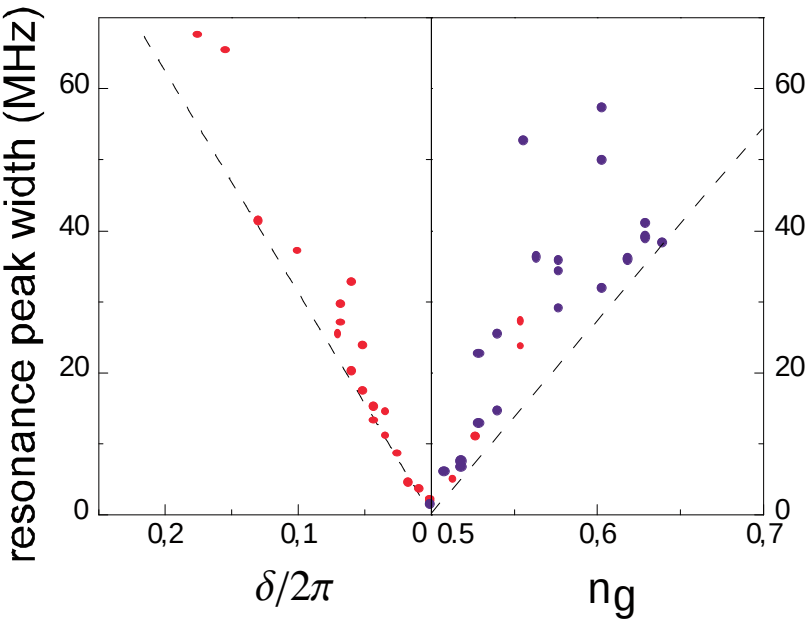

Figure 4.18: *Full width at half maximum of the resonance measured at* $T = 15$ mK *(dots) as a function of* δ *for* $n_g = 0.5$ *(left panel) and as a function of* n_g *for* $\delta = 0$ *(right panel).*

4.3.4 Coherent manipulations of the quantronium state

Principle

The above spectroscopy data indicate that quantum coherence is sufficient to attempt time domain experiments. In this section, the quantronium manipulations will be explained by using the representation of the quantronium state as a spin in the rotating frame $\mathcal{R}_p = (\overrightarrow{x}_p, \overrightarrow{y}_p, \overrightarrow{z}_p)$ defined in section 1.3. Note that all the following measurements have been performed at:

$$s = I_p / I_0^{eff} = 0.97 \ .$$

Rabi precession

We have first observed the Rabi precession of the quantronium, by applying a radiofrequency pulse with amplitude $U_{RF} = 2e\Delta n_g / C_g$, with frequency $\nu_{RF} \simeq \nu_{01}$ and with duration τ on the gate electrode. In the experiments we have performed, the box is supposed to be initially in the state $|0\rangle$, so that its representative vector $\overrightarrow{u}$ is initially along $\overrightarrow{z}_p$ (Figure 4.19). Under the influence of the radiofrequency pulse, the vector $\overrightarrow{u}$ precesses around $\overrightarrow{y}_p$ at the Rabi frequency $\nu_{Rabi} = e_p/\hbar$. In the absence of decoherence, the azimuthal coordinate θ_u of $\overrightarrow{u}$ thus becomes:

$$\theta_u = 2\pi\nu_{Rabi}\tau \ .$$

After the pulse, $\overrightarrow{u}$ precesses freely around $\overrightarrow{z}_p$ at the Ramsey frequency $\nu_{Ramsey} = \nu_{01} - \nu_{RF}$, which leaves θ_u unchanged. Just before the measurement and in the absence of decoherence, the weight of the state $|1\rangle$ in the quantronium state is thus (see 1.42):

$$p_1 = \sin^2(\pi\nu_{Rabi}\tau) \ ,$$

which oscillates with τ .

Ideally, the switching probability P_u in state $\overrightarrow{u}$ is equal to p_1 . The variations of P_u with τ measured at the optimal point are shown in Figure 4.19, bottom panel. The quantum bit state is manipulated without inducing much decoherence since the decay of the oscillations of P_u is significant only after 1 μs . Nevertheless, the maximum amplitude of the signal at $\tau = 0$ is only 0.15 and not 0.54 as expected from the estimated discriminating power (4.8). This phenomenon, already observed in the direct current measurements, may be due a loss of polarisation of the quantronium during the readout stage (see p.218).

We have verified that the frequency of the Rabi oscillations varies linearly with the amplitude U_{RF} of the radiofrequency signal (Figure 4.20). This allows to calibrate the amplitude U_{RF} .

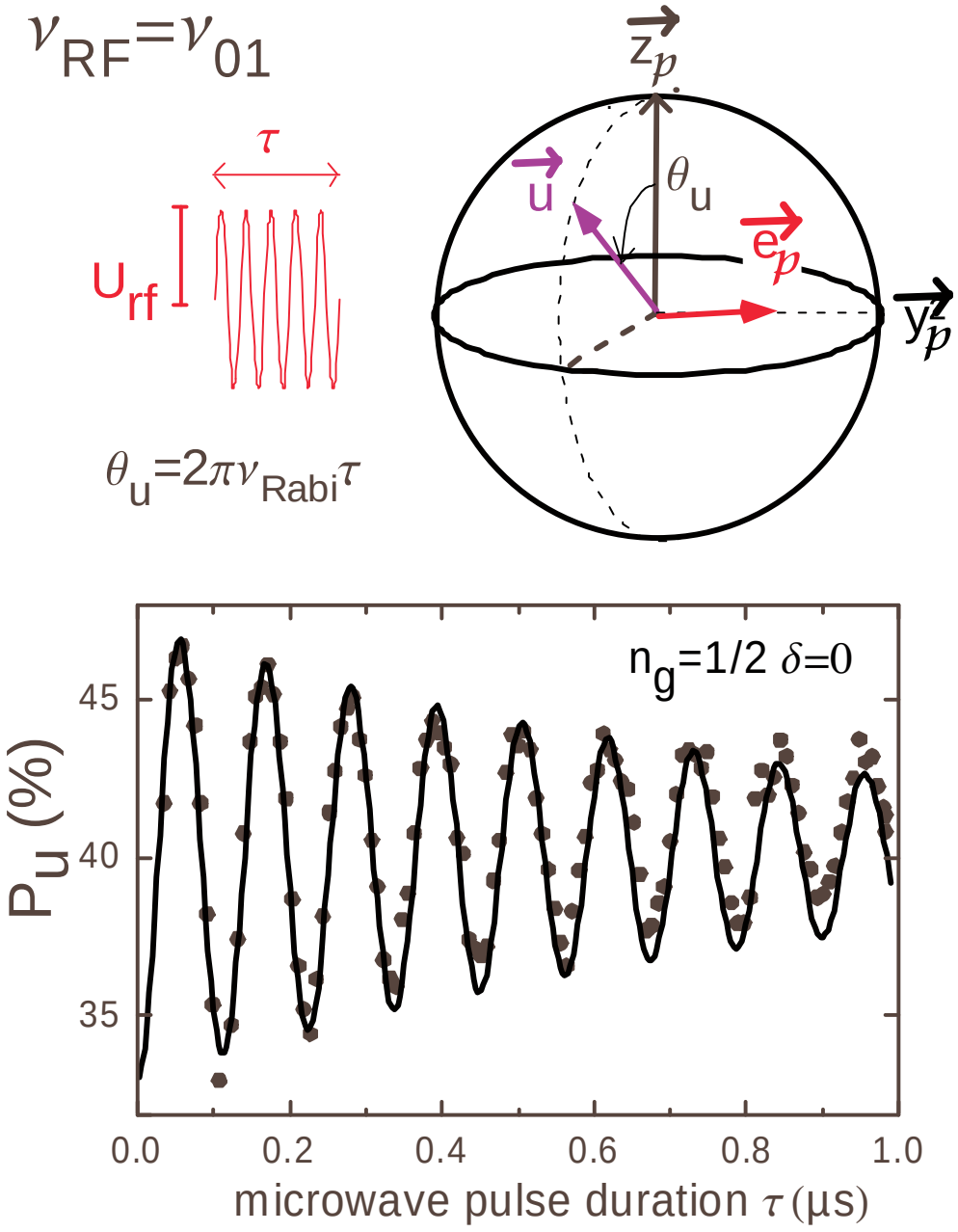

Figure 4.19: *Observation of Rabi oscillations between the states* $|0\rangle$ *and* $|1\rangle$ *of the quantronium, measured just after a resonant radiofrequency pulse with duration* τ*. Top panel: Representation of the experiment on the Bloch sphere. A radiofrequency pulse with duration* τ *is applied on the gate just before the measurement. This pulse makes* $\vec{u}$ *precess around* $\vec{y}_p$*, at the frequency* ν_{Rabi} *with an angle* $\theta_u = 2\pi\nu_{Rabi}\tau$*. Bottom panel: The experimental switching probability* P_u *(dots) of the readout junction oscillates with* τ*. The line is a fit with an exponentially damped sinusoid. The data shown here have been taken at resonance (with a* 0.1 MHz *accuracy) with the optimal point* $(n_g = 0.5,\ \delta = 0)$ *, with an average of* 5.10^4 *events per point.*

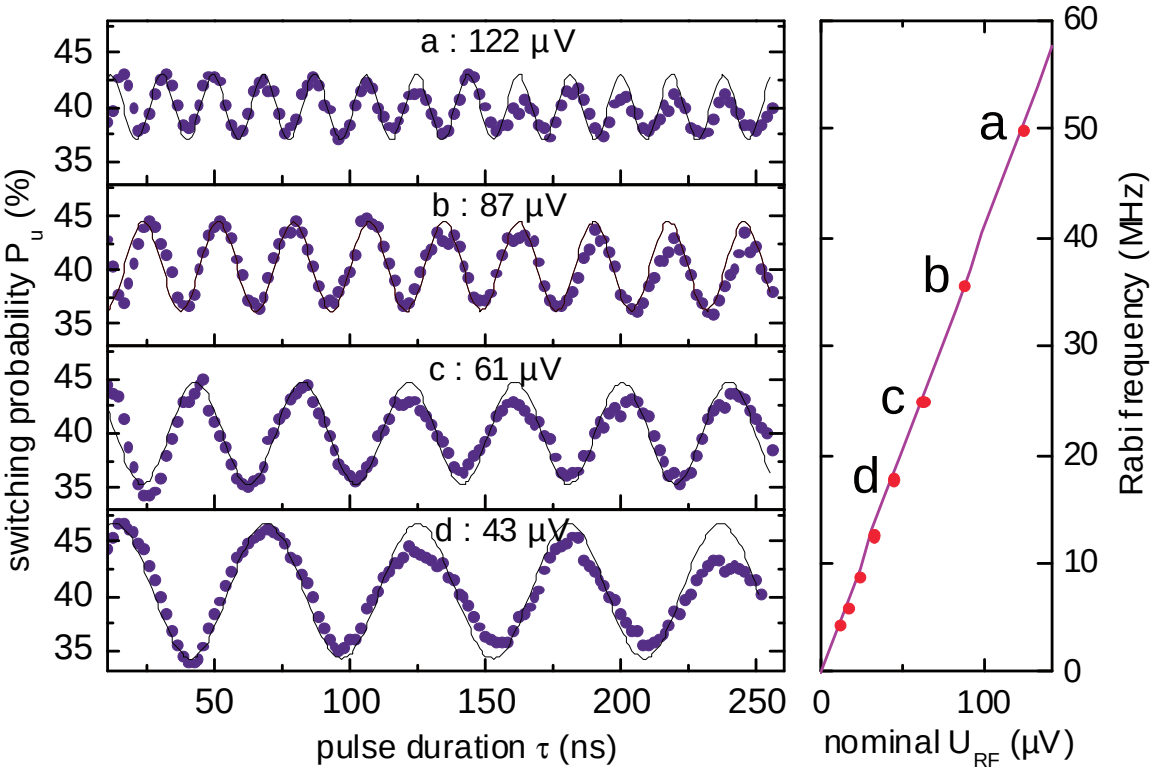

Figure 4.20: *Rabi oscillations of the switching probability P_u induced by radiofrequency pulses with duration τ and with nominal amplitude U_{RF} = 122, 87, 61, 43 μV (dots, from top to bottom in left panel). The Rabi frequency, extracted from the sinusoidal fits (continuous lines) is plotted in the right panel as a function of the amplitude of the radiofrequency pulse. The linear dependence is used to calibrate the microwave amplitude.*

Measurement of the relaxation time

Ideally, starting from the state $|0\rangle$, it is possible to prepare the state $|1\rangle$ using a radiofrequency pulse with a duration such that the spin rotates by an angle $\theta_u = \pi$ around $\overrightarrow{x}$. When varying the delay t_d between the end of the π pulse and the readout pulse, the resonance peak height decays with a relaxation time T_R (Figure 4.21). At the optimal point, we have measured the relaxation time:

$$T_R^{opt} = 1.84\ \mu\text{s}\ .$$

Since $T_R^{opt} > T_2^{opt}/2$, the linewidth at the optimal point is not limited by relaxation but by dephasing. The relaxation time is of the same order as the relaxation time estimated in chapter 3, indicating that relaxation can be attributed to the impedance of the embedding circuit.

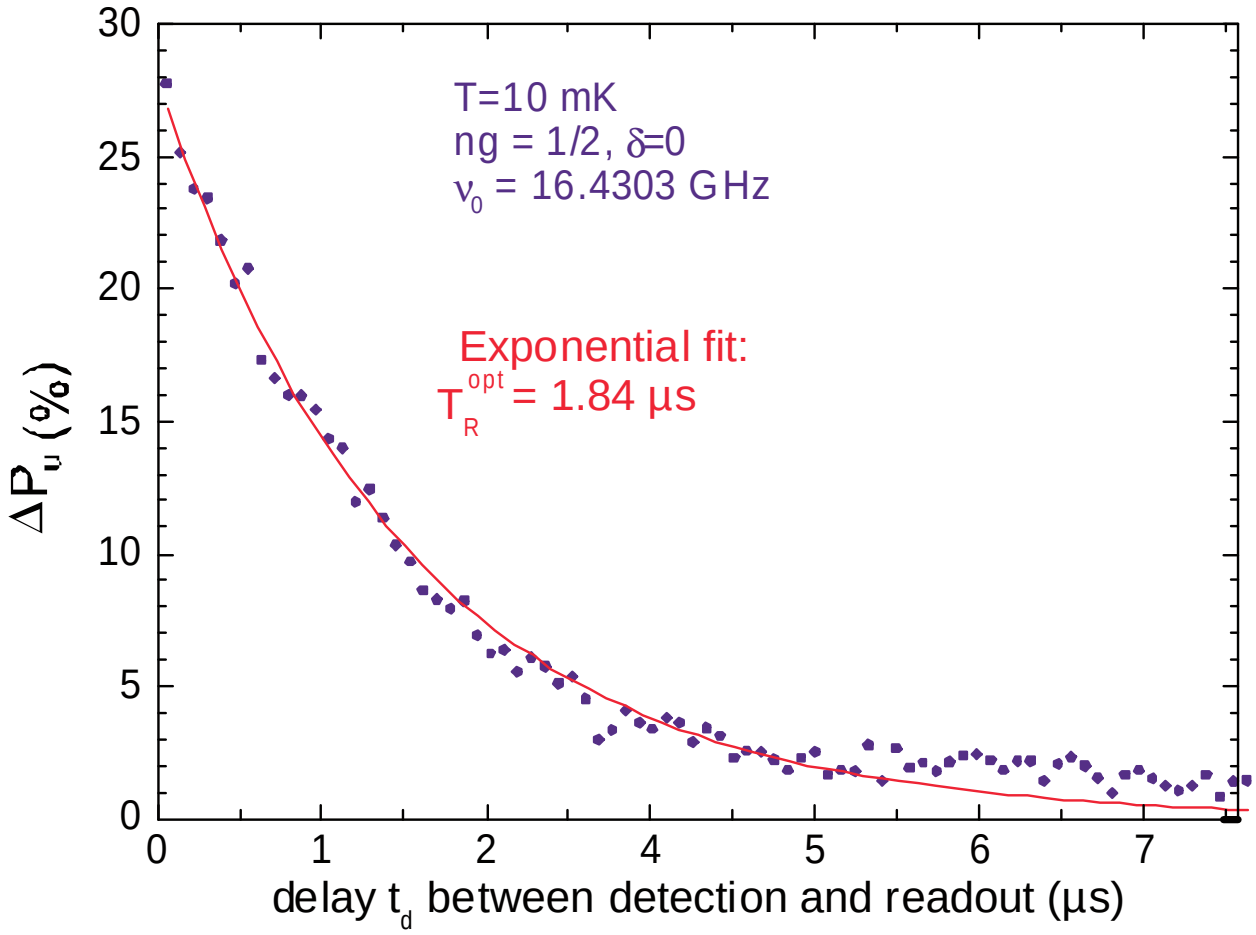

Figure 4.21: *Decay ΔP_u of the switching probability P_u as a function of the delay time t_d between the π pulse and the readout pulse, measured at the optimal point. The solid line is an exponential fit from which the relaxation time $T_R^{opt} = 1.84$ µs is obtained.*

Change in the switching probability after a π pulse

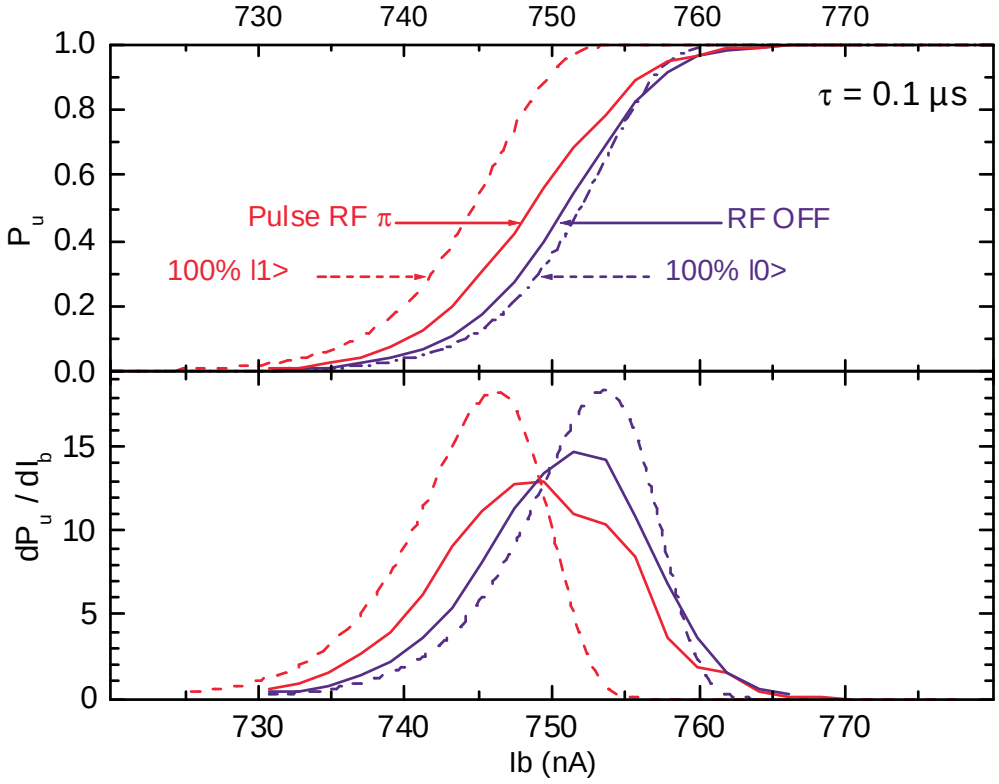

Figure 4.22: *Experimental switching probabilities P_u of the quantronium (top panel) and their derivatives dP_u/dI_p (bottom panel) after a bias current pulse with amplitude I_p and with duration $\tau = 0.1$ µs. We have tried to fit the probability curves measured when the quantronium is left unexcited (blue full line) and when it has been submitted to a π pulse (red full line) in order to determine the probability curve in the pure state $|0\rangle$ (blue dotted line) and in the state $|1\rangle$ (red dotted line). From these fits, one can infer that at rest, the probability to measure the state $|1\rangle$ is less than 20%, and that after a π pulse, that probability increases up to 45%. This low polarisation may be attributed to depolarisation phenomena during the readout.*

In the above single pulse experiments, the quantronium is never detected in the pure states $|0\rangle$ or $|1\rangle$. In order to analyse this feature, we have compared the switching probability of the large junction when the quantronium is left unexcited with the switching probability just after a π pulse (Figure 4.22). These fits infer that when the quantronium is left unexcited, the occupation of the level $|1\rangle$ is less than 20% and that after a π pulse, this occupation of $|1\rangle$ is at best 45% .

This loss of polarisation may be attributed to changes in the $|0\rangle \rightarrow |1\rangle$ transition frequency and in the environment mode frequencies during the risetime of the readout pulse, due to the large change in the phase difference across the readout junction. Any resonant coupling between a mode in the environment and the $|0\rangle \rightarrow |1\rangle$ transition would induce a strong relaxation prior to measurement.

Measurement of the coherence time

The spectroscopic measurements give an indirect access to the coherence time T_2 through the quality factor Q of the spectroscopic resonances. In order to determine this time more directly, one can perform a two pulse Ramsey-like experiment [38] which allows to observe the free evolution of the circuit. The box state $\overrightarrow{u}$ is first driven from $\overrightarrow{z}_p$ to $\overrightarrow{x}_p$ by a $\pi/2$ radiofrequency pulse. Then, it is left to precess freely around $\overrightarrow{z}_p$ during a time Δt . In the absence of decoherence, the expected azimuthal angle of precession after Δt is:

$$\Delta\varphi_u = 2\pi\nu_{Ramsey}\Delta t \ .$$

A second $\pi/2$ pulse is used to convert $\Delta\varphi$ into a polar angle:

$$\Delta\theta_u = \pi - \Delta\varphi_u \ ,$$

which results ideally in:

$$p_1 = \cos^2(\pi\nu_{Ramsey}\Delta t) \ .$$

In reality, we have found out that, at the optimal point, the box suffers essentially from dephasing. Considering that the box state is dephased during the free evolution stage, one has:

$$p_1 = \cos^2(\pi\nu_{Ramsey}\Delta t) f_\varphi(t) \ ,$$

with $f_\varphi(t)$ the dephasing factor introduced in chapter 3. The experimental switching probability after a Ramsey sequence is presented in Figure 4.23. Oscillations at the frequency $\nu_{01} - \nu_{RF}$ are observed. The transition frequency is stable enough to allow suppressing all oscillations at resonance. (Figures 4.24 and 4.25). This can be used to determine the transition frequency ν_{01} with accuracy.

Dephasing is revealed by the decay of the amplitude of the oscillations with Δt, which can be fitted by an exponentially damped sinusoid, with a decay time:

$$T_2^{opt} = 0.5 \ \mu\text{s} \ .$$

This time is very close to the lifetime $T_2^{opt} = 0.4$ μs of a coherent superposition inferred by the quality factor at the optimal point. As expected from the spectroscopy linewidths, the coherence time decreases strongly when the Ramsey experiment is performed away from the optimal point (Figure 4.26).

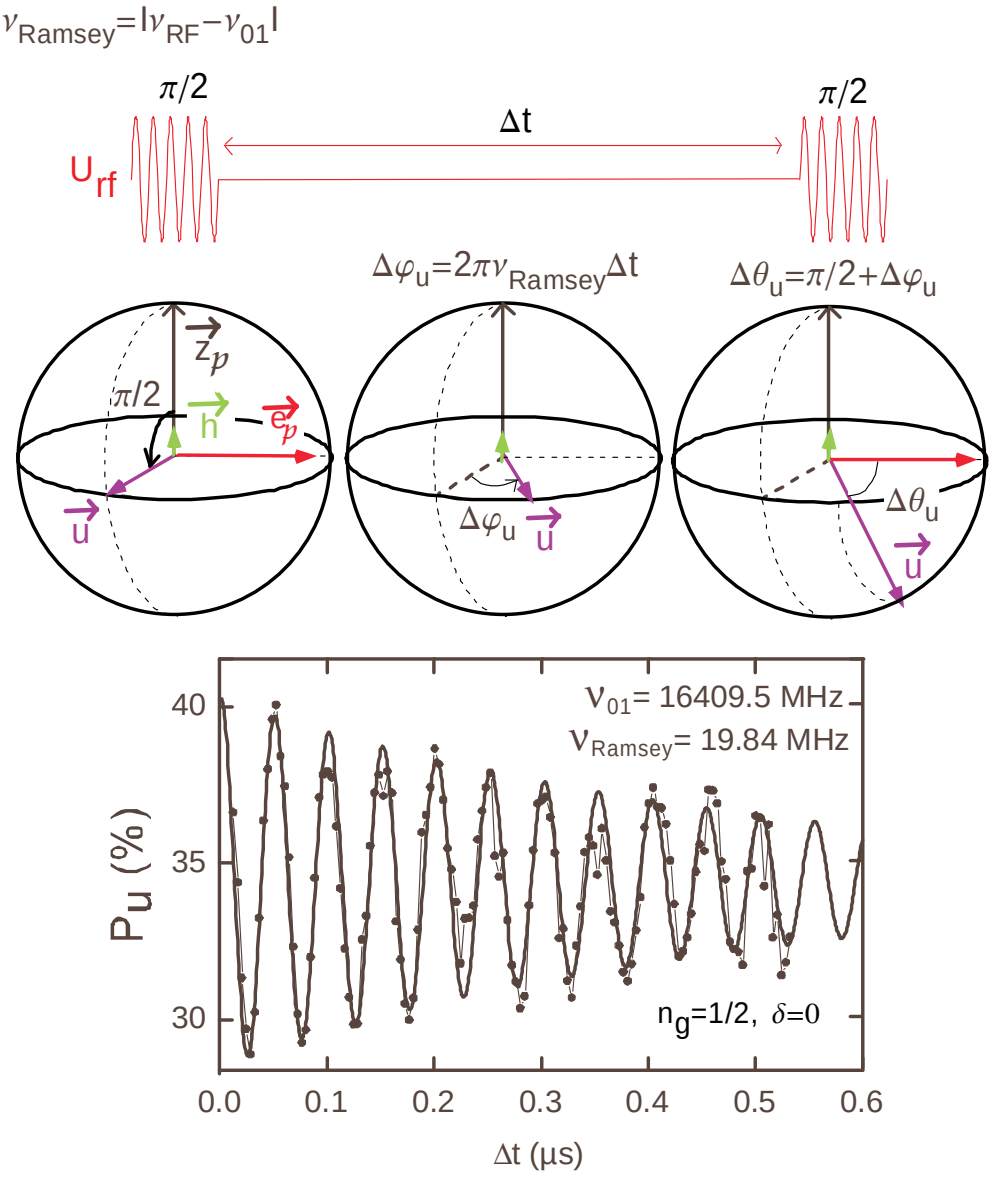

Figure 4.23: *Direct measurement of the coherence time T_2. Top panel: representation of the experiment on the Bloch sphere. A first $\pi/2$ pulse is applied to the gate in order to bring $\overrightarrow{u}$ to the $\overrightarrow{x_p}$ axis. The spin $\overrightarrow{u}$ then precesses freely around $\overrightarrow{z_p}$ during a time Δt. It thus acquires an azimutal angle $\Delta\varphi_u = 2\pi\nu_{Ramsey}\ \Delta t$. A second $\pi/2$ pulse is used to convert this angle into a polar angle $\Delta\theta_u = \pi/2 - \Delta\varphi_u$. Bottom panel: the Ramsey oscillations of the switching probability P_u decays with a transverse relaxation time T_2. The data (dots) are given here for the optimal point $(n_g = 0.5, \delta = 0)$. They are fitted by an exponentially damped sinusoid with time $T_2 = 0.5$ μs at the optimal point (continuous line). Note that similarly to what happens in the Rabi experiment, the amplitude of the switching probability P_u at $\tau = 0$ is lower then expected.*

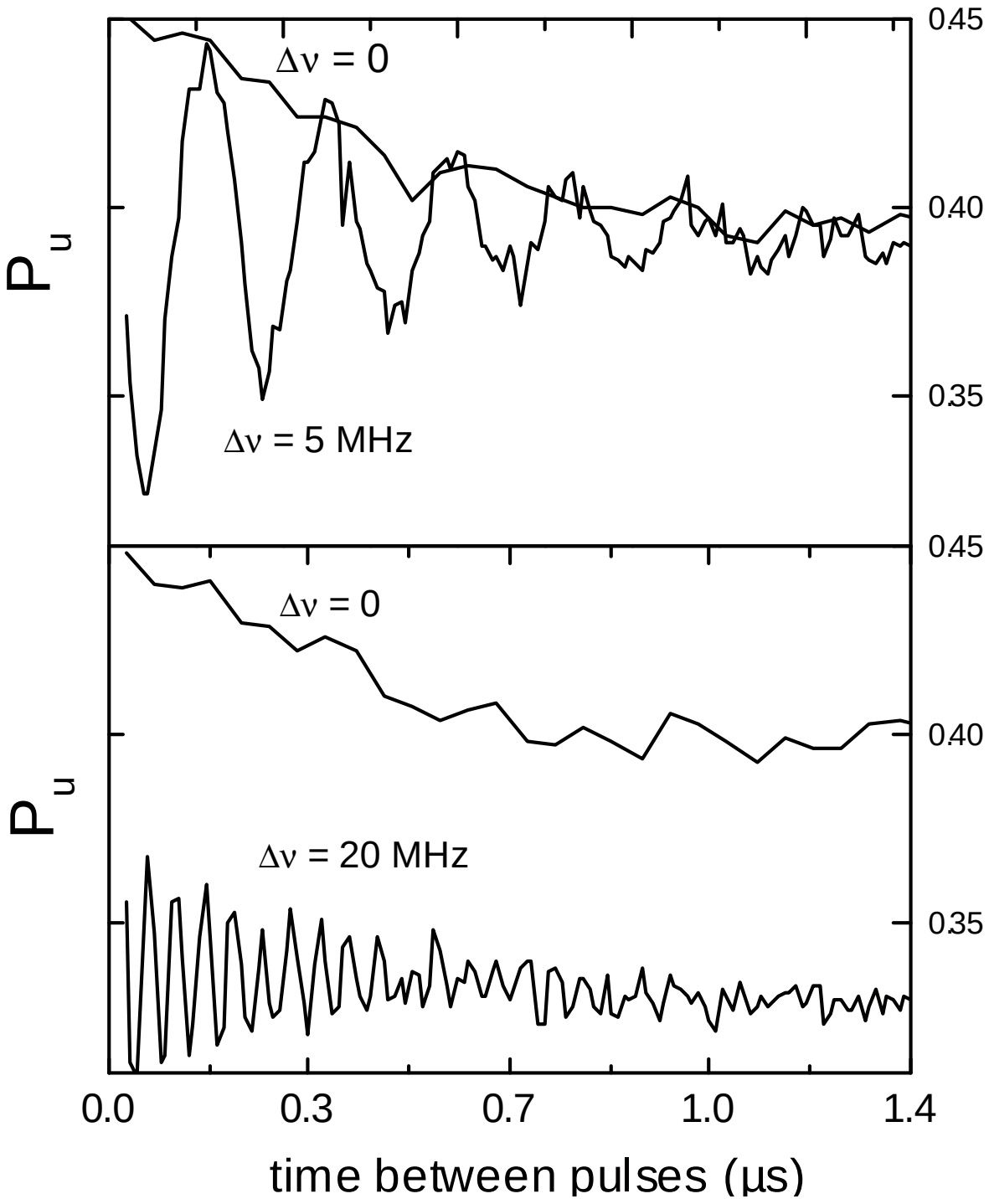

Figure 4.24: *Observation of Ramsey oscillations at the optimal point $n_g = 1/2$ and $\delta = 0$, for two different values of $\nu_{RF} - \nu_{01}$. When ν_{RF} is exactly tuned at $\nu_{RF} = \nu_{01}$ (top curves), the oscillations disappear.*

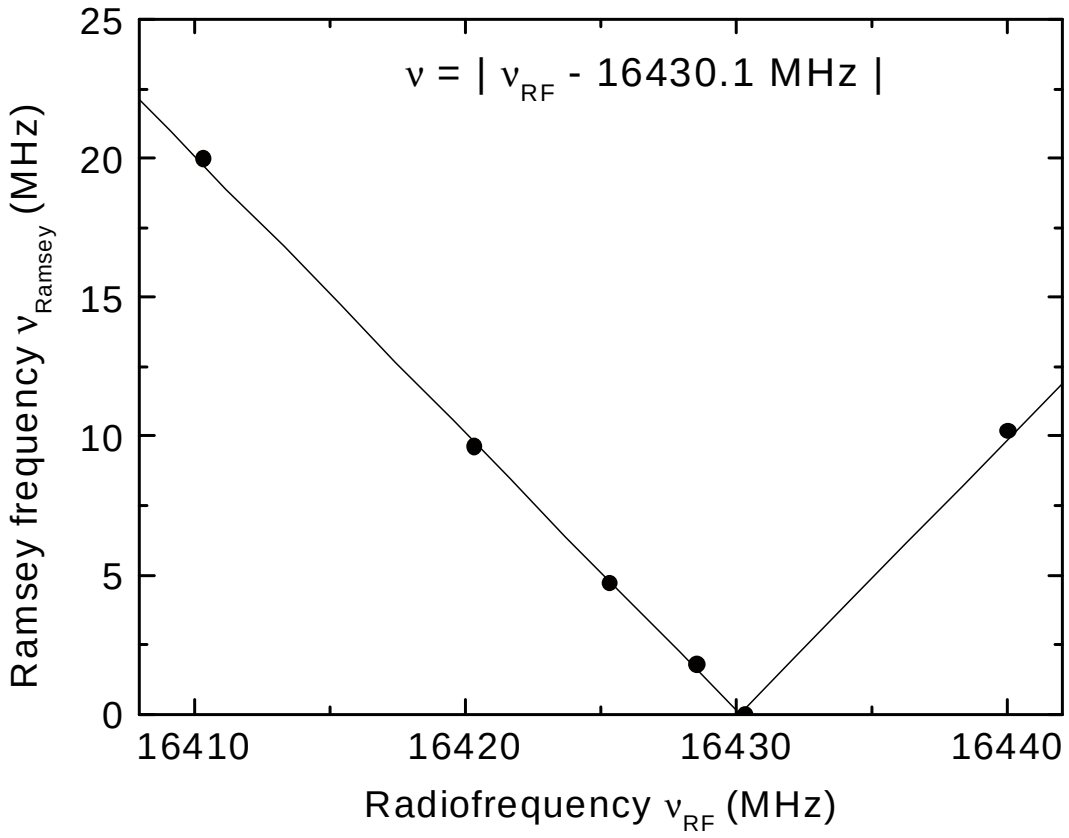

Figure 4.25: *Measured frequency of the Ramsey oscillations as a function of the microwave frequency ν_{RF}. The line is a best fit $\nu_{Ramsey} = |\nu_{01} - \nu_{RF}|$, with $\nu_{01} = 16430.1$ MHz. Note that this value is slightly different from the value recorded a few days before during the spectroscopic measurements.*

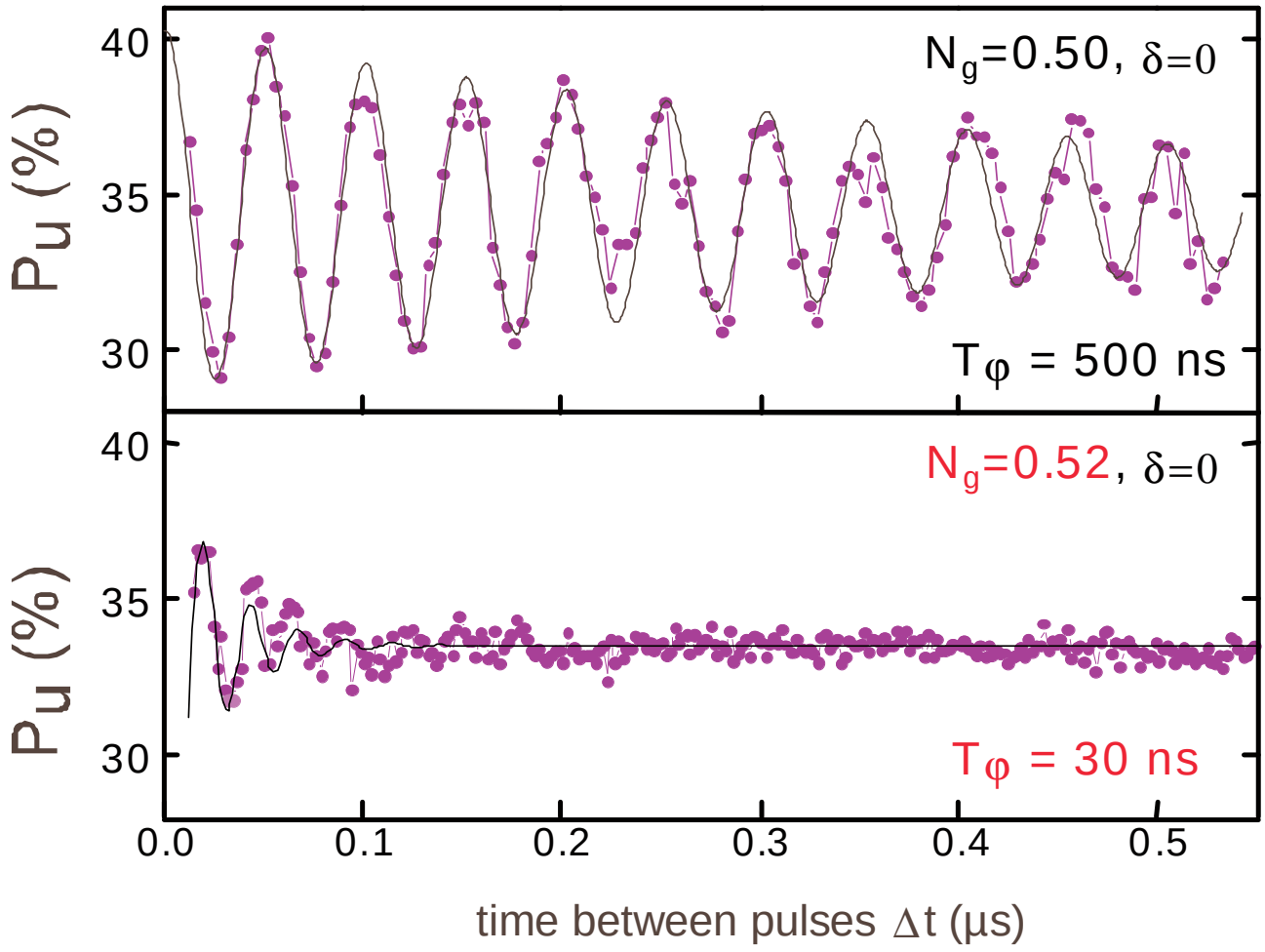

Figure 4.26: *Comparison between the Ramsey oscillations of the switching probability* P_u at *the optimal point* $(n_g = 0.5, \delta = 0)$.*(top panel) and at the point* $(n_g = 0.52, \delta = 0)$. *These data are fitted by an exponentially damped sinusoid with time* $T_2 = 500$ *ns at the optimal point and* $T_2 = 30$ *ns when* n_g *is detuned by* 0.02.

Controlled rotations around the z axis

The Rabi precession allows controlled rotations of $\overrightarrow{u}$ around the $\overrightarrow{x}$ and $\overrightarrow{y}$ axis. In order to implement arbitrary manipulations of the quantum state, controlled rotations of $\overrightarrow{u}$ around the $\overrightarrow{z}$ axis are also required. This can be achieved by applying small amplitude bias current pulses which change δ and thus shift the transition frequency by $\delta\nu_{01}(t)$ during a short time The rotation angle is then:

$$\alpha = \int \delta\nu_{01}(t)dt \ .$$

We have measured this effect by inserting such a pulse between the two radiofrequency pulses of a Ramsey sequence with $\nu_{RF} = \nu_{01}$(see Figure 4.27).

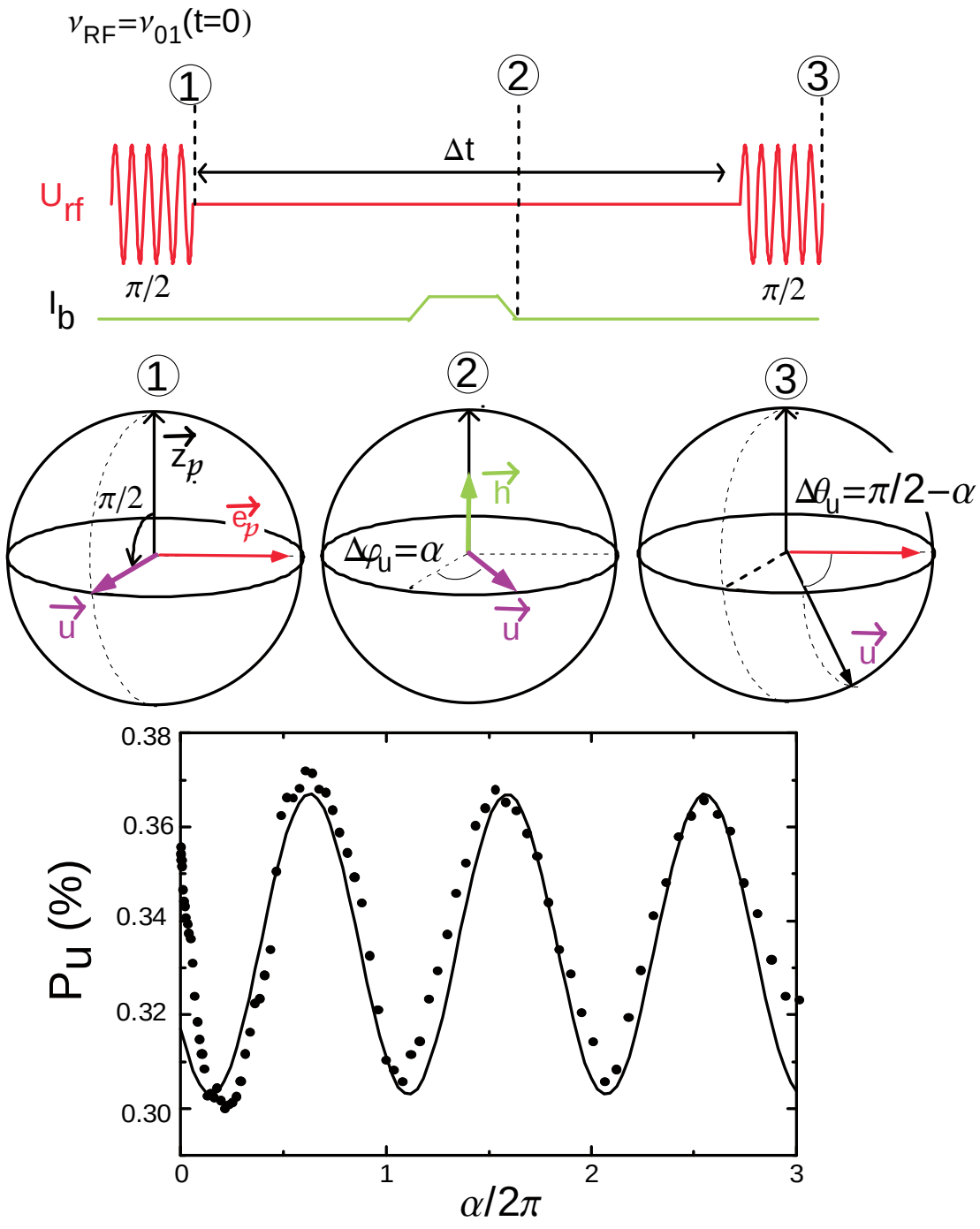

Figure 4.27: *Controlled rotations around* $\vec{z}$. *Top panel: representation of the experiment on the Bloch sphere. A sequence of two* $\pi/2$ *radiofrequency pulses with* $\nu_{01} = \nu_{RF}$ *separated by* Δt *is applied to the gate. Between both pulses, a small adiabatic current pulse with variable amplitude* I_p *and duration* $\tau = 100$ ns *is applied to the readout out junction in order to shift the resonance frequency and induce controlled rotations of* $\vec{u}$ *around* $\vec{z}$. *Bottom panel: Switching probability* P_u *as a function of the calculated angle. The solid line is a sinusoidal fit.*

Echo experiments

The echo experiment is a modified Ramsey experiment in which the free evolution time Δt is divided into two intervals Δt_1 and Δt_2 separated by a π pulse with duration $\Delta t_\pi \ll \Delta t_1, \Delta t_2$ (Figure 4.28). Due to dephasing, during Δt_1 and Δt_2, the quantronium acquires phase shifts named respectively $\Delta\varphi_1$ and $\Delta\varphi_2$.The π pulse is used to reverse the sign of the dephasing acquired during the time Δt_1 :

$$\Delta\varphi_1 \rightarrow -\Delta\varphi_1$$

At the end of the radiofrequency sequence, the total dephasing acquired by the circuit is thus:

$$\Delta\varphi = \Delta\varphi_2 - \Delta\varphi_1 \ .$$

For $n_g = 0.52$ and $\delta = 0$, we have measured the switching probability for fixed values of the total duration:

$$\Delta t = \Delta t_1 + \Delta t_2 + \Delta t_\pi \simeq \Delta t_1 + \Delta t_2$$

of the experiment as a function of Δt_1 (Figure 4.29). For $\Delta t \leq 1.2$ μs, this probability oscillates with $\Delta t_1 - \Delta t_2$ and shows a maximum amplitude at the point where:

$$\Delta t_1 = \Delta t_2 \simeq \frac{\Delta t}{2} \ .$$

The observation of such echoes at times much longer than the decay time of the Ramsey fringes indicates that the decoherence due to charge fluctuations is essentially due to fluctuations at frequencies lower than $1/\Delta t \simeq 1$ MHz, so that $\Delta\varphi_2 \simeq \Delta\varphi_1$. This is in agreement with the low frequency spectrum expected for charge noise. No echo was seen in the experiments performed at $\delta \neq 0$, suggesting that the phase noise inducing dephasing occurs above 1 MHz . This is in contradiction with the indications given by the phase dependence of the resonance linewidth. No echoes were either seen at the optimal point at times longer than the decay time of Ramsey oscillations.

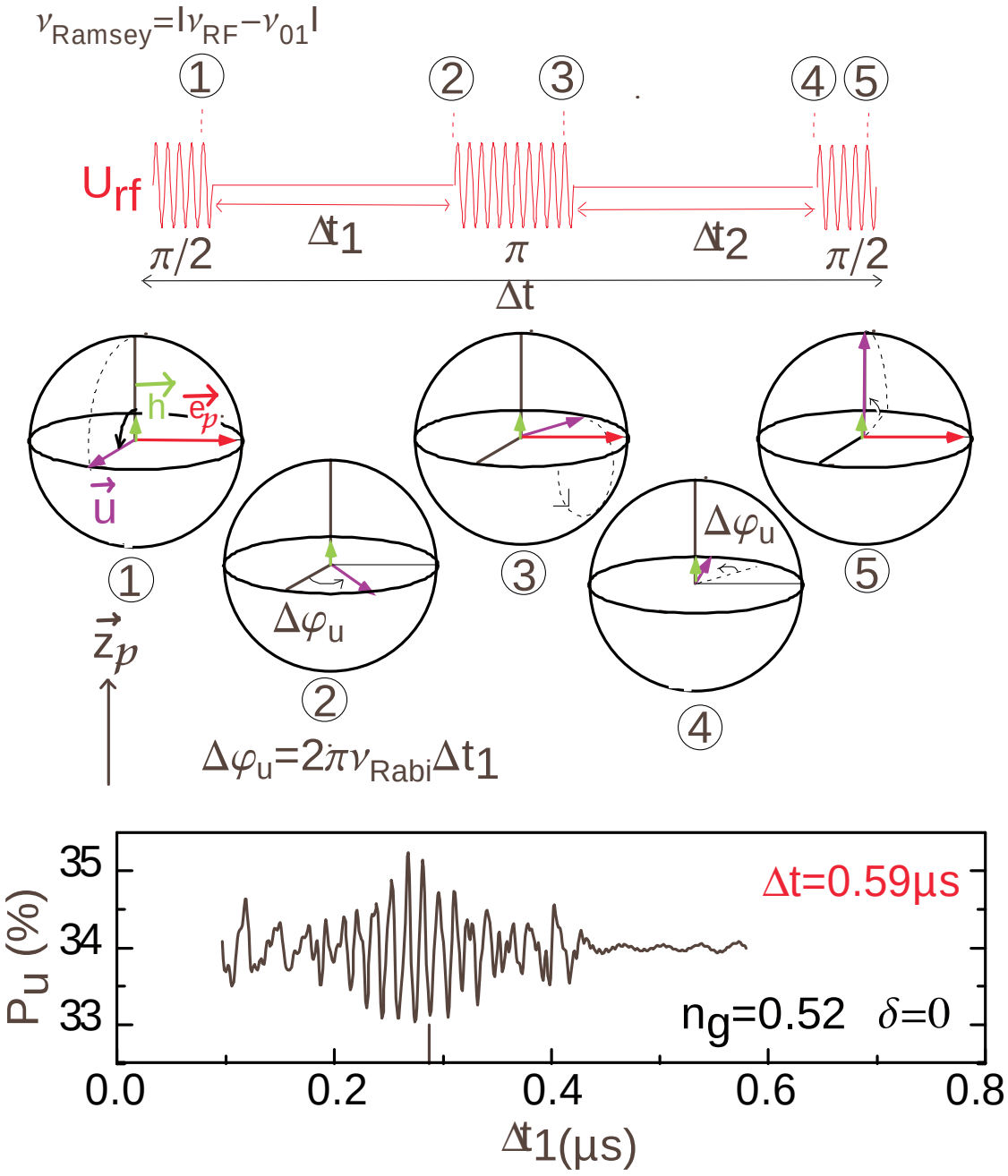

Figure 4.28: *Echo experiment. Top panel: Representation of the experiment on the Bloch sphere. A first $\pi/2$ pulse brings $\vec{u}$ to the $\vec{x}_p$ axis. Follows a free precession during the time Δt_1. A π pulse is used to bring $\vec{u}$ to the symmetric position with respect to the $\vec{x}_p$ axis. Follows a free evolution during the time Δt_2, and a second $\pi/2$ pulse. Bottom panel: At $n_g = 0.52$ and $\delta = 0$, the switching probability P_u oscillates with $\Delta t_1 - \Delta t_2$ and shows a maximum amplitude when slow fluctuations of the field $\vec{h}_p$ are best compensated, that is when $\Delta t_1 = \Delta t_2$.*

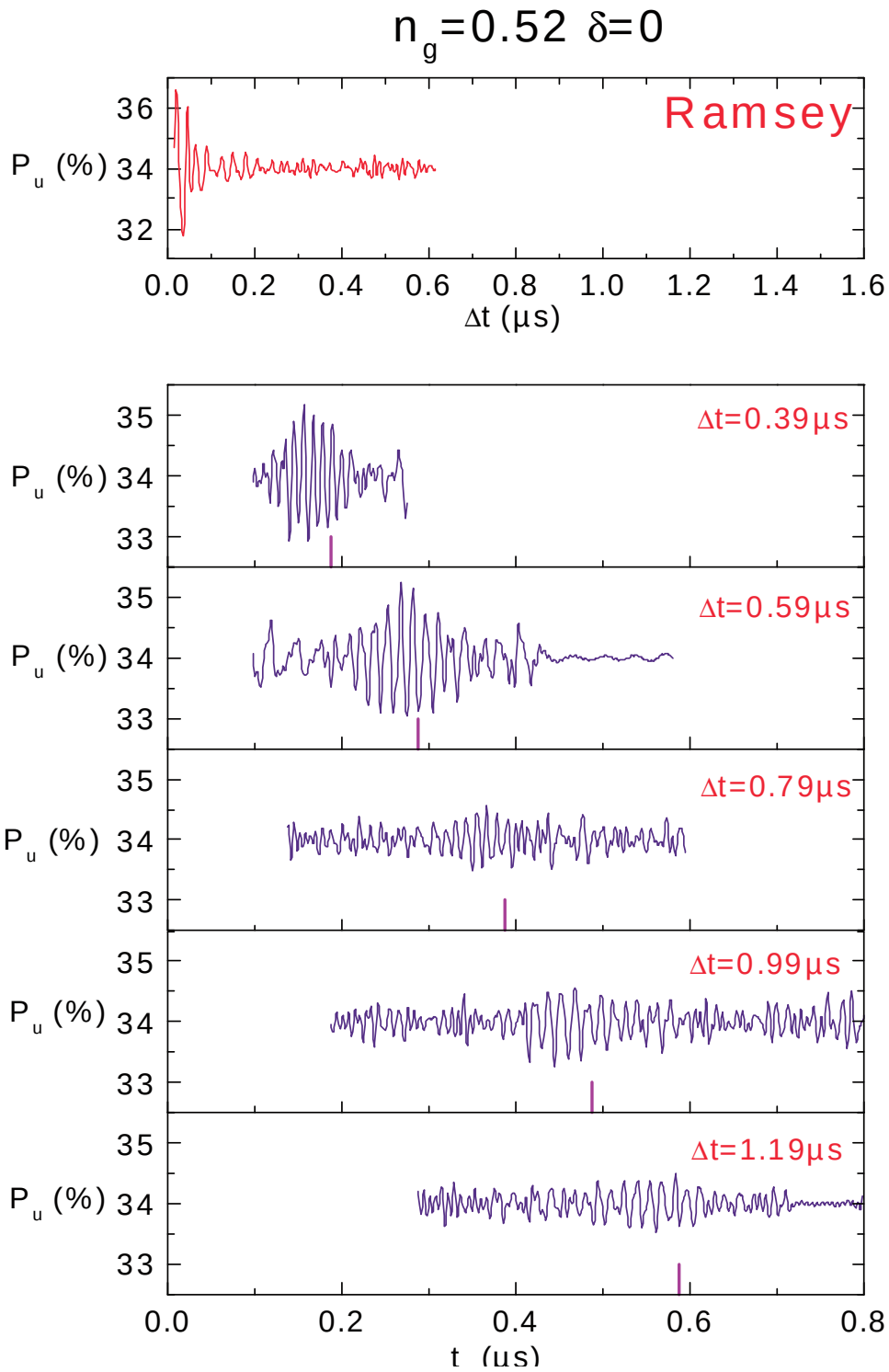

Figure 4.29: *Top panel: Ramsey oscillations at* $(n_g = 0.52, \delta = 0)$. *The dephasing time* $T_\varphi = 30$ ns *is significantly shorter than at* $(n_g = 0.50, \delta = 0)$. *Bottom panel: Echo experiments at* $(n_g = 0.52, \delta = 0)$ *for different values of* Δt. *The echo technique partially compensates dephasing effects up to* $\Delta t = 1.2$ μs.

4.4 Conclusion

Experiment 5 is the first operation of a quantronium. In this experiment, the coherence time $T_2^{opt} = 500$ ns reached at the optimal point allows 8000 coherent oscillations of the box before a $1/e$ decay of their amplitude. We have succeeded in driving an arbitrary quantum evolution of the quantronium state by applying radiofrequency pulses on the gate and bias-current pulses. However, this first quantronium prototype needs to be improved on several points. First, it suffers from a residual dephasing. Secondly, it is delicate to tune at the optimal point where the best coherence times are obtained. Thirdly, the readout is imperfect: its sensitivity is not optimal and it probably induces a loss of polarisation during the measurement. Improvements of the quantronium are possible:

- A larger ratio E_J/E_C would reduce the sensitivity to charge noise.
- Implementing a magnetic shielding would possibly allow to reduce the phase noise.
- The readout line must be engineered more carefully in order to eliminate the problem of the loss of polarisation at readout.

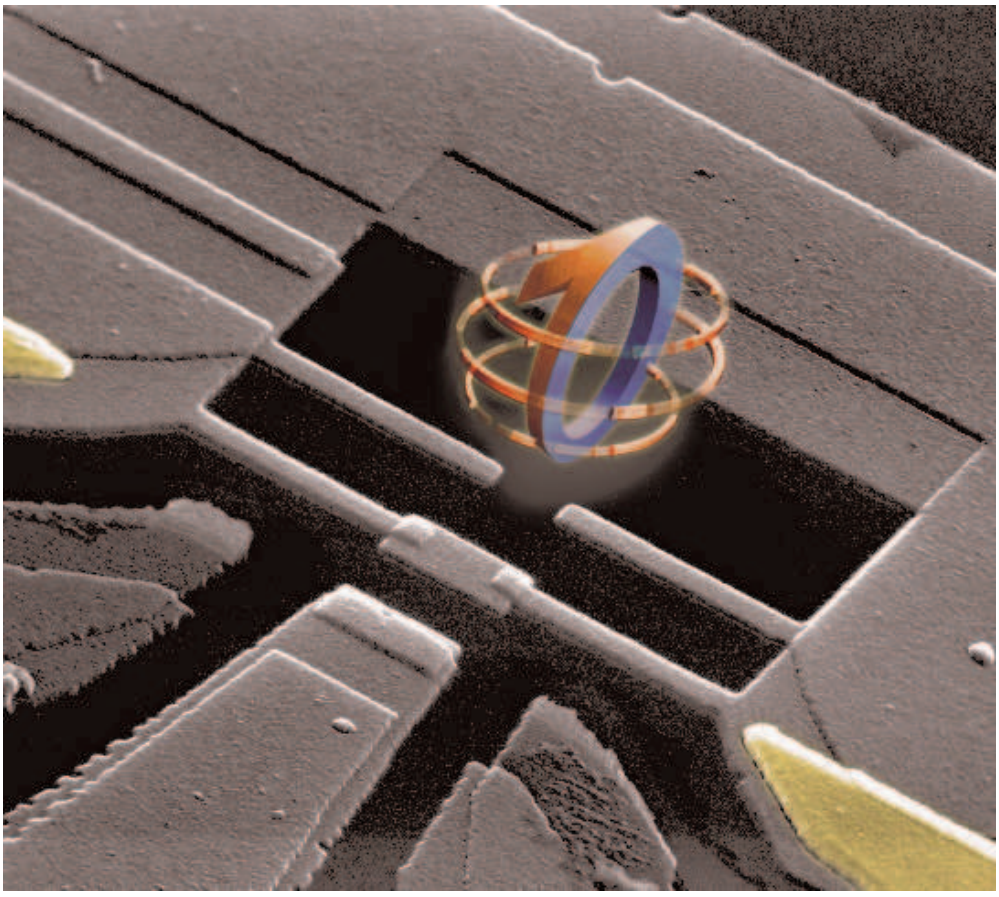

Figure 4.30: Artist view of the Quantronium

Appendix 4-A: Physical implementation of the quantronium

(In experiment 4, the Cooper pair box is disconnected, but the electrical lines are the same as in experiment 5)

4-A-1 Sample description

We have first implemented the capacitor C_L on-chip as an interdigitated capacitor using electron beam lithography (EBL) with a $UV3$ resist. In fact, three capacitors were engineered on-chip (Figure 4.32, picture 1) in order to tune C_L . The connection between these interdigitated capacitor and the box is an EBL fabricated triangular interdigitated capacitor.(Figure 4.32, 2). The split Cooper pair box and micron size junction have been engineered in a second EBL stage on a PMMA/MAA resist (The low scale part of the mask used and the device after evaporation are shown is picture 4.31). The sample wears a true quantronium and two test ones (Figure 4.32, 3). The box of the left quantronium and the readout junction of the right quantronium are disconnected on purpose, in order to test the sample before cooling it down. Figure 4.32, 4 shows the Cooper pair box and the readout junction of the middle quantronium. Two gold quasiparticle traps are connected to the bias line in order to prevent quasiparticle from tunneling into the island. The dimensions of the box junctions are 175 nm×175 nm and those of the big junction 300 nm×3.3 μm (Figure 4.32, 5)

4-A-2 Printed circuit board

The sample is gold-wire bounded to a miniature PCB used to facilitate the connection between the sample and the SMC components R_s and R_1 (Figure 4.33). The PCB is placed inside the sample holder (Figure 4.34) and connected to electrical lines which go up to the room temperature bias sources and amplifiers.

4-A-3 Electrical lines

Figure 4.35 presents a global schematics of the electrical lines of experiment 5, from the sample to the room temperature amplifiers. The capacitance $C_s = 10$ pf is provided by the cable connecting the bias line to the sample. All the lines are carefully filtered [66, 67] in order to reach thermal equilibrium at the base temperature. Note that in experiments 4 and 5, the noise filtering is not made with (R,C) microfabricated filters but with microcoaxial line which act as (R,C) filters. The bandwidth of the current-biasing line is however kept large enough to pass submicrosecond readout square pulses.

Next page:

- *Top: Figure 4.31. Left panel: Low scale representation of the lithography mask used for the fabrication of the quantronium. Right panel: Result of the two angles evaporation of this mask. The first layer evaporated (in yellow) is oxidized before the evaporation of the second layer (in transparent blue). The overlap zones, which appear in green include the three Josephson junctions.*

- *Bottom: Figure 4.32. Micrographs of the quantronium sample at different scales. (The zoom increases from left to right and top to bottom. The red square in a photograph indicates the part zoomed in the next picture.*

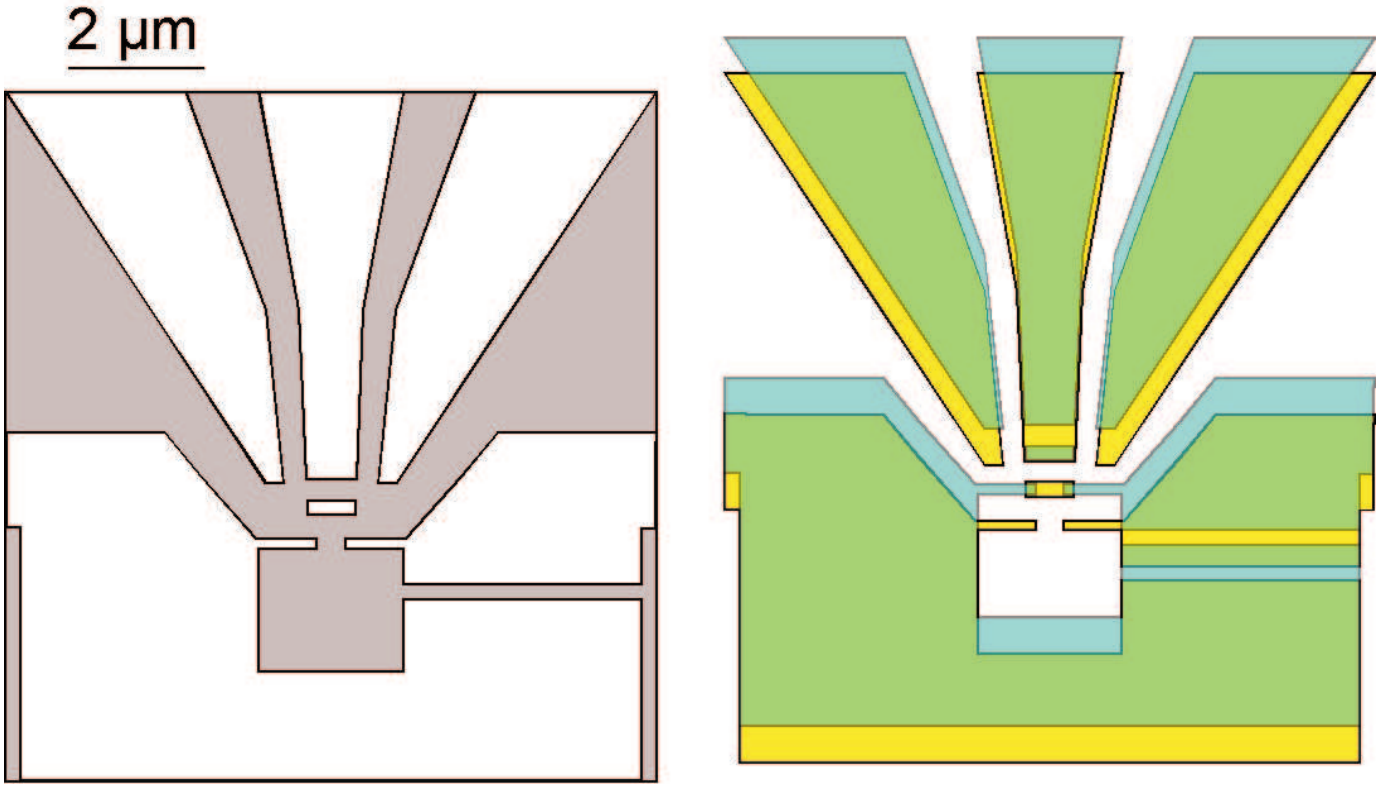

Figure 4.31

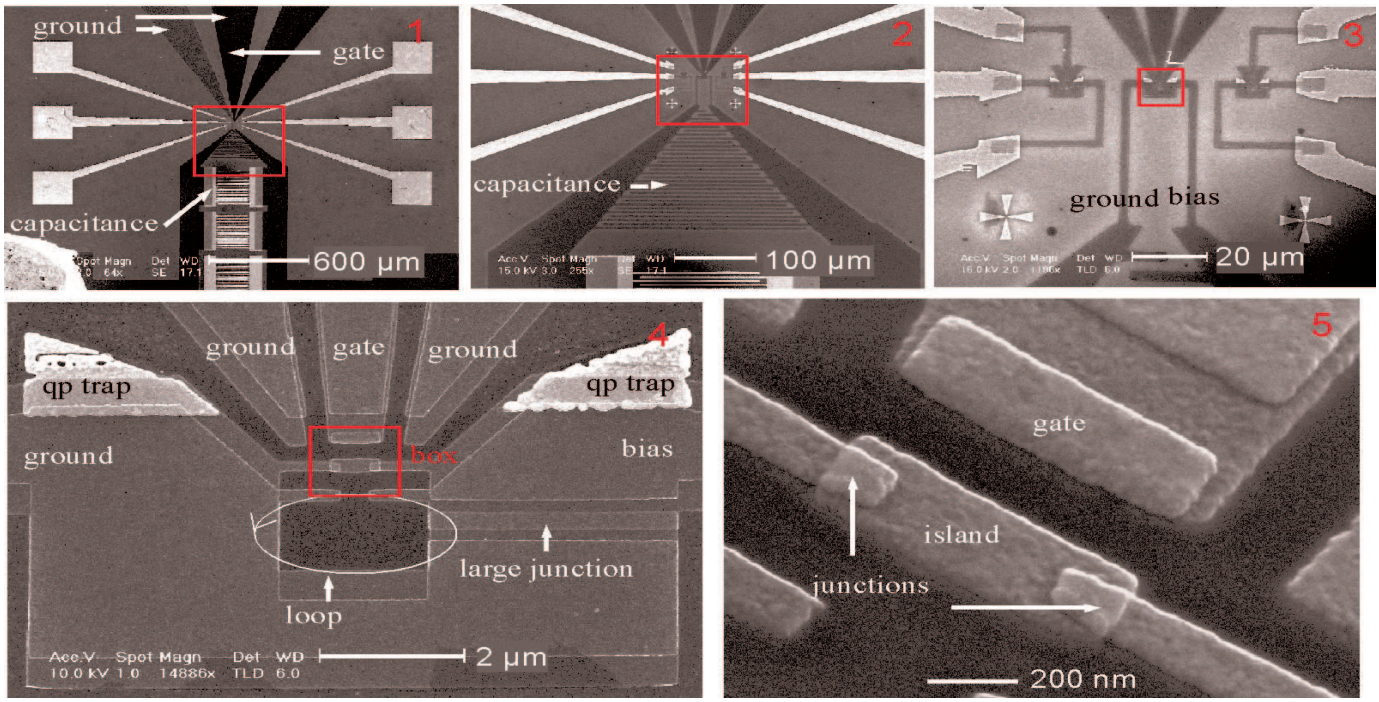

Figure 4.32

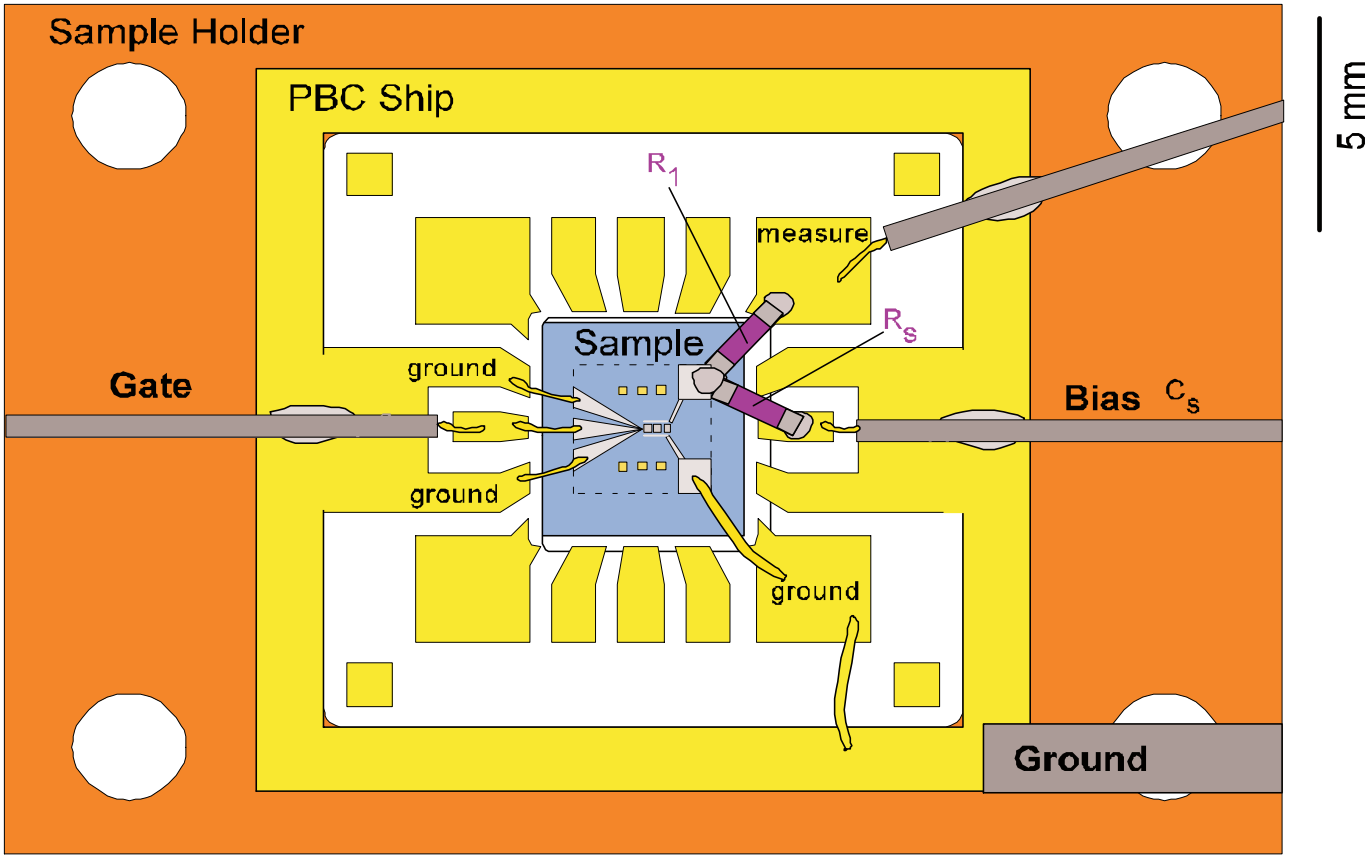

Figure 4.33

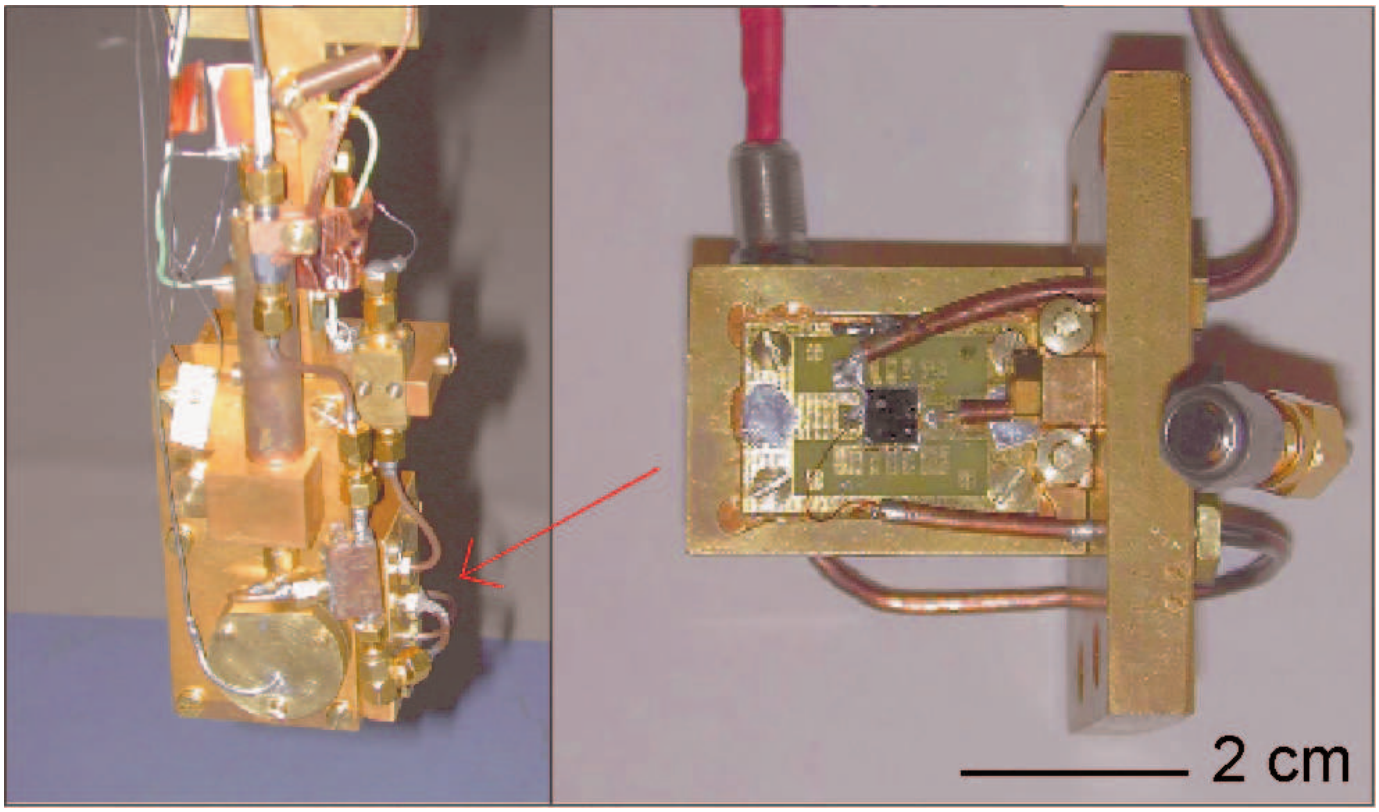

Figure 4.34

Previous page:

- *Top: Figure 4.33.. Sketch of the PCB ship (in white and yellow) which allows to connect the SMC components R_s and R_1 (in pink) to the sample (in light blue). The PCB is put on the sample holder (orange). The yellow areas are the gold tapes of the PCB and the gold boundings. The grey rectangles are the coaxial cables connecting the sample holder to the outside electrical lines. The bias coaxial line has a capacitance $C_s = 10$ pF.*
- *Bottom: Figure 4.34. Picture 1: Photograph of the sample holder closed and connected to the dilution unit of the dilution fridge (the long cylinder is a copper powder filter). Picture 2: Photograph of the sample holder, showing the coaxial lines connected to the PCB chip.*

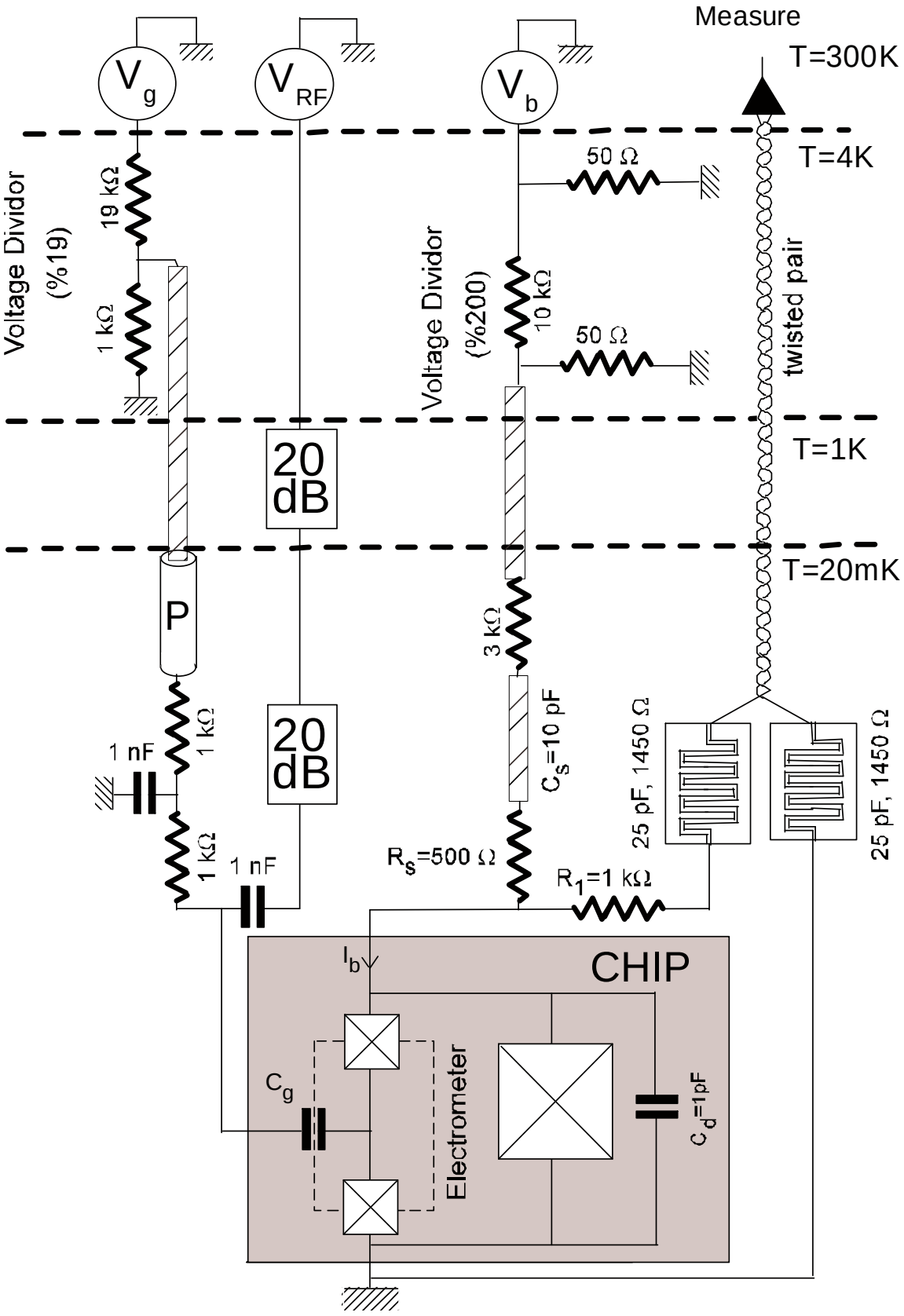

Figure 4.35: *Global schematics of the wiring of experiment 4 (The symbols used are defined in Figure* 2.21*).*

Appendix 4-B: Articles reporting experiments on the quantronium

The articles reproduced here are:

[28] A. Cottet, D. Vion, P. Joyez, A. Aassime, D. Esteve, M.H. Devoret, *Implementation of a Combined Charge-Phase Quantum Bit in a Superconducting Circuit,* Physica C **367**, 197 (2002). *Beware that the definition used for E_J in this paper is different from those used in the body of the thesis.*

[29] D. Vion, A. Aassime, A. Cottet, P. Joyez, H. Pothier, C. Urbina, D. Esteve, and M.H. Devoret, *Manipulating the quantum state of an electrical circuit,* Science **296**, 886 (2002).

The work on the quantronium has also been reported in:

[30] D. Vion, A. Aassime, A. Cottet, P. Joyez, H. Pothier, C. Urbina, D. Esteve, and M.H. Devoret, *Ramsey fringe measurement of decoherence in a novel superconducting quantum bit circuit based on the Cooper pair box,* Phys. Scripta **T102**,162-166 (2002).

[31] D. Vion, A. Aassime, A. Cottet, P. Joyez, H. Pothier, C. Urbina, M.H. Devoret, D. Esteve, *Rabi oscillations, Ramsey fringes and spin echoes in an electrical circuit,* Fortschritte der Physik, **51**, 462 (2003).

[32] D. Vion, A. Aassime, A. Cottet, P. Joyez, H. Pothier, M.H. Devoret, C. Urbina, D. Esteve, *Towards Quantum Electrical Circuits,* to be published in Physica E.

[33] D. Vion, A. Aassime, A. Cottet, P. Joyez, H. Pothier, C. Urbina, D. Esteve, and M.H. Devoret, *Superconducting quantum bit circuit based on the Cooper pair box,* in "Experimental Quantum Computation and Information", F. De Martini and C. Monroe eds., IOS Press 2002, pp. 475-491.

ELSEVIER

Physica C 367 (2002) 197–203

PHYSICA C

www.elsevier.com/locate/physc

Implementation of a combined charge-phase quantum bit in a superconducting circuit

A. Cottet, D. Vion, A. Aassime, P. Joyez, D. Esteve *, M.H. Devoret

Service de Physique de l'Etat Condensé, CEA-Saclay, Quantronics group, F-91191 Gif-sur-Yvette, France

Abstract

We discuss a qubit circuit based on the single Cooper-pair transistor (which consists of two ultrasmall Josephson junctions in series) connected in parallel with a large Josephson junction. The switching of this junction out of its zero-voltage state is used to readout the qubit. We report measurements of the discriminating power of the readout process, and we discuss its back-action on the qubit. © 2002 Elsevier Science B.V. All rights reserved.

PACS: 03.67.Lx; 73.23.Hk; 85.25.Na
Keywords: Qubits; Quantum computing; Charging effects; Quantum coherence

1. Introduction

The recently proposed quantum computing schemes are based on the controlled evolution of a set of two-level systems, called qubits (see Ref. [1] for a review). Suitable qubits should have a quantum coherence time much longer than the duration of an elementary operation, and be measurable when necessary. Among the various systems proposed for implementing qubits, nanofabricated solid-state circuits are particularly attractive because they are more easily scalable. The presently most investigated solid-state qubits are the ''single Cooper-pair box'' [2], in which Rabi precession of a coherent superposition of the qubit states has been demonstrated [3], and the ''flux box'' [4]. In the Cooper-pair box, the qubit states are spanned by discrete charge states of a superconducting small metallic island, and are controlled by the gate charge coupled to the island. In the flux box, the qubit states are spanned by flux states of a small superconducting loop, and are controlled by the flux threading the loop. Whereas some simple qubit manipulations have already been realised in these systems, no readout of a single qubit has yet been achieved. In the case of the Cooper-pair box, the measurement of the island potential either by means of a radio-frequency single electron transistor [5] or of a single Cooper-pair transistor [6], is nevertheless believed to reach a sensitivity sufficient for such a ''single-shot'' readout. In this paper, we discuss a qubit circuit which is controlled both by a charge and by a phase. In this combined charge-phase qubit, qubit control is performed by acting on the gate charge like in the Cooper-pair box, but the measured quantity is a supercurrent, like in the flux box. The main interest of this Q–δ design is to provide (i) a good immunity respectively to the

* Corresponding author. Tel.: +33-016-908-5529; fax: +33-016-908-7442.
E-mail address: esteve@drecam.saclay.cea.fr (D. Esteve).

PII: S0921-4534(01)01014-0

offset charge noise, which is presently considered as the major source of decoherence in charging devices, (ii) a good decoupling from the measuring system when readout is not active, and (iii) a fast pulsed readout. We explain below the operating principle of this Q–δ qubit, and we report first measurements of the readout system resolution.

2. Operating principle of a combined Q–δ qubit based on the single Cooper-pair transistor

The qubit circuit we consider (see Fig. 1a) is based on the single Cooper-pair transistor (SCPT) [7], which consists of two nominally identical ultrasmall junctions in series. When a phase difference δ is imposed across the transistor by means of a small superconducting loop threaded by an applied flux, this device is equivalent to a single Cooper-pair box with an effective Josephson coupling $E_J = 2E_J^0 \cos(\delta/2)$, where E_J^0 is the Josephson energy of each junction with critical current $i_C = E_J^0/\varphi_0$ ($\varphi_0 = \hbar/2e$). The hamiltonian of the transistor depends both on the phase δ and on the gate charge $n_g = C_g U/2e$, and can be written as:

$$H = -2E_J^0 \cos(\delta/2) \cos\widehat{\theta} + E_C(\widehat{n} - n_g)^2. \quad (1)$$

Here, the conjugated variables $\widehat{\theta}$ and $\widehat{n}$ are respectively the difference between the phases across each junction of the transistor, and the number of excess Cooper pairs in this island; $E_C = (2e)^2/(2C_\Sigma)$ is the charging energy of the island with total capacitance C_Σ, and n_g the reduced gate charge in units of $2e$. This hamiltonian is easily diagonalised in the eigenbasis of the charge operator $\widehat{n}$. The eigenstates $|i\rangle$, with energy $E_i(\delta, n_g)$, sustain a supercurrent $I_i = \varphi_0^{-1}(\partial E_i/\partial\delta)$ and correspond to an island voltage $V_i = (2e)^{-1}(\partial E_i/\partial n_g)$. When E_J^0 is not much larger than E_C, and n_g close to $1/2$, the two lowest energy states, labelled 0 and 1 are well separated from the other levels and can be used to implement a qubit. In this circuit, the qubit manipulation can be performed by applying microwave pulses at the qubit transition frequency $\Omega/2\pi = (E_1 - E_0)/h$ on the gate electrode. When E_J^0 is not large compared to E_C, the energies of the qubit levels are well approximated by:

$$E_{0,1} = \mp\sqrt{(E_J^0 \cos(\delta/2))^2 + (E_C(1 - 2n_g))^2}. \quad (2)$$

Although the qubit states can be used over a wide parameter range, some biasing points are more attractive. In particular, at the electrostatic energy degeneracy point $n_g = 1/2$, one has $\partial E_i/\partial n_g = 0$, and, at $\delta = 0$, $\partial E_i/\partial\delta = 0$. At the biasing point ($n_g = 1/2$, $\delta = 0$), the qubit frequency is set by the Josephson energy of the junctions, and is only affected in second order by fluctuations of the control parameters. Dephasing of the qubit should thus be minimized at this biasing point. In particular, the random offset charge noise [9] should less affect this circuit than the Cooper-pair box [8]. In the proposed set-up, the qubit is maintained at the biasing point ($n_g = 1/2$, $\delta = 0$) during its ma-

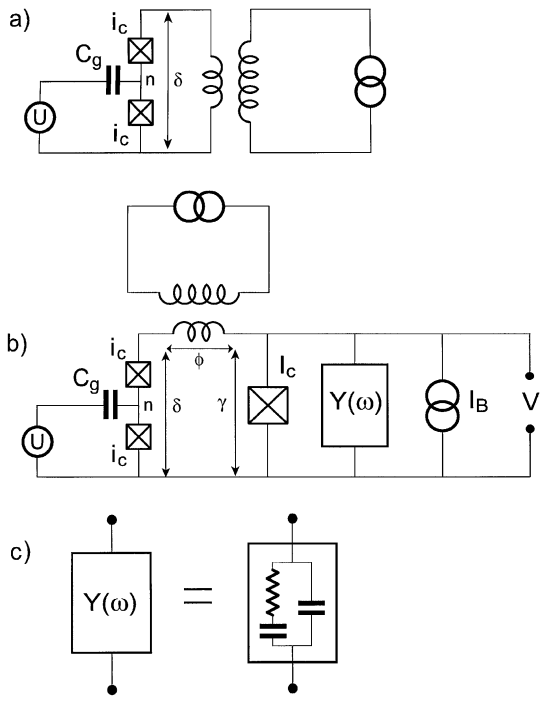

Fig. 1. (a) Schematic circuit of a Q–δ qubit based on a superconducting SCPT in a flux-biased loop; (b) full circuit with a readout Josephson junction, and a bias-current source with admittance $Y(\omega)$. Readout is based on the dependence of the critical current of the system on the qubit state. (c) Effective admittance implemented in the present experiment. An on-chip capacitor $C \approx 1$ pF is connected in parallel with an 500 Ω–10 pF RC-series circuit made with surface mounted components.

nipulation, and the phase δ is varied only during the readout.

The qubit circuit is shown in Fig. 1b: another Josephson junction, with a Josephson energy $E_J = \varphi_0 I_C \gg E_J^0$, is inserted in the loop in order to readout the qubit. The principle of the readout is based on the dependence on the qubit state i of the critical current I_{Ci} of the parallel combination of the transistor and of the large junction. This critical current is the maximum value of $I_{Ci}(\gamma) = I_C \sin\gamma + I_i(\phi+\gamma)$, where γ is the phase across the readout junction, and $(\phi+\gamma)$ the phase across the SCPT. Because the large junction imposes to a good approximation the phase across the transistor, the critical current almost corresponds to $\gamma = \pi/2$. We demonstrate in the following that the critical current can be determined with sufficient accuracy to discriminate both qubit states.

3. Readout resolution

The determination of the critical current can be performed by detecting the transition to a finite voltage state when the bias-current approaches it. This switching transition is easily detected by monitoring the voltage across the system. The switching out of the zero-voltage state of a current-biased Josephson junction has been thoroughly investigated. The current-biased junction is indeed a model system for the dynamics of a single degree of freedom whose coupling to an environment can be controlled [10,11]. The dynamics of the phase γ is that of a particle with mass $C\varphi_0^2$, placed in a tilted washboard potential $U = -E_J \times (\cos\gamma + s\gamma)$, with $s = I/I_C$, and subject to retarded friction determined by the admittance $Y(\omega)$ of the circuit in parallel with the junction. Below the critical value $s = 1$, the potential has metastable equilibrium positions. The phase dynamics is characterised by the frequency $\omega_P/2\pi$ and the quality factor Q of the oscillations at the bottom of the wells. For s close to 1, the oscillation frequency is

$$\omega_P/2\pi \simeq \left(\frac{\sqrt{2}I_C}{\varphi_0 C_{eff}}\right)^{1/2}(1-s)^{1/4}. \tag{3}$$

In this expression, we have assumed that the capacitance C_{eff} includes the eventual contribution of the environment. The quality factor is then $Q = C\omega_P/\mathrm{Re}Y(\omega_P)$. For underdamped or moderately damped junctions ($Q \geqslant 1$), escape out one of these wells triggers the run-away of the phase down the washboard potential, and a finite voltage develops. At high temperature, the phase across the junction is an almost classical variable and switching occurs by thermal activation over the potential energy barrier. The rate of this process follows Kramers' law:

$$\Gamma_{cl} = a\frac{\omega_P}{2\pi}\exp\left(-\frac{\Delta U}{k_B T}\right), \tag{4}$$

where $\Delta U \simeq (4\sqrt{2}/3)E_J(1-s)^{3/2}$, and a is a prefactor of order 1 in the regime $Q \approx 1$. Below the cross-over temperature defined by $k_B T_{CO} = \hbar\omega_P/2\pi$, escape occurs mainly by quantum tunneling "through" the potential energy barrier [11]. For $Q \geqslant 1$, the quantum rate does not depend on Q and is:

$$\Gamma_q = 52\sqrt{\frac{\Delta U}{\hbar\omega_P}}\frac{\omega_P}{2\pi}\exp\left(-7.2\frac{\Delta U}{\hbar\omega_P}\right). \tag{5}$$

It is useful to define the escape temperature T_{esc} through the relation:

$$\Gamma = \frac{\omega_P}{2\pi}\exp(-\Delta U/k_B T_{esc}). \tag{6}$$

The theoretical predictions for a junction in the $Q \geqslant 1$ regime are $T_{esc} \simeq T$ above the cross-over temperature T_{CO}, and $T_{esc} \simeq \hbar\omega_P/7.2k_B$ below. Quantum corrections in the thermal activation regime, and thermal corrections in the quantum regime slightly increase the escape temperature above these values.

When a bias-current pulse I is applied during a time τ, the switching probability for each qubit state i is $P_{Si} = 1 - \exp(-\Gamma_i\tau)$. If these probabilities are different enough, switching provides a single-shot measurement of the qubit. We define the discriminating power of the readout system as $\alpha = |P_{S1} - P_{S0}|$. Single-shot readout is achieved when α is close to 1. The relations (4) and (5) show that the discriminating power is determined by thermal and quantum fluctuations, which limit the slope $\mathrm{d}\Gamma/\mathrm{d}I$.

In order to increase this slope, one should decrease the escape temperature till it reaches the temperature of the experiment, and decrease I_C. Since the quantum escape temperature is set by the readout junction plasma frequency, which is imposed if all junctions are fabricated in the same pump-down, the only way to decrease it significantly is to add an extra capacitance to the readout junction capacitance. Decreasing the critical current I_C is in conflict with the requirement of a good phase bias of the SCPT, and a compromise has to be found, as discussed below. In the present design, the ratio between the readout junction critical current $I_C \approx 1$ μA and the SCPT supercurrent is about 100. Finally, the time resolution is limited by the readout pulse duration, provided that the readout junction stays at thermal equilibration in its potential well when the bias-current is raised. For that purpose, its Q factor should not be too large.

4. Back-action of the environment and of the readout system on the qubit

In fine, the sensitivity of a readout system has to be weighted by its back-action on the qubit during manipulation and readout. As already discussed in the case of the single Cooper-pair box measured by an electrometer [5,12,13], different processes contribute to this back-action. First, the qubit can undergo a transition from the upper state to the ground state by transferring the energy $\hbar\Omega$ to the degrees of freedom it is coupled. This process defines the relaxation time T_R. The reverse excitation process is also possible, and is characterised by an excitation time T_E. Both T_R and T_E are expected to differ when readout is off or on. In particular, T_E is expected to be much longer in the off state, when no energy is available to excite the qubit, than in the on state. When a coherent superposition of qubit states is prepared, it is furthermore randomly dephased by the low frequency fluctuations of the qubit hamiltonian due to both the environment and the measuring system. Dephasing is expected to occur much faster when readout is on because the qubit is no longer decoupled from phase fluctuations.

We first discuss the back-action when readout is off, i.e. at zero-bias-current. In this case, phase fluctuations are small, and the whole circuit connected to the SCPT can be treated as an effective impedance $Z_{\rm eff}(\omega) = (Y(\omega) + jC_{\rm eff}\omega - jI_C/\varphi_0\omega)^{-1}$. Symmetry arguments show that the qubit is not coupled to its environment when the SCPT junctions are balanced, as already mentioned. When SCPT junction asymmetry $d = |E_{J_1}^0 - E_{J_2}^0|/(E_{J_1}^0 + E_{J_2}^0)$ is taken into account, the relaxation time T_R is:

$$T_R \approx \frac{4}{d^2}\frac{\varphi_0}{\mathrm{Re}[Z_{\rm eff}(\Omega)]i_C}, \tag{7}$$

in which we have used Eq. (2). Excitation is negligible ($T_E \gg T_R$), and no dephasing still occurs. Taking into account practical limitations on the junction asymmetry ($d > 0.1$), we estimate $T_R > 20$ μs for the admittance shown in Fig. 1c, and for the parameters $E_J^0 = 2E_C = 0.4k_B$ K. Assuming that the gate charge can be tuned at better than $0.02e$, we estimate that the phase coherence time is limited by the offset charge noise [9] at $T_\varphi > 1$ μs. Note that a duration of 1 μs allows to perform about 100 qubit manipulations.

When readout is on, the phase excursions are not bounded, and only approximate expressions have been obtained. The main result is that the phase coherence time is extremely short $T_\varphi \simeq 50$ ns. This simply means that the readout system has dephased the qubit before the ''pointer'' has moved. We find that T_E is still longer than $T_R > 10$ μs, which we have calculated by averaging over the phase dynamics, assuming that the readout junction plasma frequency is lower than the qubit transition frequency. Circuit design thus results from a trade-off between efficient readout, long relaxation and dephasing times when readout is off, and weak relaxation/excitation when readout is on.

5. Sample fabrication and experimental set-up

Samples were fabricated by electron-beam lithography in a two-step process. First, an interdigitated 1.0 pF capacitor and small metallic

islands, made out of gold, were deposited. The role of the capacitor is to decrease the readout junction resonance frequency in order to improve the discriminating power, while that of the metallic islands is to provide a normal metal sink for spurious quasiparticles in the SCPT electrodes [7]. It is indeed essential to avoid a single quasiparticle entering the SCPT island, which would destroy the desired qubit states at $n_g = 1/2$. In a second step, the SCPT and the readout junction were fabricated by depositing aluminum layers at two angles through a suspended shadow-mask [14]. The first layer was oxidized in order to grow the tunnel junction barriers. Similar SCPT and readout junction are fabricated together with the qubit circuit for the sake of tunnel resistance control. The sample was wire-bonded onto a miniature circuit-board with surface mounted components. The board was fitted in a shielded copper box thermally anchored to the mixing chamber of a dilution refrigerator. All lines were carefully filtered [15] in order to reach thermal equilibrium at the base temperature 14 mK. The bandwidth of the current-biasing line was however kept large enough to pass submicrosecond readout square pulses. When switching occurs, the voltage on the measuring line with capacitance $C_M \approx 0.5$ nF rises at a rate $I_C/C_M \approx 1$ mV/μs. The switching was detected by monitoring the voltage across the readout junction using a low-noise amplifier with a 1 MHz bandwidth.

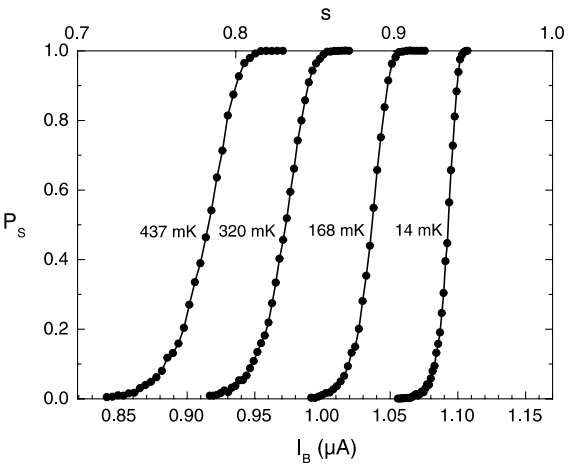

Fig. 2. Switching probability P_S of the readout junction when 0.5 μs long bias-current square pulses with variable amplitude are applied. The critical current is $I_C = 1.17$ μA. The steepest step, obtained at the lowest temperature, would correspond to a discriminating power of 0.6 in a single shot readout of the qubit.

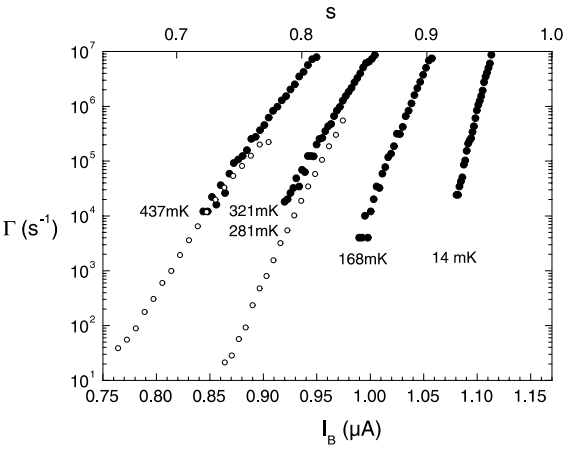

Fig. 3. Switching rate of the readout junction as a function of bias-current $I_B = sI_C$ at different temperatures. Full symbols correspond to 0.5 μs long bias-current square pulses, and open symbols to linear bias-current ramps at $dI_B/dt = 0.84$ μA/ms.

6. Experimental results

We report here switching experiments in a sample with the SCPT disconnected on purpose. We have measured the switching rate of the readout junction alone as a function of bias-current and temperature, using square pulses with adjustable height, or linear ramps [16] for current-biasing the readout junction. The variations of the switching probability when the height of 0.5 μs readout pulses is varied are shown in Fig. 2 for different temperatures. The maximum slope, obtained at the lowest temperature, would correspond to a discriminating power of 0.6 for the readout. Switching rates obtained using both measurement techniques are shown in Fig. 3 as a function of bias-current, for different temperatures. The escape temperature defined by Eq. (6), and determined following the procedure described in Ref. [17], is plotted in Fig. 4. The lowest measured escape temperature is about 90 mK, which is

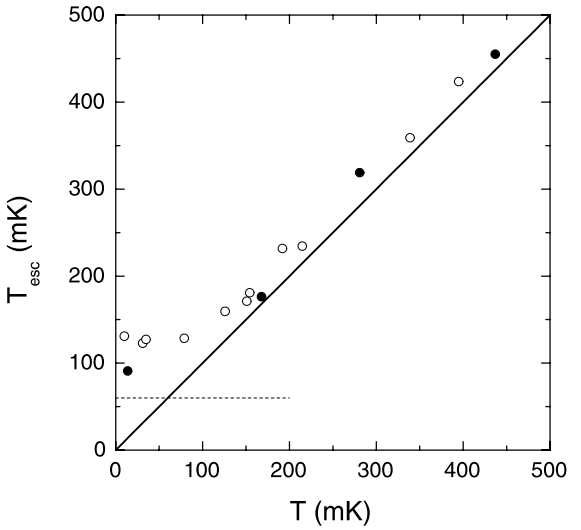

Fig. 4. Escape temperature versus sample temperature. Full symbols correspond to bias-current square pulses, and open symbols to linear bias-current ramps. We attribute the difference found at low temperature between both methods to the larger heating of the damping circuit when linear ramps are used. The dashed line indicates the predicted escape temperature assuming that the on-chip capacitance fully adds to the junction capacitance, and that no spurious heating occurs.

higher than the design value of 60 mK predicted using Eq. (5), assuming that the on-chip capacitor fully contributes to the capacitance C_{eff}. We attribute this discrepancy to two effects. First, the SMC resistor in the bias-current line is slightly heated by the bias-current, as indicated by the increase observed when relatively slow bias-current ramps are used instead of fast pulses. Second, the on-chip added capacitance is not fully effective because of the residual inductance of the connecting lines and of the capacitance itself. Quantitatively, we have calculated that the quantum tunneling rate is the same as if about half of the on-chip capacitance was effectively contributing [18]. These two effects explain well the value of the minimum escape temperature, and of the resulting discriminating power. These results, which already allow interesting measurements on the qubit to be performed, can be improved, and a discriminating power of 0.95 with 200 ns long readout pulses could be achieved if the predicted escape temperature of 60 mK is reached.

7. Conclusions

We have discussed a new design for a combined charge-phase qubit, based on a SCPT connected in parallel with a large readout junction. Whereas the qubit is addressed using the gate charge coupled to the transistor island, the readout is performed using the supercurrent driven by the phase difference across the transistor, which controls the switching of the readout junction out of the zero-voltage state. From measurements of the switching probability of this junction when a square bias-current pulse is applied, we have determined the discriminating power of the readout. We conclude that single-shot measurements should be possible in this system. Experiments on a full qubit circuit are in progress.

Acknowledgements

We gratefully acknowledge discussions with C. Urbina and Y. Nakamura, and the help of H. Pothier.

References

[1] M. Nielsen, I. Chuang, Quantum Computation and Quantum Information, Cambridge University Press, Cambridge, 2000.
[2] V. Bouchiat, D. Vion, P. Joyez, D. Esteve, M.H. Devoret, Physica-Scripta 76 (1998) 165;
V. Bouchiat, D. Vion, P. Joyez, D. Esteve, M.H. Devoret, J. Supercond. 12 (1999) 789.
[3] Y. Nakamura, Y.A. Pashkin, J.S. Tsai, Nature (London) 398 (1999) 786;
Y. Nakamura, Y.A. Pashkin, J.S. Tsai, Proceedings of the MQC2 Conference, Napoli, 2000;
Y. Nakamura, J.S. Tsai, J. Superconduct. 12 (1999) 799;
Y. Nakamura, J.S. Tsai, J. Low. Temp. Phys. 118 (2000) 765.
[4] J.E. Mooij et al., Science 285 (1999) 1036;
C.H. van der Wal, A.C. ter Haar, F.K. Wilhelm, R.N. Schouten, C.J.P.M. Harmans, T.P. Orlando, S. Lloyd, J.E. Mooij, to be published.
[5] A. Aassime, G. Johansson, G. Wendin, R.J. Schoelkopf, P. Delsing, Phys. Rev. Lett. 86 (2001) 3376.
[6] A. Cottet, A. Aassime, D. Vion, P. Joyez, D. Esteve, M.H. Devoret, in preparation.
[7] P. Joyez, P. Lafarge, A. Filipe, D. Esteve, M.H. Devoret, Phys. Rev. Lett. 72 (1994) 2548.

[8] Y. Nakamura, Y.A. Pashkin, J.S. Tsai, Physica-B 280 (2000) 405;
Y. Nakamura, Y.A. Pashkin, J.S. Tsai, in: D.V. Averin, B. Ruggiero, P. Silvestrini (Eds.), Macroscopic Quantum Coherence and Quantum Computing, Kluwer, 2001, p. 17.
[9] A.B. Zorin, F.J. Ahlers, J. Niemeyer, T. Weimann, H. Wolf, V.A. Krupenin, S.V. Lotkhov, Phys. Rev. B 53 (1996) 13682;
V.A. Krupenin, D.E. Presnov, M.N. Savvateev, H. Scherer, A.B. Zorin, J. Niemeyer, Conference on Precision Electromagnetic Measurements Digest, IEEE 140 (1998).
[10] A. Barone, G. Paternò, Physics and Applications of the Josephson Effect, Wiley, New York, 1992;
K. Likharev, Dynamics of Josephson Junctions and Circuits, Gordon and Breach, New York, 1986.
[11] A.O. Caldeira, A.J. Leggett, Ann. Phys. (New York) 149 (1983) 374.
[12] A. Cottet, A. Steinbach, P. Joyez, D. Vion, H. Pothier, D. Esteve, M.E. Huber, in: D.V. Averin, B. Ruggiero, P. Silvestrini (Eds.), Macroscopic Quantum Coherence and Quantum Computing, Kluwer, 2001, p. 111.
[13] M.H. Devoret, R.J. Schoelkopf, Nature 406 (2000) 1039.
[14] G.J. Dolan, J.H. Dunsmuir, Physica B 152 (1988) 7.
[15] D. Vion, P.-F. Orfila, P. Joyez, D. Esteve, M.H. Devoret, J. Appl. Phys. 77 (1995) 2519.
[16] T.A. Fulton, L.N. Dunkleberger, Phys. Rev. B 9 (1974) 4760.
[17] M.H. Devoret, J.M. Martinis, D. Esteve, J. Clarke, Phys. Rev. Lett. 53 (1984) 1260;
J.M. Martinis, M.H. Devoret, J. Clarke, Phys. Rev. Lett. 55 (1985) 1543;
M.H. Devoret, D. Esteve, C. Urbina, J.M. Martinis, A. Cleland, J. Clarke, in: Yu. Kagan, A.J. Leggett (Eds.), Quantum Tunneling in Condensed Media, Elsevier, The Netherlands, 1992, p. 1543.
[18] A.J. Leggett, Phys. Rev. B 30 (1984) 1208;
D. Esteve, M. Devoret, J.M. Martinis, Phys. Rev. B 34 (1986) 158.

to ~150 GPa, consistent with the modulus values of large SWNT bundles (*22*). Although an individual SWNT has an elastic modulus of ~1 TPa, the value can decrease to ~100 GPa for nanotube bundles, owing to the internanotube defects (for example, imperfect lattice of nanotube bundles owing to different nanotube diameters) present along the bundles.

The long nanotube strands created by our direct synthesis technique are an alternative to the fibers and filaments spun from nanotube slurries (*4*). The mechanical and electrical properties of these strands are superior to the latter fibers: The strands can be produced in high yield and continuously, and the thickness of the strands and their length may be further optimized by tuning the processing conditions to produce practically useful nanotube-based macroscale cables.

References and Notes

1. S. Iijima, *Nature* **354**, 56 (1991).
2. Z. Pan *et al.*, *Nature* **394**, 631 (1998).
3. H. M. Cheng *et al.*, *Chem. Phys. Lett.* **289**, 602 (1998).
4. B. Vigolo *et al.*, *Science* **290**, 1331 (2000).
5. L. J. Ci *et al.*, *Carbon* **38**, 1933 (2000).
6. M. Endo *et al.*, *J. Phys. Chem. Solids* **54**, 1841 (1993).
7. R. Andrews *et al.*, *Chem. Phys. Lett.* **303**, 467 (1999).
8. H. M. Cheng *et al.*, *Appl. Phys. Lett.* **72**, 3282 (1998).
9. Thiophene and ferrocene were dissolved in the carbon source (liquid *n*-hexane), sprayed into the hydrogen stream, and fed from the top of a vertical heated furnace. The hydrogen flow rate was then adjusted to provide the optimum conditions for nanotube strand formation. The gas flow carried the strands downstream, and the nanotube strands were collected at the bottom of the furnace.
10. A. Thess *et al.*, *Science* **273**, 483 (1996).
11. P. Launois *et al.*, *J. Nanosci. Nanotechnol.* **1**, 125 (2001).
12. Our data correspond to the larger tube numbers in the bundle ($N = 37$; $N = 91$), as displayed in figure 4 of S. Rols, R. Almairac, L. Henrard, E. Anglaret, J. L. Sauvajol [*Eur. Phys. J. B* **10**, 263 (1999)].
13. J. E. Fischer *et al.*, *Phys. Rev. B* **55**, R4921 (1997).
14. P. H. Zhang, P. E. Lammert, V. H. Crespi, *Phys. Rev. Lett.* **81**, 5346 (1998).
15. The true strain ε_T is defined as $\varepsilon_T = \ln(L_f/L_0)$, where L_f is the real length of the sample and L_0 is the original length of the sample. The true strain could also be described as $\varepsilon_T = 2\ln(D_0/D_f)$, assuming that the sample volume is constant, where D_0 and D_f are the original diameter and the real diameter of the sample during the measurement, respectively. Therefore, the true stress can be described as $\sigma_T = P/A = 4P\exp(\varepsilon_T)/\pi D_0^2$, where P is the load and A is the real surface area supporting the load. Because $\ln(1+\varepsilon) \approx \varepsilon$ when $\varepsilon < 0.1$, the true stress versus true strain curve has almost the same slope as that of the load versus engineering strain curve in the elastic strain regime.
16. R. H. Baughman *et al.*, *Science* **284**, 1340 (1999).
17. M. M. J. Treacy, T. W. Ebbesen, J. M. Gibson, *Nature* **381**, 678 (1996).
18. E. W. Wong, P. E. Sheehan, C. M. Lieber, *Science* **277**, 1971 (1997).
19. M. F. Yu, B. S. Files, S. Arepalli, R. S. Ruoff, *Phys. Rev. Lett.* **84**, 5552 (2000).
20. J. P. Lu, *Phys. Rev. Lett.* **79**, 1297 (1997).
21. F. Li, H. M. Cheng, S. Bai, G. Gu, M. S. Dresselhaus, *Appl. Phys. Lett.* **77**, 3161 (2000).
22. L. Forró, C. Schönenberger, in *Carbon Nanotubes: Synthesis, Structure, Properties and Applications*, M. S. Dresselhaus, G. Dresselhaus, Ph. Avouris, Eds. (Springer, New York, 2001), pp. 329–390.

23. H.W.Z., C.L.X., and D.H.W. acknowledge financial support from the State Key Project for Fundamental Research of the Ministry of Science and Technology, China, under grant G20000264-04. P.M.A. acknowledges financial support from the NSF through a CAREER grant. B.Q.W. acknowledges support from the NSF Nanoscale Science and Engineering Center, at Rensselaer Polytechnic Institute, for the directed assembly of nanostructures. We also acknowledge useful discussions with N. Koratkar and technical assistance from D. Vansteele and Y. Choi.

10 October 2001; accepted 22 March 2002

Manipulating the Quantum State of an Electrical Circuit

D. Vion,* A. Aassime, A. Cottet, P. Joyez, H. Pothier, C. Urbina,† D. Esteve, M. H. Devoret‡

We have designed and operated a superconducting tunnel junction circuit that behaves as a two-level atom: the "quantronium." An arbitrary evolution of its quantum state can be programmed with a series of microwave pulses, and a projective measurement of the state can be performed by a pulsed readout subcircuit. The measured quality factor of quantum coherence $Q_\varphi \cong 25{,}000$ is sufficiently high that a solid-state quantum processor based on this type of circuit can be envisioned.

Can we build machines that actively exploit the fundamental properties of quantum mechanics, such as the superposition principle or the existence of entangled states? Applications such as the transistor or the laser, often quoted as developments based on quantum mechanics, do not actually answer this question. Quantum mechanics enters into these devices only at the level of material properties, but their state variables such as voltages and currents remain classical. Proposals for true quantum machines emerged in the last decades of the 20th century and are now being actively explored: quantum computers (*1*), quantum cryptography communication systems (*2*), and detectors operating below the standard quantum limit (*3*). The major difficulty facing the engineer of a quantum machine is decoherence (*4*). If a degree of freedom needs to be manipulated externally, as in the writing of information, its quantum coherence usually becomes very fragile. Although schemes that actively fight decoherence have recently been proposed (*5*, *6*), they need very coherent quantum systems to start with. The quality of coherence for a two-level system can be quantitatively described by the quality factor of quantum coherence $Q_\varphi = \pi\nu_{01}T_\varphi$, where ν_{01} is its transition frequency and T_φ is the coherence time of a superposition of the states. It is generally accepted that for active decoherence compensation mechanisms, Q_φ's larger than $10^4\ \nu_{01}\ t_{op}$ are necessary, t_{op} being the duration of an elementary operation (*7*).

Among all the practical realizations of quantum machines, those involving integrated electrical circuits are particularly attractive. However, unlike the electric dipoles of isolated atoms or ions, the state variables of a circuit, like voltages and currents, usually undergo rapid quantum decoherence because they are strongly coupled to an environment with a large number of uncontrolled degrees of freedom (*8*). Nevertheless, superconducting tunnel junction circuits (*9*–*13*) have displayed Q_φ's up to several hundred (*14*), and temporal coherent evolution of the quantum state has been observed on the nanosecond time scale (*10*, *15*) in the case of the single Cooper pair box (*16*). We report here a new circuit built around the Cooper pair box with Q_φ in excess of 10^4, whose main feature is the separation of the write and readout ports (*17*, *18*). This circuit, which behaves as a tunable artificial atom, has been nicknamed a "quantronium."

The basic Cooper pair box consists of a low-capacitance superconducting electrode, the "island," connected to a superconducting reservoir by a Josephson tunnel junction with capacitance C_j and Josephson energy E_J. The junction is biased by a voltage source U in series with a gate capacitance C_g. In addition to E_J, the box has a second energy scale, the Cooper pair Coulomb energy $E_{CP} = (2e)^2/2(C_g + C_j)$. When the temperature T and the superconducting gap Δ satisfy $k_BT \ll \Delta/\ln N$ and $E_{CP} \ll \Delta$, where N is the total number of paired electrons in the island, the number of excess electrons is even (*19*, *20*). The Hamiltonian of the box is then

$$\hat{H} = E_{CP}(\hat{N} - N_g)^2 - E_J\cos\hat{\theta} \qquad (1)$$

where $N_g = C_gU/2e$ is the dimensionless gate

Quantronics Group, Service de Physique de l'Etat Condensé, Direction des Sciences de la Matière, Commissariat à l'Energie Atomique–Saclay, 91191 Gif-sur-Yvette, France.

*To whom correspondence should be addressed. E-mail: vion@drecam.saclay.cea.fr

†Member of CNRS.

‡Present address: Applied Physics Department, Yale University, New Haven, CT 06520, USA.

charge and $\hat{\theta}$ the phase of the superconducting order parameter in the island, conjugate to the number $\hat{N}$ of excess Cooper pairs in it (*16*).

In our experiment, $E_J \cong E_{CP}$ and neither $\hat{N}$ nor $\hat{\theta}$ is a good quantum number. The box thus has discrete quantum states that are quantum superpositions of several charge states with different N. Because the system is sufficiently nonharmonic, the ground $|0\rangle$ and first excited $|1\rangle$ energy eigenstates form a two-level system. This system corresponds to an effective spin one-half $\vec{s}$, whose Zeeman energy $h\nu_{01}$ goes to a minimal value close to E_J when $N_g = 1/2$. At this particular bias point, both states $|0\rangle$ ($s_z = +1/2$) and $|1\rangle$ ($s_z = -1/2$) have the same average charge $\langle\hat{N}\rangle = 1/2$, and consequently the system is immune to first-order fluctuations of the gate charge. Manipulation of the quantum state is performed by applying microwave pulses $u(t)$ with frequency $\nu \cong \nu_{01}$ to the gate, and any superposition $|\Psi\rangle = \alpha\,|0\rangle + \beta\,|1\rangle$ can be prepared.

A novel type of readout has been implemented in this work. The single junction of the basic Cooper pair box has been split into two nominally identical junctions in order to form a superconducting loop (Fig. 1). The Josephson energy E_J in Eq. 1 becomes $E_J \cos(\hat{\delta}/2)$ (*21*), where $\hat{\delta}$ is an additional degree of freedom: the superconducting phase difference across the series combination of the two junctions (*22*). The two states are discriminated not through the charge $\langle\hat{N}\rangle$ on the island (*10*, *23*), but through the supercurrent in the loop $\langle\hat{I}\rangle = (2e/\hbar)\langle\partial H/\partial\delta\rangle$. This is achieved by entangling $\vec{s}$ with the phase $\hat{\gamma}$ of a large Josephson junction with Josephson energy $E_{J0} \approx 20\,E_J$ inserted in the loop (*17*, *24*). The phases are related by $\hat{\delta} = \hat{\gamma} + \phi$, where $\phi = 2e\Phi/\hbar$, Φ being the external flux imposed through the loop. The junction is shunted by a capacitor C to reduce phase fluctuations. A trapezoidal readout pulse $I_b(t)$, with a peak value slightly below the critical current $I_0 = 2eE_{J0}/\hbar$, is applied to the parallel combination of the large junction and the small junctions (Fig. 1C). When starting from $\langle\hat{\delta}\rangle \approx 0$, the phases $\langle\hat{\gamma}\rangle$ and $\langle\hat{\delta}\rangle$ grow during the current pulse, and consequently an $\vec{s}$-dependent supercurrent develops in the loop. This current adds to the bias current in the large junction, and by precisely adjusting the amplitude and duration of the $I_b(t)$ pulse, the large junction switches during the pulse to a finite voltage state with a large probability p_1 for state $|1\rangle$ and with a small probability p_0 for state $|0\rangle$ (*17*). This readout scheme is similar to the spin readout of Ag atoms in a Stern and Gerlach apparatus, in which the spin is entangled with the atom position. For the parameters of the experiment, the efficiency of this projective measurement should be $\eta = p_1 - p_0 = 0.95$ for optimum readout conditions. The readout is also designed so as to minimize the $|1\rangle \rightarrow |0\rangle$ relaxation rate using a Wheatstone bridge–like symmetry. Large ratios E_{J0}/E_J and C/C_j provide further protection from the environment. Just as the system is immune to charge noise at $N_g = 1/2$, it is immune to flux and bias current noise at $\phi = 0$ and $I_b = 0$, where $\hat{I} = 0$. The preparation of the quantum state and its manipulation are therefore performed at this optimal working point.

A quantronium sample is shown in Fig. 1B. It was fabricated with standard e-beam lithography and aluminum evaporation. The sample was cooled down to 15 mK in a dilution refrigerator. The switching of the large junction (*25*) to the finite voltage state is detected by measuring the voltage across it with a room-temperature preamplifier, followed by a discriminator. By repeating the experiment, the switching probability, and hence the occupation probabilities of the $|0\rangle$ and $|1\rangle$ states, can be determined.

The readout part of the circuit was tested by measuring the switching probability p at thermal equilibrium as a function of the pulse height I_p, for a readout pulse duration of $\tau_R = 100$ ns. The discrimination between the estimated currents for the $|0\rangle$ and $|1\rangle$ states was found to have an efficiency of $\eta = 0.6$, which is lower than the expected $\eta = 0.95$. Measurements of the switching probability as a function of temperature and repetition rate indicate that the discrepancy between the theoretical and experimental readout efficiency could be due to an incomplete thermalization of our last filtering stage in the bias current line.

Spectroscopic measurements of ν_{01} were performed by applying to the gate a weak continuous microwave irradiation suppressed just before the readout pulse. The variations of the switching probability as a function of the irradiation frequency display a resonance whose center frequency evolves with dc gate voltage and flux as the Hamiltonian predicts, reaching $\nu_{01} \cong 16.5$ GHz at the optimal working point (Fig. 2). The small discrepancy

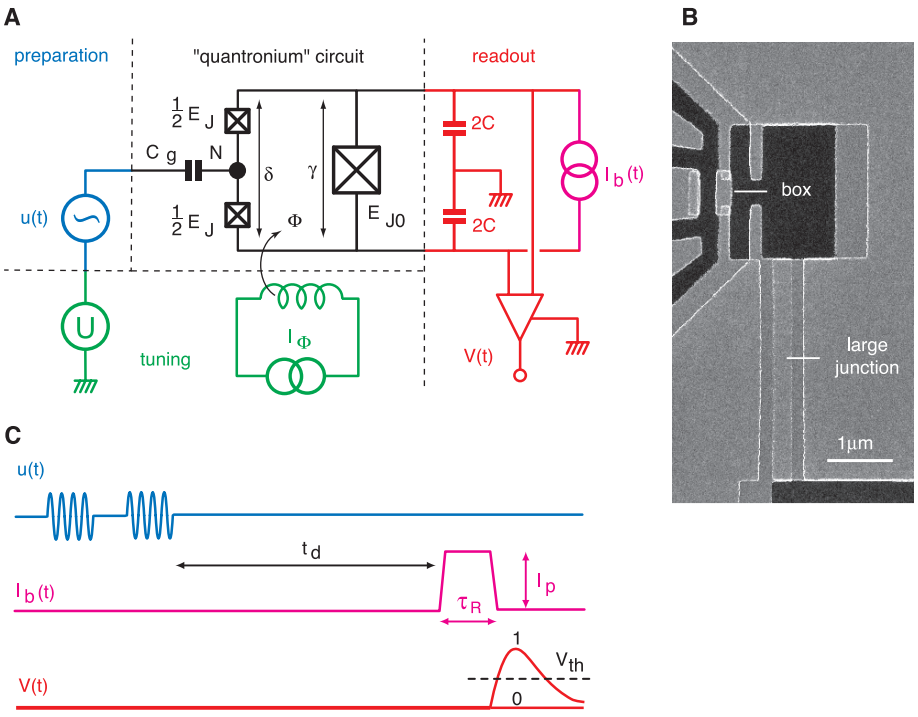

Fig. 1. (**A**) Idealized circuit diagram of the quantronium, a quantum-coherent circuit with its tuning, preparation, and readout blocks. The circuit consists of a Cooper pair box island (black node) delimited by two small Josephson junctions (crossed boxes) in a superconducting loop. The loop also includes a third, much larger Josephson junction shunted by a capacitance C. The Josephson energies of the box and the large junction are E_J and E_{J0}. The Cooper pair number N and the phases δ and γ are the degrees of freedom of the circuit. A dc voltage U applied to the gate capacitance C_g and a dc current I_Φ applied to a coil producing a flux Φ in the circuit loop tune the quantum energy levels. Microwave pulses $u(t)$ applied to the gate prepare arbitrary quantum states of the circuit. The states are read out by applying a current pulse $I_b(t)$ to the large junction and by monitoring the voltage $V(t)$ across it. (**B**) Scanning electron micrograph of a sample. (**C**) Signals involved in quantum state manipulation and measurement. Top: Microwave voltage pulses $u(t)$ are applied to the gate for state manipulation. Middle: A readout current pulse $I_b(t)$ with amplitude I_p is applied to the large junction t_d after the last microwave pulse. Bottom: Voltage $V(t)$ across the junction. The occurrence of a pulse depends on the occupation probabilities of the energy eigenstates. A discriminator with threshold V_{th} converts $V(t)$ into a boolean output for statistical analysis.

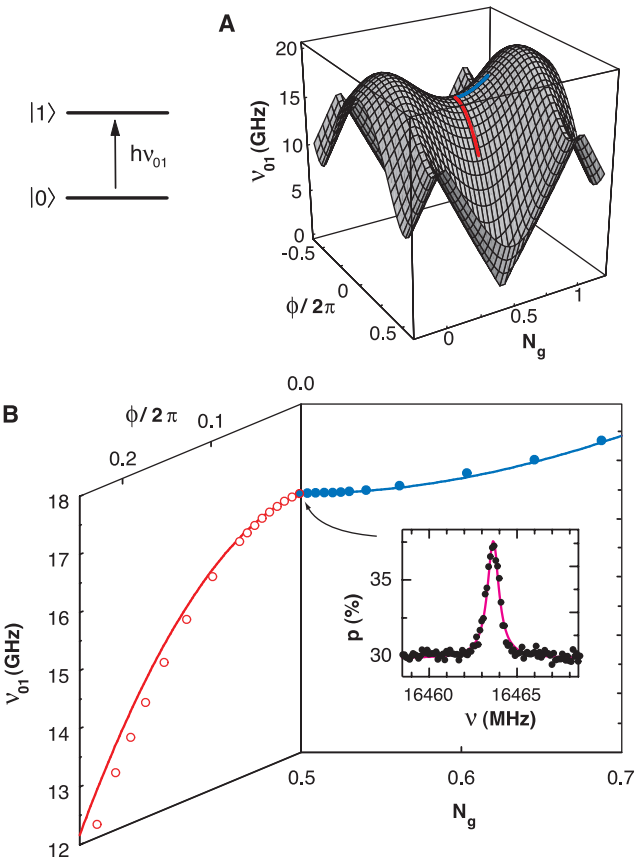

Fig. 2. (**A**) Calculated transition frequency ν_{01} as a function of ϕ and N_g for $E_J = 0.865\ k_BK$ and $E_J/E_{CP} = 1.27$. The saddle point at the intersection of the blue and red lines is an ideal working point where the transition frequency is independent, to first order, of the bias parameters. (**B**) Measured center transition frequency (symbols) as a function of reduced gate charge N_g for reduced flux $\phi = 0$ [right panel, blue line in (A)] and as a function of ϕ for $N_g = 0.5$ [left panel, red line in (A)], at 15 mK. Spectroscopy is performed by measuring the switching probability p (10^5 events) when a continuous microwave irradiation of variable frequency is applied to the gate before readout ($t_d < 100$ ns). Continuous line: Theoretical best fit leading to E_J and E_J/E_{CP} values indicated above. Inset: Lineshape measured at the optimal working point $\phi = 0$ and $N_g = 0.5$ (dots). Lorentzian fit with a FWHM $\Delta\nu_{01} = 0.8$ MHz and a center frequency $\nu_{01} = 16463.5$ MHz (solid line).

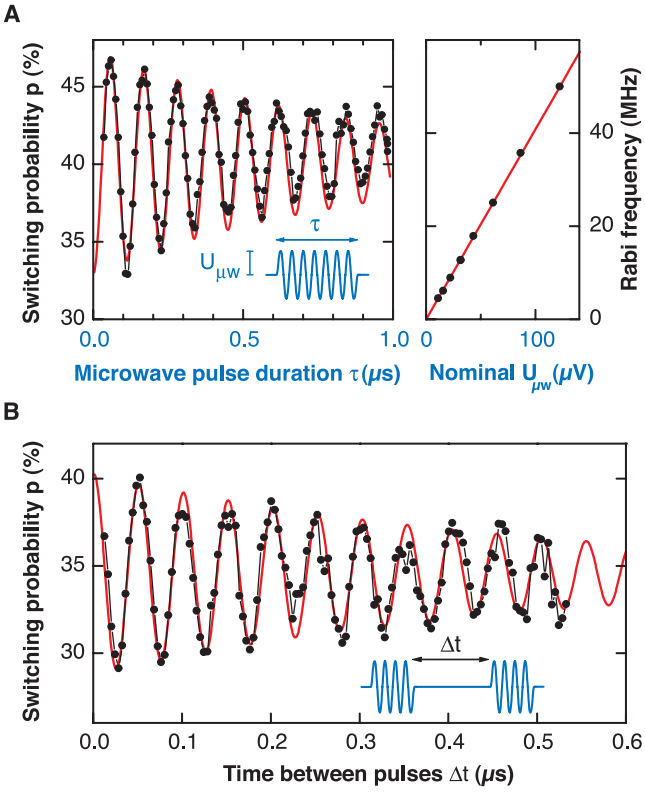

Fig. 3. (**A**) Left: Rabi oscillations of the switching probability p (5×10^4 events) measured just after a resonant microwave pulse of duration τ. Data were taken at 15 mK for a nominal pulse amplitude $U_{\mu w} = 22\ \mu V$ (joined dots). The Rabi frequency is extracted from an exponentially damped sinusoidal fit (continuous line). Right: Measured Rabi frequency (dots) varies linearly with $U_{\mu w}$, as expected. (**B**) Ramsey fringes of the switching probability p (5×10^4 events) after two phase-coherent microwave pulses separated by Δt. Joined dots: Data at 15 mK; the total acquisition time was 5 mn. Continuous line: Fit by exponentially damped sinusoid with time constant $T_\phi = 0.50\ \mu s$. The oscillation corresponds to the beating of the free evolution of the spin with the external microwave field. Its period indeed coincides with the inverse of the detuning frequency (here $\nu - \nu_{01} = 20.6$ MHz).

between theoretical and experimental values of the transition frequency at nonzero magnetic flux is attributed to flux penetration in the small junctions not taken into account in the model. These spectroscopic data have been used to precisely determine the relevant circuit parameters, $E_J = 0.865\ k_BK$ and $E_J/E_{CP} = 1.27$. At the optimal working point, the linewidth was found to be minimal, with a 0.8-MHz full width at half-maximum (FWHM). When varying the delay between the end of the irradiation and the readout pulse, the resonance peak height decays with a time constant $T_1 = 1.8\ \mu s$. Supposing that the energy relaxation of the system is only due to the bias circuitry, a calculation similar to that in (*26*) predicts that $T_1 \sim 10\ \mu s$ for a crude discrete element model. This result shows that no detrimental sources of dissipation have been seriously overlooked in our circuit design.

Controlled rotations of $\vec{s}$ around an axis x perpendicular to the quantization axis z have been performed. Before readout, a single pulse at the transition frequency with variable amplitude $U_{\mu w}$ and duration τ was applied. The resulting change in switching probability is an oscillatory function of the product $U_{\mu w}\tau$ (Fig. 3A), which is in agreement with the theory of Rabi oscillations (*27*), proving that the resonance indeed arises from a two-level system. The proportionality ratio between the Rabi period and $U_{\mu w}\tau$ was used to calibrate microwave pulses for the application of controlled rotations of $\vec{s}$.

Rabi oscillations correspond to a driven coherent evolution but do not give direct access to the intrinsic coherence time T_φ during a free evolution of $\vec{s}$. This T_φ was obtained by performing a Ramsey fringe experiment (*28*), on which atomic clocks are based. One applies to the gate two phase-coherent microwave pulses, each corresponding to a $\pi/2$ rotation around x (*29*) and separated by a delay Δt, during which the spin precesses freely around z. For a given detuning of the microwave frequency, the observed decaying oscillations of the switching probability as a function of Δt (Fig. 3B) correspond to the "beating" of the spin precession with the external microwave field (*30*). The oscillation period agrees exactly with the inverse of the detuning, allowing a measurement of the transition frequency with a relative accuracy of 6×10^{-6}. The envelope of the oscillations yields the decoherence time $T_\varphi \cong 0.50\ \mu s$. Given the transition period $1/\nu_{01} \cong 60$ ps, this means that $\vec{s}$ can perform on average 8000 coherent free precession turns.

In all the time domain experiments on the quantronium, the oscillation period of the switching probability agrees closely with theory, which proves controlled manipulation of $\vec{s}$. However, the amplitude of the oscillations is smaller than expected by a factor of 3 to 4.

This loss of contrast is likely to be due to a relaxation of the level population during the measurement itself.

In order to understand what limits the coherence time of the circuit, measurements of the linewidth $\Delta\nu_{01}$ of the resonant peak as a function of U and Φ have been performed. The linewidth increases linearly when departing from the optimal point ($N_g = 1/2$, $\phi = 0$, $I_b = 0$). This dependence is well accounted for by charge and phase noises with root mean square deviations $\Delta N_g = 0.004$ and $\Delta(\delta/2\pi) = 0.002$ during the time needed to record the resonance. The residual linewidth at the optimal working point is well explained by the second-order contribution of these noises. The amplitude of the charge noise is in agreement with measurements of $1/f$ charge noise (*31*), and its effect could be minimized by increasing the E_J/E_{CP} ratio. The amplitude of the flux noise is unusually large (*32*) and should be significantly reduced by improved magnetic shielding. An improvement of Q_φ by an order of magnitude thus seems possible. Experiments on quantum gates based on the controlled entanglement of several capacitively coupled quantronium circuits could already be performed with the level of quantum coherence achieved in the present experiment.

References and Notes

1. M. A. Nielsen, I. L. Chuang, *Quantum Computation and Quantum Information* (Cambridge Univ. Press, Cambridge, 2000).
2. *The Physics of Quantum Information: Quantum Cryptography, Quantum Teleportation, Quantum Computation*, D. Bouwmeester, A. Ekert, A. Zeilinger, Eds. (Springer-Verlag, Berlin, 2000).
3. V. B. Braginsky, F. Ya. Khalili, *Quantum Measurement* (Cambridge Univ. Press, 1992).
4. W. H. Zurek, J. P. Paz, in *Coherent Atomic Matter Waves*, R. Kaiser, C. Westbrook, F. David, Eds. (Springer-Verlag, Heidelberg, Germany, 2000).
5. P. W. Shor, *Phys. Rev. A* **52**, R2493 (1995).
6. A. M. Steane, *Phys. Rev. Lett.* **77**, 793 (1996); *Rep. Prog. Phys.* **61**, 117 (1998).
7. J. Preskill, *J. Proc. R. Soc. London Ser.* A **454**, 385 (1998)
8. Y. Makhlin, G. Schön, A. Shnirman, *Rev. Mod. Phys.* **73**, 357 (2001).
9. M. H. Devoret *et al.*, in *Quantum Tunneling in Condensed Media*, Y. Kagan, A. J. Leggett, Eds. (Elsevier Science, Amsterdam, 1992).
10. Y. Nakamura, Yu. A. Pashkin, J. S. Tsai, *Nature* **398**, 786, (1999).
11. C. H. van der Wal *et al.*, *Science* **290**, 773 (2000).
12. S. Han, R. Rouse, J. E. Lukens, *Phys. Rev. Lett.* **84**, 1300 (2000).
13. S. Han, Y. Yu, X. Chu, S. -I. Chu, Z. Wang, *Science* **293**, 1457 (2001).
14. J. M. Martinis, S. Nan, J. Aumentado, and C. Urbina (unpublished data) have recently obtained Q_φ's reaching 1000 for a current-biased Josephson junction.
15. Y. Nakamura, Yu. A. Pashkin, T. Yamamoto, J. S. Tsai, *Phys. Rev. Lett.* **88**, 047901 (2002).
16. V. Bouchiat, D. Vion, P. Joyez, D. Esteve, M. H. Devoret, *Phys. Scr.* **T76**, 165 (1998).
17. A. Cottet *et al.*, *Physica C* **367**, 197 (2002).
18. Another two-port design has been proposed by A. B. Zorin [*Physica C* **368**, 284 (2002)].
19. M. T. Tuominen, J. M. Hergenrother, T. S. Tighe, M. Tinkham, *Phys. Rev. Lett.* **69**, 1997 (1992).
20. P. Lafarge, P. Joyez, D. Esteve, C. Urbina, M. H. Devoret, *Nature* **365**, 422 (1993).
21. D. V. Averin, K. K. Likharev, in *Mesoscopic Phenomena in Solids*, B. L. Altshuler, P. A. Lee, R. A. Webb, Eds. (Elsevier, Amsterdam, 1991).
22. J. R. Friedman, D. V. Averin, *Phys. Rev. Lett.* **88**, 50403 (2002).
23. A. Aassime, G. Johansson, G. Wendin, R. J. Schoelkopf, P. Delsing, *Phys. Rev. Lett.* **86**, 3376 (2001).
24. A different Cooper pair box readout scheme using a large Josephson junction is discussed by F. W. J. Hekking, O. Buisson, F. Balestro, and M. G. Vergniory, in *Electronic Correlations: From Meso- to Nanophysics*, T. Martin, G. Montambaux, J. Trân Thanh Vân, Eds. (Editions De Physique, Les Ulis, France, 2001), pp. 515–520.
25. For $C = 1$ pF and $I_0 = 0.77$ μA, the bare plasma frequency of the large junction is $\omega_p/2\pi \cong 8$ GHz, well below ν_{01}.
26. A. Cottet *et al.*, in *Macroscopic Quantum Coherence and Quantum Computing*, D. V. Averin, B. Ruggiero, P. Silvestrini, Eds. (Kluwer Academic, Plenum, New York, 2001), pp. 111–125.
27. I. I. Rabi, *Phys. Rev.* **51**, 652 (1937).
28. N. F. Ramsey, *Phys. Rev.* **78**, 695 (1950).
29. In practice, the rotation axis does not need to be x, but the rotation angle of the two pulses is always adjusted so as to bring a spin initially along z into the plane perpendicular to z.
30. At fixed Δt, the switching probability displays a decaying oscillation as a function of detuning.
31. H. Wolf *et al.*, *IEEE Trans. Instrum. Meas.* **46**, 303 (1997).
32. F. C. Wellstood, C. Urbina, J. Clarke, *Appl. Phys. Lett.* **50**, 772 (1987).

33. The indispensable technical work of P. Orfila is gratefully acknowledged. This work has greatly benefited from direct inputs from J. M. Martinis and Y. Nakamura. The authors acknowledge discussions with P. Delsing, G. Falci, D. Haviland, H. Mooij, R. Schoelkopf, G. Schön, and G. Wendin. Partly supported by the European Union through contract IST-10673 SQUBIT and the Conseil Général de l'Essone through the EQUM project.

26 December 2001; accepted 20 March 2002

Coherent Temporal Oscillations of Macroscopic Quantum States in a Josephson Junction

Yang Yu,[1] Siyuan Han,[1]* Xi Chu,[2]† Shih-I Chu,[2] Zhen Wang[3]

We report the generation and observation of coherent temporal oscillations between the macroscopic quantum states of a Josephson tunnel junction by applying microwaves with frequencies close to the level separation. Coherent temporal oscillations of excited state populations were observed by monitoring the junction's tunneling probability as a function of time. From the data, the lower limit of phase decoherence time was estimated to be about 5 microseconds.

The question of whether macroscopic variables obey quantum mechanics has stimulated extensive theoretical interests (*1*, *2*). The experimental search for macroscopic quantum phenomena (MQP) did not start until the early 1980s, when theory showed that the experimental conditions for observing MQP in Josephson junction–based devices were achievable (*3*–*5*). Many MQP, such as macroscopic quantum tunneling (MQT) (*6*–*10*), energy level quantization (*11*, *12*), quantum incoherent relaxation (*13*), resonant tunneling and photon-assisted tunneling (*14*), and photo-induced transition and population inversion between macroscopic quantum states (*15*, *16*), have since been observed. Recent spectroscopy evidence of superposition of fluxoid states and persistent-current states in superconducting quantum interference devices has also been reported (*17*, *18*). However, time domain coherent oscillations between macroscopic quantum states (MQS), which is more direct evidence for the superposition of MQS, has thus far evaded experimental detection.

One of the methods proposed to create coherent temporal oscillations between two MQS is via Rabi oscillation, an effect that is well established and understood in atomic and molecular systems (*19*). The principle of Rabi oscillations is that by applying a monochromatic electromagnetic (EM) field to a quantum two-level system, which interacts with the EM fields, the system will be in a superposition of the two energy eigenstates that results in oscillations between the lower and upper levels with Rabi frequency Ω. The amplitude of the population oscillations is at a maximum when the frequency of the EM wave ω is in resonance with the level spacing ΔE, i.e., $\omega = \Delta E/\hbar$. Rabi oscillation is a coherent quantum phenomenon that provides the foundation to a wide variety of basic research and applications, ranging from coherent excitation of atoms and molecules by laser to quantum computation (*20*–*22*). Re-

[1]Department of Physics and Astronomy, [2]Department of Chemistry, University of Kansas, Lawrence, KS 66045, USA. [3]Kansai Advanced Research Center, Communication Research Laboratory, Ministry of Posts and Telecommunications, 588-2 Iwaoka, Iwaoka-cho, Nishi-ku, Kobe, 651-24 Japan.

*To whom correspondence and requests should be addressed. E-mail: han@ku.edu

†Present address: Institute for Theoretical Atomic and Molecular Physics, Harvard-Smithsonian Center for Astrophysics, 60 Garden Street, Cambridge, MA 02138, USA.

Index of Variables and Acronyms

This appendix recalls only the notations and acronyms which are used in several places of this thesis.

$a = |\overrightarrow{a}|$: *modulus of the generic vector* $\overrightarrow{a}$

$a_z = \overrightarrow{a}.\overrightarrow{z}$: $\overrightarrow{z}$ *component of the generic vector* $\overrightarrow{a}$

$\overrightarrow{a}_\perp = a_x \overrightarrow{x} + a_y \overrightarrow{y}$: *component transverse to* $\overrightarrow{z}$ *, for the generic vector* $\overrightarrow{a}$

$a_\perp = |\overrightarrow{a}_\perp|$: *modulus of* $\overrightarrow{a}_\perp$*, for the generic vector* $\overrightarrow{a}$

$\widehat{A}$: *quantum operator associated to a classical variable* A

$\langle A(t) \rangle$: *statistical average value of* $A(t)$

$\overrightarrow{a} \cdot \overrightarrow{\sigma}$: *symbolic notation for the quantum operator* $a_x \widehat{\sigma}_x + a_y \widehat{\sigma}_y + a_z \widehat{\sigma}_y$

AC : *Alternating Current*

B : *amplitude of charge noise* [*see* (3.69)]

BCS: *Bardeen Cooper Schriffer theory of superconductivity*

$\mathbb{C}$: *space of complex numbers*

C_g : *gate capacitance of a Cooper pair box or transistor*

C_J : *generic name for the capacitance of a Josephson junction*

$\widehat{c}_p^+, \widehat{c}_p$: *bosonic operators associated to the charge* $\widehat{Q_p^c}$ *and flux* $\widehat{\varphi_p^c}$ *of the capacitor* C_p *in a resonator* (L_p, C_p), [*see* (3.91)]

C_Σ : *total capacitance of the island of a Cooper pair box or transistor*

DC : *Direct Current*

d : *asymmetry between the two junctions of a split Cooper pair box or transistor*

$\overrightarrow{D}_\lambda$: *representative vector of the restriction of* $\frac{\partial \widehat{H}}{\partial \lambda}$ *to the subspace* $\{|0\rangle, |1\rangle\}$, [*see* (1.46)]

$e = 1.6\ 10^{-19}$ *: charge of an electron*

EBL: *Electron Beam Lithography*

$E_C = (2e)^2/2C_\Sigma$: *charging energy of a Cooper pair box or transistor with an island with total capacitance* C_Σ

E_J : *When the experiment deals with a single Josephson junction: Josephson energy of the junction (experiment 1 and experiment of reference [26]).*

When the experiment deals with a Cooper pair box or transistor: total Josephson energy of the junctions of the box or the transistor (see p.44 and experiments 2,3,4,5)

E_J^d : *Josephson energy of the readout junction in Experiments 4 and 5*

E_0^{eff} : *effective Josephson energy of a transistor* [*see* (1.67)]

E_k : *eigenenergy associated to the energy eigenstate* $|k\rangle$ *of a Cooper pair box or transistor*

$\exp()$: *exponential function*

$f_\varphi(t)$: *dephasing factor* [*see* (3.7)]

$g(\omega)$: *transfer function characterising the coupling between a Cooper pair box and an impedance [see(*3.31)].

$\mathcal{G}(n_g)$ *charge-current transduction coefficient of a Cooper pair transistor* [*see* (1.65)]

$\overrightarrow{h}$: *representative vector of the free hamiltonian* $\widehat{H}$ *of a Cooper pair box or transistor in the Bloch sphere scheme* [*see* (1.45)]

$\left|\overrightarrow{h}\right|$: *modulus of* $\overrightarrow{h}$. *(The notation h is not used to avoid confusions with the Planck constant* $\mathtt{h}$*)*

$\mathtt{h}$= 6.63 10^{-34} J.s^{-1} : *Planck constant*

$\hbar = \frac{\mathtt{h}}{2\pi} = 1.05\ 10^{-34}$ J.s^{-1}: *reduced Planck constant*

$\widehat{H}$: *free hamiltonian of the Cooper pair box (i.e. with no coupling to and outside environment)*

$\widehat{H}_c$: *linear coupling hamiltonian between a Cooper pair box and an outside element*

$\widehat{H}_{el}$: *electrostatic hamiltonian of a Cooper pair box or transistor*

$\widehat{H}_J$: *Josephson hamiltonian of a Cooper pair box or transistor*

$\widehat{h}_p$: *hamiltonian of a resonator* (L_p, C_p) [*see* (3.90)]

$\mathbf{i} = \sqrt{-1}$: *unitary imaginary number*

$\overrightarrow{i}$: *representative vector of the current through a Cooper pair box or transistor in the Bloch sphere scheme (see (1.55) in the two charge states approximation)*

i_Z : *equivalent current noise source for an impedance* $Z(\omega)$ *(see section* 3.B.3*)*

I_b : *bias current in all the experiments*

I_p : *amplitude of bias current square pulses in the experiments 3,4,5*

I_0 : *Depending on the experiment considered, critical current of a single Josephson junction (experiment 1 and experiment of reference [26]) or average critical current of the junctions of a Cooper pair box or transistor (see definition* (1.63) *and experiments 2,3,4,5*])

I_J : *Depending on the experiment considered, instantaneous current through a Josephson junction (experiment 1,4 and experiment of reference [26]) or through a Cooper pair transistor (experiment 2,3)*

$\overline{I_J}$: *for a Cooper pair transistor, value of* I_J *averaged over the phase dynamics* (*see* p.76)

I_0^{eff} : *effective critical current of a Cooper pair transistor* [*see* (1.64)]

$|k\rangle$: *generic name for an energy eigenstate of a Cooper pair box or transistor* (*see* p.39)

$k_b = 3.28\ 10^{-23}$: *Boltzmann constant*

$\max_\delta[f(\delta)]$: *maximum of the function* $f(\delta)$ *with respect to the variable* δ

$\min_\delta[f(\delta)]$: *minimum of the function* $f(\delta)$ *with respect to the variable* δ

$[\mathrm{mod}\ \lambda]$: *modulo* λ

$\widehat{\mathbf{n}}$ *: operator associated to the excess number of Cooper pairs on the island of a Cooper pair box or transistor*

$|\mathbf{n}\rangle$: *eigenstate of the operator* $\widehat{\mathbf{n}}$ *for the eigenvalue* $\mathbf{n}$

$\mathbb{N}$: *space of entire numbers*

$\mathbb{N}^*$: *space of nonzero integers*

$n_g = C_g V_g / 2e$: *reduced gate charge of a Cooper pair box or transistor*

$n'_g = C_g V'_g / 2e$: *reduced gate charge of a Cooper pair transistor when it is coupled to a Cooper pair box (in this case, the notation* n_g *is already used for the box)*

qubit: *quantum bit*

$\widehat{Q_p^c}$: *charge of the capacitor* C_p *in the resonator* (L_p, C_p)

Q : *quality factor of a quantum bit [see (4.10) and (4.12)]*

PCB: *Printed Circuit Board*

$P_s(I_p, \tau, n_g)$: *switching probability of the transistor of experiment 3 (left in its ground state) when a bias current pulse with amplitude* I_p *and duration* τ *is applied to it and that the reduced gate charge of the transistor is* n_g

$P_s(I_p, \tau)$: *switching probability of the readout junction of experiments 4 and 5 when a bias current pulse with amplitude* I_p *and duration* τ *is applied to it*

$P_u(I_p, \tau, n_g, \delta_m)$: *switching probability of the quantronium in state* $|u\rangle$ *when a bias current pulse with amplitude* I_p *and duration* τ *is applied to it, that the reduced gate charge of the transistor is* n_g*, and that the reduced flux threading the quantronium loop is* δ_m

$P_0(I_p, \tau, n_g, \delta_m)$: *switching probability of the quantronium in state* $|0\rangle$ *(see above)*

$P_1(I_p, \tau, n_g, \delta_m)$: *switching probability of the quantronium in state* $|1\rangle$ *(see above)*

RF : *radiofrequency*

$\mathcal{R} = (\overrightarrow{x}, \overrightarrow{y}, \overrightarrow{z})$: *orthonormal referential of the Bloch sphere, with* $\overrightarrow{z} = \overrightarrow{h} / \left|\overrightarrow{h}\right|$ *(see section* 1.3.1*)*

$\mathcal{R}' = (\overrightarrow{x'}, \overrightarrow{y'}, \overrightarrow{z'})$: *orthonormal referential of the Bloch sphere, defined in the case* $E_J \ll E_C$*, with* $\overrightarrow{z'}$ *the charge axis (see section* 1.3.1*)*

$\mathcal{R}_p = (\overrightarrow{x}_p, \overrightarrow{y}_p, \overrightarrow{z}_p)$: *turning orthonormal referential of the Bloch sphere, with* $\overrightarrow{z}_p = \overrightarrow{h} / \left|\overrightarrow{h}\right|$ *(see section* 1.3.1*)*

$R_k = \mathtt{h}/e^2 \simeq 25.9\ \mathrm{k}\Omega$: *resistance quantum*

SMC: *Surface Mounted Component*

$S_A^{cl}(\omega)$: *classical noise spectrum of the time varying signal* $A(t)$ *[see* (3.94)*]*

$S_A(\omega)$: *generalised noise spectrum of the quantum operator* $\widehat{A}(t)$ *[see* (3.101)*]*

$\mathrm{sinc}(x) = \sin(x)/x$: *sinuscardinal function*

SQUID : *Superconducting Quantum Interference Device*

t : *time*

t_d : *delay time between the end of the radiofrequency sequence applied to the qubit and the*

beginning of the measurement of its state (see Figure 4.1)

t_{meas} : *measurement time needed for a measuring apparatus to discriminate the states* $|0\rangle$ *and* $|1\rangle$

$t_T = \hbar/\pi k_b T$: *"thermal" time*

T : *temperature*

T_{CO} : *cross over temperature between the quantum and thermal escape regimes for a Josephson junction* [*see* (4.3)]

T_R : *relaxation time of a quantum two level system, sometimes noted* $T_R^{off\ (on)}$ *when the readout device is on (or off).*

T_E : *excitation time of a quantum two level system, sometimes noted* $T_E^{off\ (on)}$ *when the readout device is on (or off).*

T_φ : *dephasing time of a quantum two level system, sometimes noted* $T_\varphi^{off\ (on)}$ *when the readout device is on (or off).*

T_2 : *total lifetime of a coherent superposition of states in a quantum two level system, when this system is left to evolve freely* [*see* (4.11)]

$T_J = 2\pi/\Omega_J$: *Josephson period of a Josephson junction*

$|u\rangle$: *generic name for a superposition of the states* $|0\rangle$ *and* $|1\rangle$

$\overrightarrow{u}$: *representative vector of* $|u\rangle$

u_Z : *equivalent voltage noise source for an impedance* $Z(\omega)$ *(see section* 3.B.3*)*

$\widehat{V}$: *operator associated to the island potential of a Cooper pair box or transistor* [*see* (1.28)]

V_J : *instantaneous voltage across a Cooper pair box, transistor or junction, depending on the experiment considered*

$\overline{V_J}$: *for a Cooper pair transistor, value of* V_J *averaged over the phase dynamics* (*see* p.76)

V_g : *gate voltage of a Cooper pair box or transistor*

V_g' : *gate voltage of a Cooper pair transistor coupled to a Cooper pair box (In this case, the notation* V_g *is already used for the box)*

$Z_p = \sqrt{L_p/C_p}$: *characteristic impedance for a resonator* (L_p, C_p)

α : *discriminating power of a threshold detector* [*see*(2.15) and (4.7)]

δ : *superconducting phase across a Cooper pair box, transistor or junction, depending on the experiment considered*

δ_m : *magnetic flux threading the quantronium loop*

δ_D : *Dirac function*

$\mathbf{\Delta}$: *BCS superconducting gap of a metal.* $\mathbf{\Delta} \simeq 180$ μeV *for aluminium*

$\widehat{\delta\lambda}$: *shift of the control parameter* λ *of a Cooper pair box* ($\lambda = n_g$ *or* δ)

Δn_{01} : *difference between the mean charges of the states* $|0\rangle$ *and* $|1\rangle$ [*see* (1.62)]

Δn_g : *amplitude of a radiofrequency excitation in terms of reduced gate charge* [*see* (1.56)]

$\Delta\theta_u$: *variation of the polar coordinate* θ_u *of* $\overrightarrow{u}$ *during the manipulation of the quantronium state*

$\Delta\varphi_u$: *variation of the azimuthal coordinate* φ_u *of* $\overrightarrow{u}$ *during the manipulation of the quantronium state*

$\gamma = 0.577216$: *Euler constant*

λ : *generic name used for the control parameters* n_g *and* δ

$\kappa_{\rm SCPT} = C_c/C_J$: *coupling constant between a basic Cooper pair box and a measuring Cooper pair transistor (with* C_c *the capacitor connecting the two islands and* C_J *the capacitance of the box junction)*

$\kappa_d = E_J/E_J^d$: *coupling constant between the split Cooper pair box and the readout junction of a quantronium circuit*

$\kappa_g = C_g/C_\Sigma$: *coupling constant between a Cooper pair box and the resistance of its gate line*

$\kappa_L = E_J L/\varphi_0^2$: *coupling constant between a split Cooper pair box and an inductance* L *mounted in parallel*

μ_p : *coupling coefficient between a Cooper pair box and a bosonic mode with frequency* ω_p [*see* (3.14)]

$\Psi_k(\theta) = \langle\theta\,|k\rangle$: *wavefunction associated to the state* $|k\rangle$ *in the phase space associated to* $\widehat{\theta}$

$\widehat{\varphi_p^c}$: *operator associated to the phase difference across the capacitor* C_p *of a resonator* (L_p, C_p)

$\widehat{\varphi_p^l}$: *operator associated to the phase difference across the inductor* L_p *of a resonator* (L_p, C_p)

φ_u : *azimuthal coordinate of* $\overrightarrow{u}$

$\varphi_0 = \hbar/2e = 3.28\ 10^{-16}$: *reduced flux quantum*

$\Gamma_s(I_b, n_g)$: *switching rate of the transistor of experiment 3 and of that of reference [26] (left in its ground state) for a bias current* I_b *and a reduced gate charge* n_g

$\Gamma_s(I_b)$: *switching rate of the readout junction of experiments 4 and 5 for a bias current* I_b

$\Gamma_u(I_b, n_g, \delta_m)$: *switching rate of the quantronium in state* $|u\rangle$ *when its bias current is* I_b*, its reduced gate charge* n_g*, and the reduced flux threading the quantronium loop* δ_m

$\Gamma_0(I_p, n_g, \delta_m)$: *switching rate of the quantronium in state* $|0\rangle$ *(see above)*

$\Gamma_1(I_p, n_g, \delta_m)$: *switching rate of the quantronium in state* $|1\rangle$ *(see above)*

$\Gamma_R = 1/T_R$: *relaxation rate of a Cooper pair box, sometimes noted* $\Gamma_R^{off\ (on)}$ *when the off/on state of the readout device is specified.*

$\Gamma_E = 1/T_E$: *excitation rate of a Cooper pair box, sometimes noted* $\Gamma_E^{off\ (on)}$ *when the off/on state of the readout device is specified.*

$\Gamma_\varphi = 1/T_\varphi$: *dephasing rate of a Cooper pair box, sometimes noted* $\Gamma_\varphi^{off\ (on)}$ *when the off/on state of the readout device is specified.*

$\omega_p = 1/\sqrt{L_p C_p}$: *resonance pulsation of a resonator* (L_p, C_p)

Ω_{01} : *resonance pulsation between the states* $|0\rangle$ *and* $|1\rangle$ *of a Cooper pair box* [*see* (1.41)]

$\Omega_J = \overline{V_J}/\varphi_0$: *Josephson frequency of a Josephson junction*

$\nu_{01} = \Omega_{01}/\hbar$: *resonance frequency between the states* $|0\rangle$ *and* $|1\rangle$ [*see* (1.41)]
ν_{Rabi} : *Rabi frequency of a Cooper pair box* [*see* (1.58)]
ν_{Ramsey} : *Ramsey frequency of a Cooper pair box* [*see* (1.59)]
ν_{RF} : *frequency of the radiofrequency excitation sent on a Cooper pair box* [*see* (1.56)]
$\widehat{\sigma}_x$, $\widehat{\sigma}_y$, $\widehat{\sigma}_y$, : *Pauli matrices (see* [1.39]*)*
$\widehat{\sigma}_u = \overrightarrow{\sigma}.\overrightarrow{u} = u_x\widehat{\sigma}_x + u_y\widehat{\sigma}_y + u_z\widehat{\sigma}_y$: *Pauli operator associated to the* $\overrightarrow{u}$ *component of a spin*
$\widehat{\theta}$: *operator associated to the superconducting phase of the island of a Cooper pair box*
θ_u : *polar coordinate of* $\overrightarrow{u}$
$|0\rangle$: *ground state of a Cooper pair box or transistor*
$|1\rangle$: *first excited state of a Cooper pair box or transistor*

Bibliography

[1] E. Schrödinger, Naturwissenschaften, **23**, 807,823, 844 (1935).

[2] W. H. Zurek, Physics Today **44**, 36 (1991); W. H. Zurek and J. P. Paz, in *Coherent atomic matter waves*, edited by R. Kaiser, C. Westbrook and F. David, (Springer-Verlag Heidelberg 2000) [quant-ph/0010011].

[3] A. O. Caldeira and A.J. Leggett, Ann. Phys. (N.Y.) **149**, 374 (1983).

[4] J. M. Martinis, M. H. Devoret and J. Clarke, Phys. Rev. B. **35**, 4682 (1987); J. M. Martinis, M. H. Devoret and J. Clarke, Phys. Rev. Lett. **55**, 1543 (1985); M. H. Devoret, D. Esteve, C. Urbina, J. M. Martinis, A. Cleland, and J. Clarke, in *Quantum Tunneling in Condensed Media*, edited by Yu. Kagan and A.J. Leggett (Elsevier, The Netherlands, 1992).

[5] Siyuan-Han, R. Rouse, J. E. Lukens, Phys. Rev. Lett. **84**, 1300 (2000).

[6] D. Deutsch and R. Joza, "Rapid Solution of Problems by Quantum Computation," Proc. R. Soc. Lond. A **439** 553-558 (1992).

[7] P.W. Shor, in *Proceedings of the symposium on the foundations of computer science* (IEEE Computer Society press, New York, 1994).

[8] M. A. Nielsen and I. L. Chuang, *Quantum Computation and Quantum Information* (Cambridge University Press, Cambridge, 2000).

[9] A. Steane, Rep. Prog. Phys **61**, 117, (1998).

[10] P.W.Shor, Phys. Rev. A **52**, R2493 (1995).

[11] A.M. Steane Phys. Rev. Lett. **77,** 793 (1996), Rep.Prog.Phys. **61**, 117 (1998).

[12] J. Preskill, Proc. R. Soc. A. **454**, 385 (1998).

[13] D. Kielpinski, A. Ben-Kish, J. Britton, V. Meyer, M.A. Rowe, C.A. Sackett, W.M. Itano, C. Monroe, and D. J. Wineland," Proceedings of the International Conference on Experimental Implementation of Quantum Computation (in press). LANL E-print archive# quant-ph/0102086

[14] L.M.K. Vandersypen, M. Steffen, G. Breyta, C.S. Yannoni, M.H. Sherwood, I.L. Chuang, Nature, **414**, 883-887 (2001).

[15] Caspar H. van der Wal, A. C. J. ter Haar, F. K. Wilhelm, R.N. Schouten, C. J. P. M. Harmans, T. P. Orlando, Seth Lloyd and J. E. Mooij, Science **290**, 773 (2000).

[16] "*Macroscopic Quantum Coherence and Quantum Computing*", J. Pekola , B. Ruggiero, and P. Silvestrini (Kluwer Academic, Plenum Publishers, New York, 2001) and "*International Workshop on Superconducting Nano-electronic Devices*", B. Ruggiero, and P. Silvestrini eds., (Kluwer Academic, Plenum Publishers, New York, 2002).

[17] V. Bouchiat, D. Vion, P. Joyez, D. Esteve and M.H. Devoret, Physica Scripta, **76**, 165 (1998).

[18] V. Bouchiat, "*Quantum Fluctuations of the Charge in Single Electron and Single Cooper Pair Devices",* Thèse de doctorat, Université Paris VI, 1997. See www-drecam.cea.fr/drecam/spec/Pres/Quantro/Index.htm.

[19] Y. Nakamura, Yu. A. Pashkin and J. S. Tsai, Nature **398**, 786, (1999) and in "*Macroscopic Quantum Coherence and Quantum Computing*", eds. D.V. Averin , B. Ruggiero, and P. Silvestrini (Kluwer Academic, Plenum Publishers, New York, 2001), p17; Y. Nakamura and J. S. Tsai, J. of Superconductivity, **12**, 799 (1999), and J. Low. Temp. Phys. **118**,765 (2000); Phys. Rev. Lett. **87**, 246601 (2001); Y. Nakamura, Yu. A. Pashkin, T. Yamamoto, and J. S. Tsai, Phys. Rev. Lett. **88**, 47901 (2002).

[20] A. B. Zorin, F. J. Ahlers, J. Niemeyer, T. Weimann, H. Wolf, V. A. Krupenin, and S. V. Lotkhov, Phys. Rev. B **53**,13682 (1996); V. A. Krupenin, D. E. Presnov, M. N. Savvateev, H. Scherer, A. B. Zorin, and J. Niemeyer, Conference on Precision Electromagnetic Measurements Digest, IEEE, **140** (1998). H. Wolf, F. J. Ahlers, J. Niemeyer, H. Scherer, T. Weimann, A. B. Zorin, V. A. Krupenin, S. V. Lotkhov, D.E. Presnov IEEE Trans. Instrum. Meas. **46**, 303 (1997).

[21] A. Aassime, G. Johansson, G. Wendin, R. J. Schoelkopf, and P. Delsing, Phys. Rev. Lett., **86**, 3376 (2001).

[22] P. Joyez, P. Lafarge, A. Filipe, D. Esteve and M. H. Devoret, Phys. Rev. Lett. **72**, 2548 (1994).

[23] R. P. Welty and J. M. Martinis, IEEE Trans. Mag. **27**, 2924 (1991).

[24] A.H. Steinbach , P. Joyez , A. Cottet , D. Esteve , M.H. Devoret, M.E. Huber and J.M. Martinis, Phys. Rev. Lett. **87**, 137003 (2001).

[25] A. Cottet, A.H. Steinbach, P. Joyez, D. Vion, H. Pothier, D. Esteve, and M.E. Huber, in "*Macroscopic Quantum Coherence and Quantum Computing*", eds. D.V. Averin , B. Ruggiero, and P. Silvestrini (Kluwer Academic, Plenum Publishers, New York, 2001), p111.

[26] P. Joyez, D. Vion, M. Götz, M.H. Devoret, D. Esteve, J. of Supercond. **12,** 757 (1999).

[27] A. Cottet, D. Vion, P. Joyez, D. Esteve, and M.H. Devoret, Workshop on "Macroscopic Quantum Coherence and Computing", Naples, Italy (2001).

[28] A. Cottet, D. Vion, P. Joyez, P. Aassime, D. Esteve, M.H. Devoret, Physica C **367**, 197 (2002).

[29] D. Vion, A. Aassime, A. Cottet, P. Joyez, H. Pothier, C. Urbina, D. Esteve, and M.H. Devoret, Science **296**, 886 (2002).

[30] D. Vion , A. Aassime, Cottet A., Joyez P., Pothier H., Urbina C., Esteve D., Devoret M.H., to be published in Fortschritte der Physik.

[31] D. Vion , A. Aassime, Cottet A., Joyez P., Pothier H., Urbina C., Esteve D., Devoret M.H., to be published in Physica C.

[32] D. Vion, A. Aassime, A. Cottet, P. Joyez, H. Pothier, M.H. Devoret, C. Urbina, D. Esteve, to be published in Physica E.

[33] D. Vion, A. Aassime, A. Cottet, P. Joyez, H. Pothier, C. Urbina, D. Esteve, and M.H. Devoret, in "Experimental Quantum Computation and Information", F. De Martini and C. Monroe eds., IOS Press 2002, pp. 475-491.

[34] I. I. Rabi, Phys. Rev. **51**, 652 (1937).

[35] Siyuan-Han, Yang-Yu, Xi-Chu, Shih-I-Chu, Zhen-Wang, Science. **293**, 1457 (2001).

[36] J. M. Martinis, Sae woo Nan, J. Aumentado, and C. Urbina (to be published).

[37] Y. Nakamura (private communication).

[38] N. F. Ramsey, Phys. Rev. **78**, 695 (1950).

[39] Josephson B.D., Rev. Mod. Phys. **36**, 216 (1964).

[40] A. Barone and G. Paternò, *Physics and applications of the Josephson effect* (Wiley, New York, 1982).

[41] M. Büttiker, Phys. Rev. B **36**, 3548 (1987).

[42] P. Joyez, *Le Transistor à une Paire de Cooper*, thèse de doctorat (Paris VI, 1995); See www-drecam.cea.fr/drecam/spec/Pres/Quantro/Index.htm.

[43] *Single Charge Tunneling*, edited by H. Grabert and M. H. Devoret (Plenum Press, New York, 1992).

[44] Ederlyi, Magnus, Oberhettinger and Tricomi (Bateman manuscrit) *Higher transcendantal functions*, Vol 3, McGraw-Hill.

[45] A.B. Zorin, Phys. Rev. Lett. **76**, 4408 (1996).

[46] Cohen-Tannoudji C., Diu B., Laloë F., *Mécanique quantique T II*, Hermann, Paris.

[47] E. Paladino, L. Faoro, G. Falci, and R. Fazio Phys. Rev. Lett. **88**, 228304 (2002)

[48] A. Abragam, *The Principles of Nuclear Magnetism* (Clarenton press, Oxford, 1961).

[49] M.H Devoret, *Quantum Fluctuations in Electrical circuits*, in "*Fluctuations Quantiques*', Elsevier Science, 1997.

[50] Landau D.L., Lifchitz E.M, *Téoréticheskaïa fizika v10 tomakh*, Tom II Mékhanika, Naouka, Moska.

[51] M. Tinkham *Introduction to superconductivity*, second edition, McGrawHill.

[52] P. Lafarge, P. Joyez, D. Esteve, C. Urbina, and M.H. Devoret, Nature **365**, 422 (1993).

[53] D. Vion, M. Gotz, P. Joyez, D. Esteve, and M. H. Devoret, Phys. Rev. Lett. **77**, 3435 (1996).

[54] G.L Ingold and H. Grabert, Phys. Rev. Lett. **83**, 3721 (1999).

[55] K. Likharev *Dynamics of Josephson junctions and circuits*, Gordon and Breach science publishers.

[56] Y.T. Coffey, Y.P. Kalmykov, J.T. Kalmikov, *The Langevin equation* World Scientific.

[57] Yu. M. Ivanchenko and L.A. Zil'berman, Zh.Eksp. Teor. Fiz 55, 2395, (1968) [Sov. Phys. JETP 28, 1272 (1969)].

[58] V. Ambegaokar and B. I. Halperin, Phys. Rev. Lett. **22**, 1364 (1969).

[59] M. Tinkham, chapter 4, in *Single Charge Tunneling*, edited by H. Grabert and M. H. Devoret (Plenum Press, New York, 1992).

[60] M. E. Huber, A.M. Corey, K.L. Lumpkins, F.N. Nafe, J.O. Rantschler, G.C. Hilton, J.M. Martinis, and A.H. Steinbach. Applied Superconductivity **5**, 425 (1998).

[61] T.A. Fulton and L.N. Dunkleberger, Phys. Rev. B, 9, 4760 (1974).

[62] R.J. Schoelkopf *et al.*, Science, 280, 1238 (1998).

[63] G.J. Dolan and J.H. Dunsmuir, Physica B **152**, 7 (1988), J. Romijn and E. Van der Drift, Physica B **152**, 14 (1988).

[64] T.A. Fulton and G.J. Dolan, Phys. Rev. Lett. **59**, 109 (1987).

[65] K.C. Gupta , Ramesh Garg , I.J. Bahl , *Microstrip lines and slotlines*, Artech (1979).

[66] D. Vion , P.F. Orfila , P. Joyez , D. Esteve and M.H. Devoret J.Appl.Phys. **77**, 2519 (1995).

[67] J. M. Martinis, M. H. Devoret and J. Clarke, Phys. Rev. B. **35**, 4682 (1987)

[68] U. Weiss, *Quantum dissipative systems*, Volume 2 of *Series in Modern Condensed Matter Physics*, World Scientific, Singapore.

[69] H.P. Breuer and F.Petruccione *the theory of open quantum systems*, Oxford university press (2002).

[70] V. B. Braginsky and F. Ya. Khalili, *Quantum Measurement* (Cambridge University Press, 1992)

[71] Y. Makhlin, G. Schön, and A. Shnirman, Rev. Mod. Phys. **73**, 357 (2001).

[72] A.Shnirman and G. Schön, Phys. Rev. B, Vol.57, 15400-15407 (1998).

[73] A. Messiah, *Mecanique quantique T.I*, Dunod.

[74] C.W. Gardiner and P. Zoller, *Quantum noise*, second edition, Springer-Verlag, Berlin (2000).

[75] P. Joyez et D.Esteve, Phys. Rev. B, Vol.56, 1848-1853, 1997.

[76] G. Ingold and Yu. V. Nazarov, chapter 2 in *Single Charge Tunneling*, edited by H. Grabert and M. H. Devoret (Plenum Press, New York, 1992).

[77] M.H. Devoret, R.J. Schoelkopf, Nature **406**, 1039 (2000).

[78] A. B. Zorin, Physica C **368**, 284 (2002).

[79] F. W. J. Hekking, O. Buisson, F. Balestro, and M. G. Vergniory, in *Electronic Correlations: from Meso- to Nanophysics*, T. Martin, G. Montambaux and J. Trân Thanh Vân, eds. (EDPSciences, 2001), p. 515.

[80] Kramers H., Physica (Utrech) **7**, 284 (1940).

[81] M. H. Devoret, J. M. Martinis, D. Esteve and J. Clarke, Phys. Rev. Lett. **53**, 1260 (1984).

[82] A. J. Leggett, Phys. Rev. B 30, 1208 (1984); D. Esteve, M. Devoret and J.M. Martinis, Phys. Rev. B **34**, 158 (1986)

[83] J. Ankerhold and H. Grabert, cond-mat/0304232 (2003)

[84] F.C. Wellstood, C. Urbina, J Clarke, Appl. Phys. Lett. **50**,772 (1987).